Methodology for the Evaluation of Human Response Variability to Intrinsic and Extrinsic Factors Including Uncertainties

A Dissertation

Presented to

the faculty of the School of Engineering and Applied Science

University of Virginia

in partial fulfillment
of the requirements for the degree

Doctor of Philosophy

by

Daniel Perez Rapela

May 2020

APPROVAL SHEET

This Dissertation
is submitted in partial fulfillment of the requirements
for the degree of
Doctor of Philosophy

Author Signature: ______________________________

This Dissertation has been read and approved by the examining committee:

Advisor: Jeff R. Crandall

Committee Member: Jason R. Kerrigan

Committee Member: Jason L. Forman

Committee Member: Matthew B. Panzer

Committee Member: Timothy L. McMurry

Committee Member: Samuel H. Huddleston

Accepted for the School of Engineering and Applied Science:

Craig H. Benson, School of Engineering and Applied Science

May 2020

Abstract

The use of standardized anthropomorphic test devices and test conditions prevent current vehicle development and safety assessments from capturing the breadth of variability inherent in real-world occupant responses. The central idea of this dissertation is that human body models used in simulations with a diverse range of real-world impact scenarios can represent population variability and may be the key to overcome the limitations of current vehicle assessment and development methodologies. In this approach, a series of response surfaces are created that contain information about the occupant responses as a function of different input variables. Subsequently, these surfaces, in conjunction with real-world distributions of the population and impact conditions, can be used to identify populations at risk, to illustrate injurious impact scenarios, and to inform prioritization of countermeasure and design actions.

This dissertation develops a methodology to assess occupant response that accounts for sources of intrinsic (human-related) and extrinsic (non-human-related) variability, including uncertainty in the FE parameters. Although inherently generic in nature, this methodology was applied to a far-side crash scenario in order to provide an illustrative example.

For the far-side application, lateral head excursion and thoracic injury were identified as the target occupant responses, while change in vehicle velocity, impact direction and seatbelt load limiter were the extrinsic factors explored. The intrinsic factors were occupant height, weight and waist circumference and were explored by morphing the simplified GHBMC human body model. WorldSID tests were used in order to validate and estimate the parameter uncertainty in the vehicle FE model. Five regression techniques, namely, linear regression, logistic regression, LASSO linear and logistic regression, and Neural Networks (NN), were used for the generation of the response surfaces. The regression models were sequentially trained to represent the maximum lateral head excursion and the probability of 3+ fractured ribs using a total of 405 FE simulation results. The performance of these regression techniques was assessed

based on their ability to predict out-of-sample datapoints. The NN showed equal or improved performance with respect to the other regression techniques.

Based on far-side input conditions derived from US field data, Monte-Carlo simulations used the head excursion and rib fracture response surfaces to calculate the probability of head-to-intruding-door impacts and cases with 3+ fractured ribs. In addition, the Monte-Carlo analysis predicted head contact and rib fracture reductions subsequent to design changes in the restraint configuration. This analysis indicated that the vehicle used in this study would lead to a range of 667 to 2,448 head-to-intruding-door impacts and a range of 2,893 to 3,783 cases of 3+ fractured ribs, depending on the seatbelt load limiter. In the US field data, the expected number of cases with 3+ fractured ribs was 3,958. The far-side assessment illustrates how the methodology incorporates the intrinsic and extrinsic variability, generates response surfaces that characterize the effects of the variability, and ultimately permits vehicle design considerations and injury predictions appropriate for real-world field conditions.

Dedication

To my parents, for teaching me the value of effort and commitment. I would be a very different person without their example, guidance and support. This dissertation would not have happened without them. To Kasia, for her invaluable love and support during these intense times. We made it through together.

Acknowledgments

I wish to express my deepest gratitude to my advisor, Professor Jeff Crandall, who gave me the opportunity to join the CAB and guided me through this endeavor. His continuous pursuit of excellence will always be a source of inspiration for me. I would also like to extend my most sincere gratitude to the entire Advisory Committee, whose critical feedback has been invaluable for the quality of this dissertation. Special thanks to Dr. Jason Forman, whose day-to-day advice and support have been essential for me during all these years. Many thanks to Dr. Carlos Arregui-Dalmases, who introduced me to Dr. Crandall, the CAB, and the great professionals that work there. I would like to thank all CAB members for all these years of work and friendship. It has been an absolute pleasure.

Contents

List of Figures

List of Tables

Chapter 1

Introduction

1.1 Background

1.1.1 Current state of occupant safety

Improvements in vehicle safety have contributed to saving over 600,000 lives from 1960 through 2012 in the US (Kahane, 2015). In spite of this success, more than 1.2 million people lose their lives on the road worldwide annually, and as many as 50 million others are injured (WHO, 2017). Even though high-income countries have taken a number of actions to reduce these figures, the number of traffic-related injuries and fatalities in these countries is still in the range of the millions and thousands per year, respectively (NHTSA, 2019).

These global traffic statistics provide the overall summary of the millions of traffic crashes and the individual occupant responses derived from them. The variability observed in the individual responses is a consequence of the differences in the input crash conditions. These input conditions, that can be defined by intrinsic (human-related) and extrinsic (non-human-related) factors, can theoretically be described by probability distributions and play a major role in the crash outcome (figure 1.1). Current knowledge about the input distributions and their effects on the individual occupant response is sparse and only relatively available for a limited number of factors (e.g., Δv, age). Therefore, the distributions, effects and interactions of most of the input factors remain uncertain.

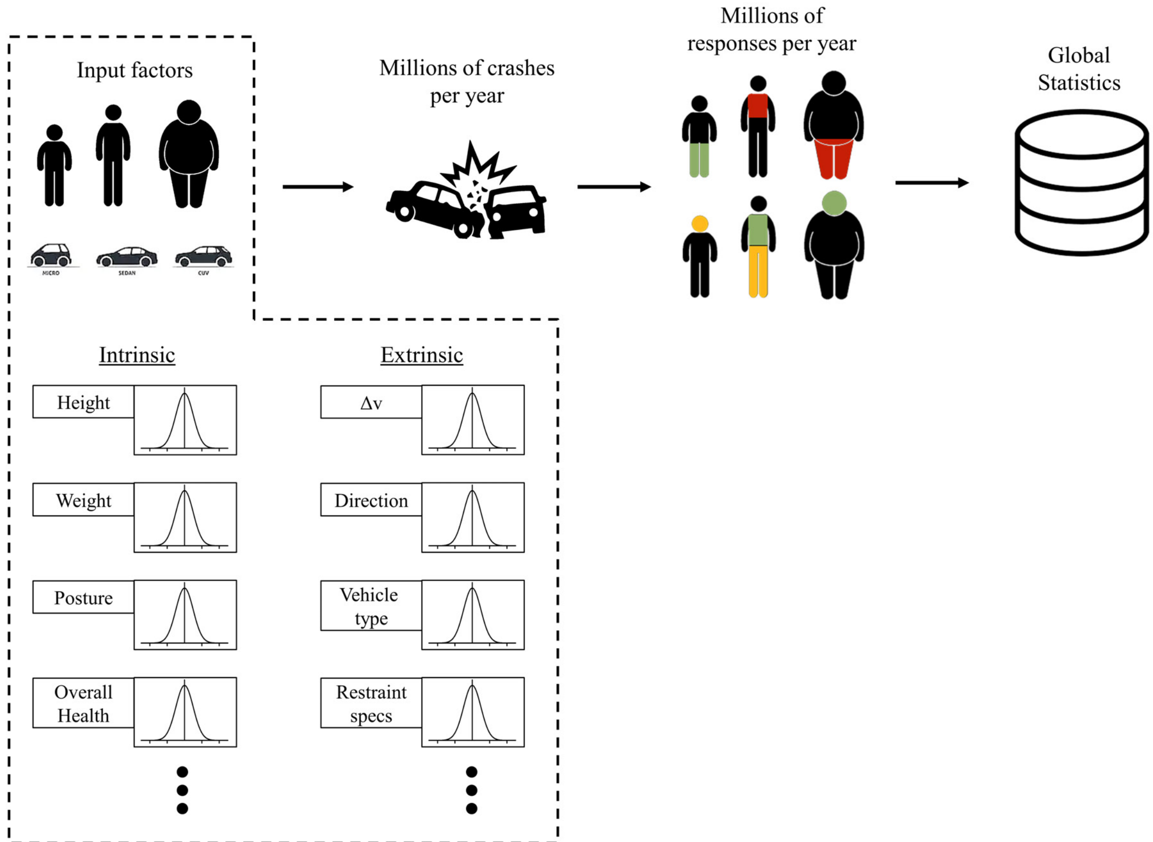

Figure 1.1: Flowchart from crash input factors to global crash statistics

1.1.2 Current strategies for the assessment and development of occupant safety

Historically, most of the vehicle improvements for safety have been encouraged by regulation and enabled by the development of biofidelic Anthropomorphic Test Devices (ATD).

ATD are human surrogates developed to represent specific human populations in specific crash conditions. These devices are designed to meet specific population height and weight percentiles and response corridors based on PMHS and volunteer data. Additional factors like sex and age are indirectly contemplated via injury risk functions. The cost of developing, fabricating and using these devices limits the breadth of the population and impact conditions they can represent. Therefore, most of the human variability and the interaction among human attributes remains totally unexplored. Restrictions in their construction due to durability, manufacturability, repeatability and reproducibility requirements, limit their ability to replicate human behavior and can have a negative influence on biofidelity (Crandall et al., 2011). The difficulty of reproducing omnidirectional human-like responses has led to the development of direction-specific ATD. These devices are optimized to perform in a particular environment, sitting posture and impact mode. Relatively small changes in the impact conditions can lead to a severe drop in the ATD's ability to represent human-like responses (Sunnevång et al., 2014). Therefore, the interpretation of ATD results in scenarios other than their design impact mode is questionable (Crandall et al., 2011). This lack of versatility further limits our ability to explore human response to changes in sitting posture, vehicle restraint, impact direction, etc. Since most ATD cannot assess failure in a direct manner, these devices use kinematic and kinetic injury criteria to assess injury risk. The metrics required for the different injury criteria are measured by sensors build into the ATD. These sensors are located to capture a limited number of load-case-specific injury mechanisms and are only capable of recording body region kinetics and kinematics rather than tissue specific stress-strain attributes. This may lead to missing multiple injury sources and mechanisms when the ATD is used outside of its impact direction specifications or in non-standard vehicle environments.

Current regulation includes a number of standardized physical tests, where occupant safety is assessed using specific ATD. In addition to regulatory tests, non-governmental entities (e.g., IIHS, Euro NCAP) perform additional standard ATD-based tests to inform consumers about the occupant safety levels of specific vehicles. Given the limited resources and the expensive nature of ATD tests, the number of input factors explored in these standardized tests is very reduced. These tests are performed in specific impact configurations (e.g. velocity, angle, barrier overlap, etc.) that are the same for all vehicles. These conditions are normally set through an estimated benefit analysis or targeted to represent an average event based on impact or injury severity (Hollowell et al., 1998; Ellway et al., 2013).

Although many vehicle manufacturers implement some degree of human body modeling in their decision making, most them rely on these ATD tests to assess and develop their vehicles (figure 1.2). This approach to safety assumes that the individual occupant responses can be represented using a very limited number of datapoints and that, therefore, improving the vehicle's performance in these tests would scale to other, not represented, impact conditions and generate a positive impact in the global statistics (e.g., total number of injuries).

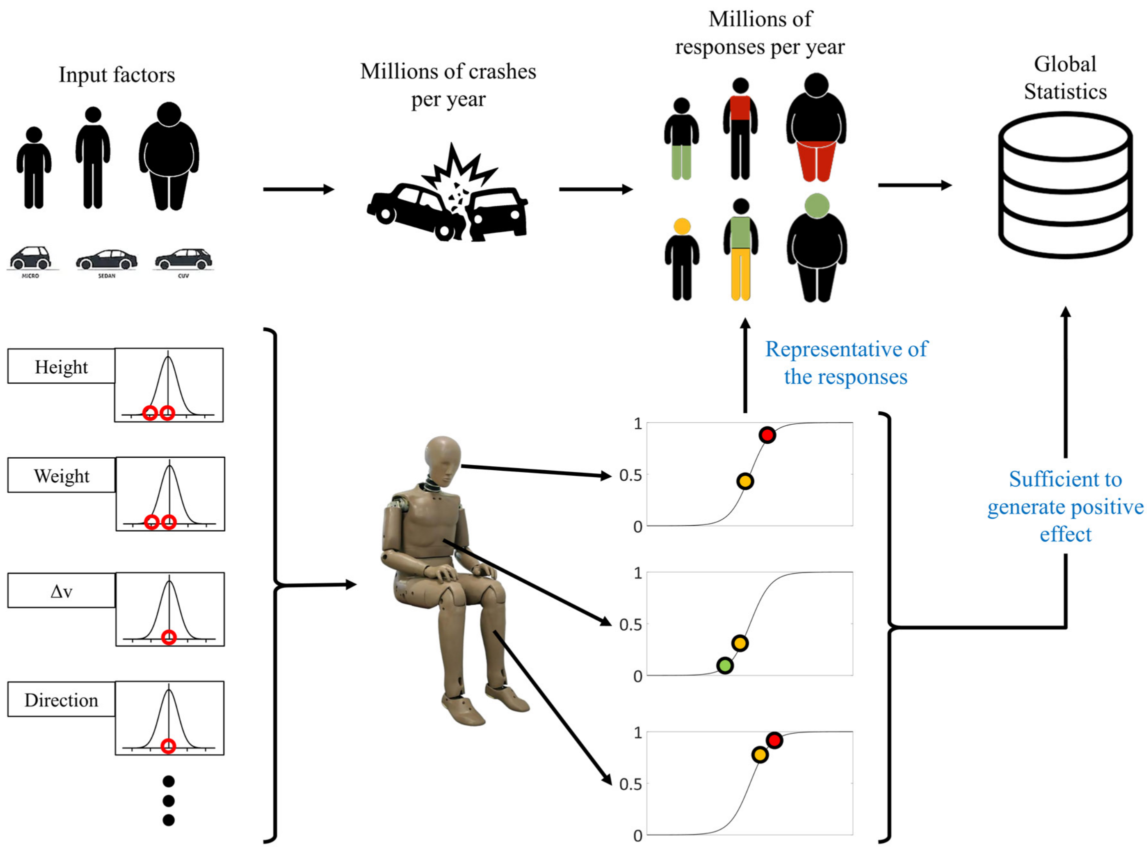

Figure 1.2: ATD-based approach to vehicle assessment and development (main assumptions in blue)

1.2 Motivation

Although current vehicle safety assessment and development methodologies have led to saving thousands of lives, future improvements require strategies targeted at greater degrees of specificity of intrinsic and extrinsic factors. Current methodologies show limitations that need to be addressed in order to increase current levels of vehicle safety for a wider range of the population and impact conditions.

1.2.1 Limitations of current vehicle safety assessment and development methodologies

Complying with vehicle safety regulations and consumer tests is still the main safety focus of vehicle manufacturers. As a consequence, current vehicle development is largely based on a very small sub-sample of impact scenarios unable to capture human response variability. This ATD-based approach prevents the exploration of the effect that most of the input factors and their interactions have on human response or restraint performance. This lack of variability exploration overlooks potential injurious scenarios and may lead to hyper-optimized restraints. That is, restraints that may not be effective for a large percentage of the population and impact conditions. The consequences derived from these limitations may partially explain the differences in protection observed for different segments of the population (Viano et al., 2008; Bose et al., 2011; Forman et al., 2019).

Moreover, vehicle safety performance criteria would ideally be associated to the probability of injury or fatality for the entire population in any impact condition. This would directly target the global reduction of the injuries and fatalities observed in the field. This requires a level of understanding of occupant, vehicle and restraint response that ATD-based assessments cannot provide. The limited number of available tests forces these assessments to contemplate a limited number of populations and impact conditions in their performance criteria. This leads to assessments that rank vehicles and restraint systems according to their associated probability of injury for a limited number of populations but are not able to quantify the effect that releasing a particular vehicle would have in the global number of injuries and fatalities observed in the field.

Thus, improving vehicle safety requires the implementation of vehicle safety assessment and development methodologies that take into account human response variability to intrinsic and extrinsic factors.

1.2.2 Challenges in introducing human response variability in the assessment and development of occupant safety

Current ATD-based vehicle safety assessments use ATD to understand human response. However, these devices show limitations for their use in the exploration of human variability.

ATD only represent a limited number of populations. This limits our ability to explore human variability. Moreover, these devices are unidirectional in nature. That is, they are designed to represent human kinematics and kinetics in a narrow range of impact directions. The injuries these devices can represent are also limited to a number of known injury mechanisms. These mechanisms are direction dependent and, sometimes, also restraint dependent. Therefore, ATD offer very limited ability to explore non-standard restraints or impact directions. These limitations, in combination with the time and cost associated with their development and use, make these surrogates unfit to explore human response variability.

On the other hand, Finite Element (FE) Human Body Models (HBM) show characteristics that make them the best available tool to understand human response variability (Gayzik et al., 2011; Schwartz et al., 2015). HBM are computational models that, when correctly validated, are capable of predicting human response. These models are developed to represent the anthropometry and, sometimes, morphology of specific individuals or populations. The abilities of HBM are not constrained by limitations or costs derived from physical manufacturing and, therefore, offer advantages over ATD. Their computational nature allows for the creation of multiple models to represent diversity in the population by changing their geometry (e.g., through morphing), connectivity or material properties. Moreover, provided appropriate validation, HBM can also be used in multiple impact modes and sitting postures. These models also have the ability to predict not only injury risk through the use of injury criteria but also strain-based tissue-level injury. Therefore, their injury prediction abilities are not constrained to specific injury mechanisms. However, in spite of their advantages and decades of use in research (Yang et al., 2006), their use in vehicle development is still very limited. Although some manufacturers do implement these models as part of their decision making, most of the development decisions are made based on ATD results alone. This resistance to use HBM is multifactorial:

First, manufacturers have to comply with existing testing-based regulation. This limits their ability to introduce additional human surrogates since potentially conflicting results need to be resolved to favor ATD performance.

Second, improvements based on HBM results are difficult to market since they have no influence in regulation or consumer tests ratings. This limits their ability to commit to the potential investments and costs derived from the use of surrogates not contemplated in regulation or consumer tests.

Based on this, it is clear that implementing variability-based assessments in regulation and consumer tests is key for their introduction in vehicle design. Although these entities have shown willingness to introduce HBM in their assessments (NHTSA, 2016; NCAP, 2017b) some key issues remain unaddressed:

First, utilizing HBM requires the use of FEM and therefore introduces uncertainty in the assessment. Part of this uncertainty is inherent to any model, not only FEM, since models are only approximations of reality. Another contributor to uncertainty is the lack of knowledge of the specific parameter values to be used in the models (e.g., friction between parts). Controlling for uncertainty is key for a realistic assessment. Therefore, methods for controlling uncertainty in the FEM need to be developed for the introduction of HBM in standardized assessments.

Second, there is currently no published methodology for the evaluation of human response variability that takes into account intrinsic, extrinsic and model uncertainty factors.

1.2.3 Central idea of the dissertation

The central idea of this dissertation is that HBM, capable of representing population variability, in combination with validated vehicle models subjected to a diverse range of field-based impact scenarios may be the key to overcome the limitations of current ATD-based vehicle assessment and development methodologies. In this new approach a series of response surfaces are created and contain information about the occupant responses of interest as a function of intrinsic (human) and extrinsic (non-human) factors. These response surfaces can be used, among other things, to quantify the estimated number of injury or fatality cases associated to a vehicle design taking into account the underlying real-world distribution of the population and impact conditions (figure 1.3).

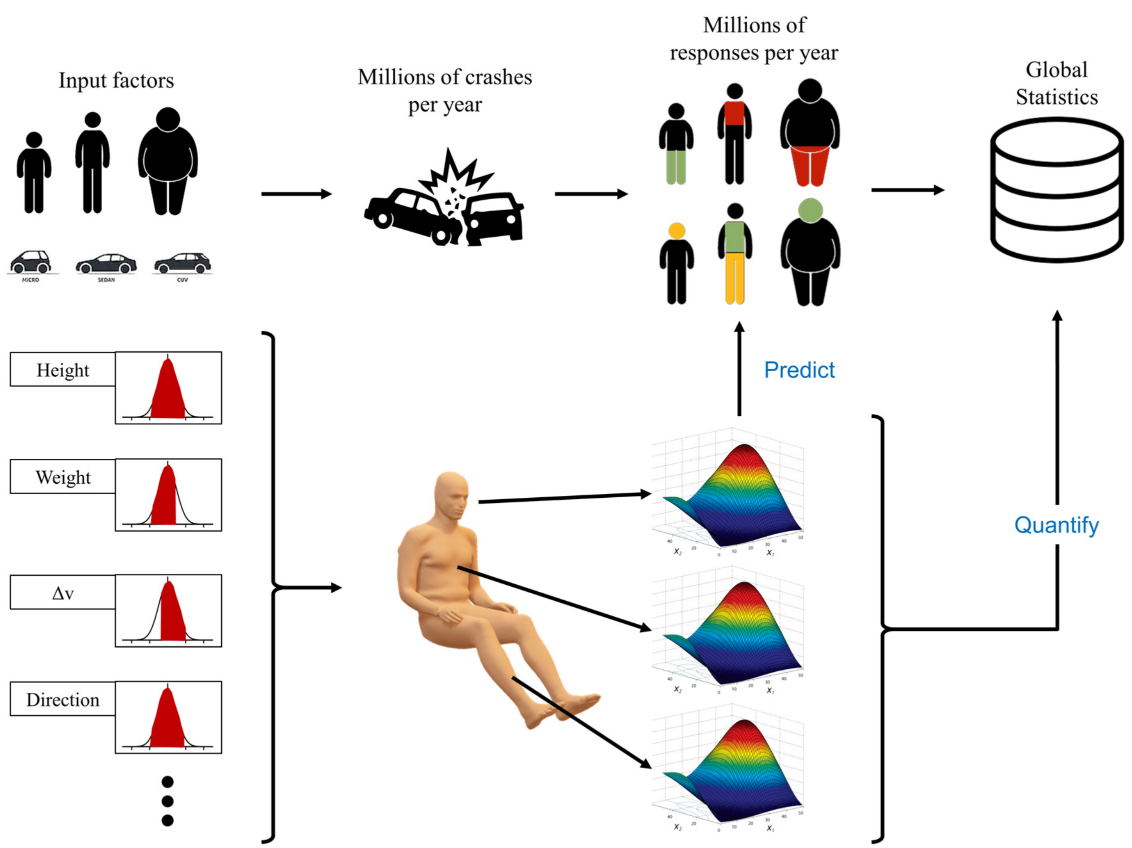

Figure 1.3: Variability-based approach to vehicle assessment and development (main assumptions in blue)

One of the key differences of this new approach with respect to ATD-based assessments is that the intrinsic and extrinsic factors explored in the assessment are defined as distributions and not as discrete datapoints. The specific factors and the ranges to be explored in this methodology depend on the specific end application. The goal is to identify factors that may have an effect on human response for the identified case of interest, the range of variation to explore and their probability of occurrence. In order to reduce the number of input factors to a feasible exploration domain, their selection may be conducted based on a prioritization methodology. Using probability distributions as input factors, instead of discrete points, allows for the calculation of the probability distributions of the human responses of interest, taking into account variability in the population and impact conditions.

As in the selection of input factors, studies may focus on different human responses (e.g., chest injury) depending on their end goal. However, these responses should be selected with the aim of evaluating injury potential. These responses may be selected and prioritized based on their frequency on the field, although selection based on other criteria should also be considered, especially if the vehicle presents features that may shift injury patterns from those observed in the field (e.g., particular restraint configurations).

The HBM selected for the generation of the response surfaces should be able to represent the responses of interest and the selected intrinsic factors. These factors can be represented by modifying the model geometry, connectivity or constitutive definitions in order to explore variability in anthropometry or tissue characteristics, among others.

The vehicle environment should be validated using physical tests. These tests may be created in a hierarchical manner and build up to a full model. Traditional FEM calibrations (figure 1.4 - up) optimize the value of a number of model parameters to match the results of physical tests. This deterministic approach does not take into account any uncertainty in the estimation of the model parameters and leads to a unique model with a unique set of model parameters (e.g., $\mu_{seatbelt} = 0.5$). As mentioned in section 1.2.2, controlling for model uncertainty is key for the acceptance of FEM in vehicle assessment. In order to ensure that uncertainty in the vehicle FEM is taken into account, the calibration process should lead not to optimized parameter values but to ranges of parameters that meet the a predetermined validation criteria (figure 1.4 - down). This is especially important for those parameters that may have an influence in occupant response. The resulting parameter ranges may be used to explore the effects of model uncertainty in the resulting human response.

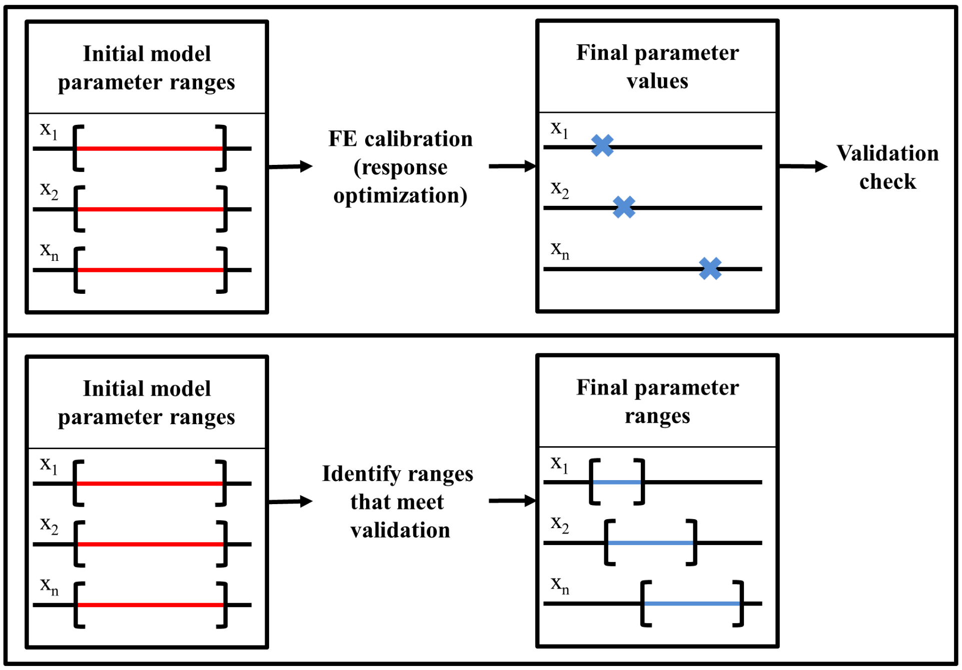

Figure 1.4: Traditional validation (up) and model parameter uncertainty ranges (bottom)

Once the intrinsic, extrinsic and model uncertainty factors are identified, their effects on the occupant responses of interests are evaluated running FE simulations representing these factors. The simulation results are used to construct response surfaces as a function of the different input factors. These surfaces are generated using Machine Learning regression techniques due to their ability to converge to the underlying mathematical model response. A Monte-Carlo (MC) analysis on these surfaces, following the probability distribution of the inputs, leads to the calculation of the probability distributions of the human responses of interest. Since the inputs follow field-based probability distributions, the MC analysis results in field-equivalent occupant response distributions. These resulting distributions are used to estimate the effect that the assessed vehicle would have in the real-world (global statistics). That is, the expected number of events (e.g., injuries) it would be involved in if released in the field. If the data is available, this field-equivalent probability distributions could be directly compared to current real-world data frequency distributions to establish if the assessed vehicle would contribute to a reduction or an increment of injuries or fatalities observed in the field. This would shift vehicle assessment and development from an ATD-based approach, where the probability of injury is only estimated for a very limited portion of the population in very specific impact cases, to an approach able to predict human response and quantify the effect of the vehicle in the real-world statistics.

1.3 Research Goal and Overview

The goal of this dissertation was to develop a methodology that accounts for variability of intrinsic and extrinsic factors including model uncertainties for the evaluation of human response in vehicle impacts.

The proposed methodology, although sufficiently generic to be implemented in any type of impact condition, will be explored using far-side impacts as an application example. Far-side impacts have been recently introduced in Euro NCAP as one of the vehicle safety assessments. Its recent adoption, the lack of a far-side specific ATD and the possibility of testing the scenario in a simple sled environment makes this load case ideal for virtual assessment.

Chapter 2 focuses on the definition of the extrinsic factors and occupant responses to be explored and the HBM and vehicle environment to be used in the study. The extrinsic factors, their frequency in the field and occupant responses were identified based on previously-published field studies. Although multiple extrinsic factors could be selected, this study focused on exploring Δv, impact direction and seatbelt load limiter, based on their, already established, significant effects on occupant response. The vehicle environment was defined to represent the most injurious interior struc-

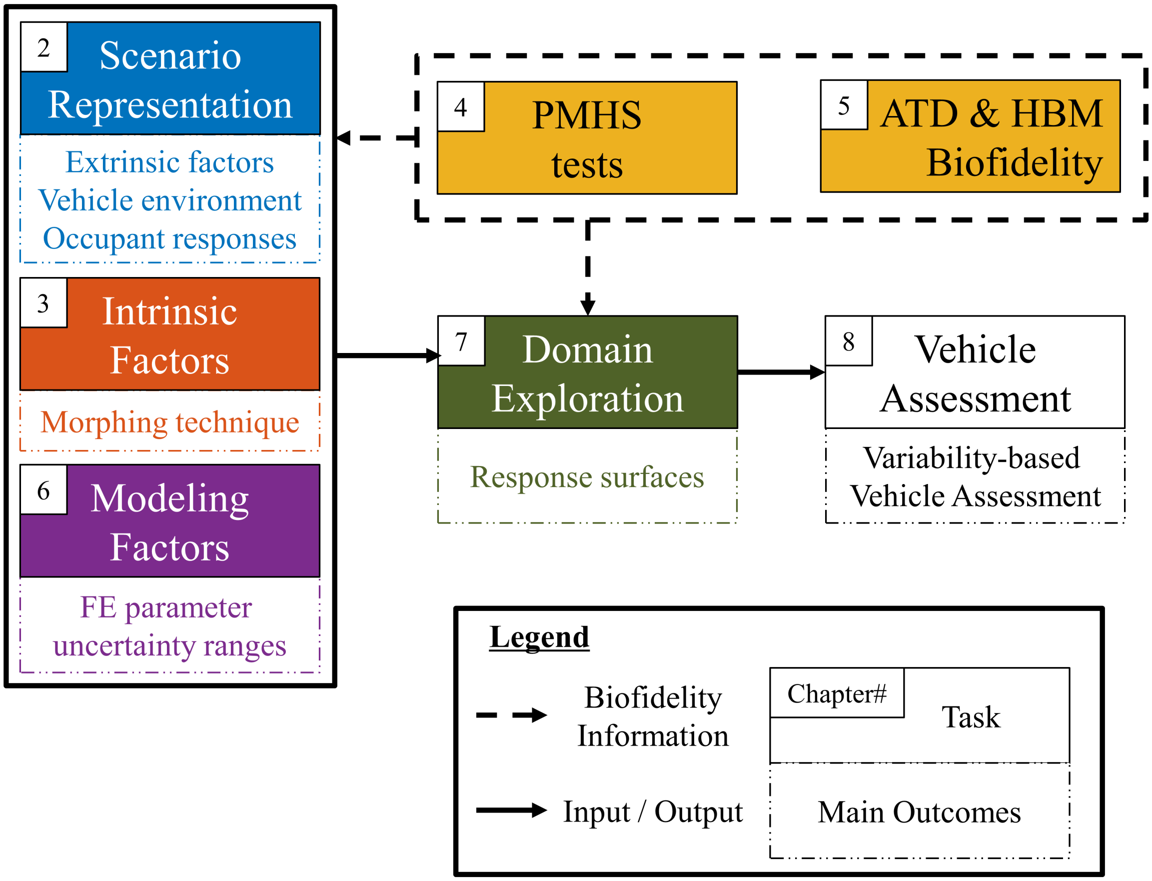

Figure 1.5: Dissertation Flowchart

tures while maintaining model simplicity. The occupant responses to evaluate were identified based on the most commonly injured body regions. Chapter 3 identifies the intrinsic factors to be explore and how to represented them in the HBM. Although multiple intrinsic factor could be selected, this study focuses on the implementation of human anthropometry variability. This chapter presents a methodology for the implementation of human anthropometry variability through morphing. The anthropometry parameters to be controlled for are identified using previously published PMHS tests. The ANSUR-II database is used as the representation of the occupant population distribution. Chapter 4 presents a series of PMHS tests conducted using a physical representation of the vehicle environment described in chapter 2. These tests were conducted to better understand in-vehicle human kinematics and injury response in far-side scenarios and to be used in the biofidelity evaluation of the surrogates used in this dissertation (i.e., the WorldSID and the simplified GHBMC). These biofidelity evaluations are presented in chapter 5. In situations where occupant response and surrogate biofidelity is sufficiently understood (e.g., frontal impacts), chapter 4 and 5 may not be necessary. In chapter 6, the vehicle FE model environment is validated based on WorldSID tests. This chapter identifies the model parameter ranges (model uncertainty) to be explored in following steps of the methodology. Chapter 7 presents a methodology for the generation of response surfaces as a function of the intrinsic, extrinsic and model factors identified in chapters 2, 3 and 6, respectively. This chapter uses and compares the performance of linear regressions, logistic regressions, LASSO regularization, and neural networks for the generation of response surfaces. Finally, chapter 8 uses the resulting response surfaces to illustrate their use to assess the vehicle in the study. This assessment gives an estimation of the annual number of occupants that would contact the intruding door or suffer 3+ fractured ribs as a consequence of far-side impacts involving the assessed vehicle.

THIS PAGE INTENTIONALLY LEFT BLANK

Chapter 2

Representation of Far-Side Scenarios

This chapter focuses on identifying the key aspects to be taken into account in the representation of far-side scenarios. The results from this chapter are used to define the vehicle environment to be used for the physical tests and the FEM simulations in chapters 4, 5, 6 and 7 and to determine the human responses, the extrinsic factors and their ranges and the HBM to be explored in chapter 7.

2.1 Introduction

Traditional ATD-based vehicle occupant safety assessment focuses on the evaluation of subsets of the occupant population in a limited number of impact configurations. The expensive nature of physical tests prohibit a broad exploration of variability in the occupant and impact conditions. Thus, the experimental approach limits our ability to understand the performance of a vehicle and restraint configuration for protecting society as a whole.

In far-side scenarios, the only available testing protocol, uses a sled buck with a 50^{th} percentile WorldSID ATD on the driver seat subjected to a Δv of approximately 33 km/h (depending on the vehicle) in a 75-degree PDOF (NCAP, 2017c). This approach, although useful as an initial evaluation, lacks consideration of the effects that variability in the occupant or impact conditions may have on occupant response.

FE models provide an opportunity to explore a broader range of occupant crash and vehicle parameters. Therefore, instead of running a small number of physical test in selected conditions, a virtual assessment can explore ranges of input conditions across a larger portion of the population in a wider set of impact conditions.

The goal of this chapter is to identify the extrinsic factors to be explored in the present methodology, identify the human responses to be evaluated, and the HBM and vehicle environment to be used in this evaluation.

2.2 Methods

The existing literature was used to identify the most commonly injured body regions, injury causation and the impact conditions that have an effect on human kinematic response and injury in far-side crashes. This information is later used to identify and establish ranges for the extrinsic factors to be explored, identify the human responses to be evaluated in the assessment and the HBM and vehicle environment to be used for the evaluation.

2.3 Results

Far-side impacts represent 9.5% and 8.3% of all police-reported automobile crashes and MAIS3+ injury cases, respectively (Bahouth et al., 2015). Multiple far-side studies point to the head and chest as the most commonly injured body regions (Mackay et al., 1993; Frampton et al., 2000; Ryb et al., 2009; Viano and Parenteau, 2010; Bahouth et al., 2015). Current literature quantifies head and chest injury (figure 2.1) as being present in 50% and 69% of all MAIS 3+ occupant cases and 23% and 38% of all AIS 3+ injuries, respectively. Injuries to other body regions range from 7% to 14% of all MAIS 3+ occupant cases and 5% to 17% of all AIS 3+ injuries (Yoganandan et al., 2014; Bahouth et al., 2015). This trend remains similar when sampling only vehicles with good safety score ratings (Brumbelow et al., 2015). Far-side injuries are presumably caused by intruding structures and other components of the vehicle interior adjacent to the occupant including the seatbelt, center console and seat (Mackay et al., 1993; Frampton et al., 2000; Ryb et al., 2009; Yoganandan et al., 2014; Bahouth et al., 2015; Brumbelow et al., 2015). In particular, head injuries were found to be mainly caused by the intruding side of the vehicle (figure 2.2) and chest injuries were attributed to a wider variety of impact sources (figure 2.3).

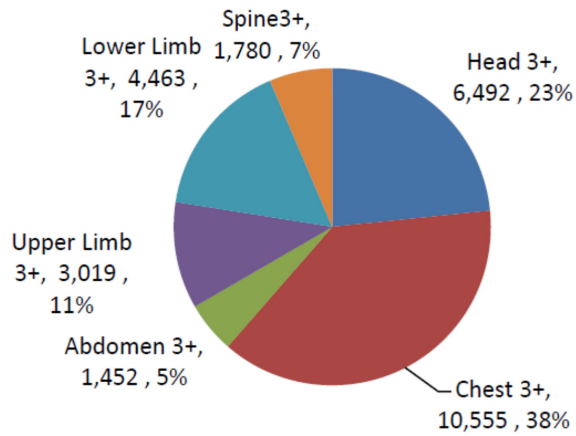

Figure 2.1: Distribution of AIS 3+ injuries (AIS 1998) by body region, belted front seat outboard occupants in far-side crashes NASS CDS 2004-2013 (Annualized data, weighted) (Bahouth et al., 2015)

It is well established that human response varies significantly with changes in the impact conditions. Occupant kinematics show significant differences in head excursion with changes to the Principal Direction of Force (PDOF), Δv and the use of a seatbelt pretensioner (Forman et al., 2013). PDOF and Δv also have a major effect on the injury severity and location observed in the field (figure 2.4). The median Δv is 15 km/h for all far-side cases and 32 km/h for MAIS 3+ injuries. Most of the far-side events and injuries occur at a 60-degree PDOF followed by 90-degree cases. While 30-degree PDOF are also common impact directions, these event are often classified as frontal-oblique rather that far-side scenarios.

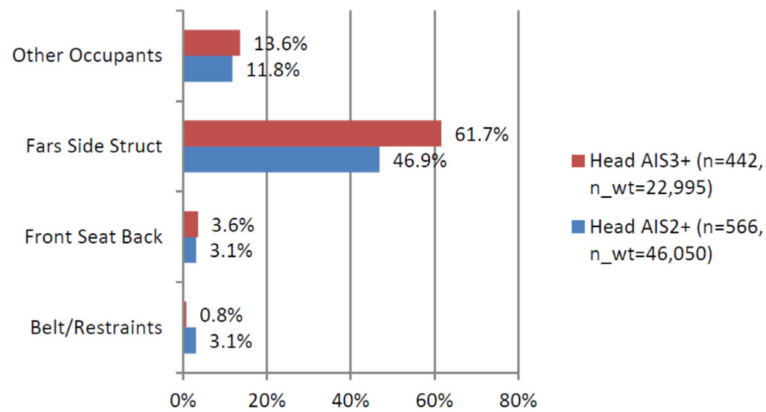

Figure 2.2: AIS 2+ and AIS 3+ head injuries (AIS 1998) by injuring contact for belted front outboard seat occupants in far-side crashes NASS CDS 2004-2013 (Bahouth et al., 2015)

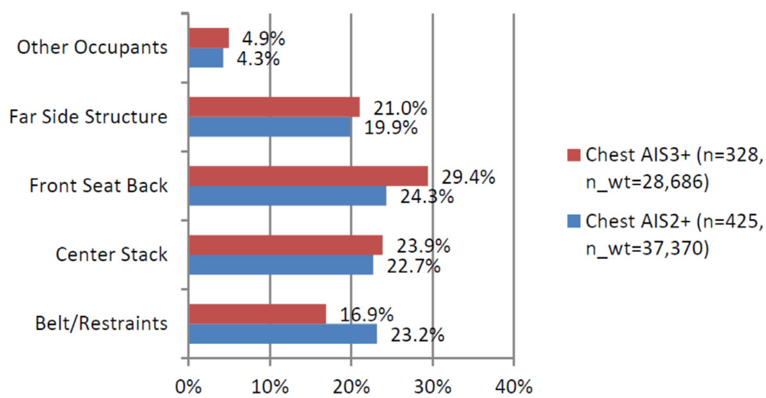

Figure 2.3: AIS 2+ and AIS 3+ chest injuries (AIS 1998) by injuring contact for belted front outboard seat occupants in far-side crashes NASS CDS 2004-2013 (Bahouth et al., 2015)

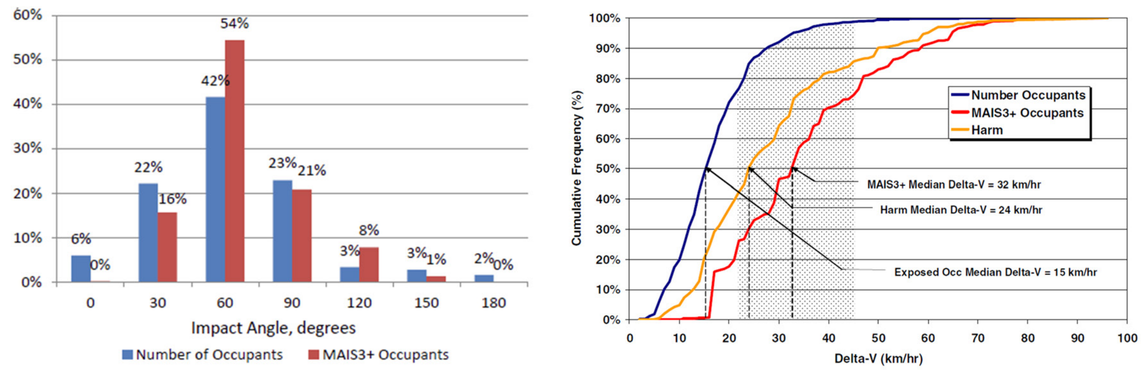

Figure 2.4: Left: Distribution of PDOF (Bahouth et al., 2015). Right: Distribution and explored (shaded area) Δv (Gabler et al., 2005)

2.4 Discussion

2.4.1 Extrinsic factors

Since literature indicates that PDOF and Δv have an effect on occupant kinematics and injury, exploring these factors is essential to understand vehicle performance in the field. This dissertation explored PDOF between and 60 degrees and 90 degrees and Δv between 22 km/h and 45 km/h (chapter 7). The Δv range was selected to represent injurious and non-injurious scenarios and to maintain simulation stability. These ranges encompass most of the injurious PDOF and 50% of the injurious Δv in the field (figure 2.4).

The seatbelt is one of the most important sources of occupant restraint and injury. Since seatbelt parameters have an important influence in restraint performance, this methodology also explored the effect that changes in the seatbelt load limiter have in occupant response.

2.4.2 Vehicle environment

While virtual assessments have the ability to explore a large number of impact scenarios in a relatively inexpensive manner, this computational costs can become an important factor as the model complexity increases. Another important aspect to take into consideration is that the uncertainty of the FE model increases with model complexity. Therefore, the vehicle model environment should be as simple as possible but still maintain the ability to assess the vehicle performance. In this dissertation, relevant interior, restraint, as well as a the vehicle environment was represented by a sled buck able to represent the different Δv and PDOF.

Existing literature demonstrates that the seatbelt, seat and center console are the most common injurious interior structures in far-side scenarios. Therefore, the FE vehicle environment used in this dissertation included these interior structures. While the literature also indicates that the intruding side of the vehicle is responsible for an important percentage of the injuries, representing intrusion via FE can be costly and complex. In order to represent intrusion, the model would need to represent at least the Body in White (BiW), doors, door panels and the impacting counterpart. This level of complexity would require a significantly longer time to run and introduce more model uncertainty than a simpler sled configuration. Although this approach can be implemented in future applications of the present methodology, in this application, the intrusion was estimated as a function of Δv based on literature data (Sunnevång et al., 2010).

2.4.3 Occupant responses

Since head and chest are the most commonly injured body regions in far-side scenarios, the maximum lateral head excursion and the probability of 3+ fractured ribs were evaluated for the occupant represented in the simulations. The minimum head-to-intruding-door distance was calculated using maximum lateral head excursion in combination with the estimated vehicle intrusion. This represents the majority of the AIS3+ head injuries observed in the field (figure 2.2). The probability of 3+

fractured ribs was calculated using a stochastic approach developed by Forman et al. (2012). This probability represents an estimation of the probability of thoracic AIS 3 (AAAM, 2015). Since computational efficiency is prioritized for this particular application, the simplified GHBMC was used to explore the methodology. The simplified GHBMC exhibits a biofidelic chest model validated to match PMHS corridor force-deflection and force time-history responses in frontal and side impacts (Schwartz et al., 2015). Moreover, far-side-specific biofidelity evaluation regarding kinematics, kinetics and injury severity prediction indicate that the GHBMC surrogate exhibits sufficient biofidelity to demonstrate the methodology presented in this dissertation (chapter 5).

THIS PAGE INTENTIONALLY LEFT BLANK

Chapter 3

Identification and Representation of Far-Side-relevant Intrinsic Factors

This chapter identifies the anthropometry measurements to explore and presents a morphing methodology for the representation of varied occupant anthropometries. This methodology is used in chapter 7 for the exploration of the effect of human variability on occupant response.

3.1 Introduction

Anthropometry variability has been shown to have significant effects on human kinematic and injury response (Viano et al., 2008; Kent et al., 2010). The field of biomechanics has traditionally overlooked a large part of this variability by dividing the population in different height and weight percentiles with some consideration to age and sex. Although current HBM are capable of incorporating other sources of human variability, the traditional approach of only height-weight consideration continues to be the trend in the literature. Recent studies (Hwang et al., 2016; Hu et al., 2017), introduced a methodology for the morphing of HBM to account for height, weight, age and sex. Although this approach can generate a large number of surrogates, it misses important sources of variation by failing to explore variability within surrogates of the same height, weight, age and sex. The exploration of alternative factors of variability factors and their interactions may be needed to fully understand their contribution to human response. The methodology presented in this study enables the exploration of any set of intrinsic factors and therefore, it encourages the exploration of any factor that may contribute to human response.

Previous PMHS tests (Pintar et al., 2007; Forman et al., 2013) and epidemiology studies (Mackay et al., 1993) have highlighted the effect of upper-body-to-belt engagement in far-side kinematics and injury. Analysis of the results presented by Forman et al. (2013) show that variability in the shoulder belt engagement cannot be fully explained by accounting only for the surrogates' height and weight (Perez-Rapela et al., 2019b). The abdominal region of the surrogates contributes to differences in the shoulder belt routing and the generation of a pocketing effect that prevents the shoulder belt from slipping out of the shoulder (figure 4.22). Since this factor may have an effect on the occupant injury response, the present morphing methodology will incorporate waist circumference as an intrinsic factor along with height and weight.

3.2 Methods

The ANSUR-II database (Gordon et al., 2014) was used to create a joint (multivariate normal) probability distribution between the population height, weight and waist circumference. Once height, weight, and waist circumference of a particular individual were selected for morphing, the remaining anthropometric parameters (figure 3.1) (i.e., the non-controlled parameters) were obtained using a Simulated Annealing (SA) optimization (Kirkpatrick et al., 1983; Vandekerckhove, 2008). The SA process ensured that the weight of the final morphed model met the specified input weight (figure 3.2). This optimization workflow started with the estimation of the Prediction Intervals (PI) for each non-controlled parameter. These PI were created using a linear regression with height, weight and waist circumference as regressors. Subsequently the algorithm selected a random point for each non-controlled parameter within their corresponding PI. The coherence of each parameter with the remaining parameters was checked to ensure compatibility among the different body regions. This was done by ensuring that each parameter value was contained within the PI created using the remaining parameters as regressors. A body (i.e., a set of anthropometric measurements) was considered coherent if all its measurements met this criterion. Once a coherent set of parameters were selected, a Neural Network (NN) was used to provide the expected weight of the morphed HBM as a function of the selected anthropometry parameters (appendix A). The expected HBM weight was compared to the target weight. The anthropometry measurements were accepted for morphing if the weight error was lower than 3% or the SA determined the optimization had finished. Otherwise, a new set of non-controlled parameter values was selected and the cycle continued.

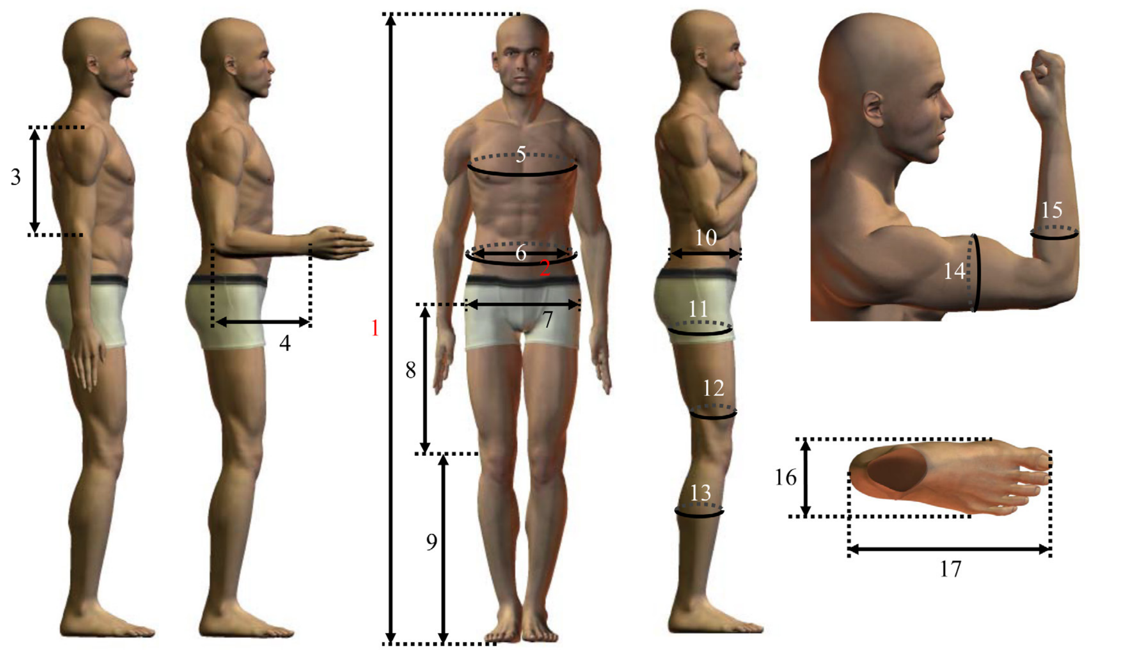

1: Stature (controlled); 2: Waist circumference (controlled); 3: Shoulder-elbow length; 4: Elbow-wrist length;
5: Chest circ.; 6: Waist breadth; 7: Hip breadth; 8: Thigh link; 9: Lateral femoral epicondyle height;
10: Waist depth; 11: Thigh circumference; 12: Lower thigh circumference; 13: Calf circumference;
14: Flexed biceps circ.; 15: Flexed forearm circ.; 16: Horizontal foot breadth; 17: Foot length

Figure 3.1: Anthropometry measurements for morphing (Gordon et al., 2014)

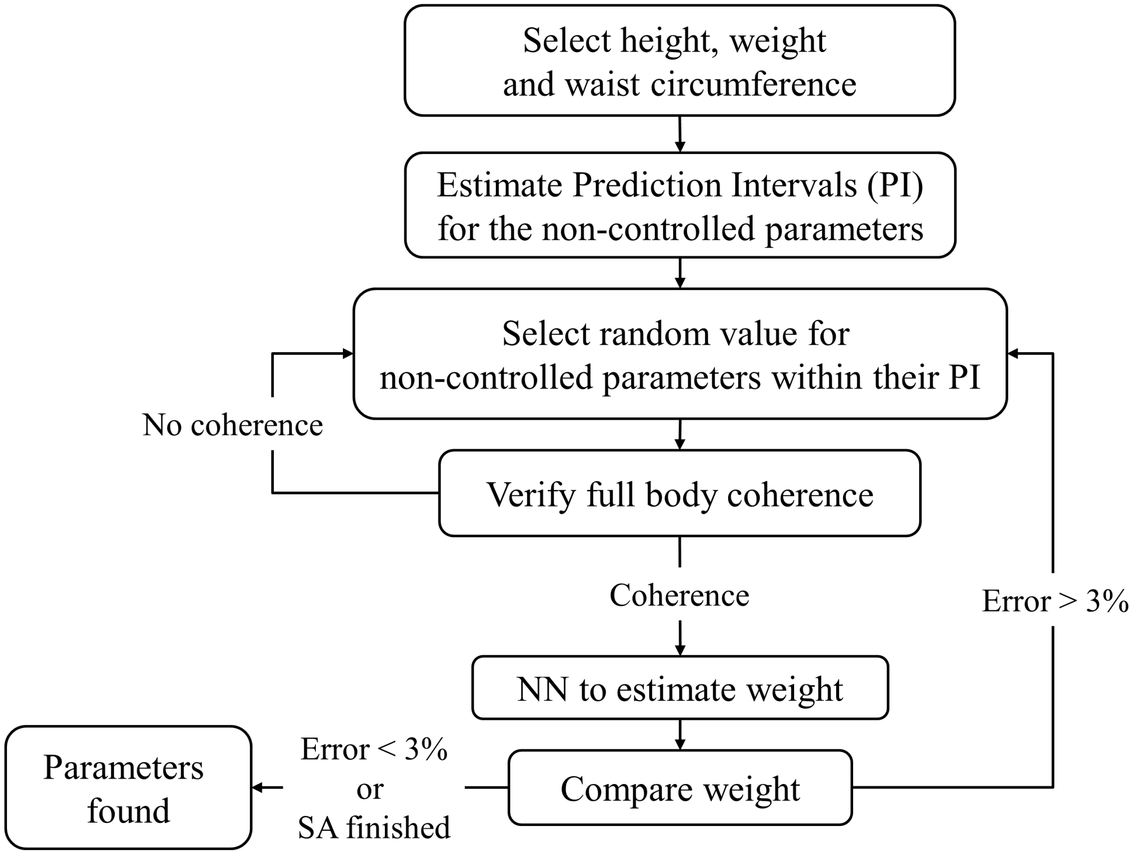

Figure 3.2: Workflow for the selection of non-controlled anthropometry measurements to optimize final HBM weight

Once all parameters were identified, the morphing procedure was conducted using an custom developed Matlab/Piper script (PIPER-Project, 2019) (figure 3.3). This methodology morphed the HBM using a kriging interpolation (Trochu, 1993) conducted in four steps. In a first step, the Matlab script read the original HBM anthropometry, introduced control points in the internal and external structures of the model, calculated the target control points and created a preliminary morph of the model. This preliminary morph was only temporary and served to inform the script of the pelvis deformation needed to maintain sphericity in the acetabulum area in the subsequent morphing steps. In a second step, the target morphing points were recalculated taking into account the acetabulum area and the HBM was morphed again. In this step the HBM was morphed to meet all anthropometry measurements but the waist, arm, forearm, calf, lower thigh and thigh circumferences. In the third step, the model was morphed to capture the waist, arm, forearm, calf and lower thigh circumferences while maintaining a constant bone geometry. On the final step, the thigh region was morphed while maintaining a constant bone geometry.

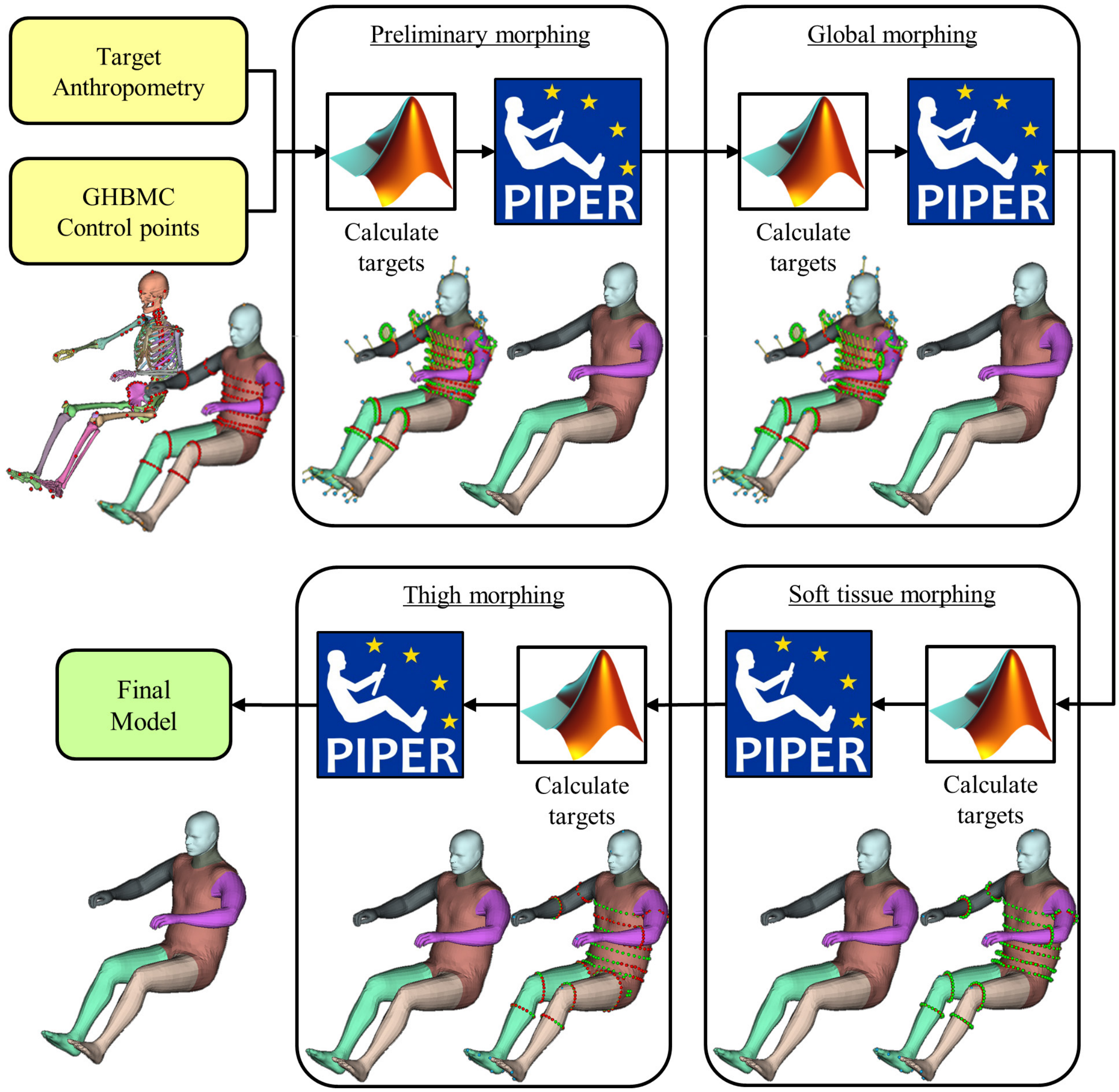

Figure 3.3: Matlab/Piper morphing process

300 surrogates were created to explore the ability of the morphing methodology to represent 90% of the population described by the joint probability distribution using

the simplified GHBMC. The accuracy of the morphing methodology was checked for each body region. Additionally, the resulting Chest Wall Thickness (CWT), bicristal breadth and pelvic link of the morphed models were compared to the population distribution. CWT was measured as the distance between the skin and the pleural cavity measured at the sternum (Frank et al., 2011). Bicristal breadth was measured as the straight-line distance between the right and left iliocristale landmarks (i.e., the superior aspect of the iliac wings) (Gordon et al., 2014). The pelvic link was measured as the vertical distance between the iliocristale right landmark and the level of the trochanterion landmark (Gordon et al., 2014).

3.3 Results

Table 3.1 shows the average and standard deviation error between the anthropometries of the final morphed models and the targets used for their morphing. All average errors and their standard deviations were below 2%. The final distributions of height, weight and waist circumference of the HBM showed good agreement with the underlying ANSUR-II population (figures B.1, B.2 and B.3). The resulting CWT (figure B.4) of the morphed models followed the distribution of previously published volunteer measurements (Frank et al., 2011). The bicristal breadth and the pelvic link of the HBM were contained within the bounds of the ANSUR-II datapoints (figures B.5 and B.6).

The morphing process required approximately 30 minutes per surrogate.

Table 3.1: Morphing average and standard deviation error percentage

Measurement	**% Error (Std. Dev.)**
Height	0.0 (0.0)
Weight	0.8 (0.6)
Waist circumference	1.6 (1.0)
Shoulder-elbow length	0.0 (0.0)
Elbow-wrist length	0.0 (0.0)
Thigh link	0.0 (0.0)
Lateral femoral epicondyle height	0.0 (0.0)
Waist breadth	0.0 (0.1)
Hip breadth	0.0 (0.1)
Waist depth	0.1 (0.2)
Biceps circumference	0.1 (0.2)
Thigh circumference	0.4 (0.6)
Lower thigh circumference	0.5 (0.4)
Chest circumference	0.1 (0.1)
Forearm circumference	0.1 (0.2)
Calf circumference	0.1 (0.1)
Foot length	0.0 (0.1)
Foot breadth	0.3 (0.4)

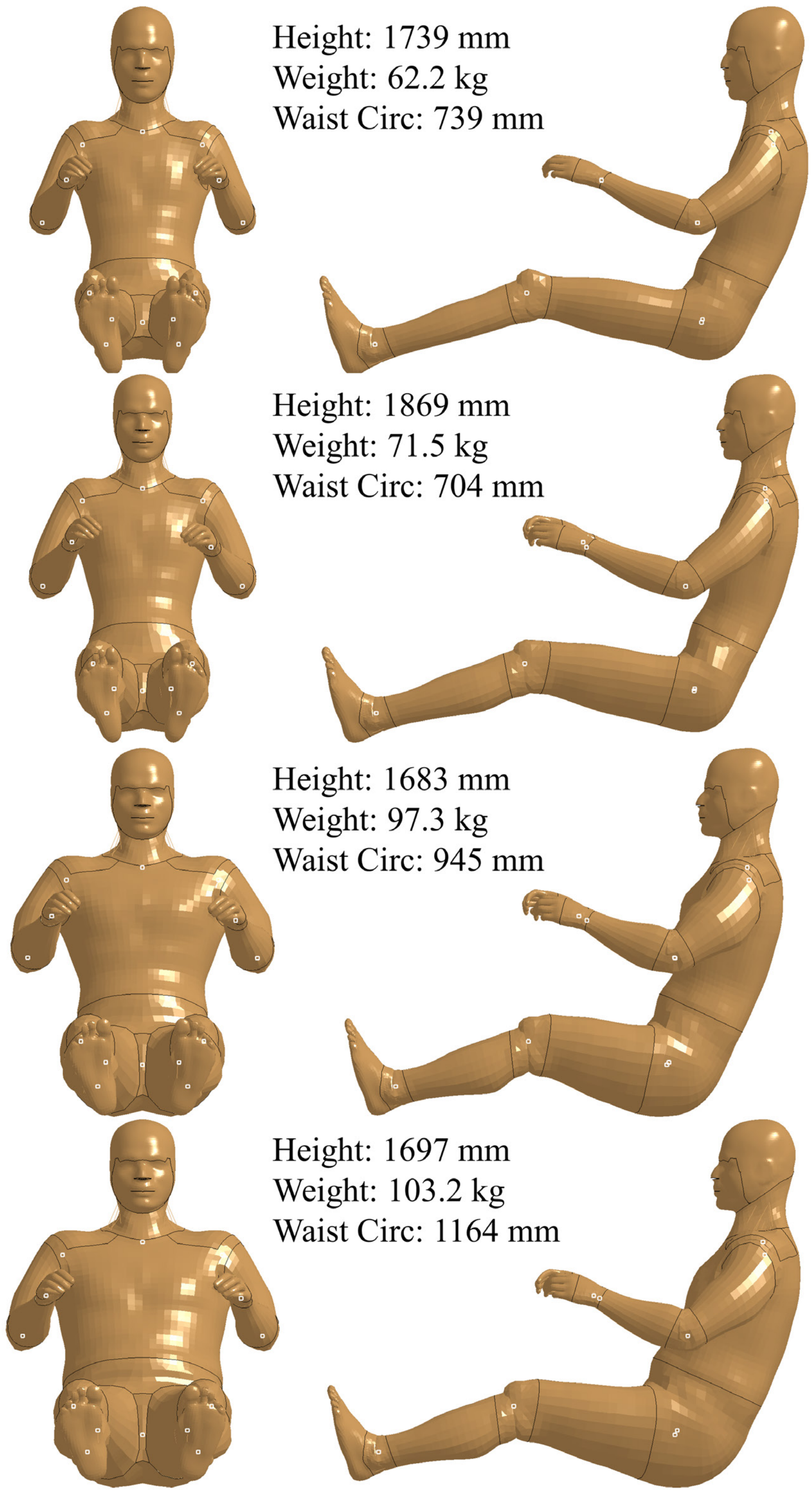

Figure 3.4: Examples of morphed HBM

3.4 Discussion

The present methodology was able to morph the HBM to accurately represent the inputs anthropometries (table 3.1). The joint probability distribution created to relate height, weight and waist circumference was able to represent the underlying ANSUR-II population (figures B.1, B.2 and B.3).

This methodology, unlike those previously published (Hwang et al., 2016; Hu et al., 2017), explores not only variability in height and weight but also waist circumference. In previous studies, this dimension was confounded with height and weight since it was calculated as a result of a deterministic relationship. This fact impedes our ability to understand and account for the effects associated with differences in the shape of the abdominal region. The addition of this dimension may generate meaningful information and help to identify trends and to optimize restraint systems. This is particularly important for load cases like far-side where belt interaction with the abdomen has been shown to have an effect on occupant response (Forman et al., 2013; Perez-Rapela et al., 2019b).

Previously published methodologies estimate the non-controlled parameters in a deterministic fashion. This may lead to discrepancies between the final HBM weight and the initial target weight. In contrast, the present methodology is able to ensure that the final morphed model matches the target morphing weight with an average error smaller than 1% by carrying out a stochastic optimization for the calculation of the non-controlled parameters. This is critical because an uncontrolled weight may lead to a reduction in the explored space or morphed models that do not represent the underlying population. This optimization is conducted using a SA routine that loops through thousands of possible anthropometries with the goal of obtaining a set of anthropometry parameters that minimizes the difference between the target weight and the final model weight (figure 3.2). Since morphing thousands of models to optimize the final weight is not feasible, this implementation uses a NN able to estimate the final weight of the HBM, using the anthropometry measurements as an input variables. The optimization algorithm also ensures that the anthropometry parameters selected in each iteration are coherent with each other. That is, it ensures that the final anthropometry parameters represent a surrogate consistent with the underlying population. It is important to note that, since the non-controlled parameters are estimated in a stochastic manner, the repeated use of this morphing methodology may lead to slightly different surrogates, even if the controlled parameters (height, weight and waist circumference) are kept constant.

The ANSUR database was the only available source of anthropometry information for the development of this methodology. Since this database is a survey on military personnel, the underlying population may not fully representative of the general population (figure 3.4). However, the present methodology is not limited to the use of the ANSUR database and could be potentially followed using different databases (e.g., CAESAR database). The use of broader databases (i.e., those with broader anthropometry ranges) may need of slight modifications to the methodology (e.g., introduction of multiple initial HBM for different regions of the database). Similarly, the methodology can be followed to represent the female population provided that the initial model and database are representative of the female population.

The ANSUR database includes information mainly about external anthropometry. Therefore, the size and shape of the internal bony structures cannot be controlled for. In spite of that, the fact that the CWT, bicristal breadth and pelvis link of the morphed models fit within the underlying population distributions shows that the final morphed models are able to represent the chest and pelvis gross size.

The population exploration was limited to 90% of the space since this is the maximum range of population that can be explored without extrapolation in the controlled parameters (table 3.2).

Table 3.2: Percentage of population database

	90 % of population*	**95 % of population***	**ANSUR (min-max)**
Height [mm]	1585 - 1928	1565 - 1948	1491 - 1993
Weight [kg]	51.5 - 119.1	47.5 - 123.0	39.9 - 145.6
Waist Circumference [mm]	661 - 1220	628 - 1253	648 - 1379

* based on the joint probability distribution

A particular challenge of morphing surrogates in a seated posture is the modification of the abdomen, pelvis and lap region. Since these body regions are adjacent, modifications in the shape of the abdominal region lead to unrealistic pelvic bone and thigh section shapes and, therefore, to potentially incorrect occupant interaction with the lap belt. The morphing methodology presented in this chapter overcomes these issues by conducting independent morphing steps for the pelvis, abdomen and thigh regions. This ensures models with realistic pelvic bones shapes (e.g., spherical acetabula) and thigh sections.

The morphing methodology presented in this chapter was followed to morph the HBM used in this dissertation (chapter 7).

THIS PAGE INTENTIONALLY LEFT BLANK

Chapter 4

PMHS Kinematic and Injury Response in Far-Side Events in a Vehicle-Based Test Environment

This chapter presents a series of PMHS tests conducted to complement current literature and, to understand better the in-vehicle far-side occupant kinematic and injury responses. The sled buck used in these PMHS tests was designed following the requirements defined in chapter 2. The PMHS head and shoulder motion, seatbelt forces, chest deflection and probability of rib fractures will be used in chapter 5 for the biofidelity evaluation of the WorldSID and the simplified GHBMC. These results have been published in Perez-Rapela et al. (2019a).

4.1 Introduction

Far-side impacts represent 9.5% of all automobile crashes and 8.3% of all MAIS3+ injury cases (Bahouth et al., 2015). Numerous studies point to the head and thorax as the most commonly injured body regions (Mackay et al., 1993; Frampton et al., 2000; Ryb et al., 2009; Viano and Parenteau, 2010; Yoganandan et al., 2014; Bahouth et al., 2015; Brumbelow et al., 2015) with a typical intrusion profile between 3 and 4 for AIS 3+ injury severity based on the SAE collision deformation standard (SAE, 1980; Gabler et al., 2005; Yoganandan et al., 2014). These injuries are presumably caused by intruding structures and adjacent components of the vehicle including the seatbelt, center console and seat (Mackay et al., 1993; Frampton et al., 2000; Ryb et al., 2009; Yoganandan et al., 2014; Bahouth et al., 2015; Brumbelow et al., 2015). Understanding human response and improving vehicle performance in this impact condition have recently become the focus of certain consumer test programs (NCAP, 2017c; Pipkorn et al., 2018).

Recent studies have focused on understanding the kinematic and kinetic responses of Post-Mortem Human Subjects (PMHS) in far-side impacts in oversimplified test environments (Fildes et al., 2002; Pintar et al., 2007; Forman et al., 2013). Although these studies have contributed to the understanding of PMHS response in far-side scenarios, they offer limited information about their response in a realistic vehicle environment. Moreover, the parametric evaluations conducted in most of these studies required the repeated use of each PMHS. This limits the evaluation of injury occurrence, causation and timing.

The present study evaluates PMHS kinematics, kinetics and injury response in a vehicle-based sled environment subjected to far-side impacts.

4.2 Methods

4.2.1 Specimen selection and instrumentation

Five male PMHS, were selected for a series of five far-side sled tests (Table 4.1). The specimens were selected targeting the 50^{th} percentile male and were acquired and prepared in accordance with the policies and procedures of the UVa Center for Applied Biomechanics Oversight Committee. The subjects were preserved by freezing and confirmed free of infectious diseases including HIV and Hepatitis B and C. Full-body Computed Tomography (CT) scans were taken of each subject prior to testing to confirm the absence of bony trauma and abnormalities. Dual-energy X-ray absorptiometry (DXA) or Quantitative Computed Tomography (QCT) was performed to assess bone quality. Additional surrogate information can be found in Appendix C. The extremities and upper body of the subjects were wrapped in Coban™(3M™) prior to testing to limit the spread of biological fluids, to serve as a marking surface and to protect the instrumentation wires. This technique has been successfully used in past PMHS tests (Shaw et al., 2009; Forman et al., 2013) and does not affect kinematics when used in moderation (i.e., applying only one or two layers). Short cotton/polyester pants were used to cover the upper section of the lower body (i.e., lap and buttock).

Table 4.1: Specimen information

Test no.	**Donor no.**	**Age**	**Cause of Death**	**Weight [kg]**	**Stature [cm]**	**Chest Breadth* [mm]**	**BMI**	**Bone Quality**
490	758**	69	Alcoholic Liver Failure	72	168	327	25.5	Osteopenia
491	847***	44	Colon Cancer	58	175	302	18.9	Normal
492	764	65	Stage IV Melanoma	81	183	345	24.1	Osteopenia
512	897	70	Liver Cancer	61	169	308	21.3	Osteopenia
513	765	67	Cardiogenic Shock	87	178	356	27.6	Osteopenia

* Measured at chestband (ISO, 2013)

** Bilaterally amputated at wrist

*** Bilaterally amputated at proximal forearm

The PMHS were instrumented with 6 degree-of-freedom accelerometer and angular rate sensor packages mounted to the head, T1, T8, L2 and pelvis and with one degree-of-freedom accelerometer mounted to the sternum. A chestband was wrapped around the torso at the height of the sixth and the eighth ribs. Strain gauge rosettes were affixed to the left clavicle and fourth, sixth and eighth right ribs. A 3D tracking array of retroreflective targets was mounted to the head and single 3D tracking markers were attached to thorax, upper and lower limbs. The accelerometers and angular rate sensors were rigidly attached to the different bony structures (figure 4.1). The head sensor package was affixed to the superior aspect of the head using screws to attach it rigidly to the skull. The sternum accelerometer was rigidly attached to the anterior aspect of the sternum to measure anterior-posterior acceleration. The sensor packages for T1, T8, L2 and the pelvis were located underneath the skin in order to allow the use of a standard vehicle seatback (figure 4.2). The spine sensor packages were mounted on a bracket surgically attached to the corresponding vertebral body. These brackets allowed the sensor packages to be located between the spinous and the transverse process of the corresponding vertebra. The pelvis sensor package was rigidly attached to the posterior aspect of the sacrum.

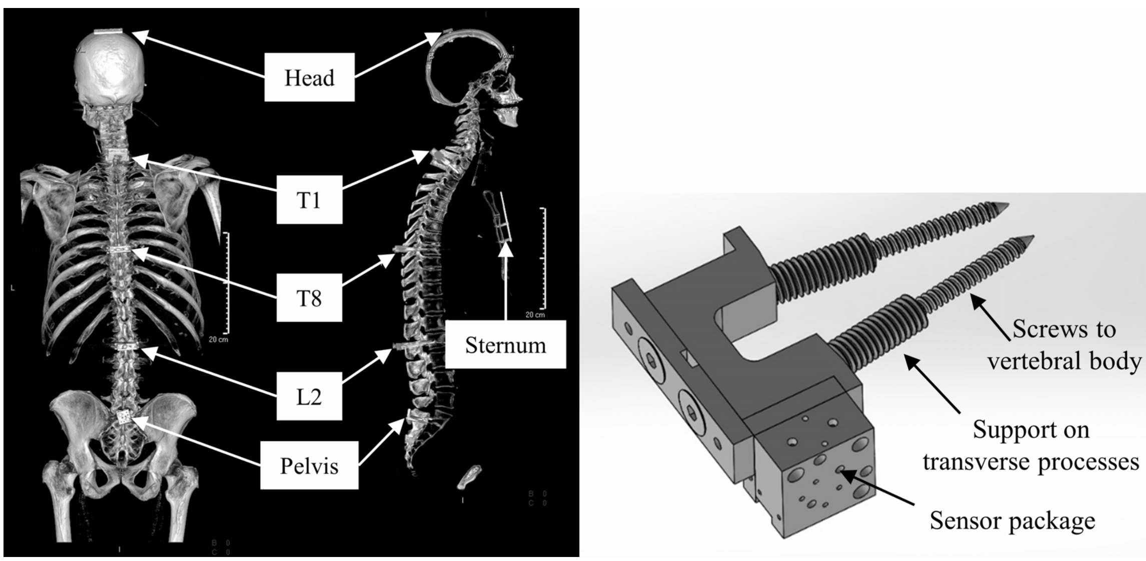

Figure 4.1: Specimen sensor packages (left), detail of vertebral mount (right)

Figure 4.2: Close-up of the suture around spine instrumentation

The accelerations and angular rates for the head, spine and pelvis were transformed to the head center of gravity (Robbins, 1983), the center of the corresponding vertebral body and the Posterior Superior Iliac Spine (PSIS), respectively. The local coordinate systems were defined per Robbins (1983) for the head and following a process similar to Wu et al. (2002) for the spine and pelvis (figure 4.3).

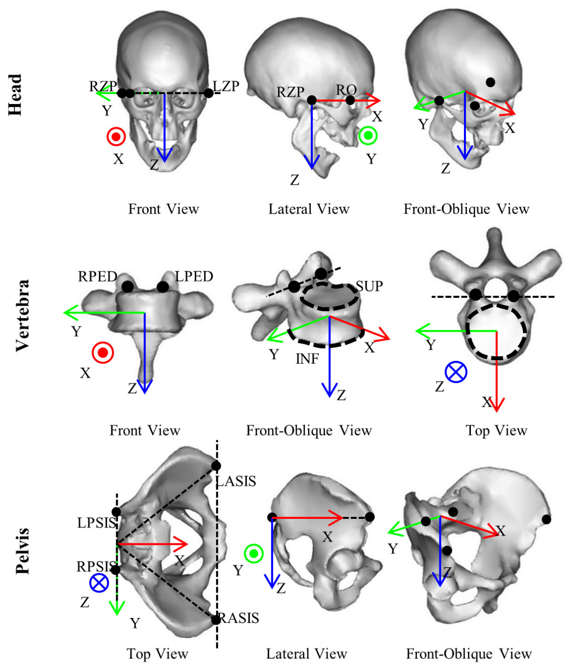

Figure 4.3: Local coordinate systems

Strain gauge rosettes (Micro-Measurements® C2A-06-062WW-350) were affixed to locally exposed sections of the left clavicle and fourth, sixth and eighth right ribs. The resulting in-plane maximum principal strain (MPS) was computed, when possible, based on the individual channels.

A 1000-Hz three-dimensional (3D) camera-based motion capture system (Vicon MX™) was used to track the PMHS motion. A four-marker 3D tracking array was affixed to the superior aspect of the head using screws to rigidly attach it to the skull. The resulting motion was transformed to the head center of gravity (Robbins, 1983) using the method described by Lessley et al. (2011) and Shaw et al. (2009). Individual 3D tracking markers were attached to both acromia, elbows, wrists, knees and ankles (figure 4.4). The present study reports the motion in the vehicle coordinate system defined with the X coordinate pointing front to back in the longitudinal axis of the vehicle, the Y coordinate pointing left to right in the transverse axis of the vehicle and the Z coordinate pointing up in the vertical axis (figure 4.5).

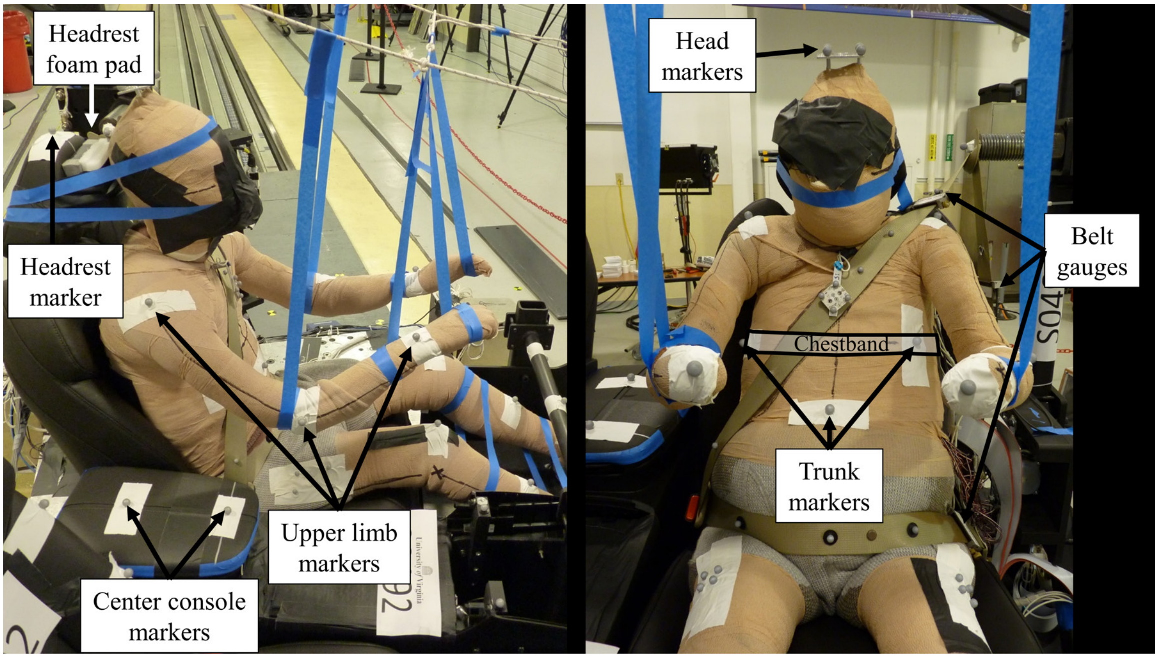

Figure 4.4: PMHS instrumentation and position

4.2.2 Test environment

The tests were performed using a reverse acceleration sled system (Seattle Safety (Kent, WA) 1.4 MN ServoSled®). The test fixture was designed to accurately represent the vehicle interior of a commercially available mid-size sedan (figure 4.5). The vehicle fixture included the driver and passenger seat, center console and seatbelt. The seatbelt included the webbing, latch, buckle, D-ring and a retractor with a 2 kN load-limiter and a pretensioner activated 6 ms into the event. Two driver seat designs, with the same external side bolster shape but different sizes of internal side bolster structures, were tested (figure 4.7). The difference between the large and small bolster structure consist on a 60 mm by 230 mm metal bracket. All the parts, including the bolster structure bracket, were OEM originals from the same vehicle year model. The parts were located in the vehicle geometric position and replaced after each test. The seats were attached to the floor using their original deformable mounting brackets. The floor and the tunnel of the vehicle were replicated in the fixture using flat rigid metal parts. The lower edge of the dashboard was replicated with a rigid tubular bar (figure 4.6).

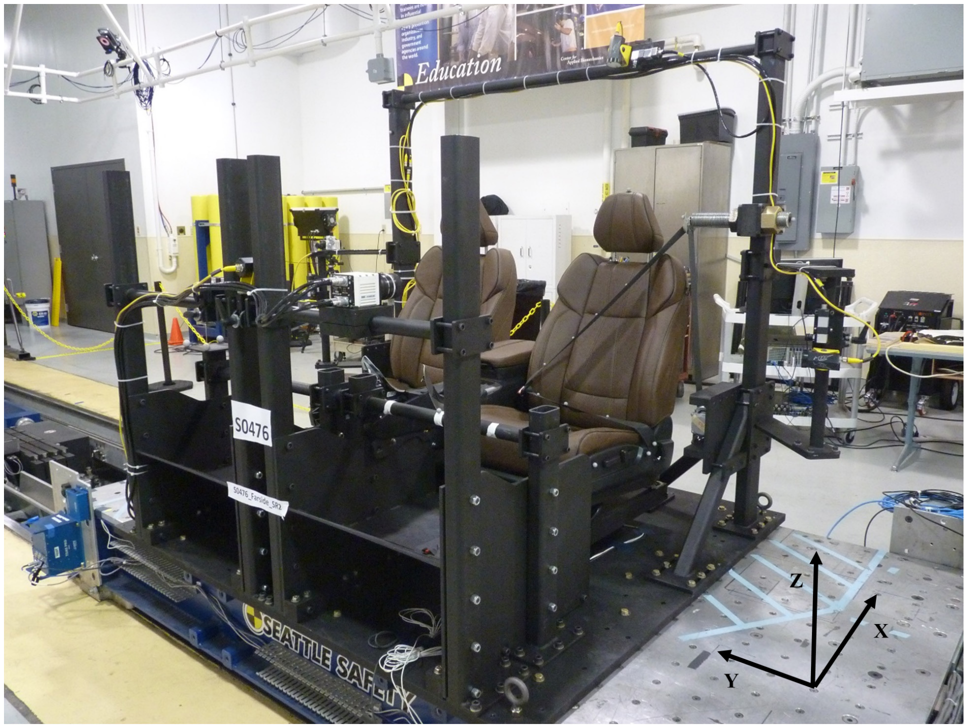

Figure 4.5: Sled fixture and vehicle coordinate system

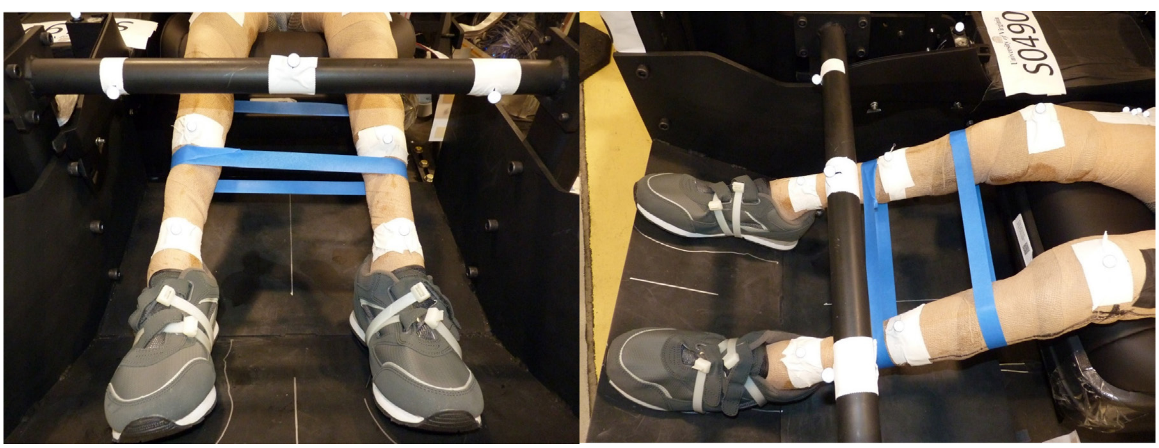

Figure 4.6: Detail of floor pan, tunnel and center console area

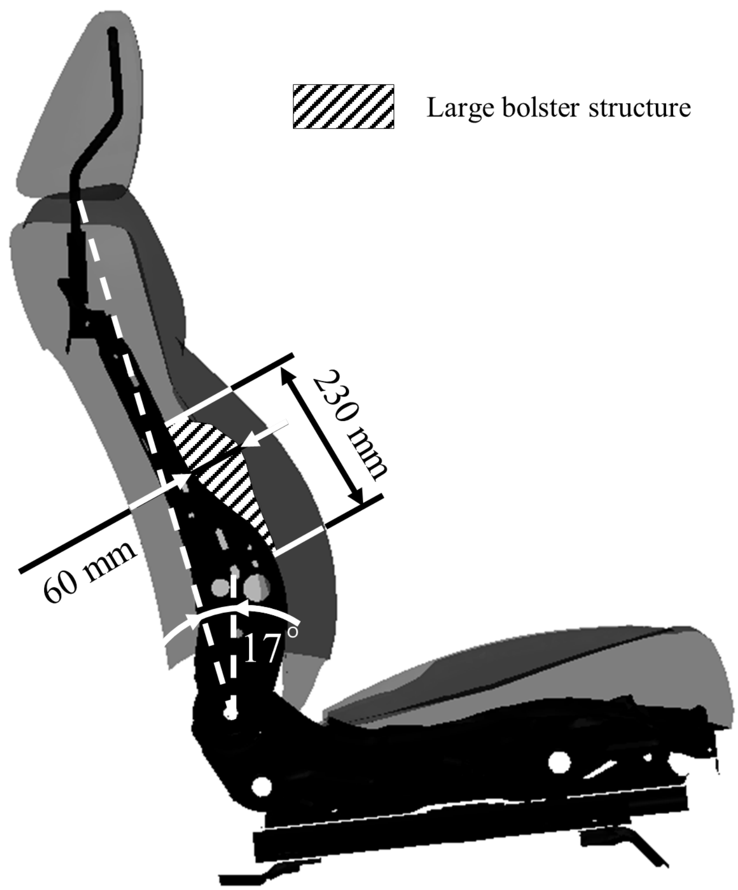

Figure 4.7: Different bolster structure and seatback angle

Figure 4.8: EPP blocks in center console and passenger seat

The spaces between the passenger seat and the frame and center console were filled with EPP60 to represent the behavior of the struck side seat and center console due to crash-induced intrusion and deformation following Euro NCAP guidelines (NCAP, 2017c). The EPP blocks were dimensioned and positioned to fill up the available space and constrain the motion of the seat and center console (figure 4.8). The tests were performed with the surrogate always positioned in the driver seat. The driver and passenger seats were positioned to represent the standard Euro NCAP position (NCAP, 2017c). The driver and passenger seatbacks were set to an angle of 17° measured as the projection in the sagittal plane of the angle between the line joining the recliner and the headrest bar at the point where it exits the seatback and the transverse plane of the vehicle (figure 4.7).

The PMHS were positioned with their greater trochanter matching the X-coordinate of the position of the WorldSID H-point in Euro NCAP configuration. The PMHS head and arms were held on the head rest and above the lap, respectively, using painters tape. This tape was nicked to ensure it tore easily at the beginning of the test. A foam pad was located between the knees of the surrogates to ensure a constant initial distance between them for all the surrogates. The Frankfurt plane of the PMHS was set to zero degrees with the horizontal and kept in position using painters tape and a foam pad between the head and the headrest. The shoulder belt angle at the torso, and between the shoulder and angle D-ring were kept constant at around 52 and 34 degrees, respectively, by moving the D-ring location in the frontal plane. These angles are representative of the resulting WorldSID seatbelt angles in the Euro NCAP test configuration.

The tests were recorded using two off-board and five on-board high-speed video cameras operating at 1000 Hz. The off-board cameras provided images of the front and back of the sled. These images were used to provide an overall view of the sled motion. The on-board cameras (figure 4.9) were located in front, on top and on the left-hand-side of the occupant and, in front and on the right-hand-side of the passenger seat.

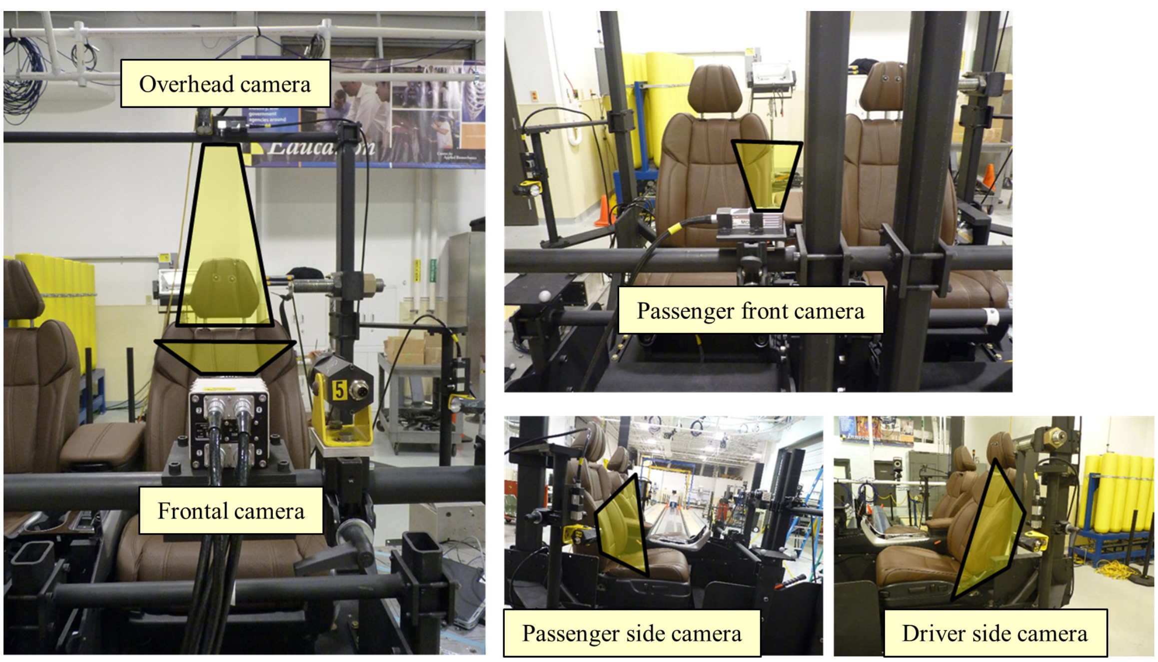

Figure 4.9: On-board high-speed cameras

The fixture was instrumented with accelerometers on the upper left side of the seatback structure of both seats, the left side of the interior compartment of the center console and the sled floor. The accelerations of the seat and the center console were measured in the direction perpendicular to the mounting surface. The sled acceleration was measured in the longitudinal and transverse direction. A four-marker 3D tracking array was located on the sled floor to create a local coordinate reference frame. Additional single 3D tracking markers were located in the center console, seatbelt webbing, seatbelt D-ring and the superior aspect of both headrests. The seatbelt webbing was instrumented with three tension gauges located between the retractor and the D-ring, in the upper shoulder belt between the surrogates shoulder and the D-ring and in the lap belt between the surrogates pelvis and the lateral lap belt anchor.

4.2.3 Test matrix

A total of five PMHS tests was performed using a 16.5 g, 33.5 km/h trapezoidal pulse (figure 4.10) in a 75-degree Principal Direction of Force (table 4.2). The pulse was obtained from a near-side Euro NCAP barrier test following the recently-developed Euro NCAP far-side assessment protocol (NCAP, 2017a,c). The resulting pulse represents approximately the median Δv for far-side related MAIS 3+ injuries (Gabler et al., 2005). The 75-degree PDOF represents a common impact direction in the field (Bahouth et al., 2015) and matches the angle used in the Euro NCAP far-side assessment protocol (NCAP, 2017c).

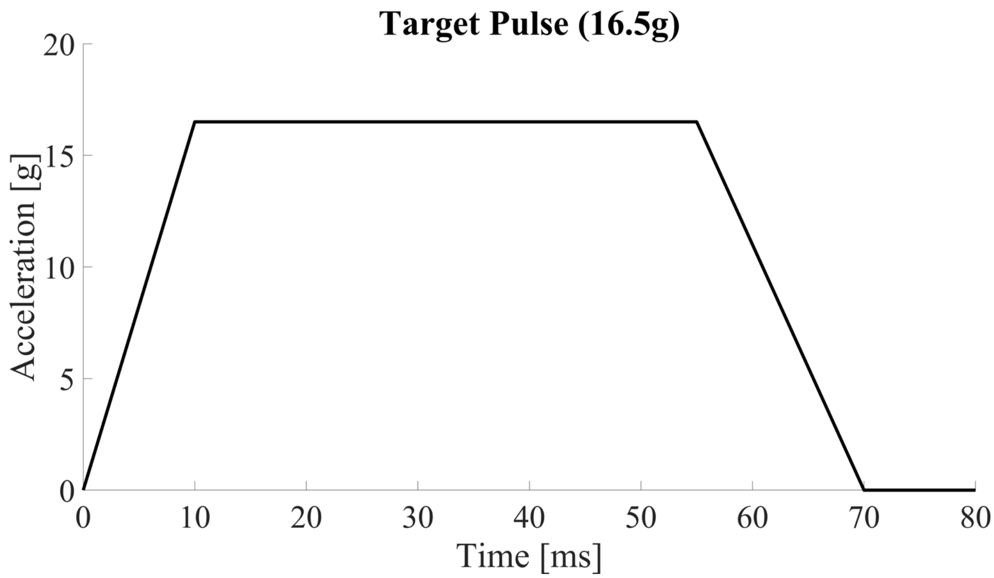

Figure 4.10: Test pulse target

Table 4.2: Test matrix

Test#	Surrogate	Bolster support
490	PMHS# 758	Large
491	PMHS# 847	Large
492	PMHS# 764	Large
512	PMHS# 897	Small
513	PMHS# 765	Small

4.2.4 Analysis

Kinematic and kinetic evaluation

The overall upper body motion and shoulder belt retention of the PMHS were qualitatively evaluated and compared using video images. The different kinematic phases and surrogate interactions were investigated using the surrogate and seat 3D tracking information and the center console accelerometer.

In order to investigate chest deflection, the different chestband contours were compared between the surrogates. The chestband was divided into four different regions of interest: the center of the sternum, the region in contact with the seatbelt, the most lateral point of the rib cage and the region in contact with the bolster (figure 4.11). Chest deflection was calculated for each point in the different regions as the change in distance between that point and the center of the chest. This value was normalized using the initial distance from that point to the center of the chest. The maximum normalized deflection is reported for each region.

Injury evaluation

The injuries sustained by the PMHS were identified via autopsy and classified according to their AIS score (AAAM, 2015). The source and timing of each injury were estimated based on different sources of information including the strain gauges, chestband contours and 3D tracking information.

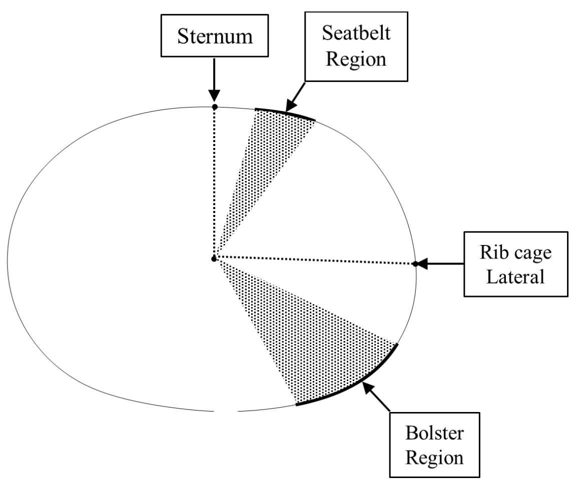

Figure 4.11: Chestband regions

4.3 Results

4.3.1 Kinematic and kinetic evaluation

Figures 4.13 and 4.14 and appendix I show the responses of the PMHS in the tests as seen from the frontal driver and passenger on-board cameras. Figures 4.13 and 4.14 correspond to the tests conducted with the large and small bolster structure, respectively. The motion started with the surrogates and the seat moving at the same time. This was a consequence of the deformation of the seat mounting brackets, seat track and seat back. Between 35 and 40 ms, the seat stopped after contacting the center console and the occupant started to slide over the seat. Peak acceleration of the center console occurred between 40 and 50 ms into the event. This peak acceleration was caused by the surrogate impacting the center console through the seat bolster. The center console was damaged in each test as a consequence of these loads. The damage was concentrated where the center console attached to the sled (figure 4.12).

Figure 4.12: After test center console damage

There was little variation in the times the surrogates reached the driver and passenger edge lines (i.e., 50±1 ms and 86±2 ms, respectively). The maximum head excursion occurred at around 120 ms for all surrogates. All the surrogates exhibited similar maximum head excursion with the exception of PMHS# 897 (i.e., test# S0512) that showed a lateral head excursion 47 mm lower than the PMHS average (figures 4.14 and 4.15).

All but one PMHS (# 847) remained in contact with the shoulder belt. As observed in figure 4.13 at the t=175 ms image. In spite of this difference in shoulder belt retention, PMHS# 847 exhibited a maximum head excursion similar to the rest of PMHS. The effect of losing contact with the seatbelt appeared to only significantly influence the occupant kinematics during the rebound phase. In this phase, only the PMHS that maintained contact with the shoulder belt returned to a relatively upright position.

PMHS spine accelerations (appendix D) did not show any noticeable bolster-related effects. That is, the use of a large bolster did not substantially affect spine accelerations. The suture used to keep the spine instrumentation under the skin remained intact throughout the event in the different tests. There was no evidence of artifactual signals cause by the direct interaction of the sensor with the environment.

Figure 4.13: PMHS# 758, 847 and 764 kinematics (left to right) with large bolster structure at 0, 50, 85, 120 and 175 ms (up to down). The dotted, dashed and solid lines are located approximately at the inboard edge of the driver seat, the inboard edge of the passenger seat and the center of the passenger seat, respectively.

Figure 4.14: PMHS# 897 and 765 kinematics (left to right) with small bolster structure at 0, 50, 85, 120 and 175 ms (up to down). The dotted, dashed and solid lines are located approximately at the inboard edge of the driver seat, the inboard edge of the passenger seat and the center of the passenger seat, respectively.

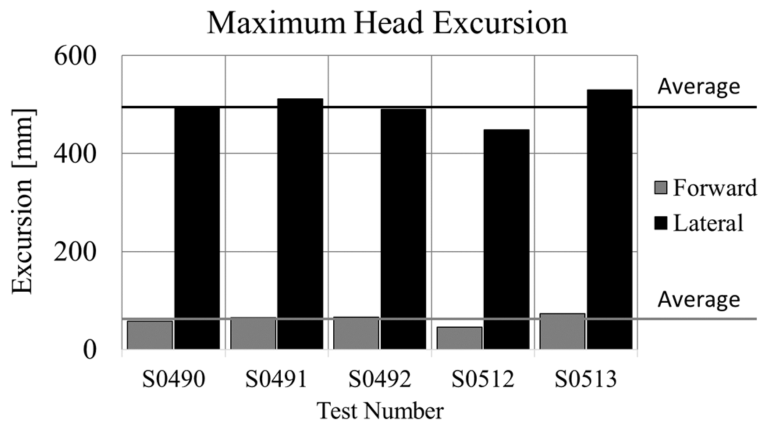

Figure 4.15: Maximum head excursion

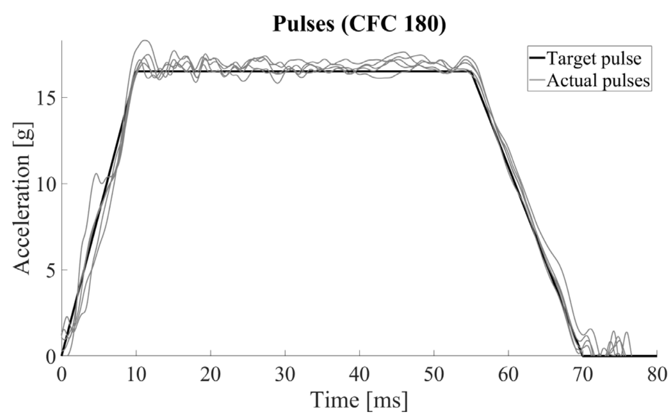

Figure 4.16: Maximum head excursion

The different bolster structures did not substantially affect overall kinematics or seatbelt forces (figure 4.17). The 3D tracking system lost visibility of the left shoulder markers in the middle section of three PMHS tests, since they were blocked by the shoulder belt in its outward motion. All surrogates exhibited qualitatively similar head excursion with the exception of PMHS# 847 which showed increase head downwards motion. The shoulder belt forces for all surrogates reached the load limiter. PMHS# 847, and to some degree PMHS# 897, showed an earlier reduction in shoulder belt force.

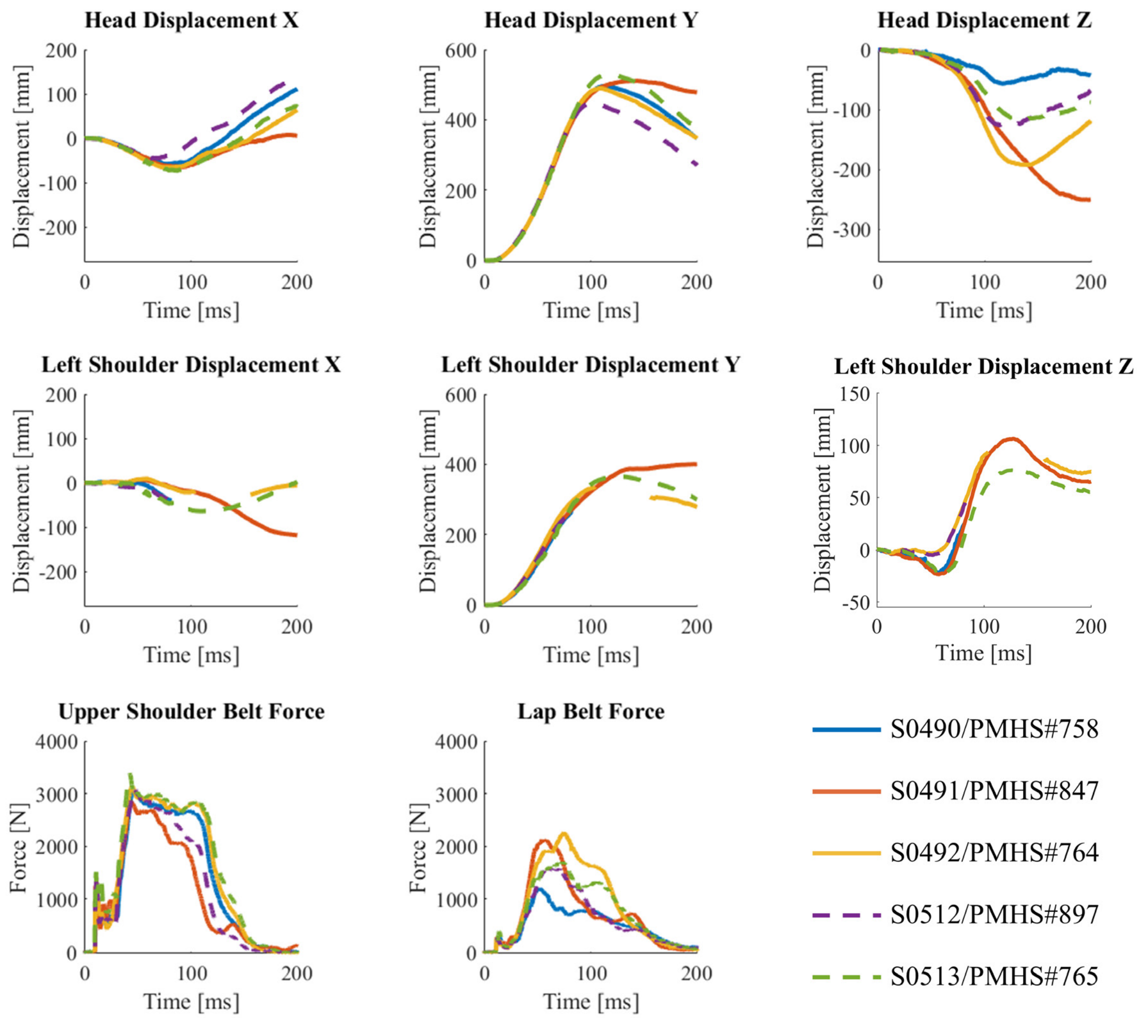

Figure 4.17: PMHS responses with large (solid line) and small (broken line) bolster structure

Figure 4.18 shows the maximum chest deflection in the different chestband regions. The seatbelt and the side bolster area generated the largest chest deflections. Two of the three PMHS tested with the large bolster structure (i.e., PMHS# 758 and 764) exhibited the maximum chest deflection in the bolster region. Two of the five PMHS showed the greatest deflection in the seatbelt area (i.e., PMHS# 847 and 897). PMHS# 765 that showed similar deflection in both regions. The small bolster structure led to a 50% reduction in average deflection in the bolster region. For one of the PMHS tested with the small bolster (# 765), the lateral deflection increased 156% from the average of the PMHS tested with the large bolster. The sternum and lateral points showed the lowest deflection numbers for all PMHS. The lateral aspect of the chest underwent different degrees of expansion after the seatbelt pretensioner. This can be observed at around 10 ms in the bottom left plot of figure 4.19. Maximum anterior-posterior deflection was reached at around 50 ms (figure 4.19 - top left and right). At this point in time the lateral and posterior aspect of the chest begun to be compressed (figure 4.19 - bottom left and right).

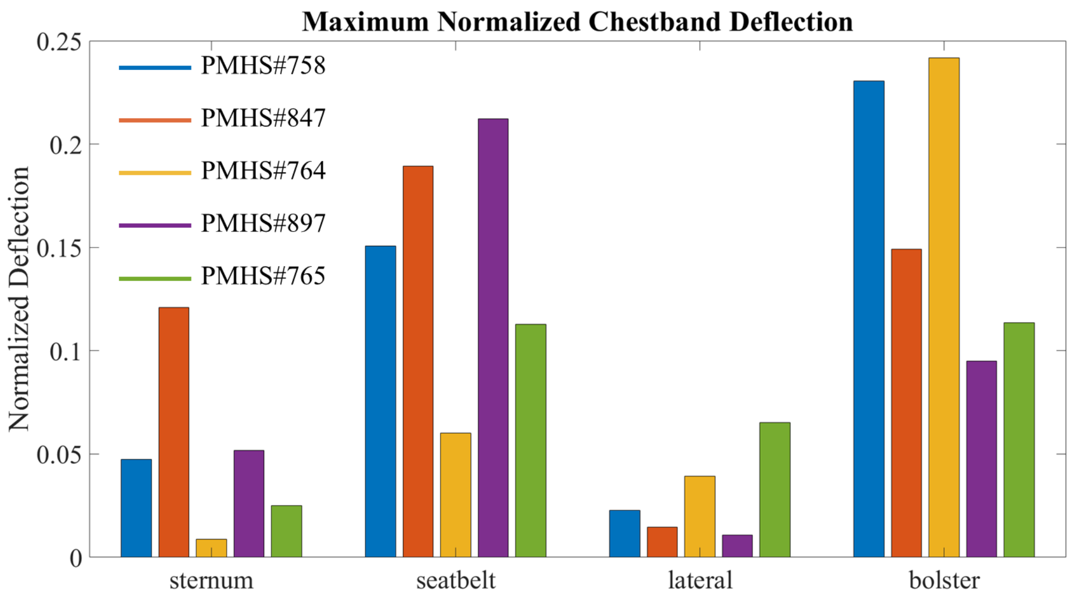

Figure 4.18: Chestband maximum deflection per region

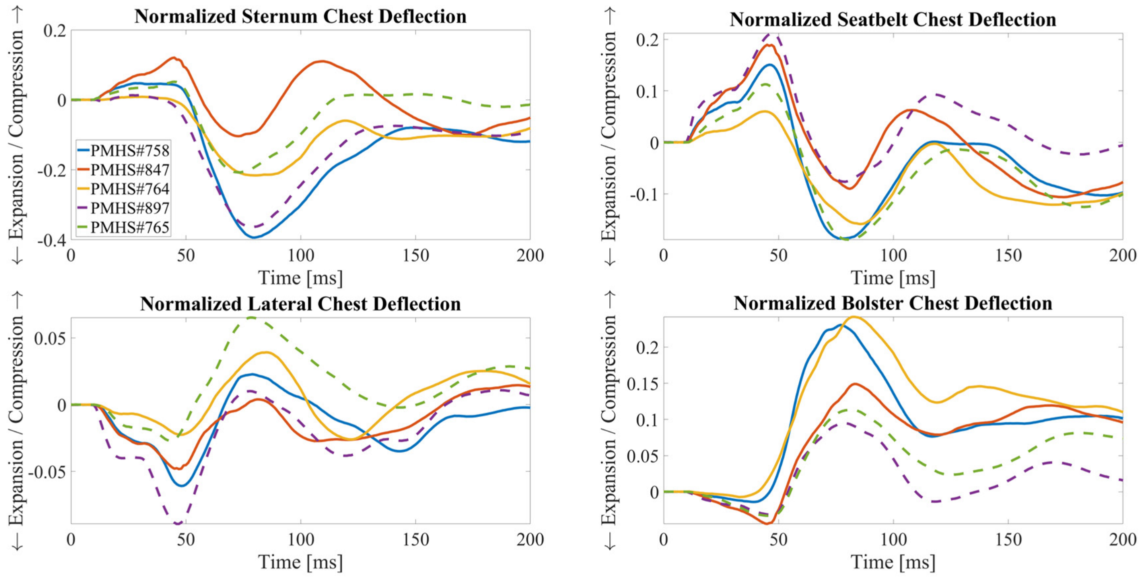

Figure 4.19: Chestband deflection time histories

4.3.2 Injury evaluation

While rib fractures were identified in post-test autopsies (table 4.3 and figure 4.21), no injuries were identified in the head, spine, limbs, joints or soft tissue. The number of rib fractures varied from 0 in the surrogate with the best bone quality (PMHS# 847) to 15 (including a unilateral flail chest) in a surrogate with worse bone quality (PMHS# 758).

The injuries occurred as a result of the combined load of the seatbelt, seat bolster and center console. Initially, the seatbelt deformed the chest. When the occupant contacted the seat bolster, which was already in contact with the center console, the chest underwent a deflection in the posterior aspect that forced the chest to expand forward (figure 4.20). This phenomenon can also be observed in the PMHS chest deformation time-histories (figure 4.19), which show how the sternum and seatbelt area of the chest expanded as the bolster-related chest deflection increased in the PMHS at around 50 ms into the event. Information about the individual PMHS bone quality and injuries can be found in appendices C and F, respectively.

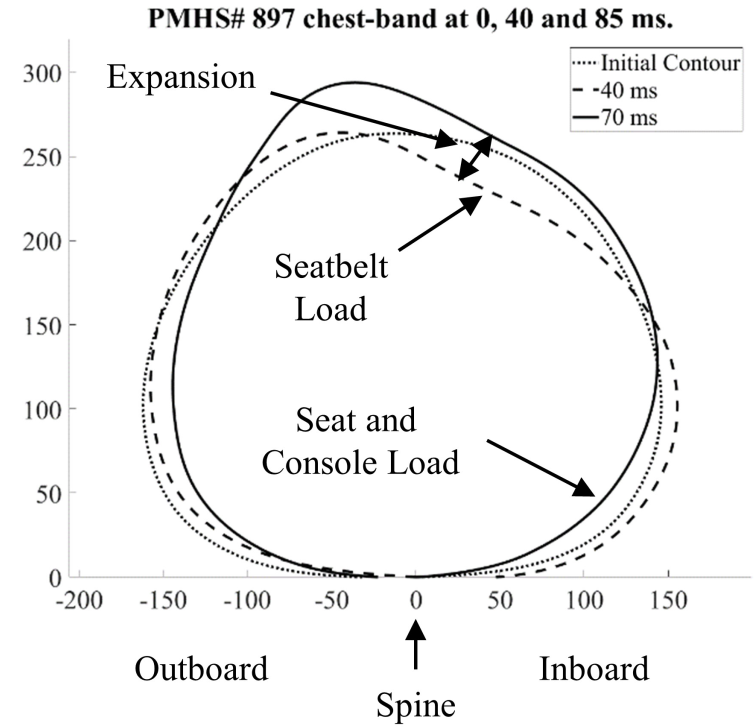

Figure 4.20: Combined load in chest

Table 4.3: Autopsy results

Test no.	PMHS no.	Age	Bone Quality	Fractured Ribs Left	Fractured Ribs Right	AIS 2015**
490	758	69	Osteopenia	Ant:4,5*,6*,7*	Ant:3,4,5,6	450212.3
					Post:9,10,11,12	450203.3
491	847	44	Normal	No fractures	No fractures	0
492	764	65	Osteopenia	No fractures	Lat: 8	450201.1
512	897	70	Osteopenia	Ant: 4	Ant: 4 Post: 11	450203.3
513	765	67	Osteopenia	Ant: 2,3,4	Lat: 9	450203.3

*Fracture present in two different locations

**(AAAM, 2015)

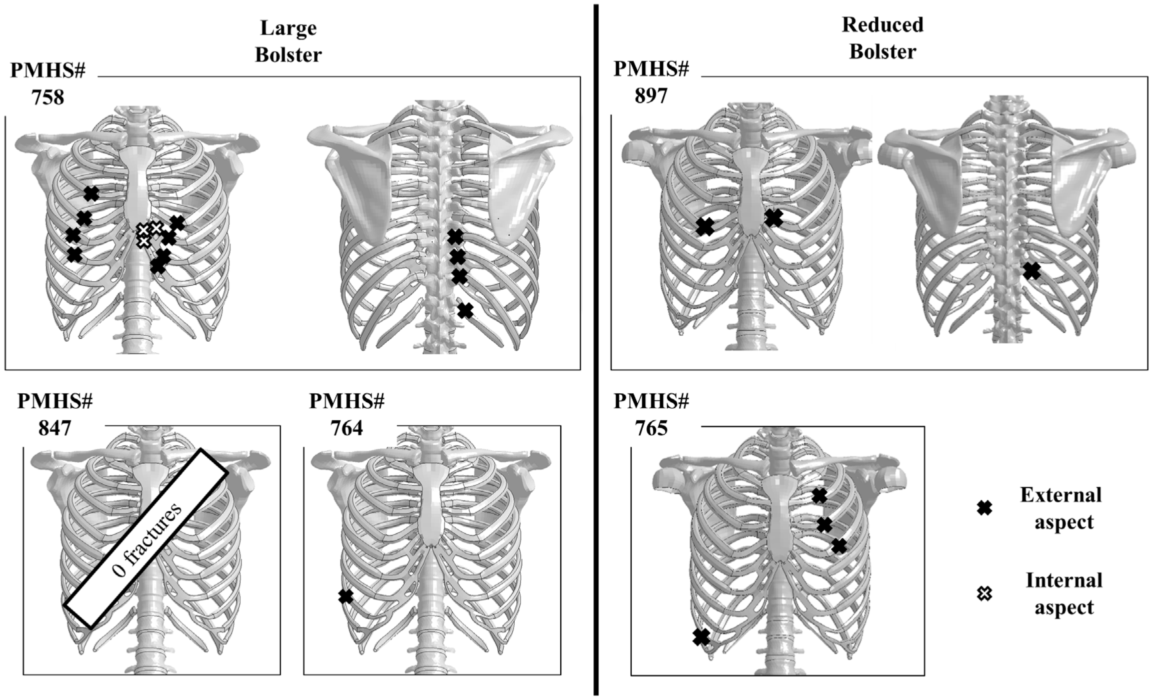

Figure 4.21: Rib fractures identified in the autopsies

4.4 Discussion

4.4.1 Kinematic and kinetic evaluation

The test results give insight into PMHS responses in a realistic vehicle environment subjected to a far-side event. In this environment, all surrogates showed very similar kinematic response, reaching the different vehicle points virtually at the same time (figures 4.13, 4.14 and 4.17).

The PMHS tests conducted in the present study exhibited similar maximum lateral head excursion to previously-published PMHS tests conducted in simplified environments (Pintar et al., 2007; Forman et al., 2013). In contrast to the response observed in some of those tests (Forman et al., 2013), the surrogate whose shoulder lost contact with the shoulder belt (i.e., test# 491) did not exhibit greater head excursion. Loss of shoulder belt engagement seemed to only affect the PMHS motion during rebound. During this phase, only the PMHS that retained the shoulder belt engagement returned to the driver seat immediately after the event.

The shoulder belt remained engaged with the shoulder in four of the five PMHS tests due to the pocketing effect caused by the deformation of the chest and abdominal soft tissue. As the left arm moved forward relative to the upper body, it contacted and deformed the chest tissue preventing the shoulder belt from slipping off the shoulder (figure 4.22 - right). A similar behavior was identified by Forman et al. (2013). Another mechanism that prevented shoulder belt slippage was the deformation of the abdominal region (figure 4.22 - left). This was particularly noticeable in PMHS with an already prominent abdomen (e.g., PMHS# 758). The PMHS that slipped out of the shoulder belt (i.e., # 847) presented a relatively low amount of soft tissue in the abdomen and chest. Moreover, this surrogate was bilaterally amputated at the proximal forearm which may have influenced the ability of the arm to locally deform the chest tissue. These two factors may have influenced its ability to pocket the seatbelt.

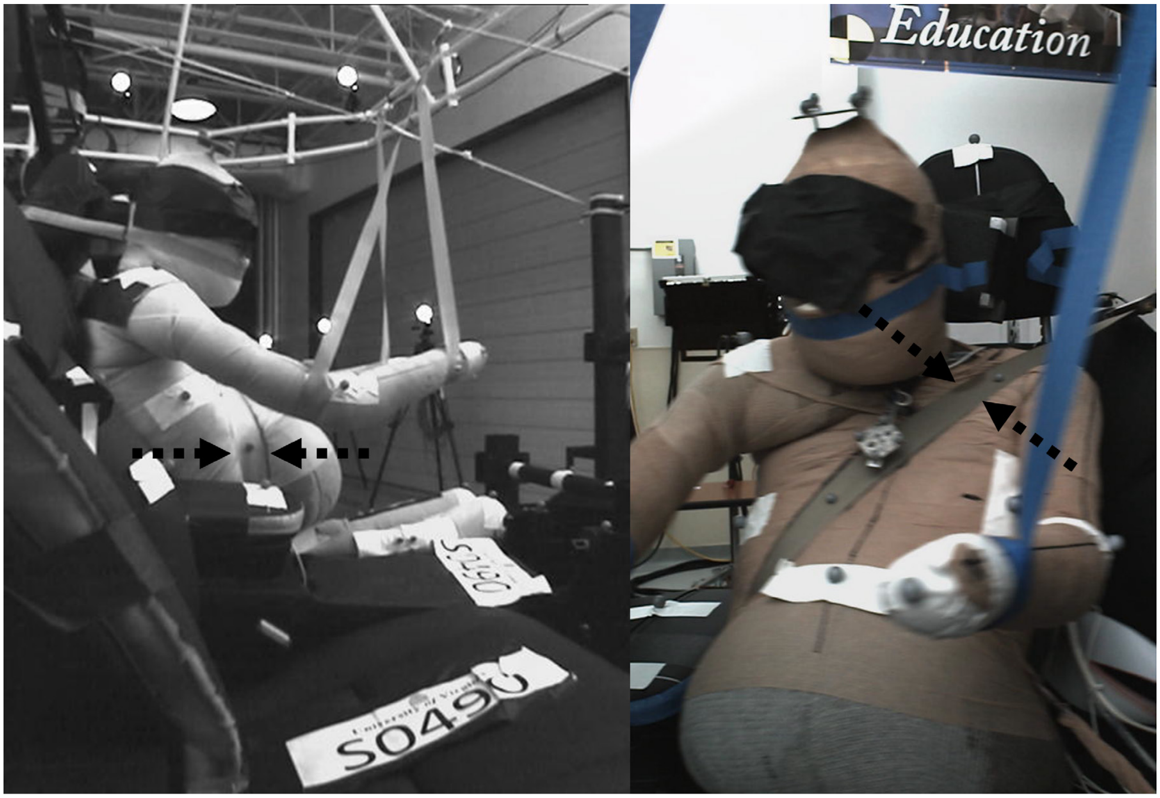

Figure 4.22: Abdomen (left) and chest/shoulder (right) pocketing effects in PMHS# 758

Although both seat bolster structures resulted in virtually equal overall body kinematics, they did generate large differences in chest deflection (figure 4.19 and appendix E). The addition of a large bolster structure consistently increased chest deflection in the bolster region in the PMHS tests (figure 4.18). On the other hand, the large bolster structure reduced lateral chest deflection in certain circumstances. This effect can be observed in PMHS# 764 and 765 which had similar height, weight and chest breadth and were tested with the large and small bolster, respectively (figure 4.19 and appendix E). Although the different bolster structures showed some degree of trade-off between the lateral and bolster region deflection, the large bolster generated a larger net chest deflection.

4.4.2 Injury evaluation

During the autopsy performed after the tests, multiple rib fractures were identified in all but one PMHS. While past studies include injurious far-side PMHS tests (Pintar et al., 2007; Forman et al., 2013), these studies conducted repeated tests with the same PMHS, which may have contributed to more severe injuries. The injuries found in the present study are comparable to those encountered by Pintar et al. (2007) in the only PMHS that was subjected to a single test.

Multiple studies point at the seatbelt as one of the major contributors to chest injury in the field (Mackay et al., 1993; Digges and Dalmotas, 2001; Gabler et al., 2005; Fildes et al., 2007). In the present study, sixteen of the twenty-three rib fractures observed in the PMHS occurred in the anterior section of the rib cage and are consistent with seatbelt-related injury patterns. The strain gauges located in the vicinity of these fractures indicate that the fractures occur as soon as 50 ms into the event (figures F.2, F.3 and F.5). The number of seatbelt-related fractures indicates that the seatbelt alone may not be able to successfully restrain the occupant and prevent thoracic injuries even when a low load-limiter is used (in this test 2 kN at the retractor). Additional countermeasures may be needed to reduce belt-related injuries, providing additional engagement of the torso prior to the onset of rib fractures (approximately 50 ms into the event).

The seatback and center console may also contribute to injury, as observed in the present study and in past studies (Digges and Dalmotas, 2001; Gabler et al., 2005; Fildes et al., 2007). Although there was no direct measurement of timing or causation, lateral and posterior injuries seemed to be caused by interaction of the occupant with the seat and center console. The large bolster structure generated a larger deflection on the posterior aspect of the chest (appendix E). This may have influenced injury occurrence in the vicinity of the seat bolster.

PMHS# 758 sustained the largest number of rib fractures, most likely as a result of its lower bone quality. On the other hand, PMHS# 847 exhibited no rib fractures. This surrogate was the youngest and presented the smallest chest breadth and the best bone quality. This combination of intrinsic factors led to the lowest overall lateral deflection and lowest bolster-related deflection out of the PMHS used in the configuration with the large bolster structure (figure 4.15).

In summary:

- All PMHS showed similar head excursions.
- The seat bolster structure had no noticeable effect on the overall PMHS kinematics and kinetics but did have an effect on the local chest deformation.
- All but one PMHS remained engaged with the shoulder belt throughout the event. Loss of contact with the shoulder belt did not lead to a larger lateral head excursion in this particular surrogate.
- A total of twenty-three rib fractures was identified in the post-test autopsies. The injury mechanism involved a complex loading by the seatbelt, bolster and center console. These fractures began to occur as soon as 50 ms into the event. Additional restraint may be needed to generate an effective occupant restraint in less than 50 ms in order to mitigate thoracic injuries.

Some results from the present study will be used in chapter 5 along with previously published PMHS tests by Forman et al. (2013) in order to evaluate the ability of the WorldSID and the simplified GHBMC to capture PMHS-like kinematics and injury severity.

Chapter 5

Simplified GHBMC and WorldSID Kinematic, Kinetic and Injury Response in Far-Side Events in a Simplified and a Vehicle-Based Test Environment

The WorldSID and the simplified GHBMC were used in the methodology presented in this dissertation for the estimation of the FE vehicle model uncertainty factors (chapter 6) and the exploration of occupant response (chapter 7), respectively. However, their biofidelity has not been fully established in the literature. This chapter used previously published PMHS tests in a simplified environment and the PMHS tests presented in chapter 4 in order to evaluate the biofidelity of the WorldSID and the simplified GHBMC. These results have been published in Perez-Rapela et al. (2018, 2019a,b).

5.1 Introduction

Understanding the biofidelity of the HBM and ATD used in the evaluation of occupant response is critical for the correct assessment of vehicle performance and restraint design. HBM and ATD have been evaluated in the most commonly tested impact directions (Shaw et al., 2002; Paek et al., 2006; Gayzik et al., 2011; Park et al., 2013; Shaw et al., 2013; Schwartz et al., 2015; Kim et al., 2016). In spite of the introduction of physical tests for the evaluation of far-side impacts (NCAP, 2017c), little has been done to understand the surrogates' response in this impact direction. The biofidelity of the simplified GHBMC has not been evaluated in far-side scenarios and the only WorldSID far-side biofidelity evaluation is the work of Pintar et al. (2007). While the kinematic evaluations conducted in the cited study focused on head excursions, the neck of the WorldSID introduces some level of passive muscle response, thus the motion of other body regions (e.g., T1) may provide a better insight on occupant motion and restraint interaction. Moreover, the cited study conducted repeated tests with the same PMHS. Therefore, the results are not suitable for injury evaluation.

Traditional biofidelity evaluations investigate the surrogates' ability to represent PMHS-like kinematic, kinetic and injury responses in isolated impact conditions. This approach establishes the degree of biofidelity of the surrogates by comparing their responses to PMHS corridors or their probability of injury considering each load case independently. While this approach provides an initial assessment of the surrogates' biofidelity, it does not provide information about the surrogates' ability to represent PMHS-like response to changes in the impact conditions. This is particularly important in cases where the surrogate is used to evaluate human response to multiple impact conditions (e.g., multiple PDOF, different restraint configurations, etc.).

This chapter utilized existing PMHS tests in simplified far-side sled environments (Forman et al., 2013) in order to evaluate the kinematic and kinetic biofidelity of the WorldSID and the simplified GHBMC (also referred to as GHBMC in this chapter). This evaluation explored upper body motion and interaction with the shoulder belt.

These PMHS tests also formed the basis for evaluation of the surrogates' sensitivity to changes in the impact conditions. The vehicle-based sled PMHS tests presented in chapter 4 were used to evaluate the in-vehicle kinematic, kinetic and injury response of the surrogates.

5.2 Methods

5.2.1 Simplified sled environment

This part of the study employed six different impact configurations (table 5.1) selected from Forman et al. (2013). Variations in pulse intensity (34 km/h and 14 g, 16 km/h and 6.6 g), impact direction (oblique 60-degree, lateral 90-degree), D-ring location (forward, intermediate, back), pretensioner usage (yes, no) and additional pelvic restraint (yes, no) were studied. The low-severity sled pulse represents the median severity of far-side tow-away crashes. The high severity pulse represents the median severity at which MAIS3+ injuries occurred (Gabler et al., 2005). The pelvic restraint consists of a metal plate rigidly attached to the right-hand side of the seat. It was implemented into the test matrix to simulate the presence of a center console.

Table 5.1: Impact configurations

Conf. #	**Δv (km/h)**	**Impact Direction**	**D-Ring Position**	**Pretensioner**	**Pelvic restraint**
1	16	Oblique	Intermediate	No	No
2	16	Oblique	Intermediate	Yes	No
3	34	Oblique	Intermediate	Yes	No
4	16	Oblique	Back	Yes	Yes
5	16	Lateral	Forward	Yes	No
6	34	Lateral	Intermediate	Yes	No

WorldSID tests

For the present study, nineteen sled tests were conducted with the WorldSID to represent the configurations in table 5.1. The tests were conducted on the same sled, sled fixture and restraint systems as the PMHS tests presented in Forman et al. (2013).

The sled fixture was designed to approximate a vehicle-based restraint environment while providing repeatable and reproducible test conditions and lines of sight for motion capture. The seat consisted of an aluminium plate mounted on top of a six-axis load cell, covered by a 6.25 mm layer of neoprene rubber (durometer value 30A). The seatback consisted of two horizontal aluminium bars whose position could be adjusted in the anterior-posterior and superior-inferior directions to produce the desired postures (figure 5.1). The seat and seatback were instrumented with single-axis accelerometers oriented with the PDOF. The restraint system consisted of a 3-point seat-belt with optional pretensioner and a 4 kN - 2.5 kN degressive load limiter. The shoulder- and lap-belt tension were tracked using four Messring 15 kN seatbelt load cells. The retractor was mounted on a six-axis load cell to verify the accuracy of the seatbelt load cells.

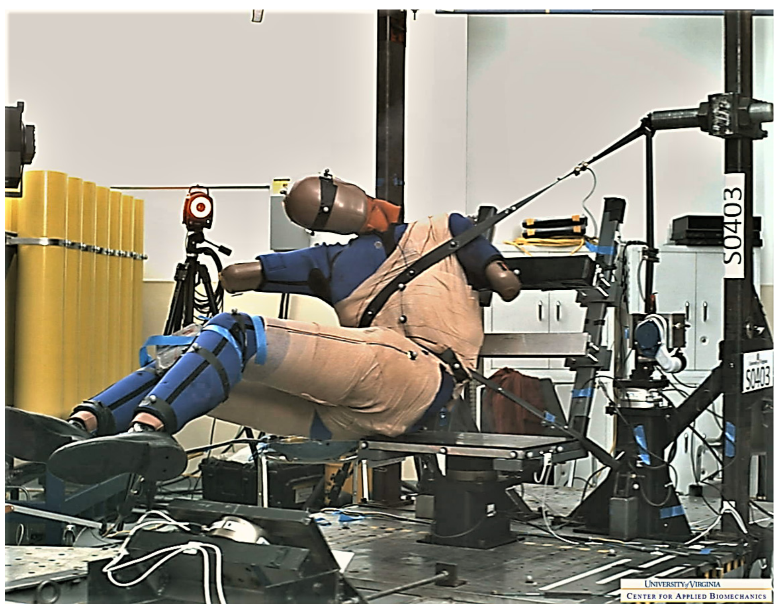

Figure 5.1: WorldSID on simplified test fixture

The ATD was positioned to match the average PMHS pelvic position, pelvis-to-shoulder angle and shoulder to D-ring vector for each D-ring position. The ATD was instrumented with its standard sensors, including linear accelerometers and angular velocity sensors for the head, T12 and pelvis. The rib deflection was measured by 2D IR-TRACC and RibEye technology in paired tests. The ATD kinematic data were captured using a 500-Hz Vicon MX$^{\text{TM}}$three-dimensional (3D), camera-based motion capture system, and three high-speed video cameras. Vicon markers were located on the ATDs surface for point tracking on shoulders, arms, legs and torso. Head, T1 and pelvis position and orientation were tracked by placing an array of markers.

GHBMC simulations

For the present study, six FE simulations were conducted in LS-Dyna v7.1.0 replicating the PMHS test configurations (table 5.1) using the simplified GHBMC v1.8.3.1 with some modifications to ensure model stability. These modifications, that did not substantially change the response of the surrogate, consisted in the definition of interior contacts and the use of the detail GHBMC soft-tissue material definition in the thorax and left arm of the model.

The FE model of the physical buck was created based on the original CAD parts. Model parts were defined as rigid, when possible, for time efficiency (figure 5.2). The seatbelt retractor parameters were reversed engineered based on quasi-static tests in combination with information derived from the WorldSID tests. The friction between the different model components was set based on quasi-static friction tests (table 6.3). Based on these tests, the friction between the HBM and the seatbelt webbing was set to 0.5.

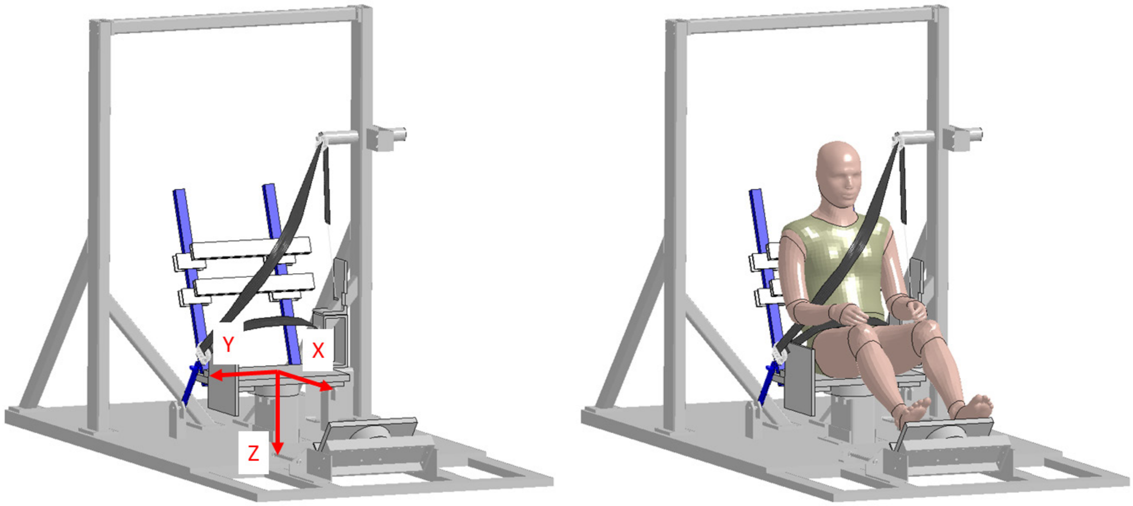

Figure 5.2: Simplified sled fixture FEM; gray: rigid; blue: deformable

The six configurations were replicated with the simplified GHBMC matching the average PSIS location and upper body angle of the PMHS used in each configuration. The HBM was settled by gravity using a one second simulation and the resulting stress and strain information was carried to define the initial state of the final simulation.

Analysis

The resulting WorldSID and GHBMC kinematics and kinetics were averaged for each impact configuration and compared to the PMHS corridors developed in Perez-Rapela et al. (2018). The coordinate system for the kinematic evaluation was defined at the center of the upper surface of the seat pan with its axis following the SAE J670 standard (SAE, 2008). The surrogates' biofidelity was evaluated using a CORrelation and Analysis (CORA) method (Gehre et al., 2009). The CORA method assigns a correlation score between the surrogate and the PMHS responses by applying two methods: the corridor method, and the cross-correlation method. The corridor method analyzes the fitting of the response into the PMHS corridor. The cross-correlation method compares the phase, shape and area below the surrogate and PMHS responses. The final CORA score is calculated as a weighted average of the two methods:

$CORA_{score} = 0.5 \cdot Score_{corridor} + 0.5 \cdot (0.5 \cdot Score_{shape} + 0.25 \cdot Score_{phase} + 0.25 \cdot Score_{area})$

A linear regression of the lateral head excursion was calculated for the WorldSID and the GHBMC using the impact parameters as predictors. The sensitivity to the different test parameters (not including the pelvic restraint) was evaluated and compared to the PMHS data.

5.2.2 Vehicle-based sled environment

This part of the study used the PMHS results presented in chapter 4 to evaluate WorldSID and GHBMC in-vehicle kinematic, kinetic and injury response. Based on the PMHS results, no distinctions were made between the cases with large and small seat bolster structure in the HBM's and ATD's responses except for the assessment of chest deflection.

WorldSID tests

Four WorldSID tests were conducted on the same sled fixture as the PMHS tests (chapter 4). The WorldSID was instrumented with the standard built-in sensors including accelerometers and angular rate sensors in the head, upper spine, T4, T12 and pelvis and a 2D IR-TRACC system to measure rib deflection. A chestband (of the same make and model as in the PMHS tests) was used in two of the four tests (table 5.2). The chestband was located around the third thoracic rib of the WorldSID to represent the same area of deflection as in the PMHS. The contour of the chestband was reconstructed using the same script used for the PMHS tests.

A 1000-Hz Vicon MX^{TM}three-dimensional (3D) camera-based motion capture system was used to track the WorldSID motion. Two 3D tracking markers were affixed to each side of the WorldSIDs head laterally to its center of gravity. The resulting motion was transformed to the head center of gravity. Individual 3D tracking markers were attached to both shoulders, the distal section of the arm, trunk, knee and ankles.

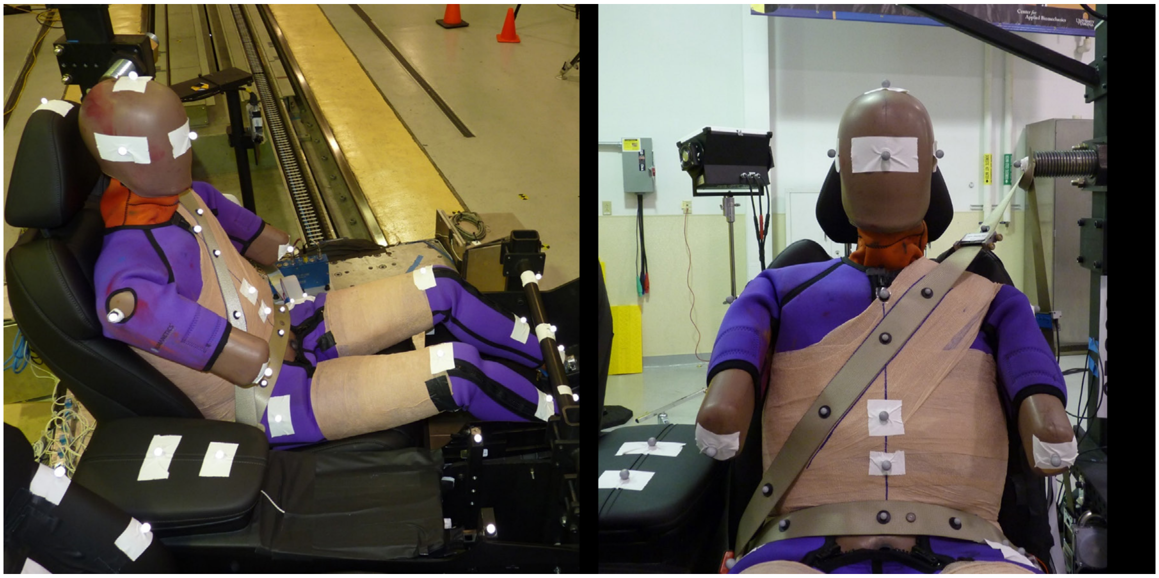

Figure 5.3: WorldSID instrumentation and position

Table 5.2: Test matrix

Test#	**Chestband use**	**Bolster support**
485	No	Large
486	No	Large
510	Yes	Large
511	Yes	Small

GHBMC simulations

For the present study, two Finite Element (FE) simulations were conducted in LS-Dyna v7.1.0 replicating the PMHS test configurations with large and small seat bolster in chapter 4 using the simplified GHBMC v1.8.3.1 with some modifications to ensure model stability. These modification did not substantially change the response of the surrogate.

The FE model of the physical buck was created based on the original OEM FE parts (figure 5.4). The metal parts of the buck (figure 5.4 - gray) were defined as rigid and OEM parts preserved their original definition. The seatbelt retractor parameters were reversed engineered based on the information derived from the WorldSID tests. The friction between the different model components was set based on quasi-static friction tests (table 6.3). Based on these tests, the friction between the HBM and the seatbelt webbing was set to 0.5.

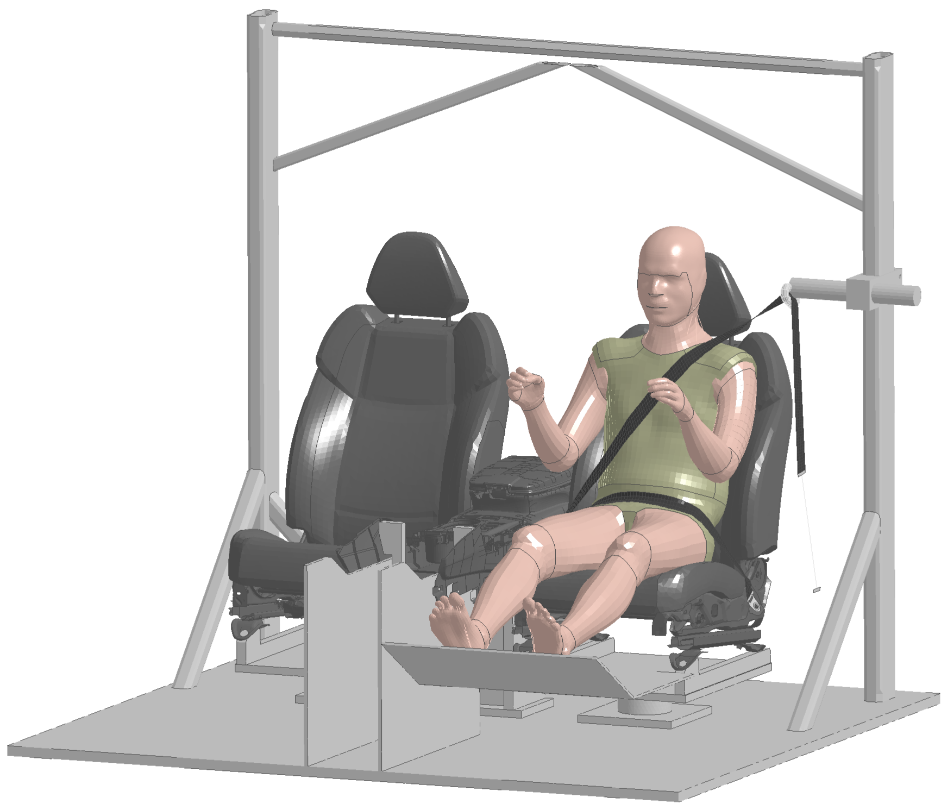

Figure 5.4: Vehicle-based sled fixture FEM

Analysis

The WorldSID and GHBMC in-vehicle kinematics and kinetics were averaged and compared to the PMHS information presented in chapter 4. The WorldSID and the GHBMC were also assessed in their ability to predict thoracic deformation and injury severity. The WorldSID chest injury severity prediction was estimated using its chest deflection injury risk curves. The GHBMC chest injury severity prediction was estimated following a strain-based methodology (Forman et al., 2012). The predicted injury severities were compared to the actual PMHS injury severities pooling the cases with large and small seat bolster structure.

5.3 Results

5.3.1 Simplified sled environment

Seatbelt engagement and upper body motion

Since the WorldSID and GHBMC neck introduces some level of muscle response in their definitions, this section focuses on T1 instead of head excursion. Moreover, since the shoulder lateral motion is highly correlated to that of T1, only the fore-aft left shoulder motion was presented in this section. More kinematic results and images can be found in appendix G and H.

Oblique impact direction

The GHBMC replicated the shoulder-to-belt engagement of at least one of the PMHS used in each configuration with the exception of the high-speed case (figures 5.5, H.1, H.2, H.3, H.4). In this loading condition, the abdomen of the PMHS expanded forward preventing the shoulder belt from sliding (figure 5.6). This led to a change in body kinematics that the GHBMC was not able to represent. In all cases, the PMHS tended to rotate towards the shoulder belt. In general the GHBMC showed a more neutral upper body rotation. On the other hand, the WorldSID consistently rotated away from the shoulder belt. This can also be observed in the increased rearward motion of the WorldSID's left shoulder, particularly in the high-speed case (configuration 3) (figure 5.7). In spite of the differences in shoulder belt engagement, T1 lateral motion showed relatively good agreement with PMHS corridors in the oblique impact direction for both surrogates (figure 5.7). T1 fore-aft motion was better captured by the WorldSID.

The shoulder belt forces exerted by the WorldSID met the PMHS corridors in all cases except in the case with a pelvis block (configuration 4). The GHBMC showed slightly reduced shoulder belt force. Lap belt forces were captured by both surrogates in all cases except in the high-speed case (configuration 3) (appendix G).

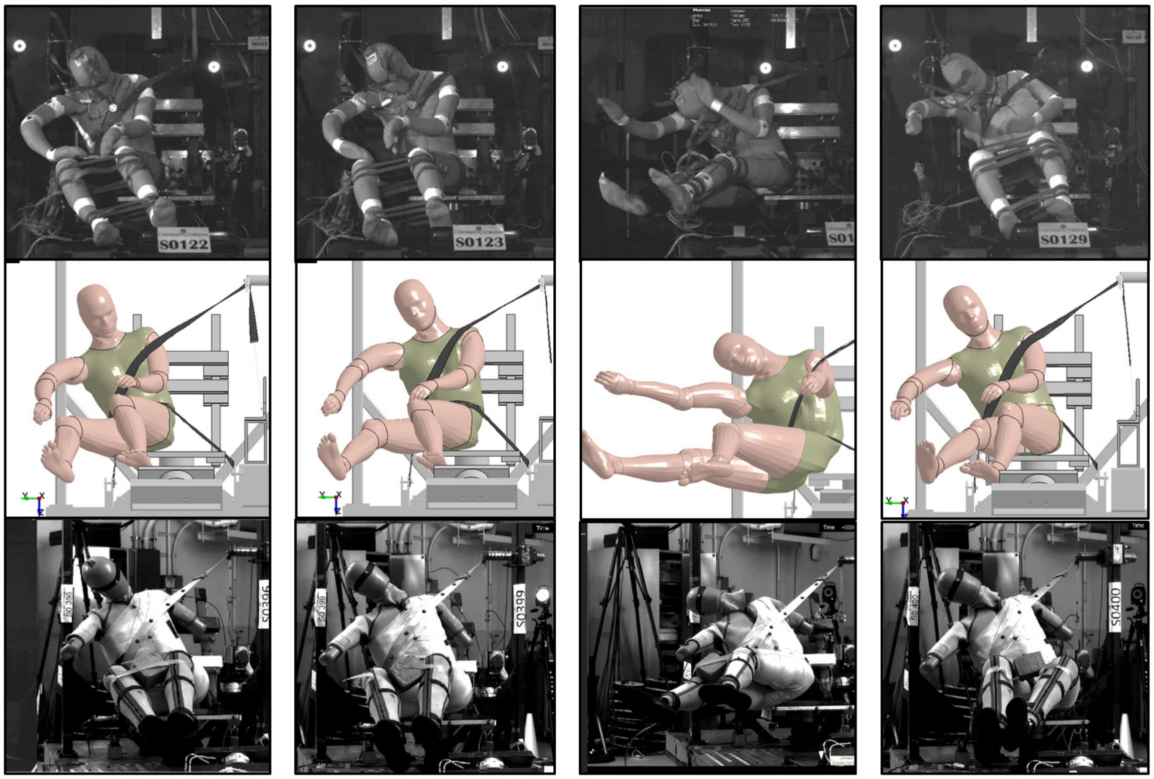

Figure 5.5: PMHS (top row), GHBMC (middle row) and WorldSID (bottom row) responses in configurations 1 to 4 (left to right) at 150 ms

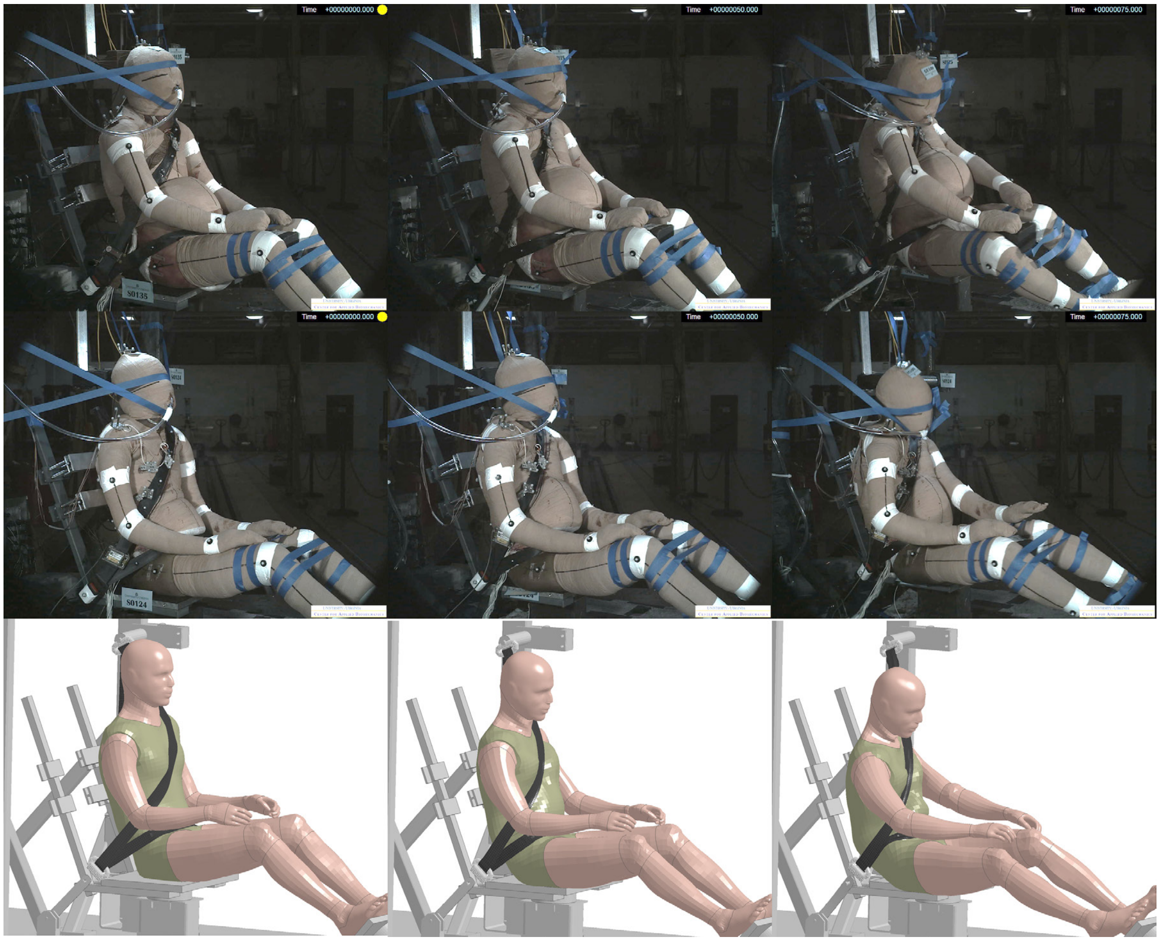

Figure 5.6: Abdominal response in PMHS (#602 - top row, #591 - middle row) and GHBMC (bottom row) at 0 ms., 50 ms., and 75 ms. in configuration 3

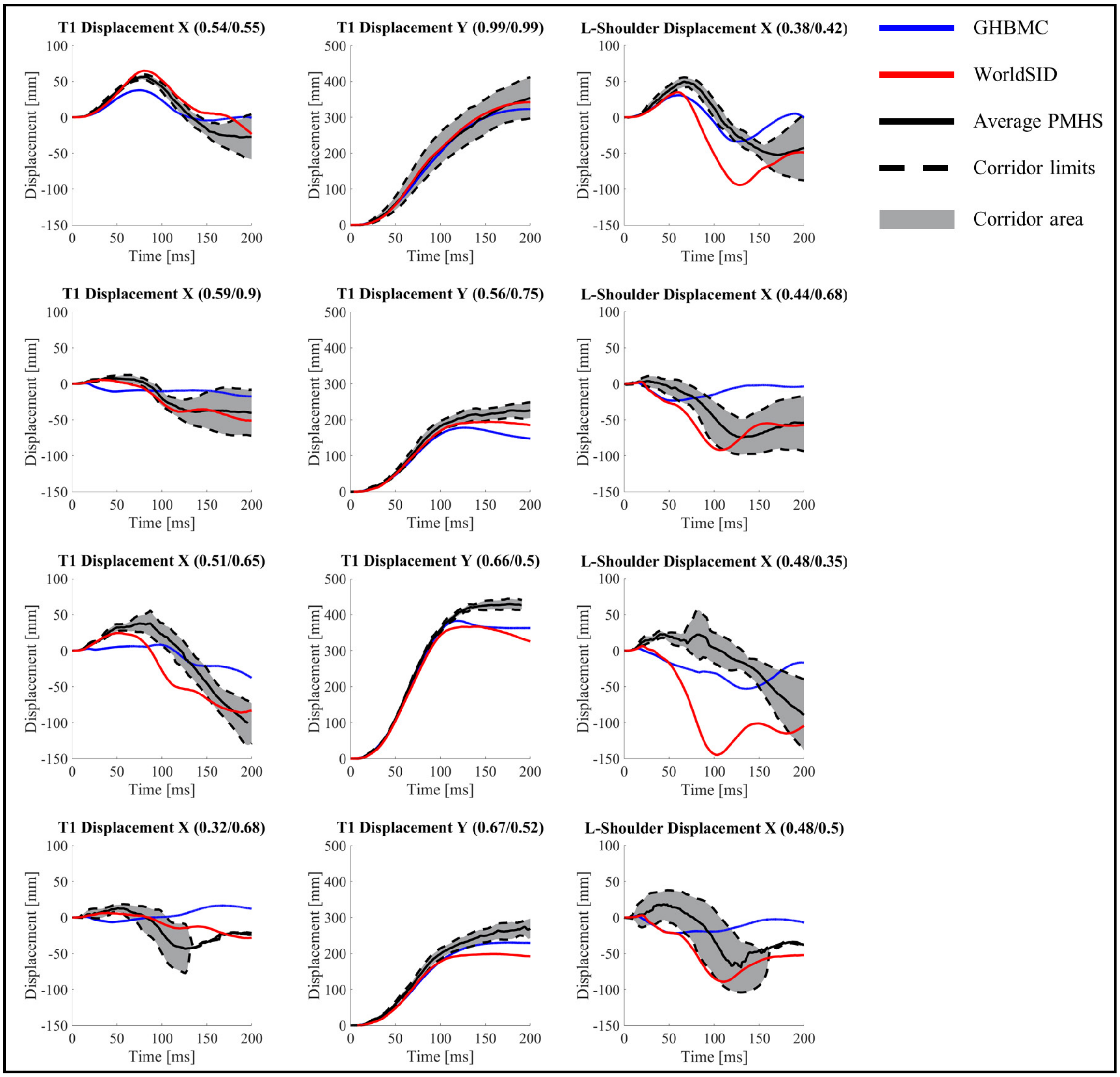

Figure 5.7: GHBMC and WorldSID upper body kinematics in oblique impact directions: Configuration 1 to 4 (up to down). CORA scores in parenthesis (GHBMC/WorldSID)

Lateral impact direction

The WorldSID and the GHBMC showed PMHS-like fore-aft motion in the lateral impact direction (figure 5.9). Although the seatbelt contacted the surrogates laterally in a similar location, both surrogates overestimate T1 lateral motion. This overpredicted lateral excursion was more acute for the GHBMC in the low-speed case where the surrogate also showed an increased loss of shoulder belt engagement (figure 5.8).

The WorldSID and GHBMC slightly underestimated shoulder force in configuration 5. The rest of the seatbelt forces exerted by the WorldSID and the GHBMC followed the PMHS response (appendix G).

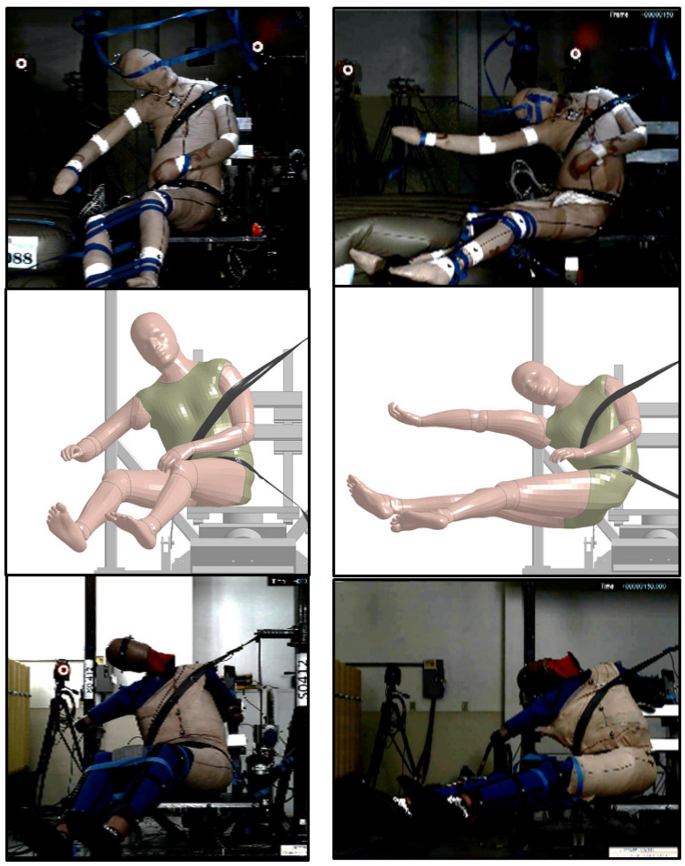

Figure 5.8: PMHS, GHBMC and WorldSID responses (up to down) in configurations 5 (left) and 6 (right)

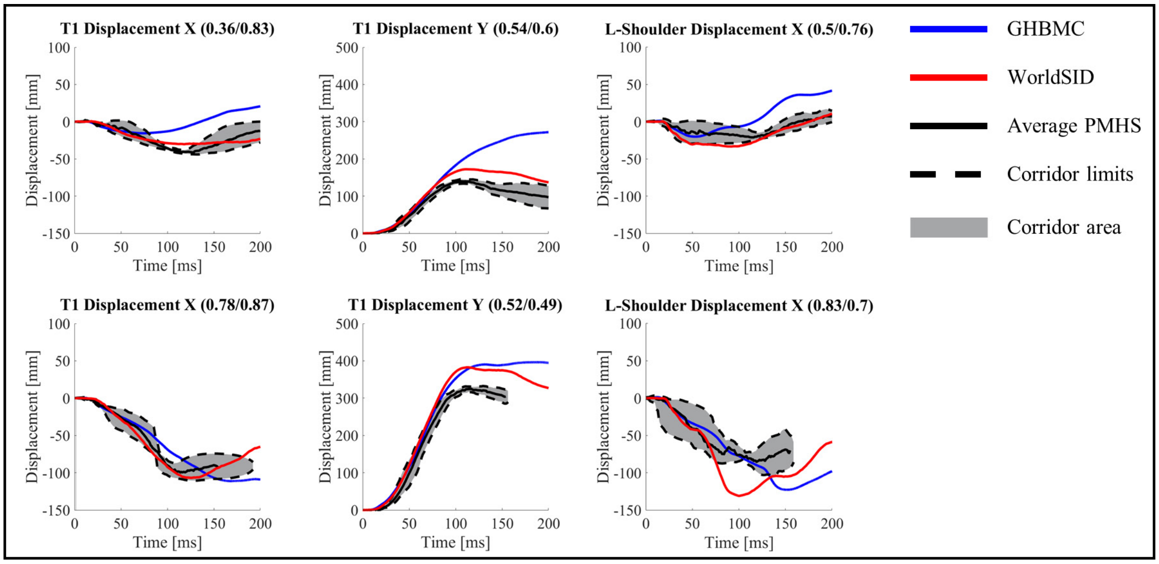

Figure 5.9: GHBMC and WorldSID upper body kinematics in lateral impact directions: Configuration 5 and 6 (up to down). CORA scores in parenthesis (GHBMC/WorldSID)

Sensitivity to parameters

Head excursion increased with increased pulse intensity and decreased with the use of a pretensioner for the PMHS, the GHBMC and the WorldSID. While purely lateral impact directions generated increased lateral head excursion compared to oblique impact direction for the WorldSID and the GHBMC, the opposite was true for the PMHS (figure 5.10).

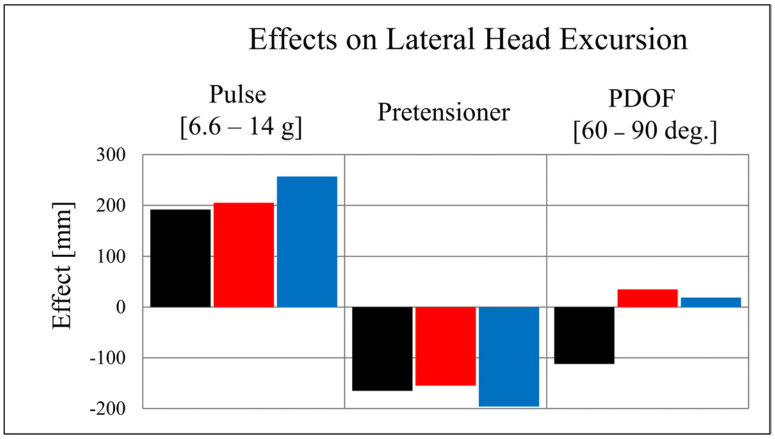

Figure 5.10: Sensitivity to parameters of PMHS (black), WorldSID (red) and GHBMC (blue)

5.3.2 Vehicle-based sled environment

Seatbelt engagement and upper body motion

Due to the use of a standard vehicle seat, the T1 motion could not be captured in the PMHS. Head and shoulder motion are reported in this section. Video images can be found in appendix I.

The WorldSID, GHBMC and PMHS reached the driver and passenger edge around the same time (i.e., 50 ms and 85ms, respectively). The maximum head excursion occurred at around 120 ms for all surrogates. The WorldSID and the GHBMC consistently slipped out of the shoulder belt during the event. Shoulder belt engagement was similar to that of the PMHS that also slipped out of the shoulder belt (PMHS# 847) (appendix I). In spite of that, the WorldSID and the GHBMC showed PMHS-like lateral excursion, although fore-aft head excursion was only correctly captured up to the point of maximum excursion. From that point on, all the PMHS return to the seat faster than the WorldSID and the GHBMC. While shoulder fore-aft motion was slightly better represented by the GHBMC, the WorldSID showed better lateral shoulder excursion (figure 5.11).

The GHBMC showed larger shoulder belt force compared to the WorldSID but both surrogates were able to replicate the PMHS loads. The PMHS lap belt forces were captured by the WorldSID and the GHBMC, although both surrogates showed a more pronounced bimodal response.

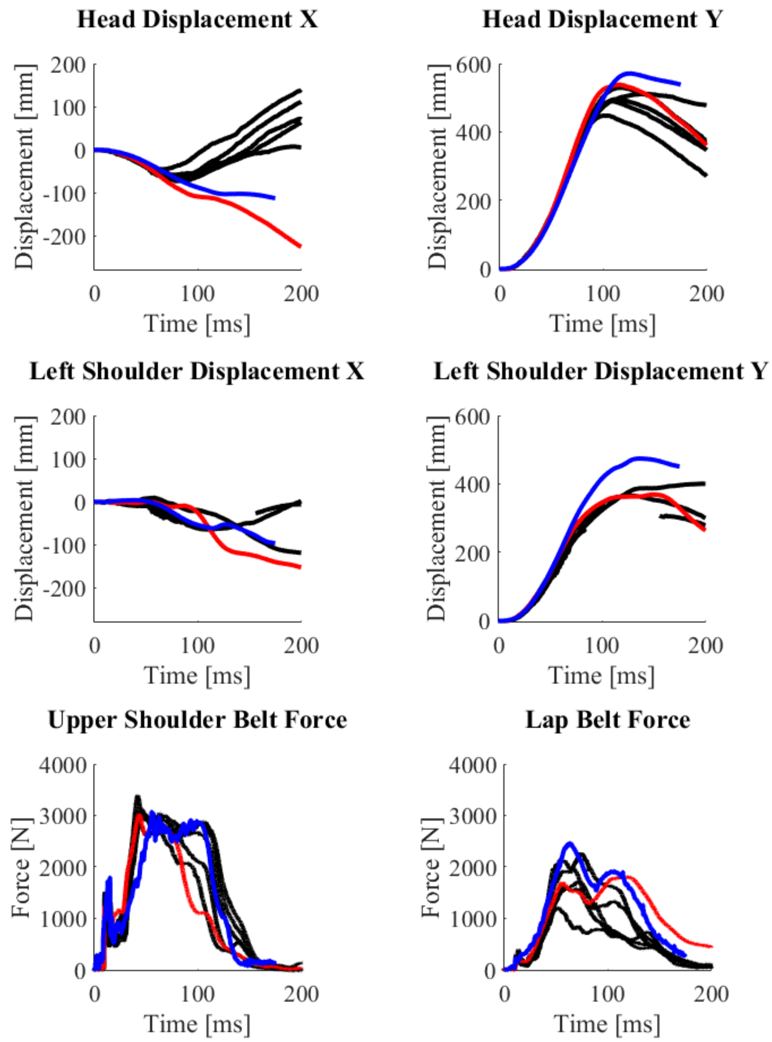

Figure 5.11: WorldSID (red), GHBMC (blue) and PMHS (black) in-vehicle response

Chest deflection and injury response

The GHBMC overestimated sternum deflection compared to the PMHS but it captured the PMHS response for the regions with the largest chest deflection (i.e., the seatbelt and the bolster regions). On the other hand, the WorldSID captured sternum and, to some extent, lateral deflection but did not capture the deflection in the seatbelt or bolster area. Overall, the GHBMC model response was closer to the PMHS than the WorldSID dummy (figure 5.12).

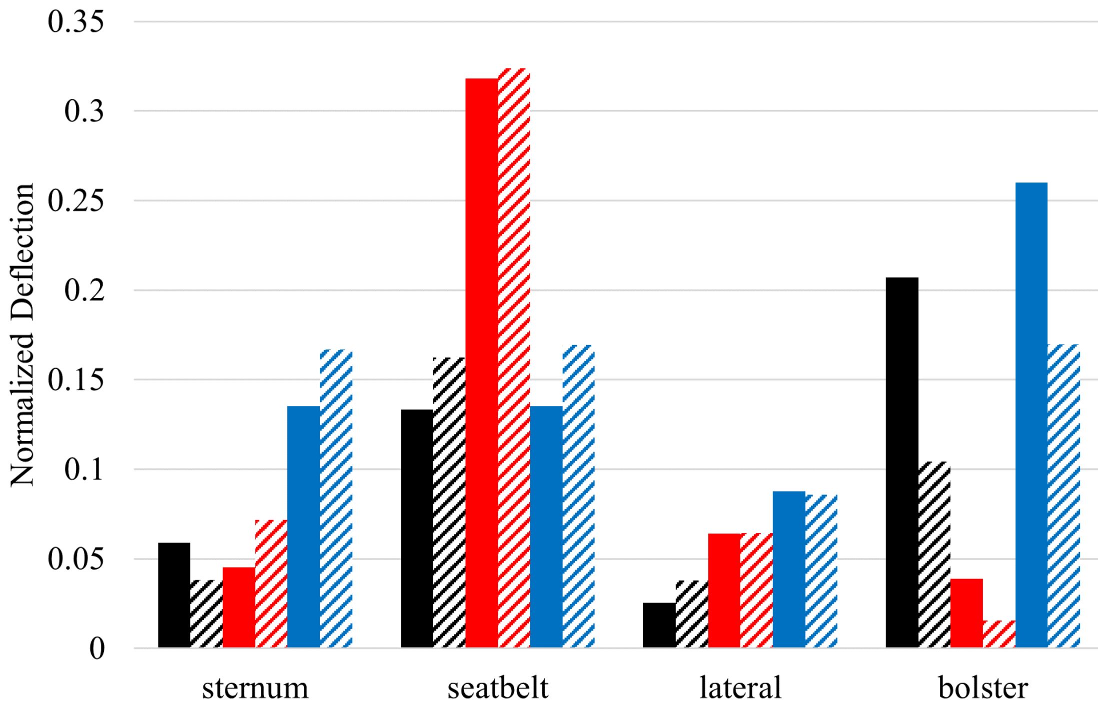

Figure 5.12: Maximum normalized chest deflection for average PMHS (black), WorldSID (red) and GHBMC (blue) with large (solid bar) and small (broken bar) seat bolster structure

The WorldSID chest deflection was calculated using the 2-D IR-TRACC elongation and angle in the transverse plane following the Euro NCAP protocol (NCAP, 2017a). The WorldSID maximum rib deflections were 15.4 and 25.0 mm for the cases with large and small bolster structure, respectively. These are associated with 0% and 1.6% probability of AIS 3+ injury to the thorax for a 63-year-old occupant (Petitjean et al., 2012), respectively. These results contrast with the PMHS tests in which three of the five surrogates (i.e., 60%) sustained in AIS 3+ chest injuries.

Figure 5.13 shows the GHBMC rib fracture probability prediction for a 65-year-old occupant, the PMHS results and the PMHS results discarding the most injured PMHS. The GHBMC rib fracture probability captured the PMHS rib fracture trend and frequency, especially for values larger than 3+ fractured ribs.

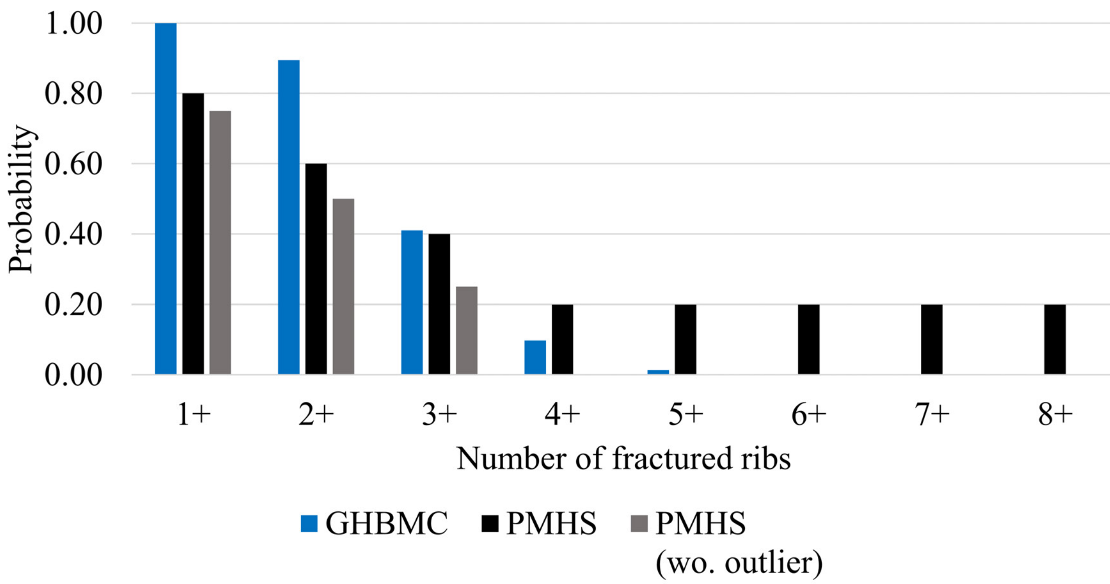

Figure 5.13: Probability of rib fracture for the GHBMC and PMHS (w/o costal cartilage)

5.4 Discussion

5.4.1 Kinematic and kinetic response

The WorldSID and the GHBMC showed improved kinematic and kinetic response in the vehicle-based sled compared to the simplified sled. This is likely due to the additional constraints provided by the vehicle interior. Both surrogates generated PMHS-like loads in the vehicle environment. This can be observed in the seatbelt loads (figure 5.11) and the motion of the seat and center consoles of the vehicle (appendix H).

In general, both surrogates were able to replicate PMHS lateral excursions although the GHBMC showed better upper body kinematics and a more biofidelity engagement with the shoulder belt. The WorldSID shows a clear lack of anterior-posterior chest deflection, which, in combination with the lack of shoulder motion, limits the ability of the ATD to correctly engage the shoulder-belt (appendix H). This is especially noticeable in the cases with a pretensioner. In these cases, the PMHS chest deforms around the shoulder-belt while the ATD torso tends to rotate out of the seat-belt. This behavior is a consequence of the ATD upper body construction whose main design focus was to represent human response in purely lateral, near-side events (ISO, 2013). The inability of the WorldSID and the GHBMC to represent the PMHS soft tissue expansion (figure 5.6) may be a contributing factor in the differences observed in shoulder belt interaction.

The WorldSID and the GHBMC also showed limited ability to capture PMHS sensitivity to changes in impact direction. This may be an issue related to the limited PMHS sample size or to the performance of the ATD and the HBM. This lack of biofidelic sensitivity may affect the ability of the WorldSID and the GHBMC to correctly assess or optimize occupant response as a function of PDOF.

5.4.2 Chest deflection and injury response

Although the WorldSID partially captured the effect of the bolster structure with the use of the chestband, the standard WorldSID only includes 2D IR-TRACC sensors attached to the center of the rib and, therefore, the system is only able to capture the motion of the lateral aspect of the rib. This, in combination with the low chest injury prediction values and the lack of a biofidelity chest deflection in the seatbelt and bolster areas (figure 5.12), suggests that the WorldSID is not able to capture a substantial portion of the rib fractures and their injury mechanisms (seat and seatbelt loading). While existing literature suggests that improving the sensor location in the WorldSID (e.g., using RibEye) may improve its injury prediction capabilities (Pintar et al., 2007), this may not be sufficient to capture the complexity of the injury mechanism. This issue is three-fold: first, the anterior aspect of the WorldSID is represented by a flexible joint which prevents the correct load transfer between the ipsi- and contralateral sides of the thorax; second, due its construction, the WorldSID is not able to represent realistic anterior-posterior thoracic response as reflected in the poor seatbelt-related chest deflections (figure 5.12); and third, the inner rib bands of the WorldSID (i.e., the instrumented bands) are not in contact with the anteroor posterolateral aspect of the torso (figure 5.14). Due to the separation between the inner and outer rib bands in the oblique aspect of the ribcage, additional sensors located anterior and posterior to the stock IR-TRACC location may not be able to capture external rib deflection resulting from oblique loading from the seatbelt or seatback.

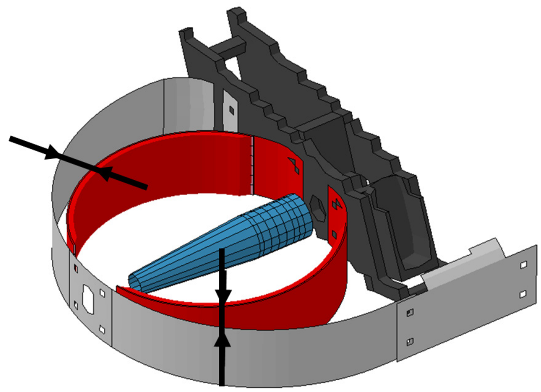

Figure 5.14: Detail of the distance between WorldSID interior and exterior rib bands

The GHBMC showed improved chest deflection compared to the WorldSID. The GHBMC, unlike the WorldSID, captures the deflection of the most affected body chest regions (i.e., seatbelt and bolster regions). Although there are aspects the can be improved (e.g., the ribs are not attached to the surrounding tissue), these results indicate that the GHBMC is able to represent the complex thoracic loading generated in the tests. The GHBMC was also able to predict the probability of rib fracture resulting from the PMHS tests.

5.4.3 General remarks

In spite of the relatively poorer performance of the WorldSID, it is important to remember that the ATD is only used in this dissertation to validate the vehicle FEM (chapter 6). Therefore, the level of biofidelity required of the ATD is lower than for the HBM. In the methodology presented in this dissertation, the ATD only needs to exhibit sufficient external biofidelity in order to load the vehicle environment in a realistic manner. On the other hand, the HBM is used to explore occupant response, create the corresponding response surfaces (chapter 7) and eventually assess the vehicle performance (chapter 8). Therefore, the HBM should show improved kinematic, kinetic and injury biofidelity. In this case, the GHBMC shows improved biofidelity with respect to the WorldSID and, at least, similar biofidelity with compared to other HBM (Katagiri et al., 2016; Pipkorn et al., 2018).

Overall, the WorldSID and the GHBMC have showed sufficient biofidelity to illustrate the methodology presented in this dissertation.

Chapter 6

Identification of Modeling Uncertainty Factors

This study estimates the uncertainty ranges of modeling parameters (model uncertainty) to be explored in chapter 7.

6.1 Introduction

The calibration and validation of the vehicle FEM is critical for the correct representation of the vehicle environment. Moreover, generating trust in the process is key for the acceptance of HBM in official vehicle test protocols (e.g., legislation). Traditional FEM calibration approaches focus on optimizing a series of model parameters (e.g., friction) to match specific physical tests responses (e.g., vehicle intrusion). These methodologies start with a range of possible values for the model parameters and optimize each parameter to determine a single final value (figure 6.1 - up). These approaches assume all the disparity between the tests and the simulation results are caused by differences in the calibration parameter values. However, this assumption may not be true when representing phenomena as complex as vehicle impacts. In these scenarios, there are multiple known and unknown factors that may have an effect on the response used to calibrate the FEM. Therefore, although a correct validation may partially reduce this effect, these deterministic calibration approaches may lead to hyper-optimized model parameters. That is, models whose parameter values optimize the effective response of the system but differ from the actual parameter values. Moreover, the selection of a single set of modeling parameters generates certain susceptibility to model tampering. That is, the selection of modeling parameters that lead to artificially improved vehicle assessments (e.g., lesser injuries). Therefore, current calibration and validation approaches are not able to generate sufficient trust in the vehicle FEM.

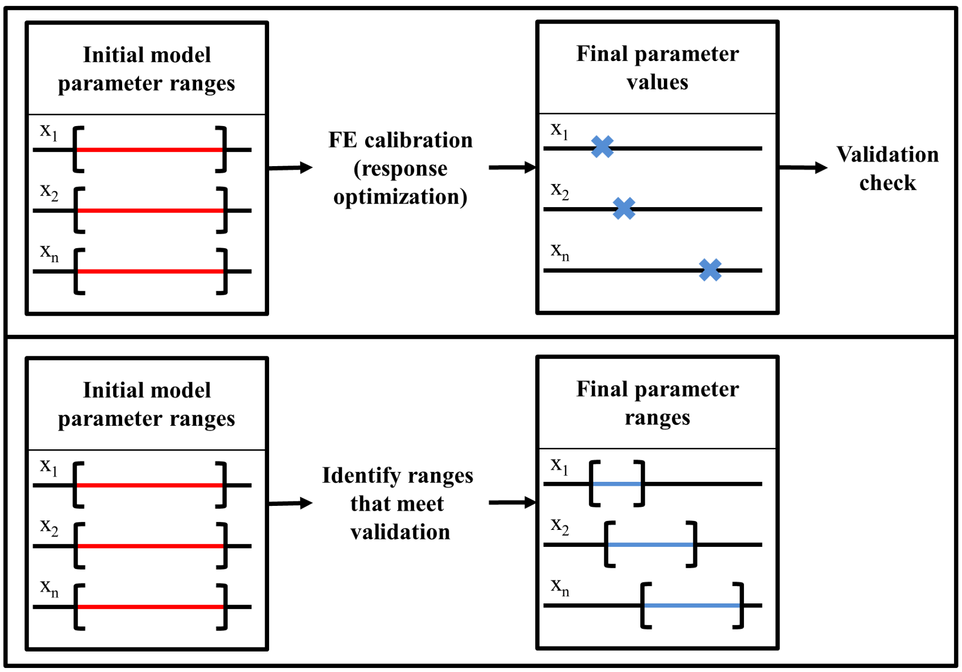

Figure 6.1: Traditional validation approach (up) and approach with model parameter uncertainty ranges (bottom)

In order to generate trust in the FEM, the validation of the vehicle model should be approached in a different manner. The alternative approach presented in this study assumes that all the values in the initial model parameter ranges are valid unless they fail to meet a predetermined validation criterion. Therefore, in this new approach, the model parameters are not optimized based on a particular response but rejected if they fail to represent it. This leads to a more conservative model validation that introduces uncertainty in the model parameters and reduces the hyper-optimization of the system and the risk of model tampering.

Variations in the friction coefficients tend to have a noticeable effect on the FE results (Cochran et al., 2015; Poulard et al., 2016; Xiao et al., 2016; Klug et al., 2017; Umale et al., 2018). Moreover, some of the injury causing structures may show variation in their mechanical properties. This is particularly true for injected polymer parts (e.g., center console) whose ultimate strain typically shows a noticeable degree of variation around its average value (Thomason, 2002). In this study, a series of simulations and physical tests were conducted to identify the friction and center console ultimate strain uncertainty ranges to be explored in chapter 7.

6.2 Methods

6.2.1 WorldSID tests

A total of six WorldSID tests (table 6.1) were conducted using the setup and vehicle-based sled environment described in section 5.2.2. These tests included the four WorldSID tests conducted in chapter 5 and two additional tests conducted without the center console of the vehicle. All the tests were conducted in a 75-degree PDOF.

Table 6.1: Test matrix

Test #	**PDOF [degrees]**	**Δv [km/h]**	**Center console**
485	75	33.5	Yes
486	75	33.5	Yes
510	75	33.5	Yes
511	75	33.5	Yes
487	75	33.5	No
488	75	33.5	No

6.2.2 WorldSID simulations and estimation of parameter uncertainty ranges

The vehicle-based sled FEM described in section 5.2.2 was used to simulate the WorldSID tests using the LSTC.WorldSID_50TH.180611_V1.100_BETA. A total of six simulations were conducted in LS-Dyna v7.1.0 varying the seatbelt friction coefficient and the center console ultimate strain (table 6.2). Head lateral excursion, seat and center console lateral motion and seatbelt forces were compared between the FEM and the physical tests. CORA scores were calculated for these responses using the standard weighting:

$$CORA_{score} = 0.5 \cdot Score_{shape} + 0.25 \cdot Score_{phase} + 0.25 \cdot Score_{area}$$

Table 6.2: Simulation matrix

PDOF [degrees]	**Δv** [km/h]	**Seatbelt friction**	**Center console**	**Center console ultimate strain**
75	33.5	0.375	No	N/A
75	33.5	0.5	No	N/A
75	33.5	0.375	Yes	90% OEM
75	33.5	0.375	Yes	110% OEM
75	33.5	0.5	Yes	90% OEM
75	33.5	0.5	Yes	110% OEM

Seatbelt friction uncertainty range

A series of quasi-static tests were conducted to determine the friction coefficients between the different materials in contact in the FEM. Based on these tests, the initial seatbelt friction range was defined from 0.375 to 0.5. The seatbelt friction final uncertainty range was estimated using the tests and simulations conducted without the center console. The final modeling parameter uncertainty ranges were defined as those that led to a "good" CORA score (i.e., CORA$\geq$0.65) (ISO, 1999) in the different responses.

Center console ultimate strain uncertainty range

Once the seatbelt friction uncertainty range was established, the center console ultimate strain uncertainty range was estimated using the test and simulation conducted with the center console. The initial range for the center console ultimate strain was defined as ±10% of the OEM-reported ultimate strain (Thomason, 2002). The final modeling parameter uncertainty ranges were defined as those that led to a "good" CORA score in the different responses.

6.3 Results

Table 6.3 shows the friction coefficients obtained in the quasi-static tests for different pair of materials. The friction coefficient for the neoprene was greater than 1 for contacts with Coban™and fabric. This was the consequence the neoprene's tendency to adhere to its sliding counterpart. Another interesting effect is that the seatbelt friction coefficient depends of the sliding direction and varies between 0.375 and 0.5 for contacts with Coban™.

Table 6.3: Friction coefficients

	Coban	Fabric
Aluminum	0.73	0.25
Leather	0.62	0.44
Neoprene	1.23	1.04
Seatbelt	0.38	0.21
Seatbelt (transverse direction)	0.50	0.30

6.3.1 Seatbelt friction uncertainty range

The simulations conducted to replicate the physical tests without center console showed that the boundary values in the initial seatbelt friction range (i.e., 0.375 - 0.5) led to similar responses and successfully generated CORA scores greater than 0.65 (figure 6.3). Therefore, any value within the range is a valid friction coefficient and the uncertainty range cannot be reduced.

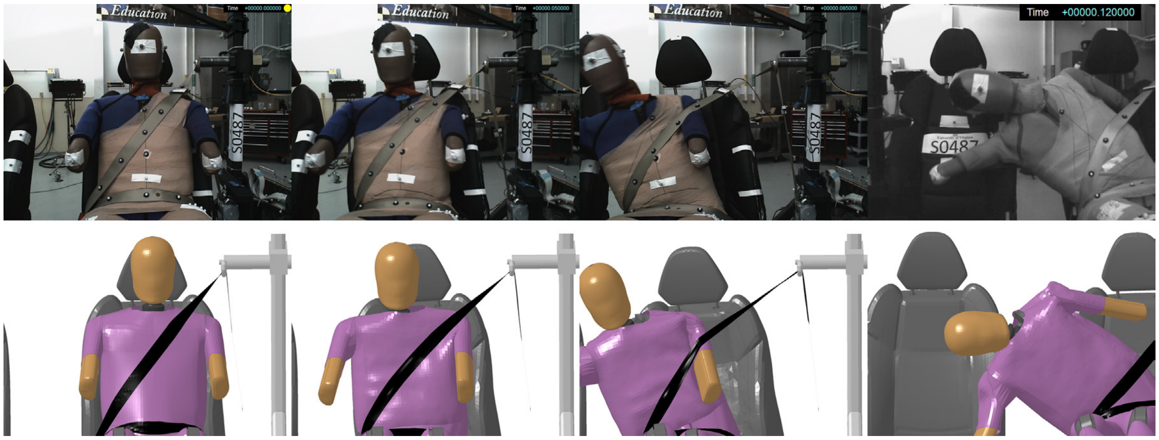

Figure 6.2: WorldSID test and simulation (μ=0.5) without center console at 0, 50, 85 and 120 ms

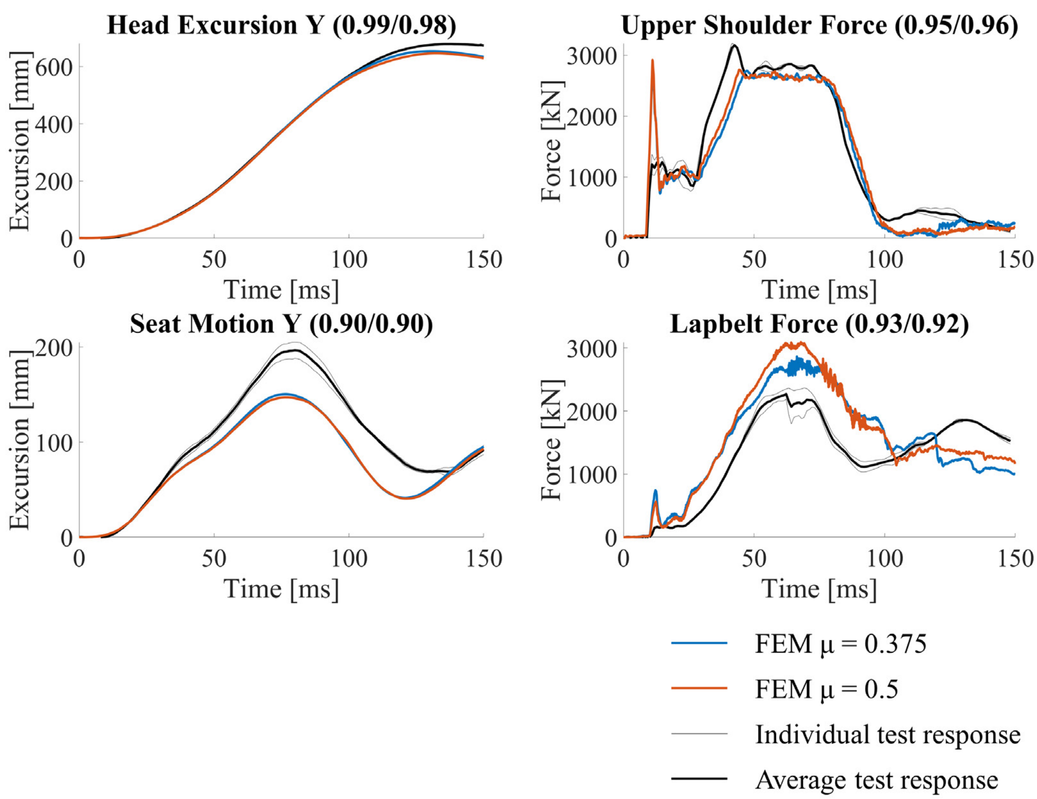

Figure 6.3: Comparison of FE response with different friction coefficients to physical test without center console. CORA scores in parenthesis (μ=0.375 / μ=0.5)

6.3.2 Center console ultimate strain uncertainty range

The simulations conducted with the center console showed that variations of the center console ultimate strain did not noticeably influence the responses or affect the CORA scores. Therefore, any value within the initial parameter range is a valid center console ultimate strain and the uncertainty range cannot be reduced.

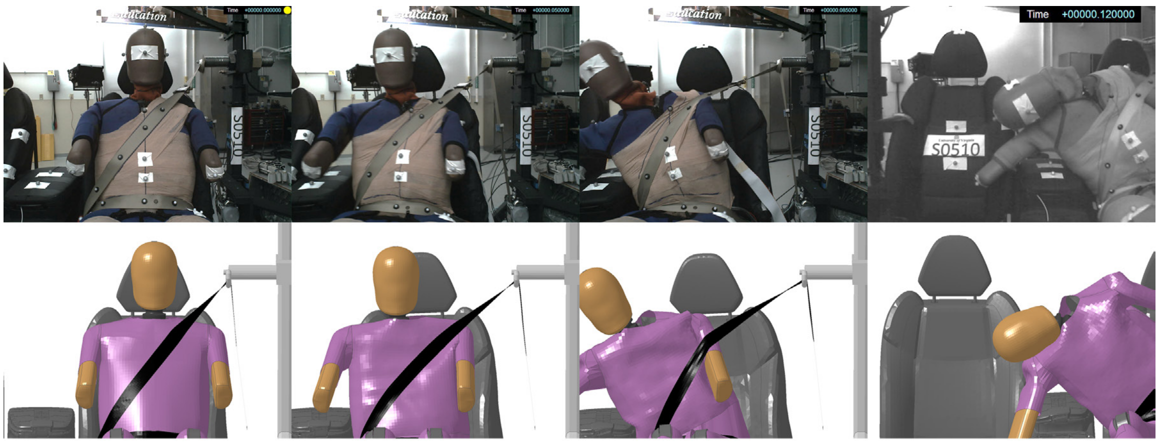

Figure 6.4: WorldSID test and simulation with center console (μ=0.5 and ϵ_f=90% OEM) at 0, 50, 85 and 120 ms

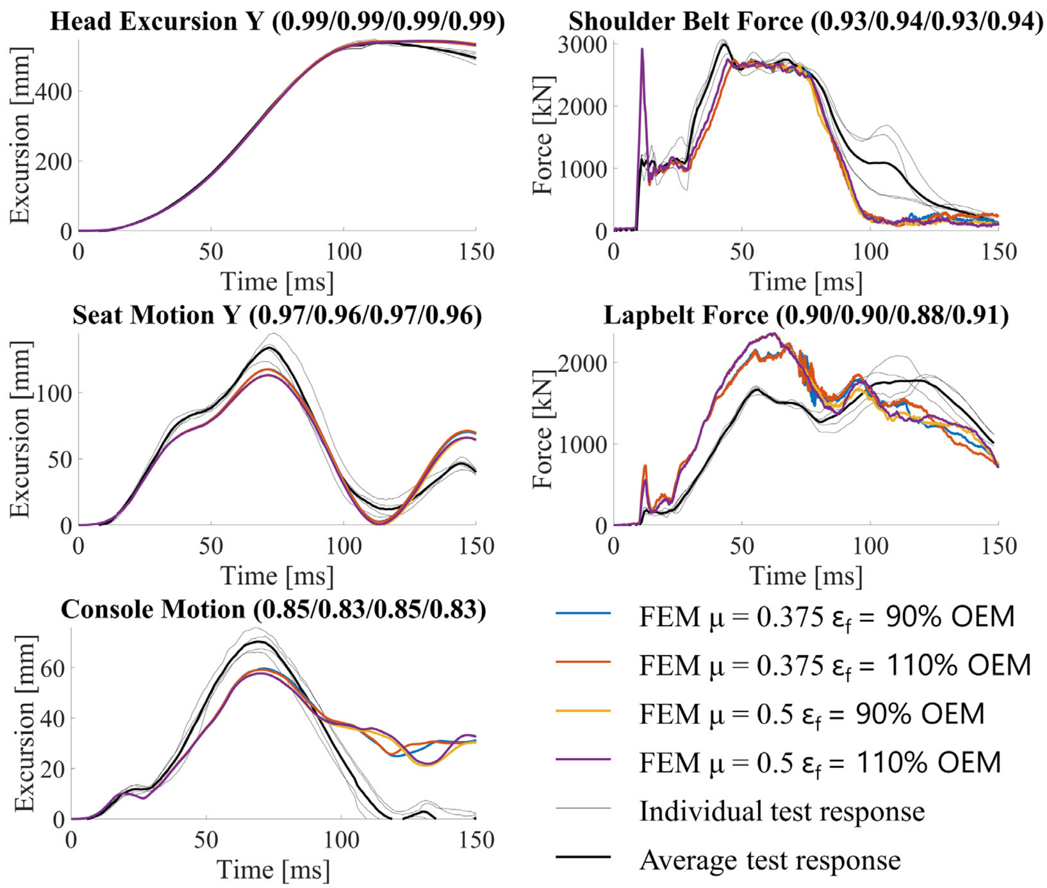

Figure 6.5: Comparison of FE response with different friction coefficients and center console ultimate strain to physical test without center console. CORA scores in parenthesis (in legend order)

6.4 Discussion

The approach described in this study assigns a range of possible values to those FE parameters whose values are uncertain (i.e., modeling uncertainty factors). In this particular application the seatbelt friction and the center console ultimate strain were identified as model uncertainty factors. The uncertainty range in the seatbelt friction was estimated using the tests without a center console in order to isolate the effect of the seatbelt friction. Once the seatbelt friction uncertainty range was established, the center console ultimate strain uncertainty was estimated using the tests with the center console. The specific model uncertainty factors to explore may vary depending on the end application. However, regardless of the end application, these factors can be defined as those that show an inherent variability (e.g., ultimate strain in injected polymers), those whose actual values are uncertain or those whose application in FE environments is complex or unfeasible (e.g., direction-dependent friction).

This study used lateral head excursion, seat and console lateral motion and seatbelt forces as the responses to be evaluated. Lateral motions were used since the uncertainty factors are assumed to have a larger effect on that direction with the recognition that other studies may evaluate other responses (e.g., level of vehicle intrusion).

In the present approach, the reduction of a parameter range (i.e., its uncertainty) is only possible if a validation criterion has been previously defined. In this particular application, the validation criterion was based on the CORA scores of the individual responses. However, many other validation criteria can be used (e.g., average CORA score, weighted scoring, etc.) for the evaluation of the FEM and reduction of the parameter uncertainty ranges. The key characteristic of this approach is that regardless of the validation criterion, the FE parameters are not obtained by optimization of a single value to meet the FE response but by reducing their range of values to those that meet the validation criterion.

This study identified initial uncertainty ranges for the seatbelt friction and center console ultimate strain. After evaluating the FEM, these uncertainty could not be reduced. Therefore, chapter 7 will use the seatbelt friction and center console ultimate strain as modeling uncertainty factors ranging from 0.375 to 0.5 and from 90% to 110% of the OEM value, respectively.

THIS PAGE INTENTIONALLY LEFT BLANK

Chapter 7

Multidimensional Domain Exploration and Response Surface Generation

Previous chapters 2, 3 and 6 have identified two occupant responses to be evaluated as well as a number of intrinsic, extrinsic and modeling factors that may have an effect on them (table 7.1) This chapter presents an efficient method for the predictive exploration these two multidimensional spaces based on Neural Networks (NN) and compares its performance to more traditional regression approaches. The resulting response surfaces are the cornerstone of this methodology since they contain all the information needed to assess human response variability. These surfaces will be used as inputs in chapter 8 for their use in the variability-based vehicle assessment.

7.1 Introduction

The generation of FE model response surfaces consists in generating a continuous response based on a discrete sample of simulations in a multidimensional space. Therefore, a successful domain exploration technique leads to the prediction of the entire response surface given a finite number of datapoints. The techniques used in the literature vary from ordinary linear regressions to the use of Neural Networks

(NN) depending the complexity of the problem at hand.

The field of biomechanics has traditionally used, among others, ordinary linear regressions in order to understand the effect that different input factors have on a particular response (Hardy et al., 2007; Forman et al., 2013; Prasad and Weston, 2011). This approach provides a direct quantification of the effects of each independent predictor, since the coefficient associated with them are proportional to their effect on the response. However, this technique has a number of limitations for its use in the generation of multidimensional response surfaces.

First, the relationship between the regression coefficients and the effect of the corresponding predictors is only valid if the inputs are independent (Rawlings et al., 1998). This poses a problem since the biomechanical data tends to be correlated (e.g height and weight). Moreover, as the order of the regression increases to represent non-linear responses, it becomes difficult to interpret the meaning of each regression coefficient (Stimson et al., 1978).

Second, ordinary linear regressions require the definition of the underlying mathematical model response (i.e., $y = ax + b$). Model selection is critical for the proper functioning of the regression since an artificially low-order model would overlook non-linearities in the data and an artificially high-order model would lead to overfitting the data. The problem arises when, as in this application, the underlying mathematical model response is unknown and the relationship between the predictors and the response cannot be observed due to the multidimensionality of the problem. In these cases, the approach used to explore the domain needs to be able to converge to the underlying mathematical model response with no a priori knowledge of the system.

Third, traditional methodologies for the estimation of the regression coefficients, like the ordinary least squares (OLS) method, often use all the available data to regress the predictors and, therefore, are not able to optimize the underlying model based on its ability to predict out-of-sample data, potentially leading to overfitting the response.

More recent techniques for the estimation of regression coefficients, like Ridge or LASSO (i.e., Least Absolute Shrinkage and Selection Operator) regularization (Hoerl and Kennard, 1970; Tibshirani, 1996), in conjunction with cross-validation (CV) techniques (James et al., 2013), are able to reduce the complexity of the model in order to optimize out-of-sample data prediction. The basics of any regularization technique consist in imposing a penalty to the value of the regression coefficients. In this scenario, the loss function to minimize in a polynomial regression is no longer just the sum of square errors $L_{OLS} = \| y_{actual} - y_{estimated} \|^2$ but $L_{reg} = L_{OLS} + \lambda \sum_n f(\hat{\beta}_n)$, where $\hat{\beta}_n$ are the predictor coefficients and λ is the regularization parameter. Some regularization techniques, like LASSO, eliminate predictors if they do not contribute to a substantial improvement of the error, reducing the model complexity and improving out-of-sample prediction. Although these methodologies have the potential to reduce overfitting, they have not been popularized in the field of injury biomechanics.

Another common technique for the creation of response surface is the use of interpolation techniques (Nie et al., 2013). These techniques are, by definition, overfitting the data since their resulting surfaces perfectly match the given datapoints. This leads to surfaces unable to learn and adapt, specially when dealing with noisy responses (Jin et al., 2001).

NN have been present for decades in multiple research fields that are rich in data, like economics (Nicholas Refenes et al., 1994), chemistry (Otto, 2016) and linguistics (Elman, 1990). On the other hand, the field of injury biomechanics has traditionally lacked the amount of data needed to use these powerful regression techniques. The irruption of Human Body Models (HBM), however, allows the field to generate the amounts of data that would benefit from the use of NN. These regression techniques offer a series of advantages that favor their use when sufficient data is available.

Since the primary criterion for the evaluation of model performance is its predictive accuracy on out-of-sample data, rather than goodness of fit on training data (Huddleston and Brown, 2019), correctly trained NN are able to represent the underlying mathematical model response of the system. NN, unlike ordinary regressions or interpolation methods, avoid under- and overfitting (also known as the bias-variance trade-off) by varying their complexity (e.g., number of neurons) to optimize out-of-sample prediction (figure 7.1). One of the most commonly used techniques for this optimization is cross-validation (CV) (Lawrence et al., 1998; James et al., 2013).

During the CV phase, the training data is divided in k groups, hence the name k-fold CV. Once the groups are created, a number of NN with different topologies (i.e., number of neurons, their connectivity and activation functions) and learning algorithms (e.g., backpropagation algorithms) are trained using k-1 groups as a training set. The resulting network performance is evaluated based on its error in predicting the responses in the remaining group (validation set). This process is repeated k times using each group once as a validation set. At the end of this process, the network with the minimum average validation error is selected as the final network topology (figure 7.2). This procedure generates a NN that generalizes well.

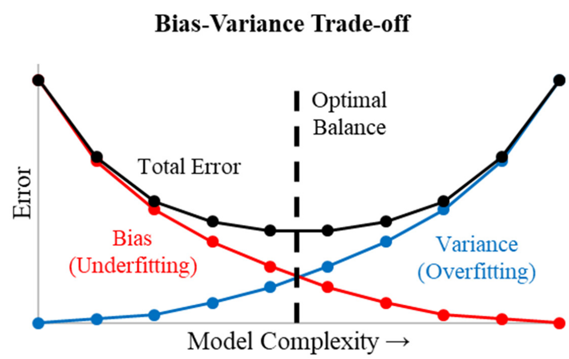

Figure 7.1: Bias-Variance trade-off

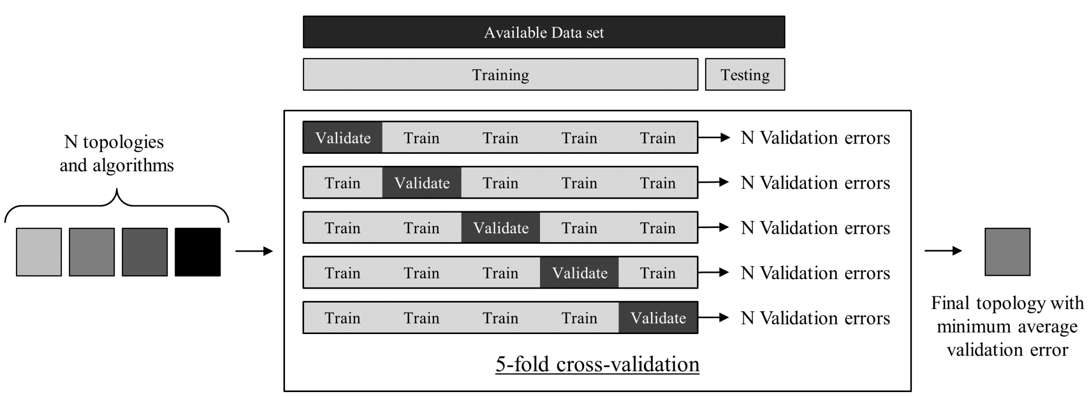

Figure 7.2: Generic 5-fold Cross-Validation workflow (adapted from Huddleston and Brown (2019))

This final topology is trained with the totality of the training set and its prediction error measured using the testing set (figure 7.3). This error is, as mentioned before, the primary criterion for the evaluation of model performance.

NN allow for the training process to be conducted in an iterative manner where the data set is progressively increased. This process minimizes the number of simulation to run since the prediction error can be checked after each iteration and the process stopped after the error meets a certain predetermined threshold.

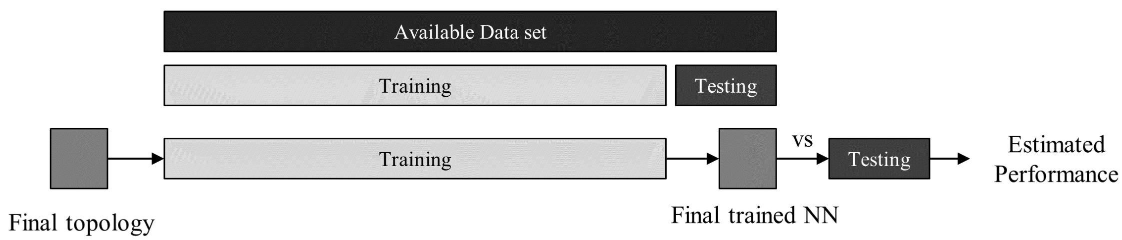

Figure 7.3: Generic training and testing of selected topology

All these characteristics and methods for NN make very robust regression techniques able to manage noisy systems and converge to the true underlying model response when sufficient training data is provided.

In this chapter, a total of 405 simulations were conducted in an iterative manner in order to generate and to evaluate the response surfaces for maximum lateral head excursion and probability of 3+ fractured ribs using ordinary linear and logistic regressions, LASSO regularization and NN techniques. Although this chapter only explores these three regression techniques, the methodology itself can be followed using any regression technique with sufficient out-of-sample predictive performance.

7.2 Methods

A total of 405 simulations generated in nine iterations were used for the definition of the response surfaces for the maximum lateral head excursion and the probability of 3+ fractured ribs to explore the intrinsic, extrinsic and modeling factors described in table 7.1.

Table 7.1: Responses and input factors for domain exploration

Responses		
Maximum Lateral Head Excursion Chest Deflection		
Input Factors		**Ranges**
Intrinsic	Height Weight Waist Circumference	158 - 193 cm 51 - 119 kg 66 - 122 cm
Extrinsic	Δv PDOF Seatbelt Load Limiter	22 - 45 km/h 60 - 90 degrees 1 - 5 kN
Modeling	Seatbelt Friction Center Console Ultimate Strain	0.375 - 0.5 ±10% of OEM value

These simulations involved the use of the vehicle environment developed in chapter 6 and series of HBM morphed following the methodology described in charter 3. The simulations were run in LS-Dyna v7.1.0 using an in-house developed Matlab script that is able to morph, settle, position the seatbelt, run and post-process any number of simulations in parallel in a fully automated manner in batch-mode. A general workflow can be found in image 7.4.

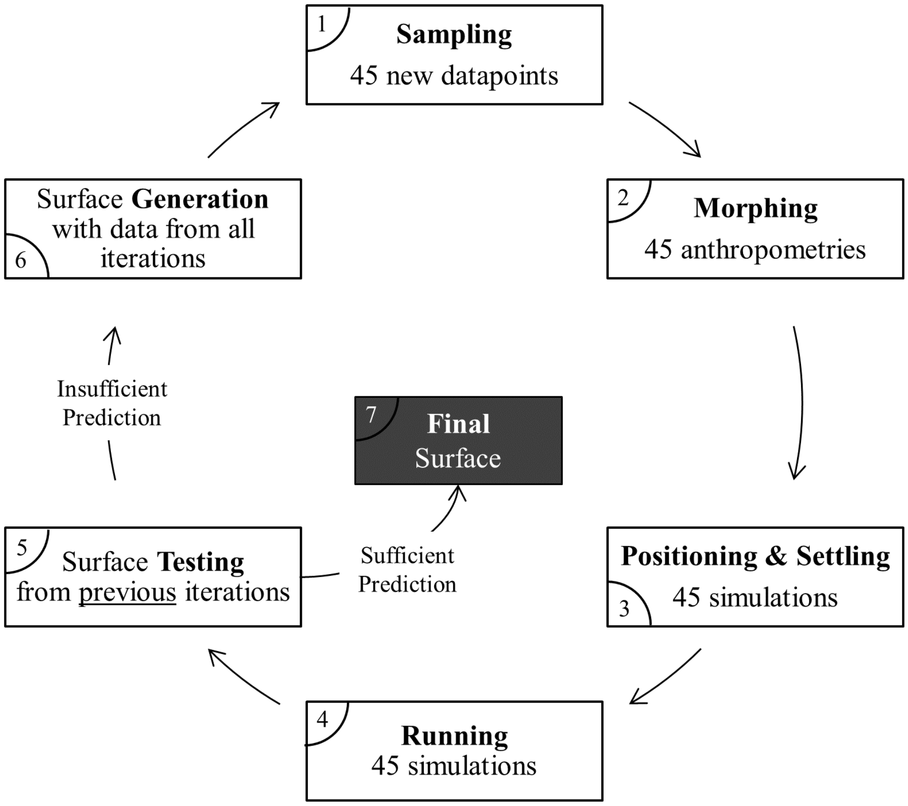

Figure 7.4: Methodology workflow

7.2.1 Sampling strategy

The space was sampled in series of 45 datapoints in order to generate a saturated quadratic sample in each iteration (figure 7.4 - 1). That is, each iteration provided sufficient information to estimate the parameters of an eight-dimensional, second order polynomial equation. The sampling strategy was set up to fill up the sampling space comprised by the intrinsic, extrinsic and modeling factors with equidistant points in each iteration. A model-free, distance-based sampling method (Santner et al., 2003; Pronzato and Müller, 2012) was coded in Matlab and utilized for creating the space-filling design (figure 7.5). This led to a uniformly explored space (i.e., all points had the same probability of being selected). In this sampling strategy, a different HBM was morph for each individual simulation following the methodology described in chapter 3 with the goal of covering 90% of the ANSUR II database male population (figure 7.4 - 2). The performance of the in-house Matlab script was benchmarked against the literature, based on its ability to maximize the distance between samples. More information about the sampling algorithm and its performance can be found in appendix J.

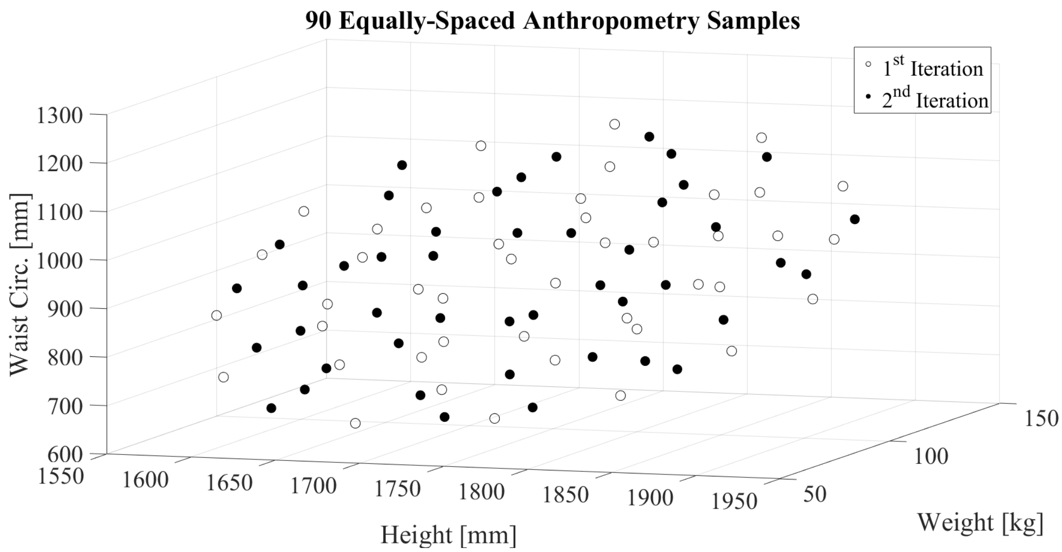

Figure 7.5: Example of two iterations of 45 anthropometry samples each obtained using the filling-space in-house Matlab script

7.2.2 HBM positioning and settling

Based on observations by Manary et al. (1994), the hip-joint-center (HJC) of the different HBM were positioned to match PMHS fore-aft target position described in chapter 5. The extremities and upper body were positioned in the same angles for all models before the settling phase. During this phase (figure 7.4 - 3), the HBM was seated by gravity and the upper body was allow to rotate to conform to the seat back. The upper and lower extremities were constrained to represent an occupant in a driving position.

7.2.3 Simulation run and data cleaning

The seat and HBM pre-stresses were extracted after the settling phase and imposed back in the final run. The vertical position of the d-ring was varied to maintain a constant angle with the occupant's shoulder in the sagittal plane in order to keep comparable shoulder belt angles among the different models (figure 7.6).

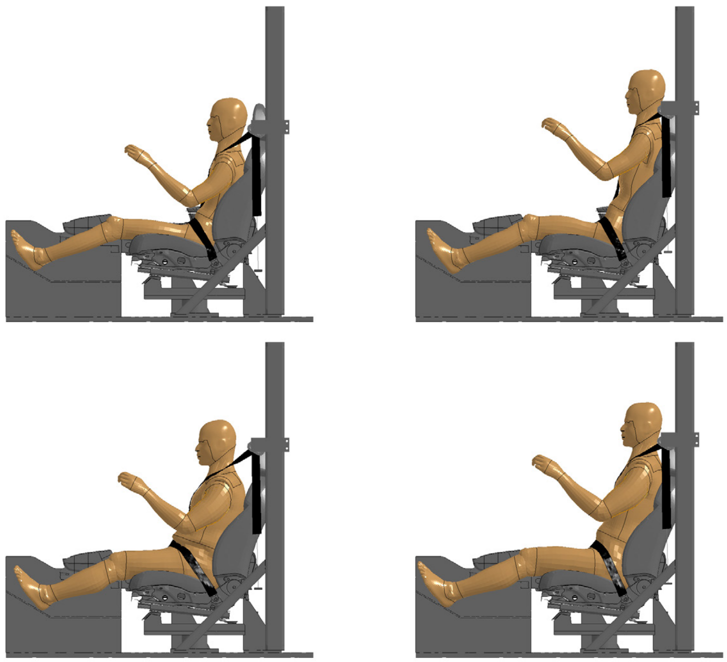

Figure 7.6: Models settled for final simulation run

Upon completion, the simulations with numerical instabilities (e.g., "exploding" elements) were identified and discarded. Valid simulations were defined as those that ran at least until the time of maximum head excursion. The data generated beyond that point was discarded (figure 7.4 - 4).

The maximum lateral head excursion and the probability of 3+ fractured ribs were calculated for all valid simulations. The methodology for the estimation of the probability of 3+ fractured ribs involves (Forman et al., 2012):

1. Collection of the maximum strain of each rib
2. Calculation of the probability of fracture for each rib using a risk curve derived from coupon testing

3. Use the binomial distribution defined by the resulting probabilities in order to estimate the probability of 3 or more fractured ribs

7.2.4 Surface testing

Once a new set of simulations was run, it was used to evaluate the performance of the surfaces created in the previous iteration (figure 7.4 - 5). The average error between the response predicted by the different surfaces and the actual response of the FE models were compared for the three regression methods. Once the error was deemed to be stable below 10% of the range of the response, the surfaces from the last iteration were considered sufficient for the exploration of the methodology presented in this dissertation and the domain exploration concluded (figure 7.4 - 7).

7.2.5 Surface generation

In each iteration, a new set of surfaces was created using all the available information (including that of previous iterations) to train the different regression models (figure 7.4 - 6). In all cases, the data inputs were standardized between -1 and 1 in order to unify scales before training the models. The parameters used as inputs in for the different regression techniques are summarized in table 7.2.

Table 7.2: Input parameters for surface generation*

Height	Weight	Waist Circ.
Eye Height Sitting	Shoulder-Elbow Length	Elbow-Wrist Length
Thigh Link	Lateral Femoral Epicondyle Height	Waist Breadth
Hip Breadth	Waist Depth	Biceps Circ.
Thigh Circ.	Low Thigh Circ.	Chest Circ.
Forearm Circ.	Calf Circ.	Foot Length
Foot Breadth	Chest Wall Thickness	Pelvic Link
Bicristal Breadth	Δv	PDOF
Seatbelt Friction	Center Console Ultimate Strain	Load Limiter

*The anthropometry measurement definitions can be found in Gordon et al. (2014)

The regression techniques used to generate the different response surfaces were:

- Ordinary linear regression

- Logistic regression
- LASSO regularization for linear and logistic regressions
- NN

Ordinary linear regression

Ordinary linear regressions were conducted using the predictors in table 7.2 to regress maximum lateral head excursion.

Logistic regression

Logistic regressions were conducted using the predictors in table 7.2 to regress the probability of 3+ fractured ribs.

LASSO regularization

LASSO regularization, also referred to as LASSO regression, was used to reduce the number of predictors in the linear and logistic regressions (Tibshirani, 1996). This regularization technique uses $L_{reg} = L \ + \lambda \sum_n |(\hat{\beta}_n)|$ as loss function, where L is the ordinary least square error or the negative log likelihood for linear and logistic regressions, respectively. For each response, the regularization parameter λ was selected to optimize the validation error using all the available data in a 3-fold CV. After the optimal λ is obtained, the final regression model is calculated using this parameter and all the available data as a training set (figure 7.7).

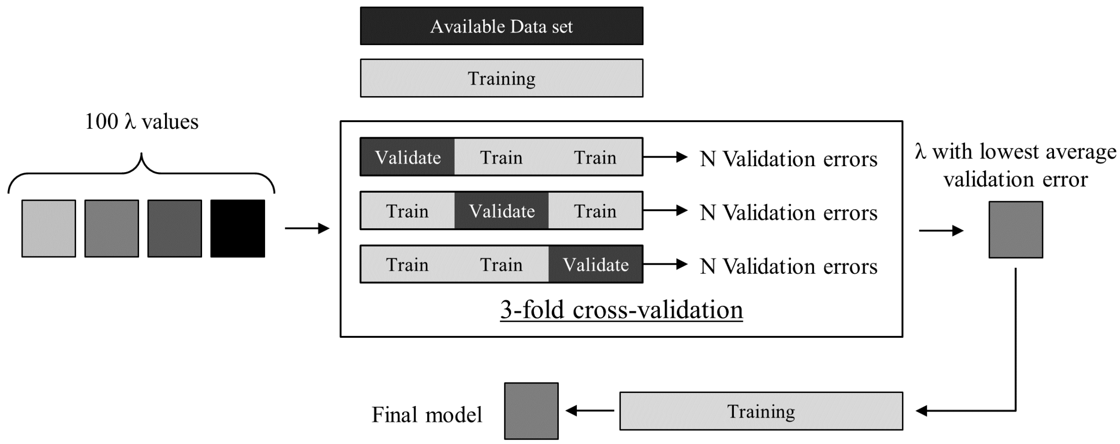

Figure 7.7: CV and training of LASSO models

Neural Network

Two NN were trained to regress the response surfaces using the predictors in table 7.2. The NN were limited to one hidden layer using sigmoid activation functions. The output neuron used a linear activation function (figure 7.9). The output was later bounded between 0 and 1 for the rib fracture probability surface. For each response a 3-fold CV was used to identify the best network topology ranging from 1 to 10 neurons in the hidden layer. This range was selected since it was able to generate sufficiently complex responses to capture the optimum model (figure 7.1). Once the optimal topology was identified, it was trained with the totality of the available data as training set (figure 7.8). In all cases, the training was conducted using Bayesian regularization backpropagation (Buntine and Weigend, 1991; Burden and Winkler, 2009).

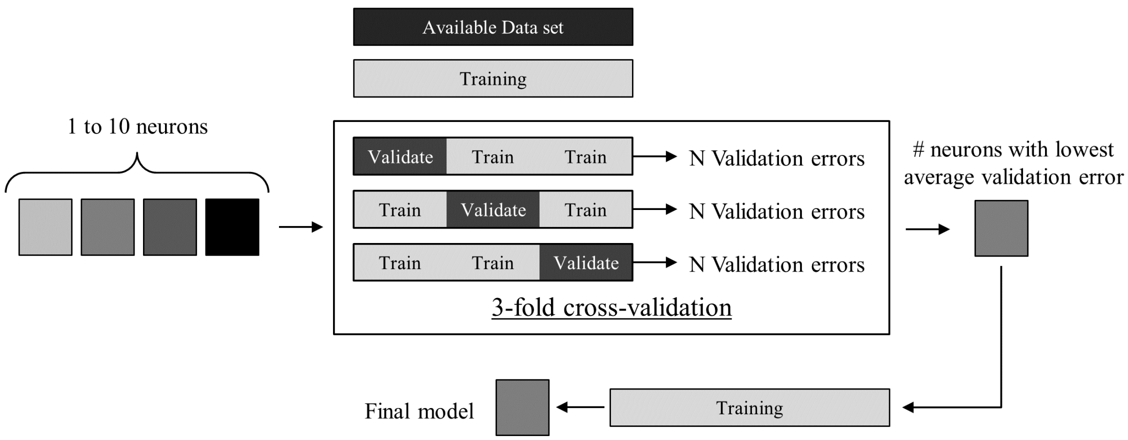

Figure 7.8: CV and training of NN

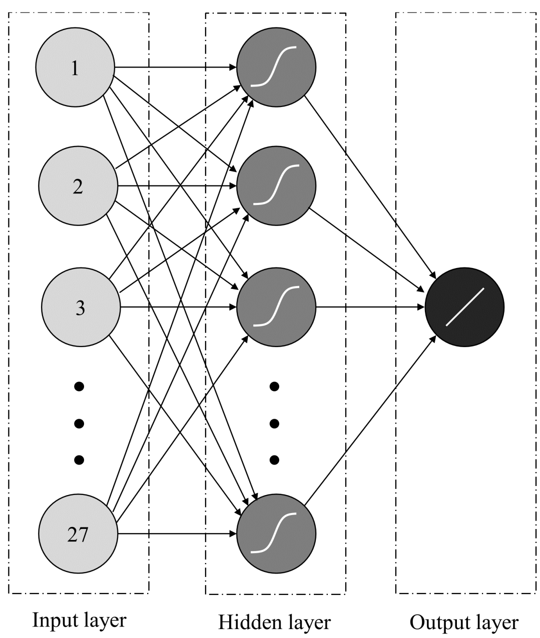

Figure 7.9: Neural network topologies used in this chapter

7.2.6 Weighted error

The final prediction errors were also calculated weighting the datapoints proportionally to their probability of occurrence in the field using the information described in chapters 2 and 3. This error gives an estimation of the expected error in predicting societal responses.

7.2.7 Additional approaches

Additional approaches were followed for the regression of 3+ fractured ribs in the NN models. These approaches included:

- Use of 10-fold CV
- Introduction of upper body angle in the sagittal plane as a regression feature (i.e., as an input)
- Reduction of the number of regression features to those shown in table 7.3
- Use of rectified linear unit (ReLu) as activation function
- Use of Levenberg-Marquardt (LM) backpropagation (Yu and Wilamowski, 2011)
- Oversampling the training data

Table 7.3: Reduced number of inputs*

Weight	Eye Height Sitting	Waist Breadth
Waist Depth	Δv	PDOF
Seatbelt Friction	Center Console Ultimate Strain	Load Limiter

*The definition of anthropometry measurements can be found in Zhou et al. (2016)

7.3 Results

Figure 7.10 shows the evolution of the testing error for the prediction of the maximum lateral head excursion. The head excursion response surface was better capture by the NN. The linear and LASSO regressions showed approximately four times larger average error (iteration 8). The best and worst performing models in the first iteration, where data was sparse, were the LASSO and the ordinary linear regression, respectively (iteration 1). The ordinary linear regression model converged to the LASSO model in the second iteration. The error stabilizes on the 2^{nd} iteration for the linear and LASSO regression and on the 6^{th} iteration for the NN. Similar responses were found in the weighted error (figure 7.11).

The predicted and actual values of the testing points for the final iteration (figure 7.12) show that the NN captured the response in all the range. The final average prediction error, the weighted average predicted error and the maximum predicted error can be found in table 7.4.

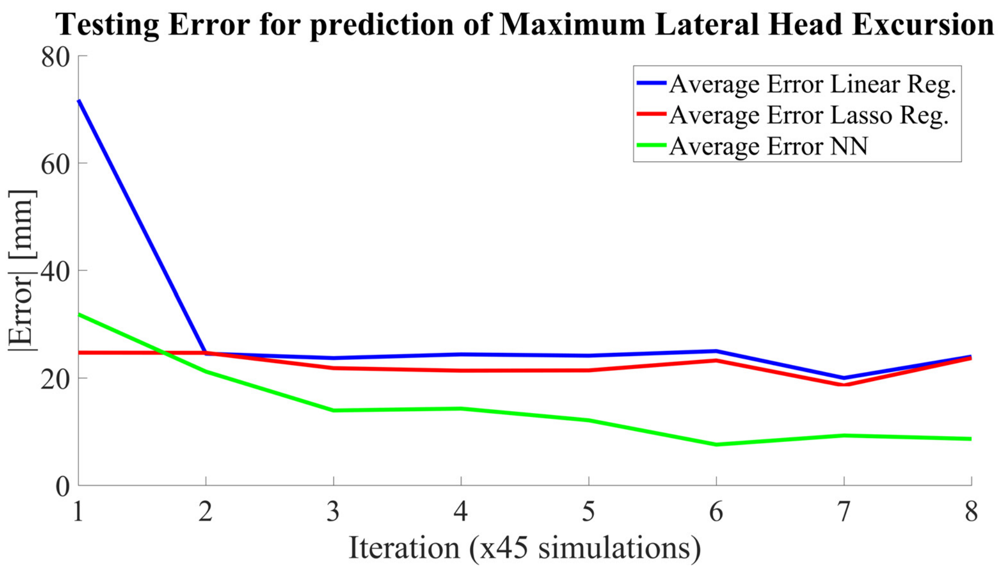

Figure 7.10: Prediction error for maximum lateral head excursion

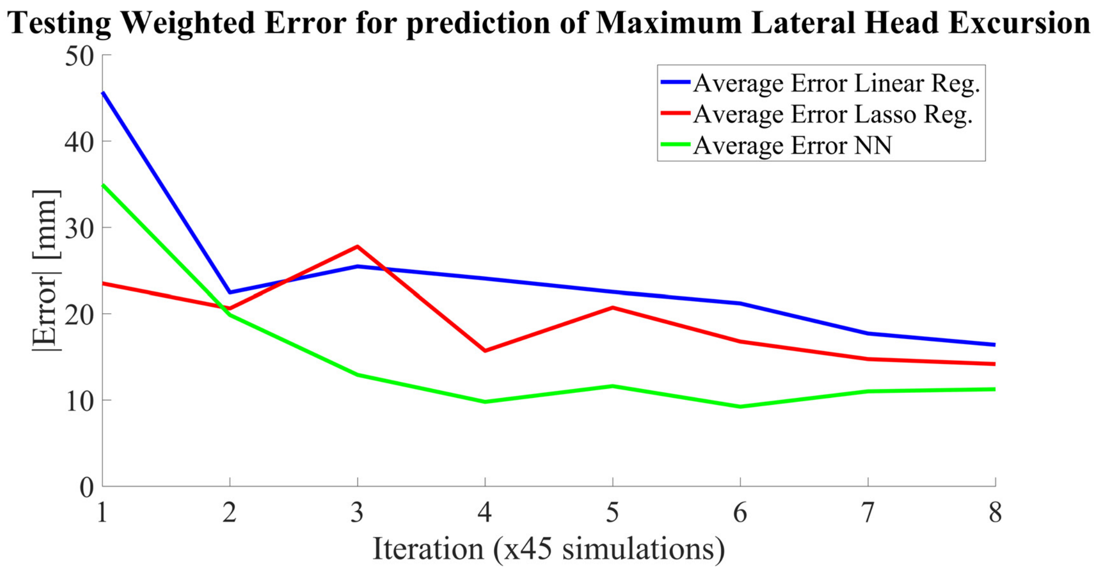

Figure 7.11: Weighted prediction error for maximum lateral head excursion

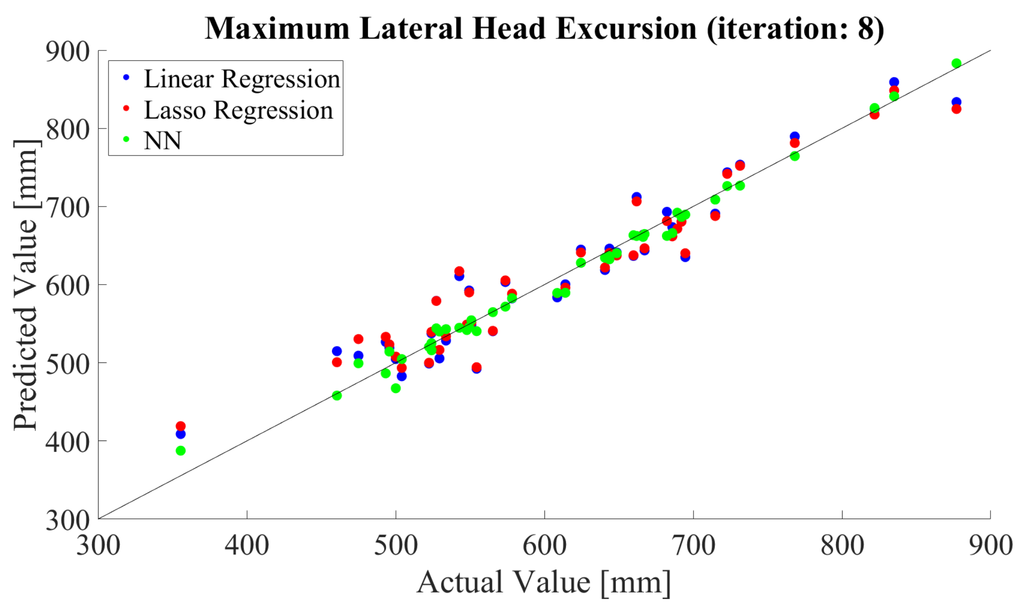

Figure 7.12: Predicted and actual maximum lateral head excursion (iteration: 8)

Table 7.4: Last iteration excursion prediction error [mm] (% with respect to the actual response range)

	Linear Reg.	**LASSO Reg.**	**NN**
Average error	24 (4%)	23.7 (4%)	8.6 (2%)
Weighted average error	16 (3%)	14 (2%)	11.2 (2%)
Maximum error	68 (12%)	74 (13%)	32.7 (6%)

Figure 7.13 shows the evolution of the testing error for the prediction of the probability of 3+ fractured ribs. The three models captured the probability of 3+ fractured ribs to a similar degree of accuracy (iteration 8). The best and worst performing model in the first iteration were the LASSO logistic regression and the logistic regression, respectively (iteration 1). The logistic regression model converged to the LASSO and NN models in the third iteration. The average error stabilizes at around 10% for all the models. The NN resulted in an improved final weighted error (figure 7.14).

Figure 7.15 shows that the response trend is captured although the prediction accuracy is lower than for the maximum lateral head excursion prediction. The final average prediction error, the weighted average predicted error and the maximum predicted error can be found in table 7.4.

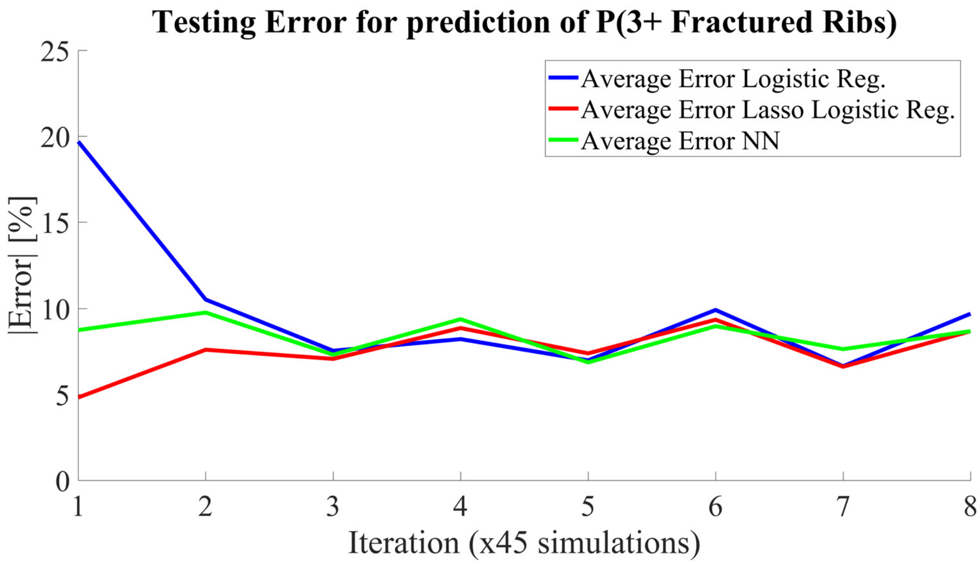

Figure 7.13: Prediction error for probability of 3+ fractured ribs

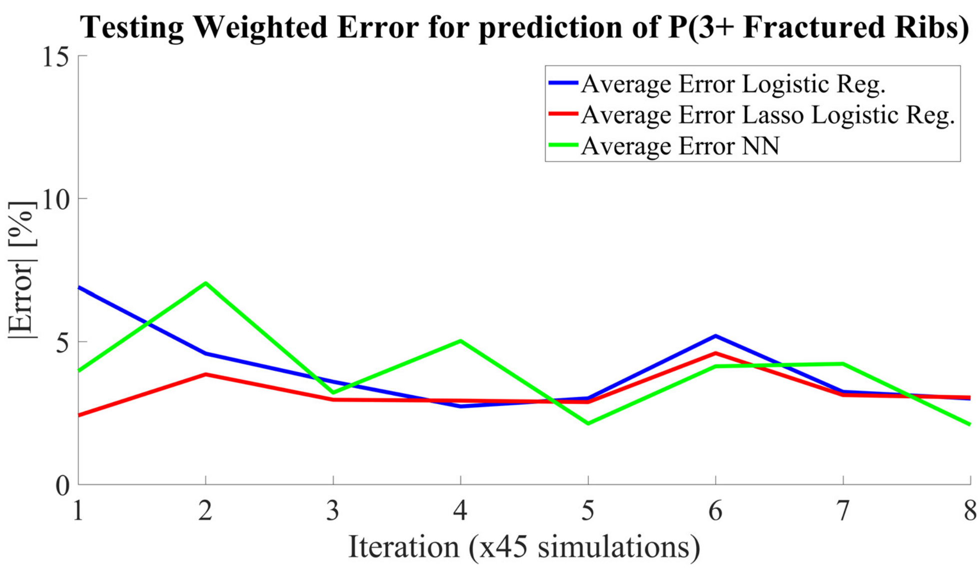

Figure 7.14: Weighted prediction error for the probability of 3+ fractured ribs

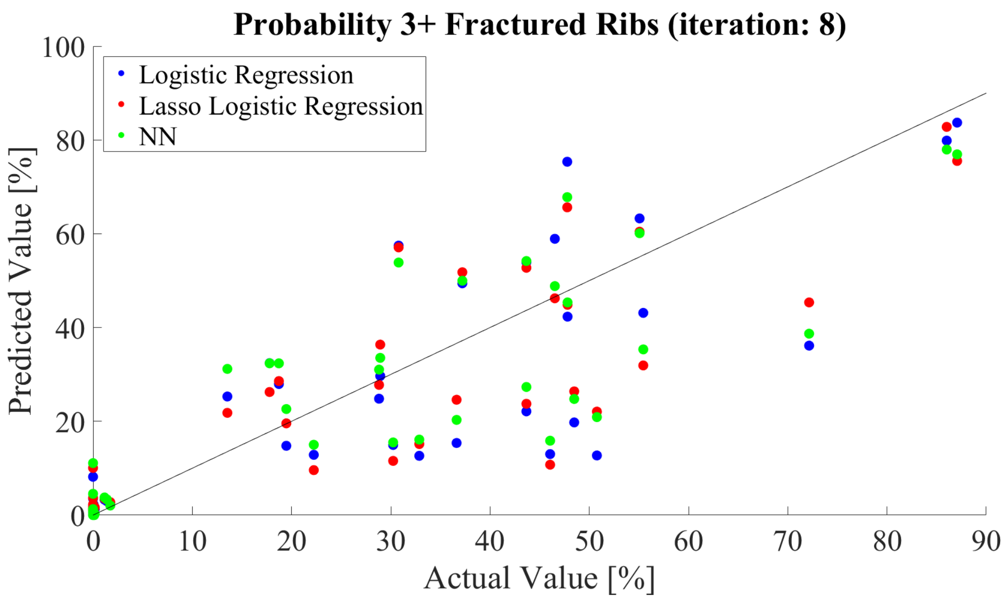

Figure 7.15: Predicted and actual probability of 3+ fractured ribs (iteration: 8)

Table 7.5: Last iteration 3+ fractured ribs prediction error

	Log. Reg.	**LASSO Log. Reg.**	**NN**
Average error	10%	9%	9%
Weighted average error	3%	3%	2%
Maximum error	38%	35%	33%

The models for excursion and probability of rib fracture do not show systematic errors with respect to the independent variables (figures K.19, K.20, K.21 and K.22). More results, including the evolution of λ in the LASSO models and the number of neurons in the NN, and the prediction of the PMHS response using NN are available in appendix K. The use of additional approaches for the NN regression of 3+ fractured ribs did not substantially improve the performance of the network (figure 7.16).

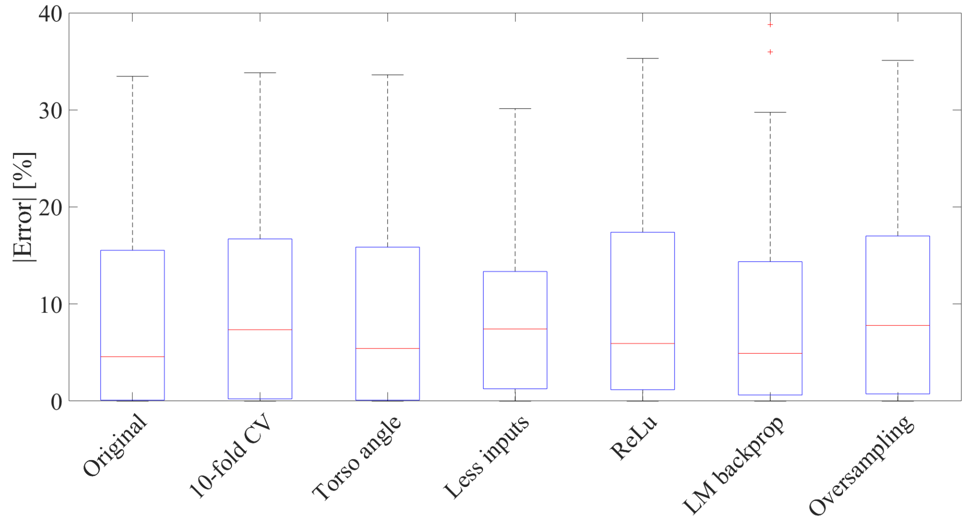

Figure 7.16: Probability of 3+ fractured ribs prediction error whiskers using NN with alternative approaches

7.4 Discussion

This chapter describes a methodology for the development of biomechanical response surfaces. An important particularity of biomechanical data is that it normally leads to non-rectangular, correlated sampling spaces. One of the difficulties in exploring these kind of domains lies on the fact that traditional distance-based sampling techniques (e.g., Latin Hypercube) assume rectangular, orthogonal sampling spaces and, therefore, are not suitable for the task. On the other hand, model-free, distance-based approaches are able to explore non-rectangular, correlated spaces. Since these sampling techniques do not discretize the space, they also allow for uncomplicated sequential sampling (figures 7.5 and 7.17). As part of this dissertation, a model-free, distance-based sampling methodology (Santner et al., 2003; Pronzato and Müller, 2012) was developed to allow sequential sampling and overcome the limitations of traditional sampling techniques. More information can be found in appendix J.

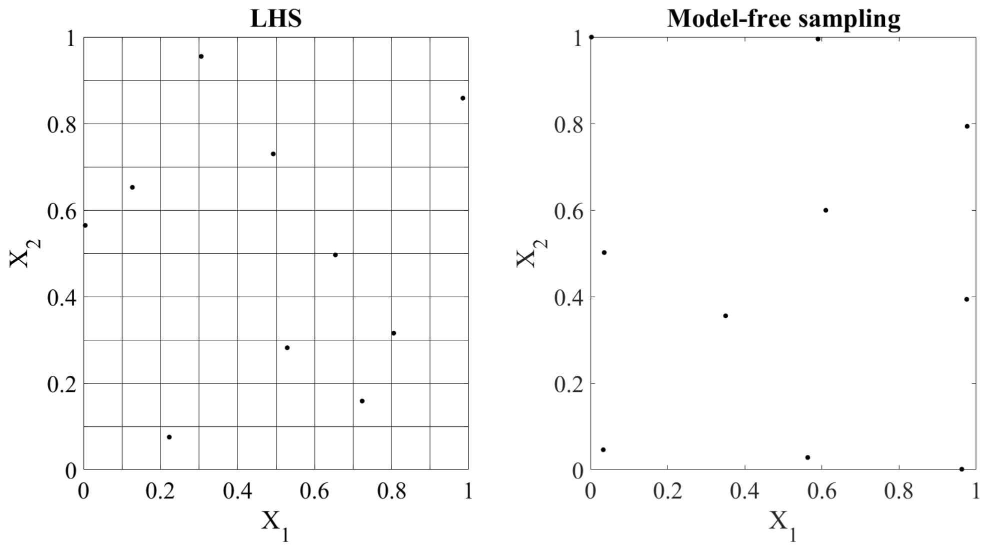

Figure 7.17: 10 points sampled using Latin Hypercube Sampling (LHS) and model-free sampling

In order to better train the models, the sampling algorithm was allowed to choose a new anthropometry for each datapoint. Therefore, each simulation was conducted with a different morphed model. This approach provides more information to the regression models since the space is more homogeneously explored. However, this is done at the expense of increased pre-processing time. Implementing this procedure requires an important degree of automation of the entire process. In a situation where the morphing and settling of the models had to be performed manually, the same sampling methodology could be followed with a pre-populated set of morphed models. This would limit the number of models to morph and settle at the expense of a potentially worse overall regression performance.

An important step in the training of any regression model is ensuring the validity of all the datapoints used in the process. Invalid datapoints in simulation are caused by numerical instabilities that generate artificial responses (e.g., "exploding" elements). Another important characteristic of valid data samples is that all datapoints in the sample must represent the same well-defined event. For this particular application, the event was defined as a far-side impact from the initial state to the state of maximum lateral head excursion. All data beyond the time of maximum head excursion was discarded. Failing to correctly define the event of interest can lead to simulations that represent different realities. For example, in this particular application, if the data was collected at the end of the simulation instead of at the time of maximum head excursion, the occupants would have experienced different degrees of rebound. Some of them may have contacted rigid parts of the sled leading to an artificially large injury risk and generating noise in the data.

In this chapter, five different regression techniques were used and evaluated in their ability to generate response surfaces for maximum lateral head excursion and probability of 3+ fractured ribs: ordinary linear regressions, logistic regressions, LASSO regularization for the linear and logistic regressions and NN. The use of interpolation techniques was discarded because they lead to purely over-fitted models unable to manage any kind of noise in the data (Jin et al., 2001). It is important to notice that, although the sampling process only controlled for height, weight and waist circumference, the measurements for the rest of the body regions included in the morphing process (e.g., length of extremities) were obtained as part of a stochastic methodology (chapter 3) and may have an effect on the responses. Therefore, they were also used as inputs in the different regression models (table 7.2).

The ordinary and LASSO regression models were limited to a linear polynomial since the interpretation of the regression coefficients, probably the greatest advantages of polynomial regressions, becomes less intuitive as the order of the polynomial increases (Stimson et al., 1978). Although the goal of this chapter was to predict the response and not necessarily quantify the effect of each factor, it is important to understand that the high level of correlation present in anthropometric data in general, and in this application in particular, poses a serious challenge to the interpretation of the regression coefficients estimated in ordinary linear regressions (Rawlings et al., 1998). This limitation was addressed with the use of the LASSO regularization since, as any other regularization technique, it reduces the effects of collinearity (Dormann et al., 2013). Therefore, the coefficients regressed using LASSO regularization are a more accurate quantification of the effect of the predictors. Moreover, LASSO regularization also reduces overfitting since it is able to eliminate "unimportant" predictors from the model. This effect was particularly noticeable when little data was available (figures 7.10 and 7.13 - iteration 1).

It is important to notice that the testing errors presented in this document (figures 7.10, 7.13, etc.), represent the ability of the response surfaces created in the iteration 'n' to capture the response of the datapoints generated in the iteration 'n+1'. As a consequence, the models and testing points are different in each iteration. This leads to oscillations in the testing errors. This effect is accentuated for the NN where the training process itself is non deterministic.

The LASSO model showed better performance compared to the other models in the first iteration. This model outperformed the NN at this point because the NN, unlike the polynomial regressions, do not have a pre-established underlying mathematical model response and, therefore, they need sufficient data to not only regress coefficients (or weights) but also choose the topology of the network. This lack of data in the initial stages prevented the NN from selecting an optimum topology in the CV phase. This could be due to multiple reasons from which one of them could be poor distribution of samples in the CV groups. Nevertheless, the NN outperformed the polynomial regressions in predicting head excursions as data became more available from the 2^{nd} iteration onward (figure 7.10). All three regression models showed similar testing error in predicting the probability of 3+ fractured ribs. Moreover, it is interesting to observe that these models, not only perform similarly in regards to their average error (figure 7.13 - last iteration) but also to their error distribution (figures K.10, K.11, K.12 - last iteration).

Although the average prediction error for 3+ fracture ribs meets the criteria to stop the training (i.e., stable at around 10%) and is sufficient to explore the methodology presented in this dissertation, the error is larger than that of the maximum lateral head excursion prediction. These differences may be related to the complexity of the phenomenon or the metric (e.g., non linearities). Rib fractures can occur as a consequence of interactions with multiple interior structures. Small changes in the occupant anthropometry, occupant position or impact conditions may have a large effect on the probability of rib fracture, if those changes lead, for example, to avoiding impact with the injury-causing structure. This causes a non-linearity that may be difficult to capture. The calculation of the injury metric itself also introduces mathematical complexity. The methodology for the estimation of fracture probability, described in 7.2.3, relies on the maximum rib strain for the calculation of the metric. As mentioned before, different parts of the ribs get in contact with different parts of the vehicle environment for the different anthropometries and impact conditions. In addition, different sections of the rib have different element quality which may increase noise in the results. The binomial distribution used in the calculation of the combined probability of fracture also introduces large non linearities in the calculation since the function is non-injective. That is, different inputs can generate the same output. In this case, different rib strain distributions can lead to the same probability of injury. This level of non-linearity in the phenomenon and the injury metric, and the disparity in the mesh quality may explain the relatively larger testing error (figures 7.13, K.10, K.11 and K.12).

Training any regression model requires the use of multiple approaches in order to identify the best performing model. Additional approaches were followed in this study in order to improve the performance of the NN model for the prediction of the probability of 3+ fractured ribs. Previous studies indicate that increasing the number of CV folds have an effect on the bias-variance tradeoff (Rodriguez et al., 2010). In this particular application, increasing the number of folds did not yield any noticeable improvement in performance. Changing the activation function and the backpropagation algorithm also showed very little effect on the model performance (figure 7.16).

Adding features to the models may improve performance if those features are responsible for part of the variability observed in the data. However, if the model uses too many features, the system may have difficulties to converge to the true underlying mathematical model response with a limited number of simulations. In such scenarios, reducing the number of inputs could contribute to a better performance. In this particular study, the upper body angle in the sagittal plane was explored as an additional feature, but this addition did not improve the model. On the other hand, reducing the number of features (table 7.3) reduced the error variance, but increased the median error (i.e., bias).

Imbalances in the training data may also lead to reduced performance. Although this phenomenon has been studied in more depth for classification problems (Alejo et al., 2007; Masko and Hensman, 2015), imbalanced training data also affects regression problems (Krawczyk, 2016). The training data should ideally cover all possible responses of the system without over- of under-representing cases, but, in the real world, not all outputs are equally likely. Therefore, training outputs often show a skewed distribution. In this particular application, a greater portion of the training data is associated to zero probability of 3+ fractured ribs (figure K.23 - left). Therefore, datapoints with low probability of injury are over-represented in the training sample. This may limit the ability of the model to predict injurious cases since these are under-represented in the sample. Oversampling techniques reduce skewness in the training data by generating interpolated datapoints (Chawla et al., 2002; Torgo et al., 2015). The resulting dataset is used to train the models (figure K.23 - right). In this particular application, this approach did not lead to substantial improvements in the model performance.

The prolonged error plateau (figure 7.13) and the fact that the logistic regression, the LASSO logistic regression and all the NN models show similar error bias and variance (figures K.10, K.11,K.12 and 7.16) are an indication that the remaining error may be irreducible (i.e., noise). Since this error is inherent to the training data (Rodriguez et al., 2010), it may vary in different applications of the methodology presented in this dissertation.

After evaluating the response surfaces created by the different regression techniques, the NN have shown improved performance in predicting head excursion and similar performance in predicting 3+ fractured ribs compared to the rest of the models. Therefore, these NN will be used in the chapter 8 in order to illustrate their use for vehicle assessment. Although the NN are the regression techniques selected for this particular application, the methodology introduced in this dissertation does not limit its applicability to the use of NN. Therefore, it enables the use of any regression technique with sufficient out-of-sample predictive performance.

Chapter 8

Variability-based Vehicle Assessment

Chapter 7 has developed a series of response surfaces representing the entire population of impacts defined within the limits described in table 7.1. This chapter uses these surfaces in the quantification of vehicle safety using the response of the entire population of interest.

8.1 Introduction

Traditional ATD-based vehicle assessment and regulations use the response of ATD in standardized physical tests in order to study the probability of injury of certain populations in specific impact conditions. Given the expensive nature of these tests, the number of events and surrogates represented in them are very limited. Therefore, these tests need to be defined based on an estimated benefit analysis or targeted to represent an average event based on impact or injury severity (Hollowell et al., 1998; Ellway et al., 2013).

Although this ATD-based approach has largely contributed to the reduction of traffic-related fatalities, targeting specific load cases with no exploration of variability in the occupant or impact conditions may lead to potentially hyper-optimized restraint systems. That is, restraints optimized to protect a narrow percentage of the population in a limited number of event but that may not be effective for a large percentage of the population and impact conditions. Although manufacturers normally have their own internal safety standards, standardize tests are their main design targets. Current lack of variability exploration allows manufacturers to develop vehicles that past the tests but overlook potential injurious impact conditions. This lack of variability exploration also generates vehicle assessments that are able to rank vehicles according to their ability to protect specific populations in specific impact conditions but cannot estimate the effect that deploying the vehicle will have of the total burden of traffic-related injuries and fatalities.

The only available far-side ATD test consists in conducting a sled test with the 50^{th} percentile WorldSID on a 75-degree PDOF using the pulse generated in the Euro NCAP pole or barrier near-side impact test (NCAP, 2017c). The test evaluates maximum lateral head excursion and the injury risk for a number of body regions based on the near-side WorldSID injury risk curves. Although the study summarized in chapter 5 shows that the WorldSID exhibit PMHS-like lateral head excursion, the validity of the ATD to predict far-side injury and the use near-side WorldSID injury risk curves are, at the very least, questionable.

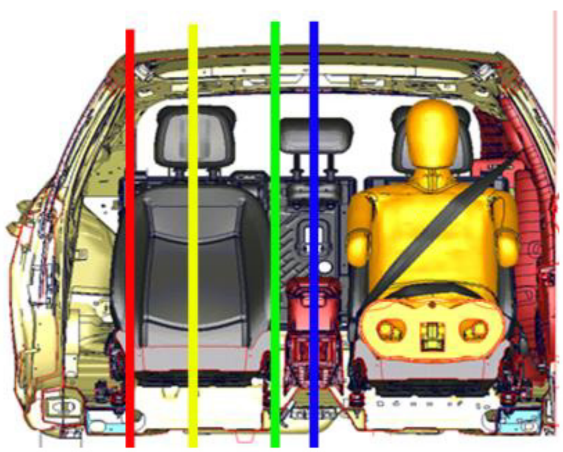

Figure 8.1: Head excursion limits in the Euro NCAP far-side assessment (NCAP, 2017c)

In the Euro NCAP far-side test, three different lateral head excursion distance are defined: the maximum intrusion line (red), the seat center-line and a line 250 mm inboards from the seat center-line called the occupant interaction limit (figure 8.1). The vehicle loses points in the assessment as the head of the occupant reaches the different levels. This methodology reduces all the possible far-side impact scenarios to a single test.

A new approach to safety that takes into account variability in the population and impact conditions is needed. This chapter presents an innovative approach to safety that uses the response of the entire studied population in a comprehensive set of impact conditions. The results from applying this methodology can be directly interpreted as the number of events (e.g. injuries) expected to occur in the field involving this vehicle. Specifically, this chapter will present the expected number of head-to-intruding-door impacts and the expected number of 3+ fractured ribs as a consequence of deploying the vehicle in the field.

8.2 Methods

A Monte-Carlo (MC) analysis was conducted to estimate the expected number of head-to-intruding-door impacts and the expected number of cases with 3+ fractured ribs. One million responses were generated for maximum lateral head excursion and probability of 3+ fractured ribs using the NN developed in chapter 7. The anthropometry inputs for the NN were defined to represent 90% of the ANSUR II male database. Inputs for height, weight and waist circumference followed the joint probability distribution described in chapter 3. The CWT was regressed from Frank et al. (2011). The rest of the anthropometry parameters (table 7.2) were obtained as a linear regressions of the first three. The PDOF and Δv were defined within the limits described in table 7.2 following the cumulative density functions for the number of occupants involved in far-side impacts described in chapter 2 (figure 2.4). Three different seatbelt load limiters were used in each of the MC analysis: 1 kN, 2.5 kN and 5kN. The model parameter uncertainty (i.e., the seatbelt friction and the center console ultimate strain) was explored using a uniform distribution.

A linear regression was conducted using information from Sunnevång et al. (2010)

to estimate the door intrusion as a function of Δv. This regression was used to estimate the door intrusion for each MC sample. The head-to-intruding-door distance was calculated for each sample as $D_0 - \Delta y_{head} - Intrusion$, where D_0 was the initial distance head-to-door distance and Δy_{head} was the maximum lateral head excursion of the sample. Those cases with negative head-to-intruding-door distance were defined as having sustained a head-to-intruding-door impact.

Once the responses where generated, the total number of expected head-to-intruding-door impacts and cases with 3+ fractured ribs were calculated using the total number of occupants involved in the accidents covered in the NN training (chapter 2). The resulting expected values are an estimation of the total number of head-to-intruding-door impacts and cases with 3+ fractured ribs that would occur in the field if all the vehicles performed like the one being assessed. This will be referred to as field-equivalent metric. The field-equivalent metrics for this vehicle were compared to the current field data.

8.3 Results

The cumulative density distribution for head-to-intruding-door distance (figure 8.2) indicated that, for the assessed vehicle, a number between 1.8 % and 6.6% of the occupants involved in a far-side accident within the impact factors defined in table 7.1 would contact the intruding door with their heads depending on the load limiter used. The expected number of cases with 3+ fractured ribs (figure 8.3) varied from 7.8 % to 10.2% depending on the load limiter used.

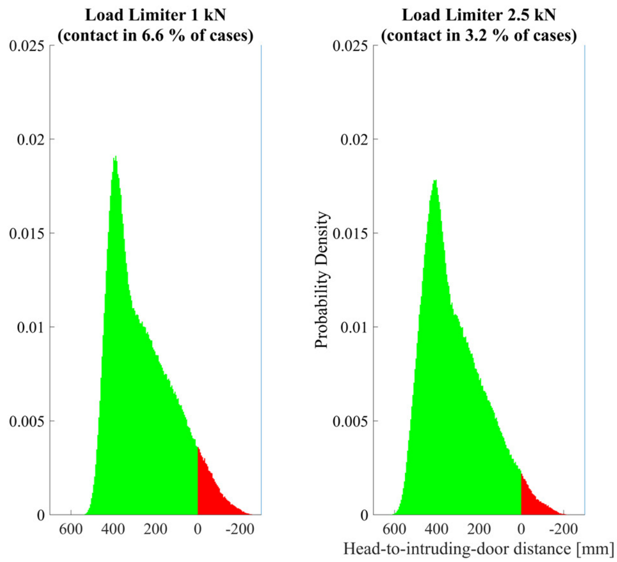

Figure 8.2: Head-to-intruding-door distance probability density for different seatbelt load limiters (green: no-contact cases, red: contact cases)

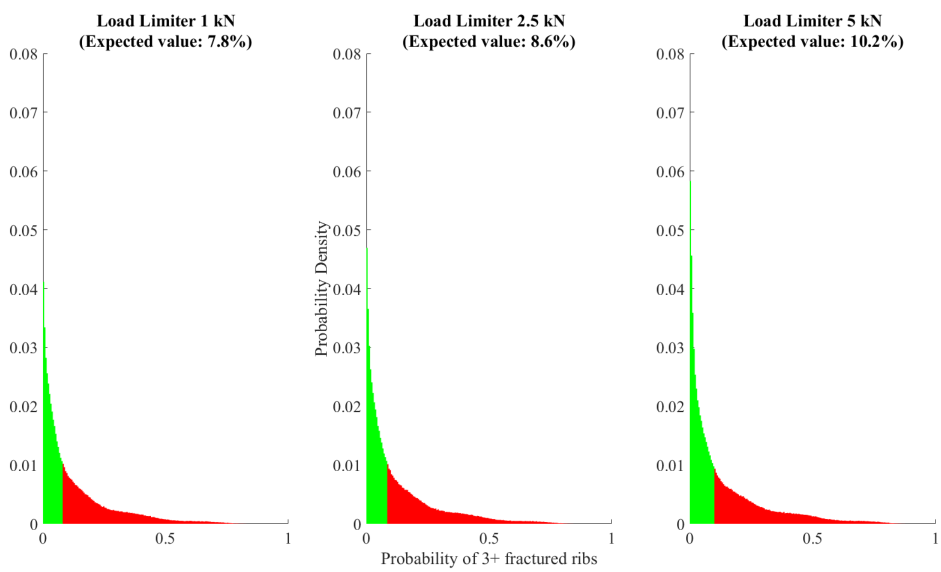

Figure 8.3: Probability density for the probability of 3+ fractured ribs for different seatbelt load limiters (green: cases below average, red: cases above average)

The histograms in figures 8.2 and 8.3 represent the occupant response in impacts between 22 and 45 km/h and between 60 and 90 degrees PDOF. Based on the data provided in chapter 2, 37,085 far-side impacts occur within these definition in the US. Figure 8.4 shows the total number of head-to-intruding-door impacts and cases with 3+ fractured ribs that would be observed in the field if all vehicles performed like the evaluated vehicle (e.i., field-equivalent metrics). The number of field-equivalent head impacts decreased from 2,448 to 667 cases with the use of larger seatbelt load limiter values. The opposite was true for 3+ fractured ribs where the number increased from 2,893 to 3,783. Adding the number of head impacts cases and with those of 3+ fracture ribs (figure 8.4 - black line) generated an inflection point at 2.5 kN.

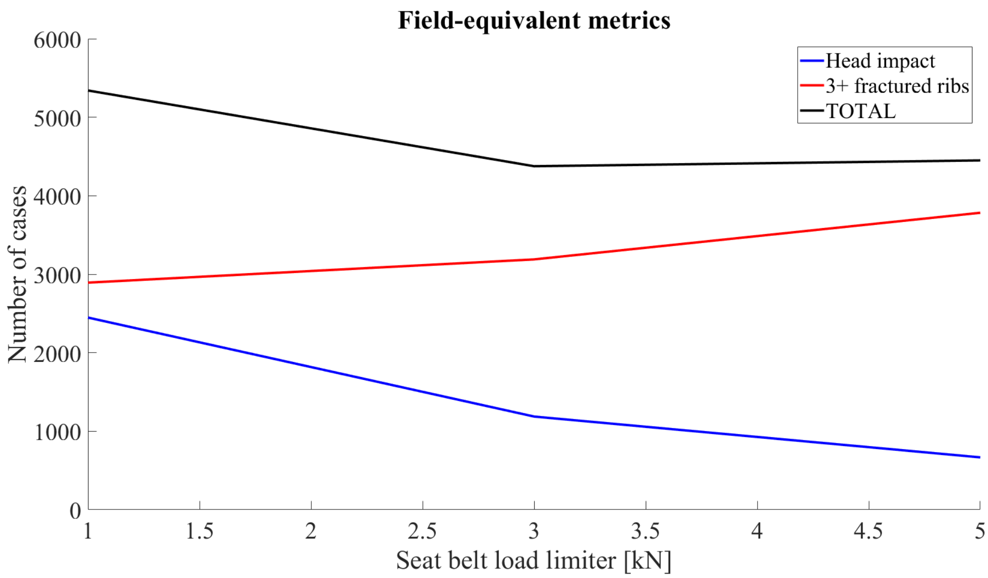

Figure 8.4: Number of head impacts, 3+ fractured rib cases and sum of both metrics

8.4 Discussion

This study introduces a new approach to vehicle assessment that transitions from ATD-based assessments, where a very limited number of tests are conducted to evaluate a vehicle, to a scenario in which the vehicle is evaluated in its ability to reduce the actual number of injuries and fatalities in the field. Therefore, this methodology, rather than only ranking the vehicle with respect to others, enables the quantification of the impact that the vehicle would have in the field. This approach is superior to ATD-based assessments even in situations in which improving the vehicle for the 50^{th} percentile would generalize for other populations since ATD-based assessments are not able to quantify the actual improvement. Moreover, the proposed method can be used not only for assessing the vehicle but also for optimizing its restraint systems. Assessments and optimizations conducted using this methodology have an impact in all levels of society and not only on the discrete number of populations and impact cases represented in ATD-based assessments.

The present methodology can be scaled to incorporate additional input factors or adapted to represent other impact scenarios (e.g., frontal impacts). Moreover, although this dissertation evaluated the probability of head impact and 3+ fractured ribs as a vehicle to explore the methodology, other injury types (e.g., TBI) and severities (e.g., cases of AIS 6) or other outcomes (e.g., level of disability) can be alternatively or concurrently utilized to evaluate vehicle performance depending on the impact scenario or the design goals (e.g., fatality reduction, disability reduction, etc.).

The assessment of the vehicle environment used in this dissertation estimates a number between 2,893 and 3,783 field-equivalent cases with 3+ fractured ribs. This number can be directly compared to the field data using the information provided in chapter 2. Each year around 10,555 far-side-related thoracic AIS3 + occur in the US. Since our Δv and PDOF ranges encompass approximately 50% and 75% of the AIS 3+ cases (Gabler et al., 2005; Bahouth et al., 2015), respectively, this results in 3,958 field cases within the impact parameters defined in table 7.1. Although 3+ fractured ribs are not the only injury that leads to thoracic AIS 3+, it is reasonable to conclude that the deployment of the vehicle used in this dissertation would contribute to a reduction in the injuries observed in the field.

The MC analysis and, therefore, the field-equivalent metrics were calculated assuming that the current Δv and PDOF distributions apply for the evaluated vehicle. However, this assumption is not inherit to the methodology. If the vehicle included any type of active system that allows it to reduce the impact speed (e.g. Automatic Emergency Breaking) or modify the impact direction (e.g., active steering) this information could be introduced in the MC analysis by modifying the sampling distribution for Δv and PDOF according to the capabilities of the system.

The ability of the proposed methodology to create field-equivalent metrics enables vehicle manufacturer, non-governmental entities and policy makers to prioritize actions taking into account the actual effect of the vehicle in the field rather than its effect on a very narrow percentage of the population.

Chapter 9

Conclusions

9.1 Concluding remarks

The goal of this dissertation was to develop a methodology for the evaluation of human response in vehicle impacts that accounts for variability of intrinsic and extrinsic factors including model uncertainties (figure 9.1).

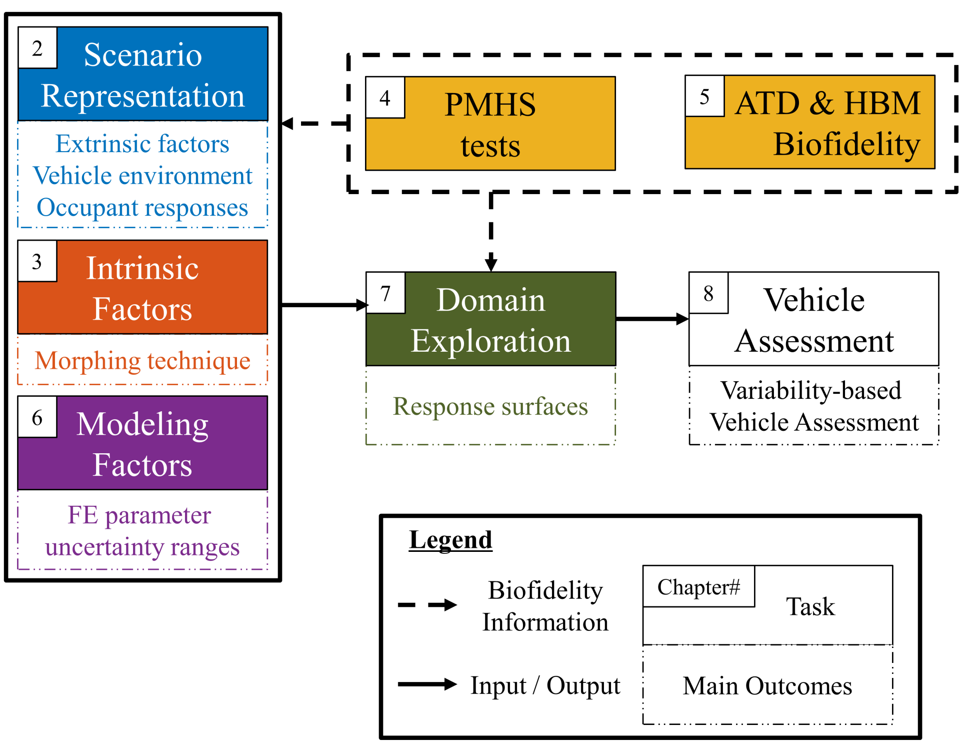

Figure 9.1: Dissertation Flowchart

In order to fulfill this goal, chapter 2 used the literature to identify the most commonly injured body regions and the impact parameters that have an effect on human kinematics and injury outcome. With this information, this chapter identified the injury metrics to evaluate in the HBM, the extrinsic factors to explore and the vehicle environment to represent the scenarios in chapter 7.

Chapter 3 identified height, weight and waist circumference as the intrinsic factors to be represented in the HBM. The chapter presented a methodology for the implementation of anthropometry variability controlling for these three intrinsic parameters. The presented methodology, unlike previously-publish methodologies, was able to generate morphed models that successfully match the target weight. This was achieved using a non-linear optimization in combination with a NN. The resulting methodology was able to represent 90% of the ANSUR-II database using a fully automated in-house Matlab/Piper script. The resulting morphed models accurately represented external anthropometry as well as pelvis and rib cage sizes. This methodology was employed in chapter 7 to explore the effect of the intrinsic factors in human response.

Chapter 6 identified the seatbelt friction coefficient and the center console ultimate strain as model uncertainty factors. Initial ranges for these parameters were defined and FE simulations were conducted and compared to WorldSID physical tests in order to identify parameter values that did not meet the validation criterion. The final ranges for the seatbelt friction coefficient and the center console ultimate strain were used in chapter 7 to explore the contribution of the model uncertainty factors in human response.

The studies in chapters 4 and 5 were conducted to complement the limited existing far-side-related literature. Chapter 4 presented a detailed insight into far-side in-vehicle human kinematics, kinetic and injury responses. The information generated in this chapter did not only contribute to improve the current state-of-the-art of the literature but was also used in chapter 5 in order to evaluate the biofidelity of the WorldSID and the simplified GHBMC. Chapter 5 conducted these biofidelity evaluations in a simplified and a vehicle-based sled. The WorldSID and the simplified

GHBMC correctly represented lateral excursion, although the HBM showed improved shoulder belt interaction. The HBM, unlike the ATD, was also able to represent the probability of rib fracture observed in the PMHS tests. The study concluded that the GHBMC shows improved biofidelity with respect to the WorldSID, although both surrogates showed sufficient biofidelity in order to explore the methodology presented in this dissertation.

The intrinsic, extrinsic and modeling uncertainty factors identified in chapters 2, 3 and 6, respectively, were explored for the creation of occupant response surfaces for maximum lateral head excursion and the probability of 3+ fractured ribs in chapter 7. Five different regression techniques were used for the creation of the response surfaces: linear regressions, logistic regressions, LASSO linear and logistic regressions, and NN. The models were trained (or regressed) using an iterative scheme in combination with a fully-automated process coded in an in-house Matlab script. The performance of the regression models was evaluated using out-of-sample datapoints. The NN outperformed the other regression techniques in its ability to predict lateral head excursion ($\overline{|\epsilon|} < 3\%$). The three regression models showed similar performance in the prediction of 3+ fractured ribs ($\overline{|\epsilon|} < 10\%$). Alternative approaches were used for the NN training but the performance could not be improved. This lack of improvement in combination with the fact that all regression models showed similar error indicates that the remaining error may be irreducible (i.e., noise). The response surfaces created in this chapter are a continuous representation of occupant response as a function of the intrinsic, extrinsic and modeling uncertainty factors.

In chapter 8, a Monto-Carlo analysis was conducted using the response surfaces created in chapter 7 and the field-related distributions for the different factors explored in the dissertation in order to assess the vehicle far-side safety performance. This evaluation, unlike ATD-based assessments, did not focus on the probability of injury for a particular population in a single impact scenario but rather on estimating the number of injurious cases for the entire population represented by the intrinsic factors (i.e., 90% of that ANSUR-II population) in the impact scenarios represented by the extrinsic factors (i.e., PDOF = [60-90] degrees, Δv = [22-45] km/h and seatbelt load limiter = [1-5] kN). The assessment proposed in this chapter led to injury figures comparable to those present in injury databases (e.g., NASS-CDS) by estimating the number of cases (e.g.,injuries) that would be observed in the field if all the vehicles performed like the assessed vehicle. These estimations are referred to as field-equivalent cases. These field-equivalent cases can be directly compared to the current number of injuries present in the databases to determine if deploying the assessed vehicle would improve or worsen the current level of safety in the field. This allows designers to use the expected number field injuries or fatalities as an objective function rather than the probability of injury for a particular population. In the particular case of the vehicle used for this dissertation, 3.2% of all crashes are expected to result in head-to-intruding-door impacts and 8.6% are expected to result in 3+ fractured ribs using a 2.5 kN load limiter. Using the total number of far-side crashes observed in the field and the results from this assessment, it can be estimated that this vehicle would lead to 1,187 head-to-intruding-door field-equivalent impact cases and 3,189 field-equivalent cases of 3+ fractured ribs. If we compared the latter figure with the current number of thoracic AIS 3+ cases (i.e., 3,958), it can be concluded that the deployment of the vehicle used in this dissertation would contribute to a reduction in the injuries observed in the field.

9.2 Future research and limitations

The performance of the methodology and its implementation in regulatory and NCAP programs would benefit from a series of research lines in the areas of FEM uncertainty quantification, HBM biofidelity, morphing techniques, stochastic methodologies and machine learning.

9.2.1 FEM uncertainty quantification

This methodology has demonstrated the implementation of model uncertainty using a vehicle-based sled. The simplicity of the model helps to keep the number of uncertain parameters low. Implementations of this methodology in more complex impact scenarios (e.g., full vehicle impacts) will require of ad-hoc identification of the uncertainty factors and their interactions. Research should be targeted to identify the FE parameters with the largest effect on the HBM response for specific impact scenarios (e.g., seatbelt friction) and develop physical tests to quantify their uncertainty in the FEM of the vehicle to be assessed or developed.

9.2.2 HBM biofidelity and injury prediction

Another field of potential improvement is the biofidelity and injury prediction of HBM. While future research should focus on improving HBM biofidelity in general, a particular emphasis should be the placed in improving the HBM's ability to predict injury. The present dissertation used a methodology by Forman et al. (2012) to estimate rib fracture probability in HBM. Although the methodology seems to provide a sufficient level of prediction in far-side scenarios, a more formal and comprehensive validation may be needed for the implementation of HBM in regulation and NCAP programs. Moreover, future research should also focus on implementing similar probabilistic approaches for other body regions.

HBM improvement should not lead to an unnecessary increase in model complexity since overly complex models could cause an important increase in computational time, reducing our ability to conduct the number of simulations needed to generate the response surfaces. Therefore, HBM selection and development should be conducted in a case-specific manner, taking into consideration the trade-offs between model performance and time efficiency.

9.2.3 Morphing techniques

The proposed methodology was demonstrated using the ANSUR-II database. This database only includes military personnel and, therefore, cannot represent the integrity of civilian population. More comprehensive databases (e.g., CAESAR database) could be used in conjunction with the morphing methodology presented in this dissertation. It is possible that the representation of a large percentage of the population in these databases require the development of additional base models. That is, instead of using the 50^{th} percentile as a base model, other percentiles may need to be introduced as base models in order to ensure mesh quality and correct model connectivity. Similarly, the morphing methodology can be followed using a female anthropometry database if the original HBM is based on the female population. Future methodologies for the exploration of population variability should incorporate additional intrinsic factors (e.g., bony structure variability) and their interactions.

9.2.4 Stochastic methodologies

Another important aspect of this new paradigm is the use of stochastic (probabilistic) safety evaluations instead of the current deterministic approaches. Further research needs to be conducted to promote a gradual implementation of stochastic approaches in the field of vehicle safety and disseminate their advantages over deterministic approaches.

9.2.5 Machine Learning

Results from the NN regressions indicate that different metrics incorporate different levels of noise. The identification and development of low-noise metrics and methodologies will be beneficial to future implementations of machine learning techniques. Future research should also be directed to investigate the possibility of reducing the number of training datapoints (i.e., simulations) by incorporating previous knowledge in the development of the response surfaces.

In general, machine learning techniques enable us to process and incorporate complex information into our evaluations. The field of injury biomechanics should try to benefit from any improvement in the field of data science. The exploration of new machine learning implementations and their adaptation to the field of injury biomechanics will help maximize our impact in the field.

9.2.6 Other considerations

This particular application of the methodology utilized previously-publish field data in order to identify the extrinsic factors to be explored. Based on these studies, Δv and PDOF were considered independently. Moreover, intrusion was only considered a function of Δv. Future applications of this methodology could benefit of ad-hoc field studies to evaluate the correlations among the different factors used in the methodology and full-vehicle simulations to establish the relationship between intrusion and the different extrinsic factors. This would improve the Monte-Carlo analysis and generate outcome distributions that better represent the field.

9.3 Contributions

The main contribution of this dissertation is the creation of a methodology for the evaluation of human response in vehicle impacts that accounts for variability in the population and impact conditions. This methodology can be used, among other things, to identify populations at risk or injurious impact scenarios, inform intervention prioritization or conduct comprehensive, variability-based vehicle assessments.

This dissertation guides the transition from deterministic ATD-based safety assessments to stochastic HBM-based safety assessments. The field would benefit of a progressive adoption of the proposed framework by implementing it initially in simplified impact scenarios (e.g., sled-based assessments) and progressively adapt it to more complex load cases (e.g., full vehicle assessments).

The variability-based vehicle assessment explored in this dissertation overcomes the limitations of current ATD-based assessments that tend to hyper-optimize restraints by focusing on a very limited set of populations and impact directions. One of the main benefits of this methodology is its ability to generate information that relates directly to field injury data. This allows manufacturers to design their vehicles with the target of reducing the actual field-related injuries and fatalities rather than the probability of injury for a particular population.

The introduction of uncertainty in the intrinsic and extrinsic factors allows not only for the evaluation of human response but also its distribution (probability of occurrence). Trends in these distributions can be used to identify populations at risk or previously overseen hazardous loading conditions, helping prioritize action. This is a great advantage over ATD-based assessments which cannot provide any information about the underlying distribution of responses. Moreover, the proposed methodology improves the confidence in the vehicle FEM by introducing uncertainty in the modeling parameters, since improving trust in the model and reducing the risk of modeling tampering is key for the adaptation of the methodology in regulation and NCAP.

This dissertation also provides the first detailed comparison of the prediction abilities of traditional regression techniques (e.g., linear regression) and those of NN in the field of injury biomechanics. This comparison showed equivalent or improved prediction with the use of NN. This dissertation presented an iterative method to track error evolution and identify the optimal regression performance. That is, those regression models that have achieved irreducible error (i.e., noise).

This dissertation presents not only a morphing technique that explores population variability beyond height and weight, but it also demonstrates its utility to explore its effects on human response. Moreover, this morphing methodology is the first able to ensure that the final morphed model meets the initial target weight, which is crucial for the correct exploration of human variability.

This dissertation provides an in-depth characterization of human response in far-side scenarios, including the first in-vehicle PMHS tests in the literature. The study of the PMHS chest deflection led to the identification of the main far-side thoracic injury mechanism. This mechanism was found to involve a seatbelt-related chest compression followed by a seat-related chest deformation and a subsequent chest expansion. The seatbelt was identified as the major contributor to injury. Injury causation occurred as soon as 50 ms into the event. Conclusions derived from these PMHS tests will have a deep impact in the improvement of human surrogates and restraint systems for far-side scenarios. This dissertation also identified restraint-related trade-offs between head and thoracic injury and predicted the effect of a specific vehicle on the injuries observed in the field.

Overall, the proposed framework will provide a fundamental contribution to the improvement of vehicle safety by incorporating diversity in the population and the impact conditions in the vehicle design process.

THIS PAGE INTENTIONALLY LEFT BLANK

Appendix A

NN to Estimate Morphed Model Final Weight

This NN is used in chapter 3 as part of the optimization carried out to select morphing anthropometry measurements to generate models that meet the target weight. So the goal of the NN is to be able to estimate the final weight of a morphed HBM based on the input morphing anthropometry measurements.

In order to train the NN, 300 morphed models were generated following the methodology explain in chapter 3 with the difference that the non-controlled parameters were selected only to maintain body coherence since they could not be optimized to meet a certain target weight. The points were selected to maximize the space between them, following the methodology presented in appendix J.

The dataset was divided in a training and a testing set following a 80/20 distribution. The final topology of the NN was obtained using 5-fold CV. Figure A.1 shows the performance of the NN to estimate the out-of-sample final HBM weight.

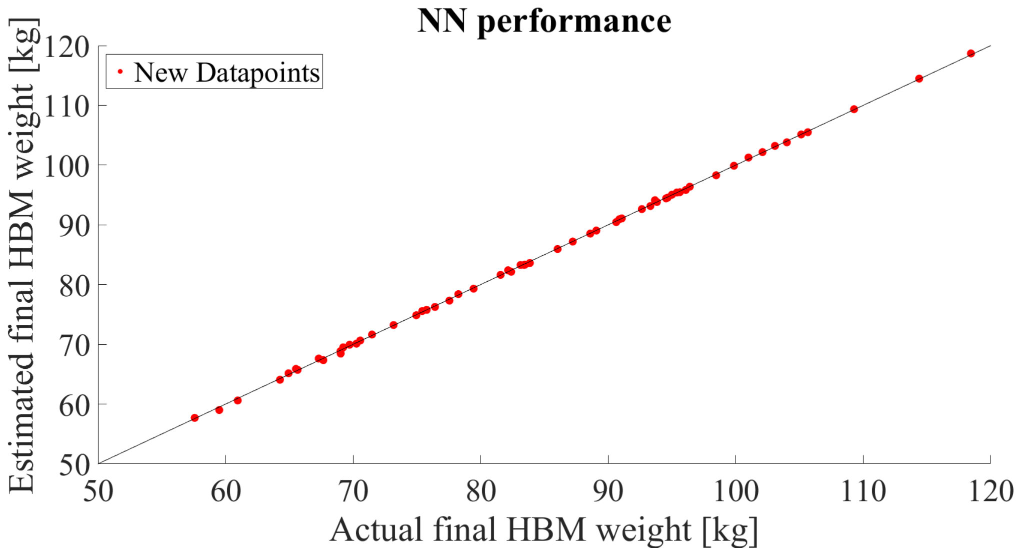

Figure A.1: NN performance in out-of-sample final HBM weight prediction

Appendix B

Distributions Resulting from the Morphing Methodology

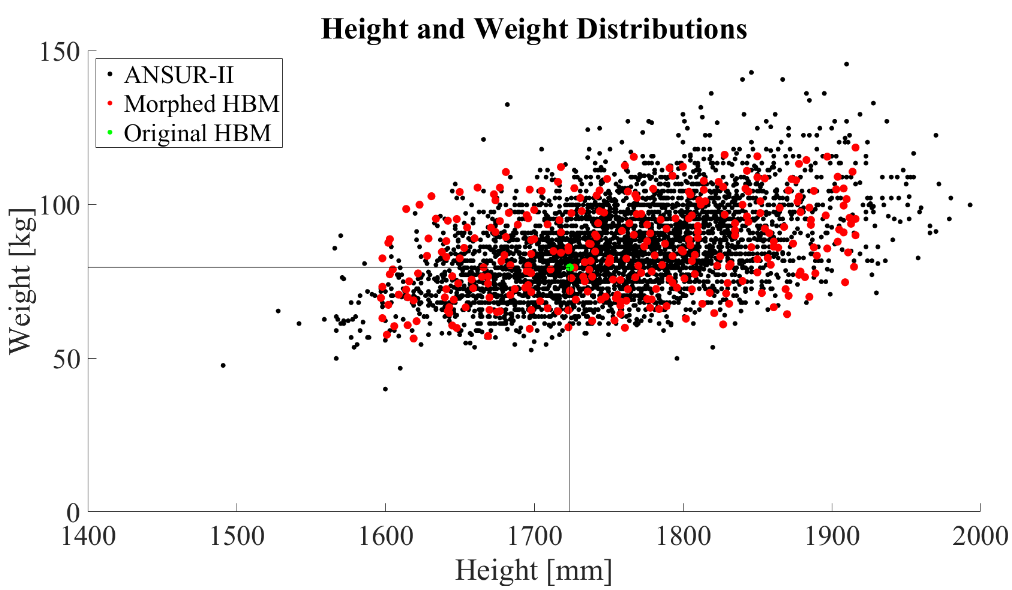

Figure B.1: Height and weight distribution for the ANSUR-II population and morphed and original HBM

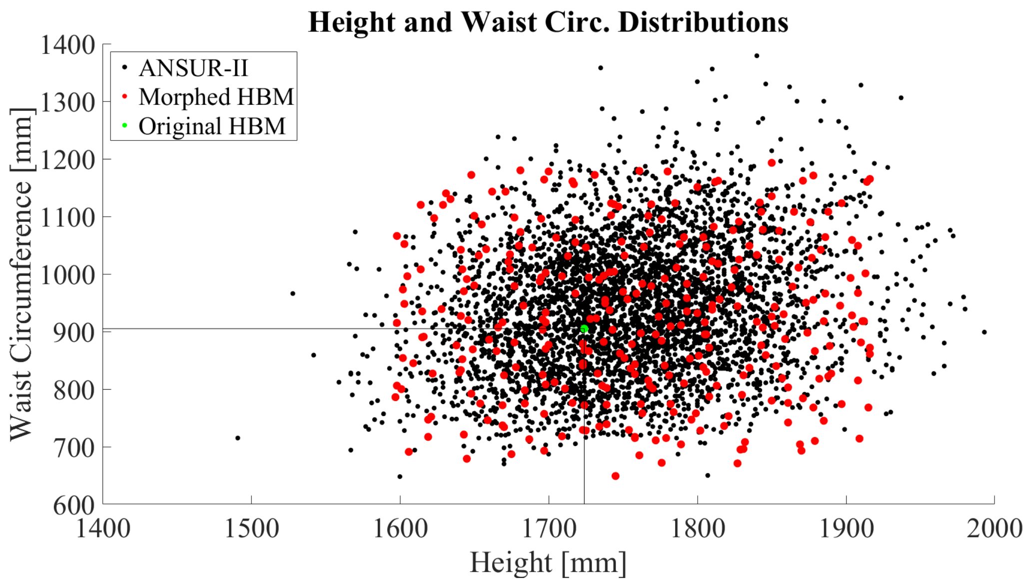

Figure B.2: Height and waist circumference distribution for the ANSUR-II population and morphed and original HBM

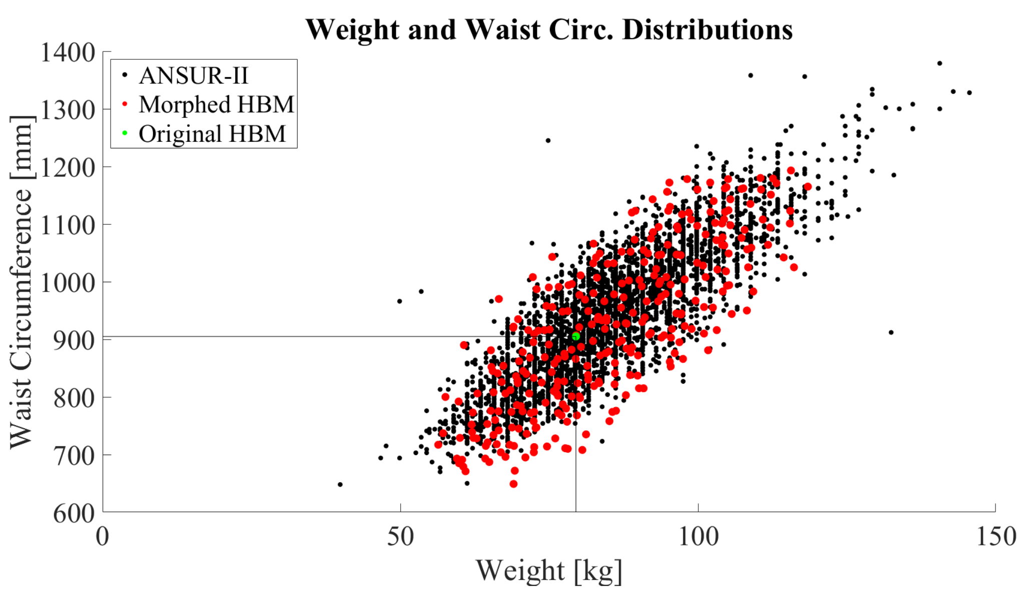

Figure B.3: Weight and waist circumference distribution for the ANSUR-II population and morphed and original HBM

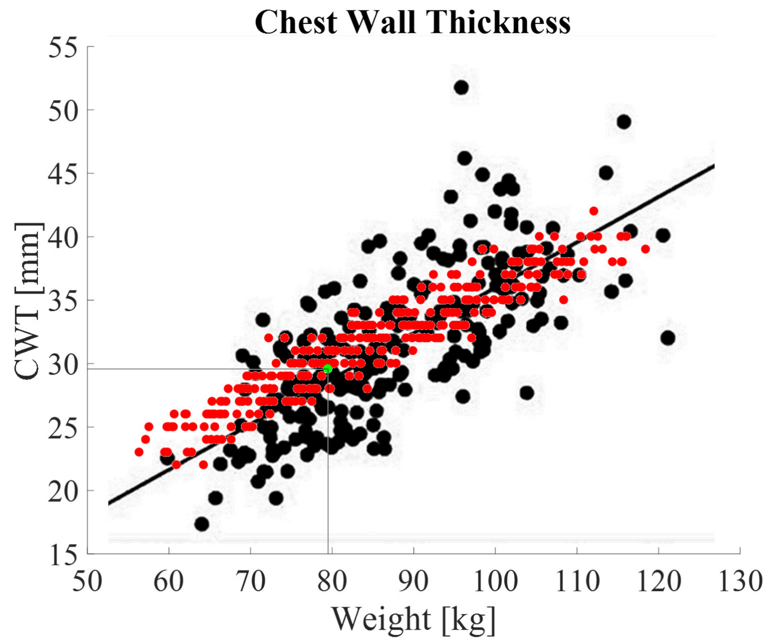

Figure B.4: CWT distribution for the morphed (red) and original HBM (green) and volunteer measurements (black) by Frank et al. (2011)

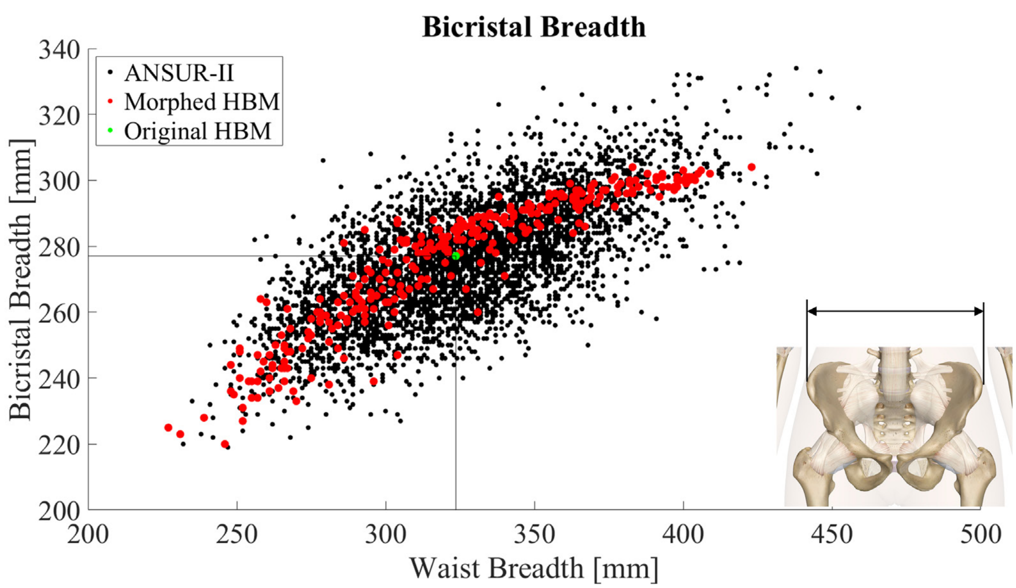

Figure B.5: Bicristal breadth and waist breadth distribution for the ANSUR-II population and morphed and original HBM

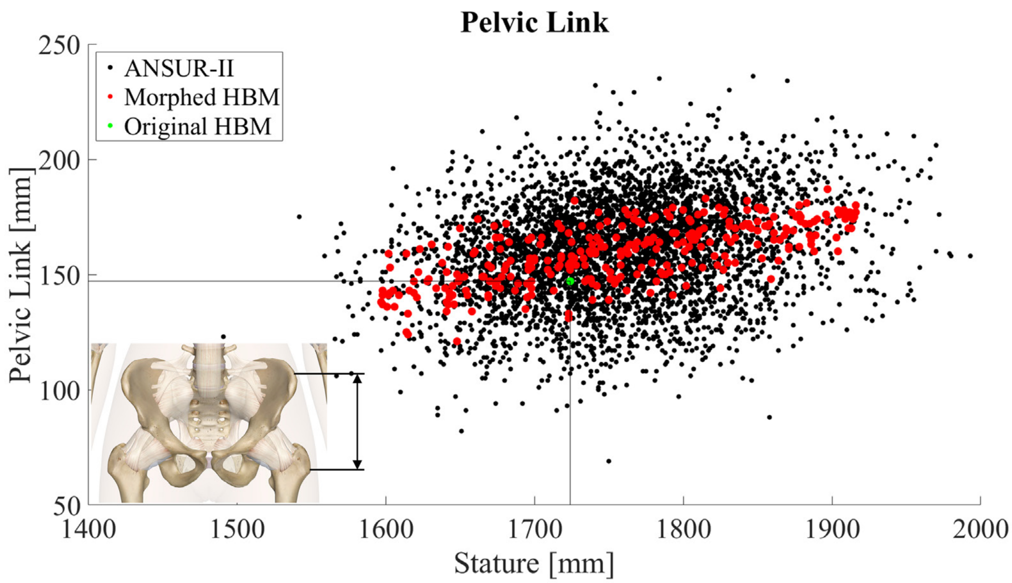

Figure B.6: Pelvic link and stature distribution for the ANSUR-II population and morphed and original HBM

Appendix C

Surrogate Information

Table C.1: Surrogate general information

Cadaver ID No.	758	847	764	897	765
Age at Time of Death	69	44	65	70	67
Sex	Male	Male	Male	Male	Male
Cause of Death	Alcoholic Liver Failure	Colon Cancer	Stage IV Melanoma	Liver Cancer	Carcinogenic Shock
Preservation Method	Freezing	Freezing	Freezing	Freezing	Freezing
Bone Mineral Density T-Score at Lumbar Spine (modality)	-1.9 (DXA)	0.4 (DXA)	-3.25 (QCT)*	-1.6 (DXA)	-2.2 (DXA)

* T-Scores calculated with QCT and DXA cannot be directly compared to each other. Bone quality is specified in Table 4.1

Table C.2: Surrogate anthropometry information (in mm unless noted)

Cadaver ID No.	758	847	764	897	765
Body Mass (kg)	71.7	58	80.7	61	87.1
Stature	1676	1753	1829	1690	1778
Vertex-to-Symphision Length	920	1000	980	950	1010
Top-of-Head to Trochanterion	810	930	935	855	950
Shoulder (Acromial) Height	1455	1524	1564	1465	1505
Waist Height (at Umbilicus)	960	955	1045	1030	1025
Waist Depth (at umbilicus)	216	171	168	160	204
Waist Breadth	312	284	341	344	382
Shoulder Breadth (Biacromial)	308	307	341	318	318
Chest Breadth - 4th Rib	329	292	331	304	371
Chest Breadth - 8th Rib	334	288	332	315	370
Chest Depth - 4th Rib	228	197	224	227	228
Chest Depth - 8th Rib	237	203	225	247	232
Hip Breadth	308	269	301	291	365
Buttock Depth	174	164	172	160	197
Shoulder-to-Elbow	365	375	375	345	395
Forearm-to-Hand	280	170*	455	455	485
Tibiale Height	480	475	520	455	470
Ankle Height (Outside)	80	68	80	70	70
Foot Breadth	87	85	93	89	87
Foot Length	235	245	260	245	250
Head Length	181	202	204	171	202
Head Breadth	158	155	145	142	151
Head Height	235	223	238	195	175
Head Circumference	588	587	583	554	545
Neck Circumference	395	366	354	378	410
Chest Circumference - 4th Rib	988	841	971	954	1091
Chest Circumference - 8th Rib	1002	843	1000	1010	1065
Waist Circumference - At Umbilicus	1000	753	928	879	1059
Waist Circumference - 8cm above Umbilicus	1057	791	948	979	1071
Waist Circumference - 8 cm below Umbilicus	962	816	1006	909	1021

Table C.3: Surrogate anthropometry information (in mm unless noted) (cont.)

Buttock Circumference	885	870	1040	914	1034
Thigh Circumference	412	400	514**	470	545
Lower Thigh Circumference	335	317	442**	390	429
Knee Circumference	359	340	453**	380	389
Calf Circumference	274	265	340**	325	338
Ankle Circumference	231	240	291**	255	255
Scye (Armpit) Circumference	380	390	420	390	465
Bicep Circumference	230	240	280	260	308
Elbow Circumference	238	240	300	250	264
Forearm Circumference	207	190	270	223	224
Wrist Circumference	164*	—*	180	170	153
Seated Chest Breadth - 4th Rib	295	284	319	290	350
Seated Chest Breadth - 8th Rib	332	319	336	326	363
Seated Chest Breadth - at Chestband	327	302	345	308	356
Seated Chest Depth - 4th Rib	235	190	253	255	245
Seated Chest Depth - 8th Rib	271	236	259	280	287
Seated Chest Circumference - 4th Rib	970	820	980	900	1035
Seated Chest Circumference - 8th Rib	1010	902	1010	970	1118
Seated Abdominal Breadth (Umbilicus)	344	277	331	295	371
Seated Interacromial Distance	389	381	394	360	364
Seated Top of Head to T1	265	240	285	257	235

* Amputated

** Asymmetric

THIS PAGE INTENTIONALLY LEFT BLANK

Appendix D

PMHS Spine Acceleration

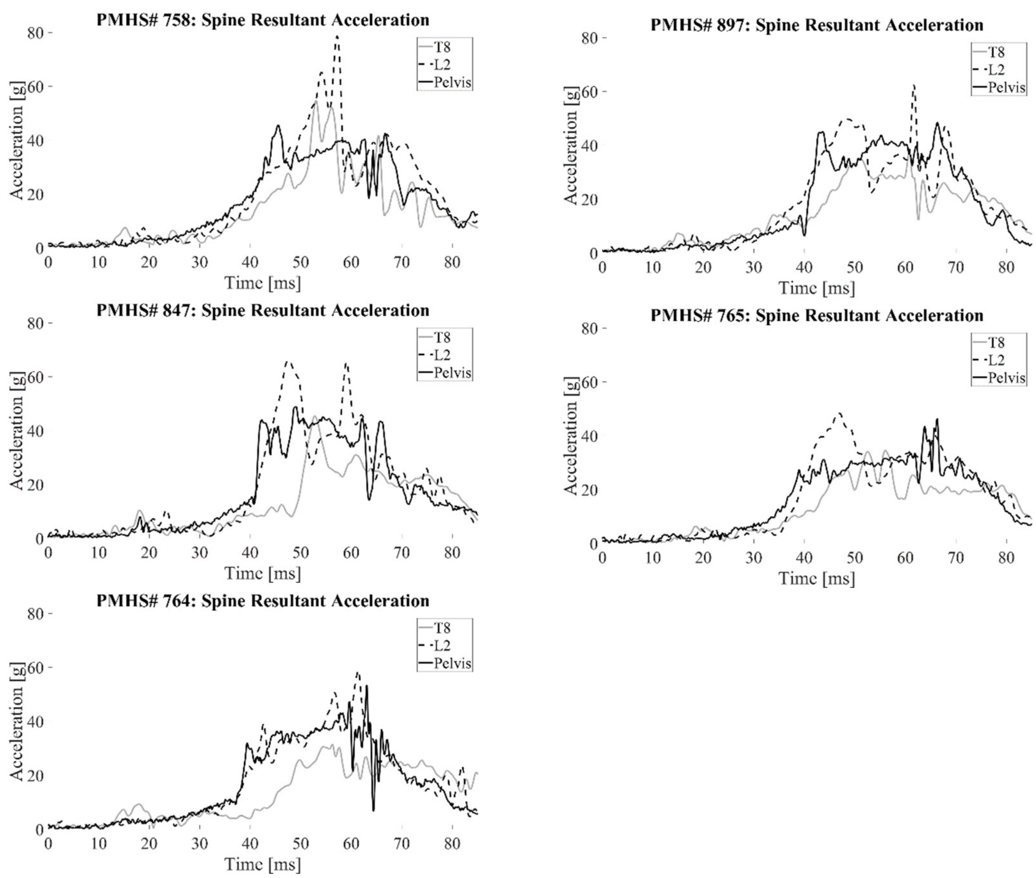

Figure D.1: PMHS spine accelerations with large (left) and small (right) bolster structure)

THIS PAGE INTENTIONALLY LEFT BLANK

Appendix E

PMHS Chestband Contours

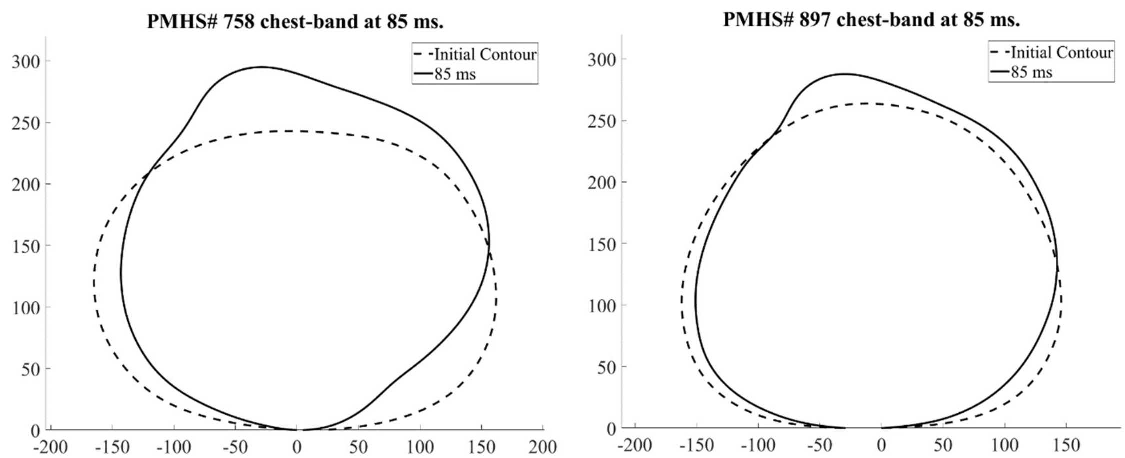

Figure E.1: PMHS chestband contours with large (left) and small (right) bolster structure)

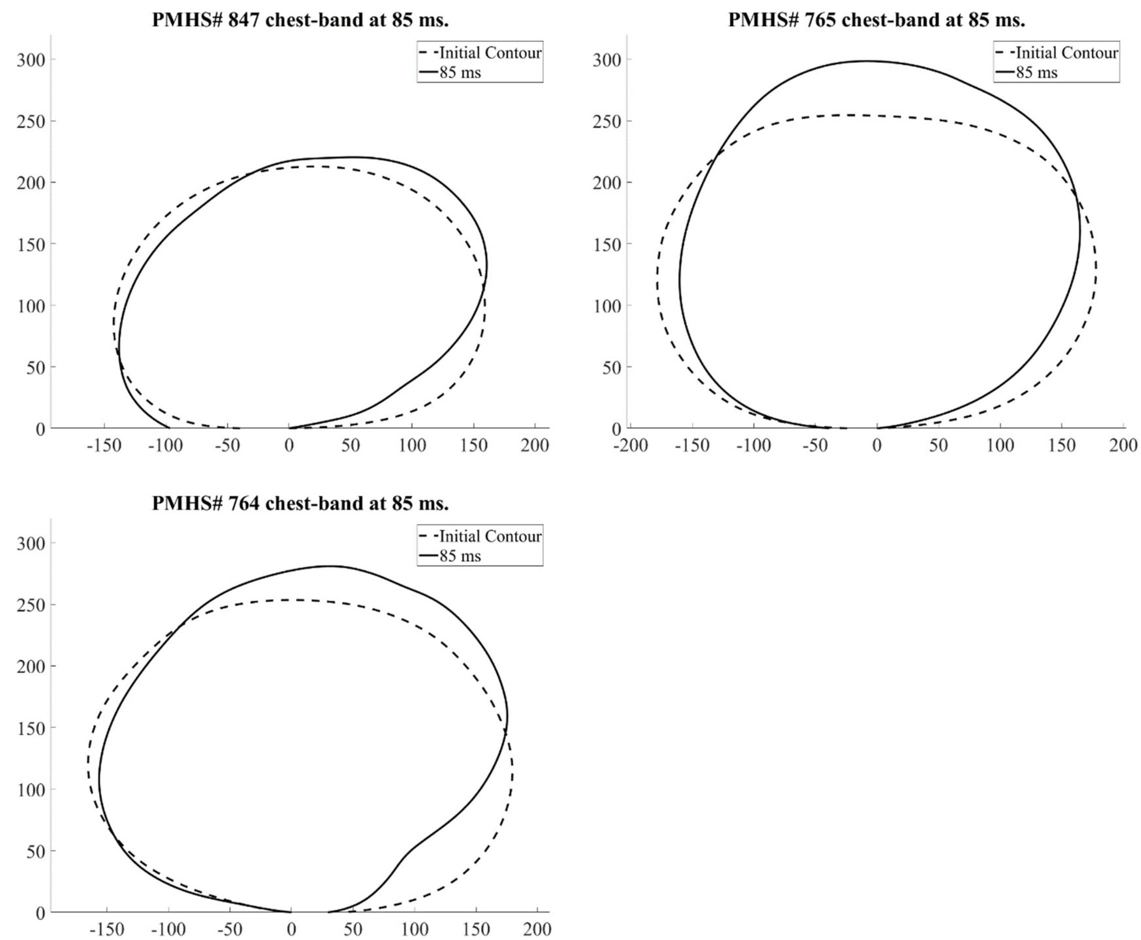

Figure E.2: PMHS chestband contours with large (left) and small (right) bolster structure) (cont.)

Appendix F

PMHS Individual Injury Evaluations

PMHS# 758

This surrogate sustained eleven anterior and four posterior rib fractures including a unilateral flail chest (figure 4.21). The anterior section of the chest presented a combination of ipsilateral and contralateral fractures along the shoulder belt path. Figure F.1 shows the PMHS chestband deflection at 85 ms. The left anterolateral deflection indicates that the rib fractures had already occurred in that area at this point in time. The strain values (figure F.2) dropped for the fourth and sixth rib gauges indicating that the rib fractures occurred between 60 to 65 ms into the event. The MPS could not be calculated for the 6^{th} rib due to the malfunction of two of the three rosette channels. Only the information of the first channel (channel A) is available.

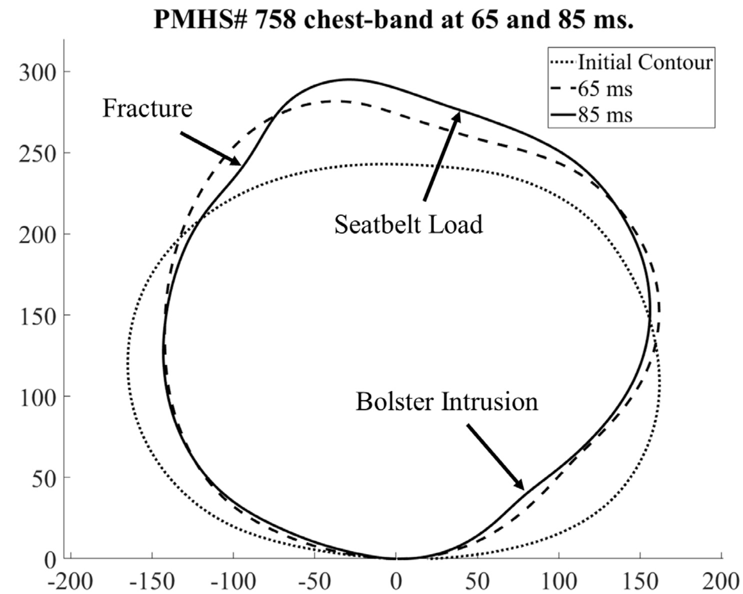

Figure F.1: Chestband deformation in PMHS# 758

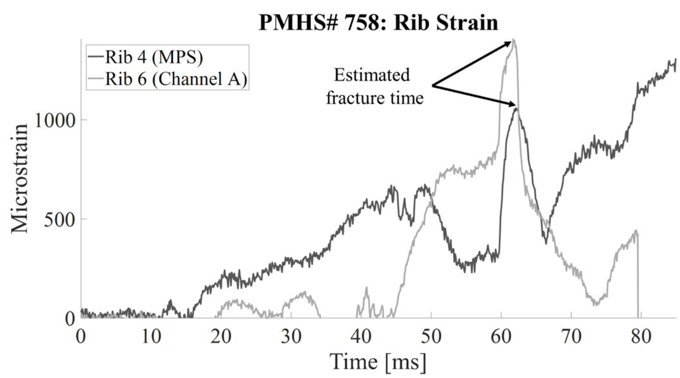

Figure F.2: Rib strain in PMHS# 758

PMHS# 847

This surrogate did not sustain any injuries (figure 4.21). This surrogate showed the lowest overall bolster-related deflection and lowest center console related deflection out of the PMHS used in the configuration with the large bolster structure (figure 4.18).

PMHS# 764

This surrogate sustained a single rib fracture (figure 4.21). This fracture occurred on the eighth left rib close to the strain gauge location. The strain gauge was found detached during the autopsy. The sudden increase in the strain reading (figure F.3), of around 1000 $\mu\epsilon$/ms, was most likely due to deformation or failure of the gauge once detached. This indicates that the strain gauge detached at around 62 ms.

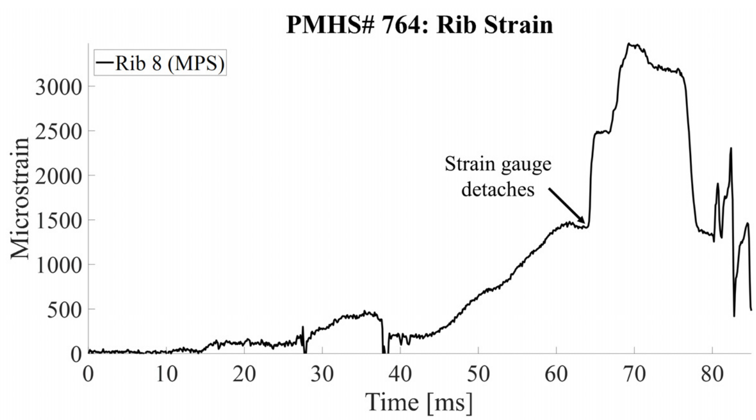

Figure F.3: Rib strain in PMHS# 764

PMHS# 764

This surrogate sustained two anterior and one posterior rib fractures (figure 4.21). The anterior rib fractures occurred on rib four bilateral to the seatbelt path. Figure F.4 shows the PMHS chestband deflection at 75 ms. The left anterolateral deflection indicates that the rib fractures had already occurred in that area at this point in time. Figure F.5 shows how the strain increased with the shoulder belt force followed by two consecutive drops in strain. This sudden drops in strain indicate that the rib fractured in a time frame between 50 and 60 ms.

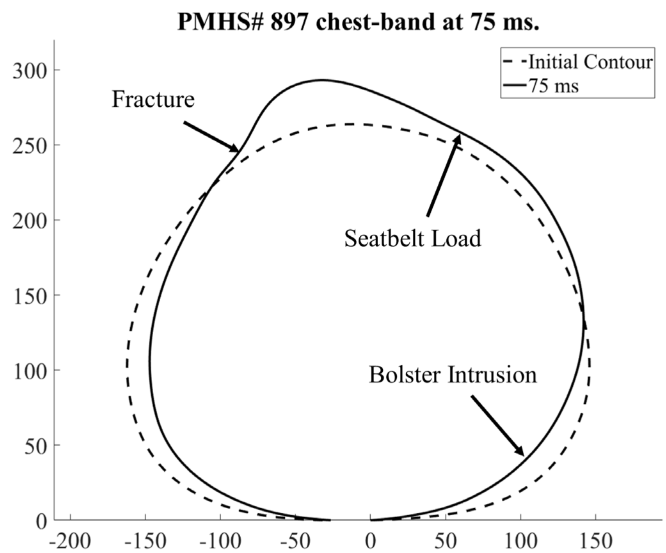

Figure F.4: Chestband deformation in PMHS# 758

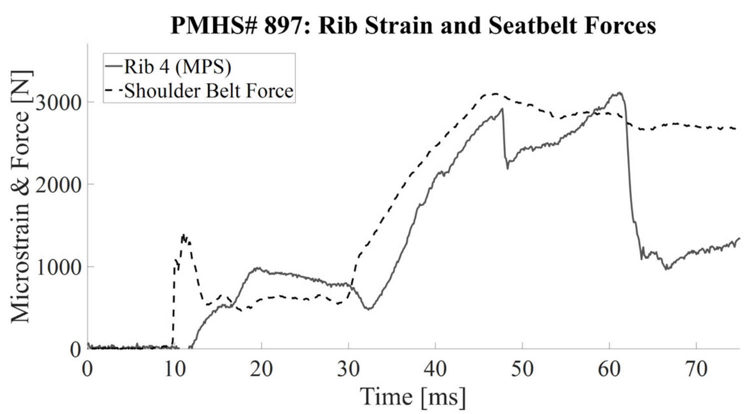

Figure F.5: Rib strain in PMHS# 758

PMHS# 765

This surrogate sustained three anterior and one lateral rib fracture (figure 4.21). The anterior fractures occurred contralaterally, close to the shoulder belt path. The lateral fracture occurred in the proximity of the center console. There was no instrumentation near the fractures. Therefore, no timing or additional information could be gathered.

Appendix G

WorldSID and GHBMC Kinematic and Kinetic Results

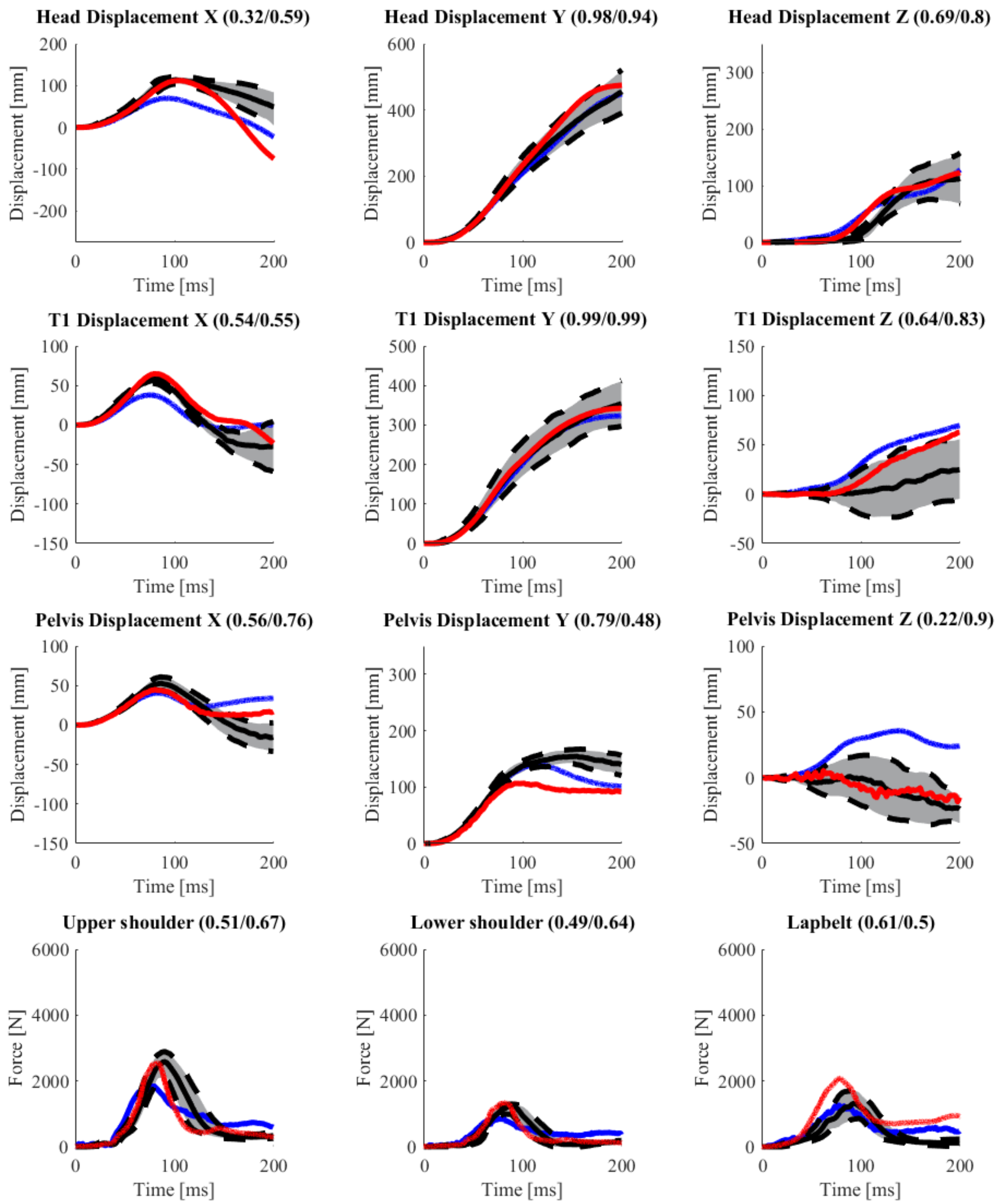

Figure G.1: GHBMC (blue), WorldSID(red) and PMHS corridors (gray) for configuration 1. CORA scores in parenthesis (GHBMC/WorldSID)

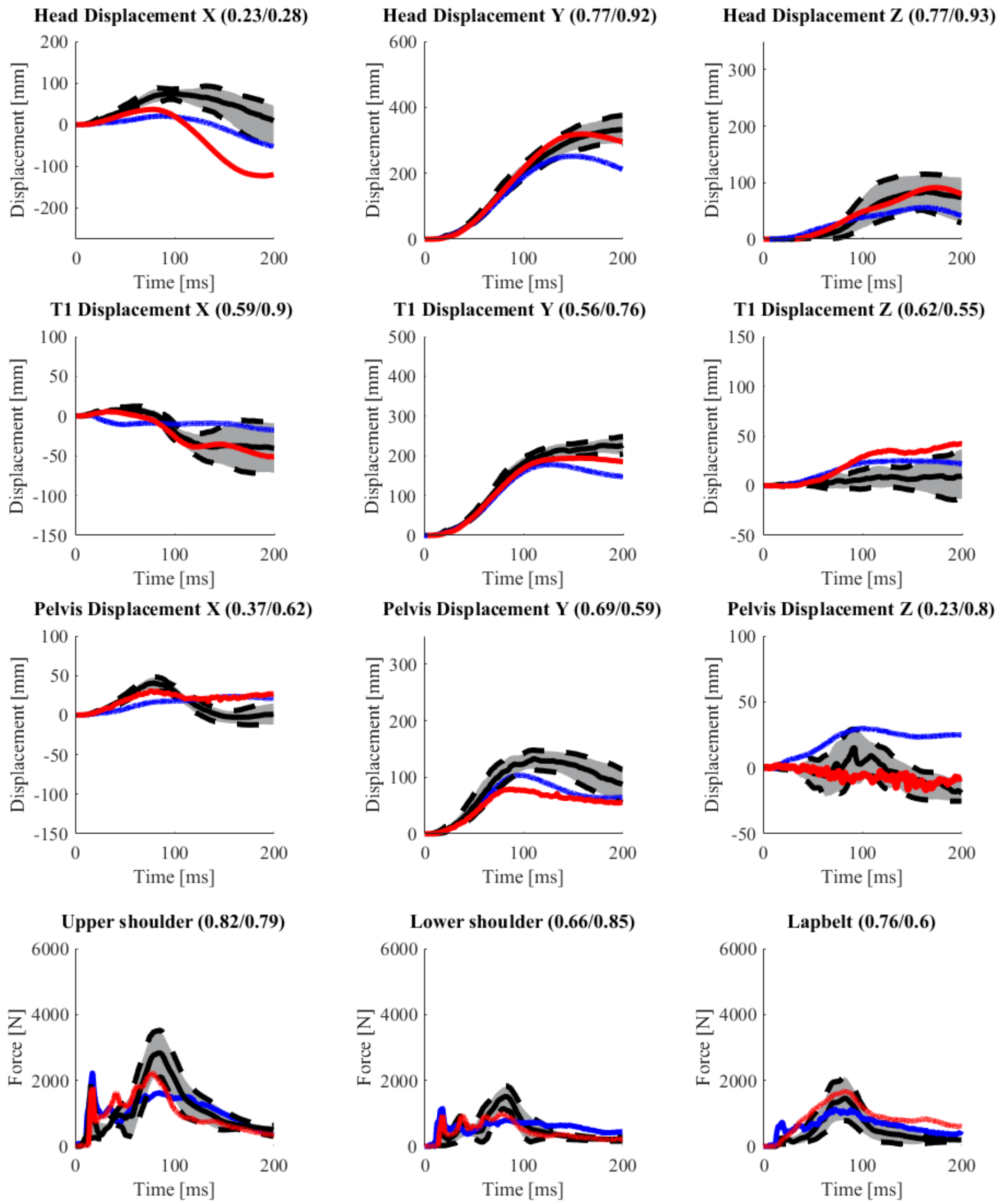

Figure G.2: GHBMC (blue), WorldSID(red) and PMHS corridors (gray) for configuration 2. CORA scores in parenthesis (GHBMC/WorldSID)

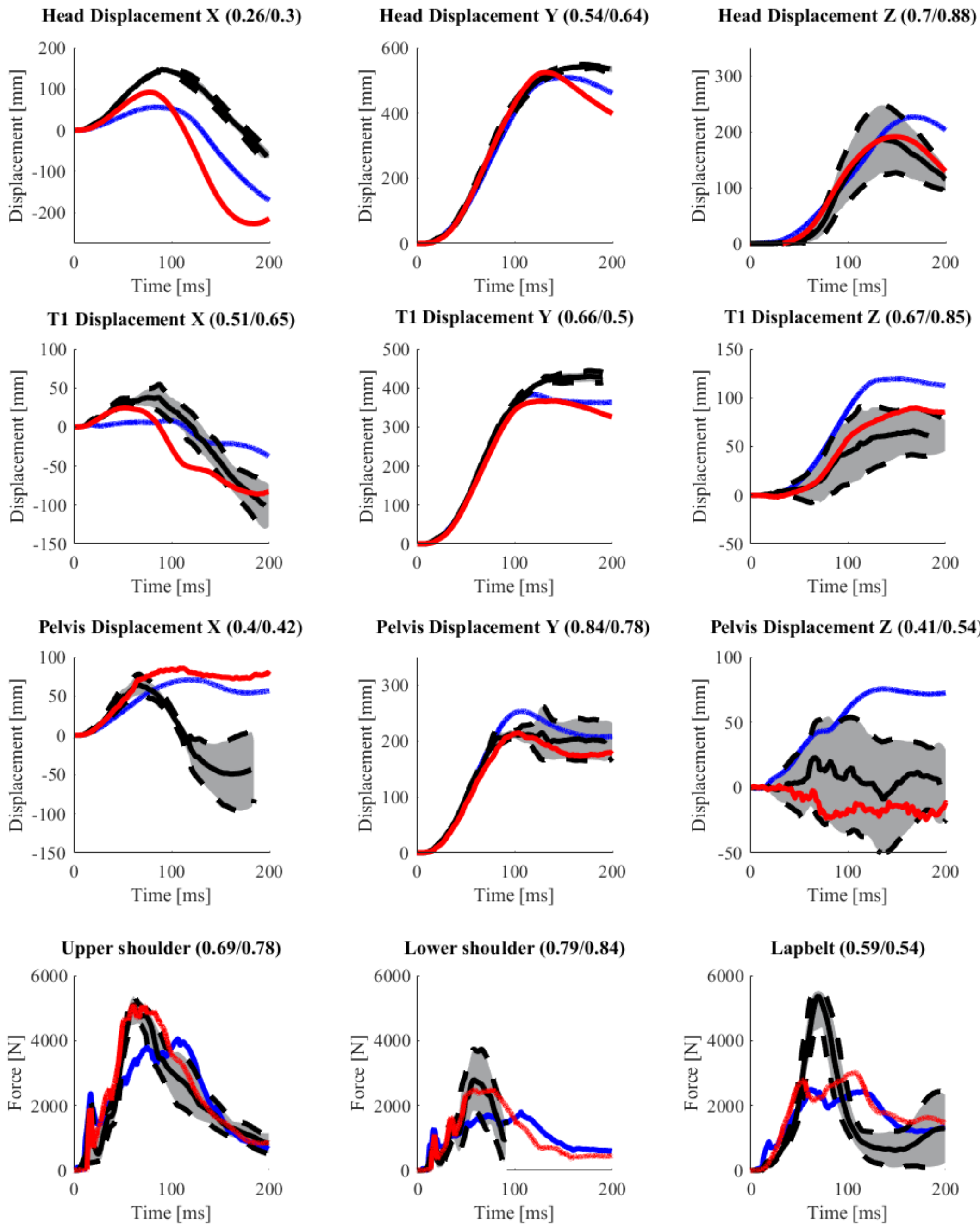

Figure G.3: GHBMC (blue), WorldSID(red) and PMHS corridors (gray) for configuration 3. CORA scores in parenthesis (GHBMC/WorldSID)

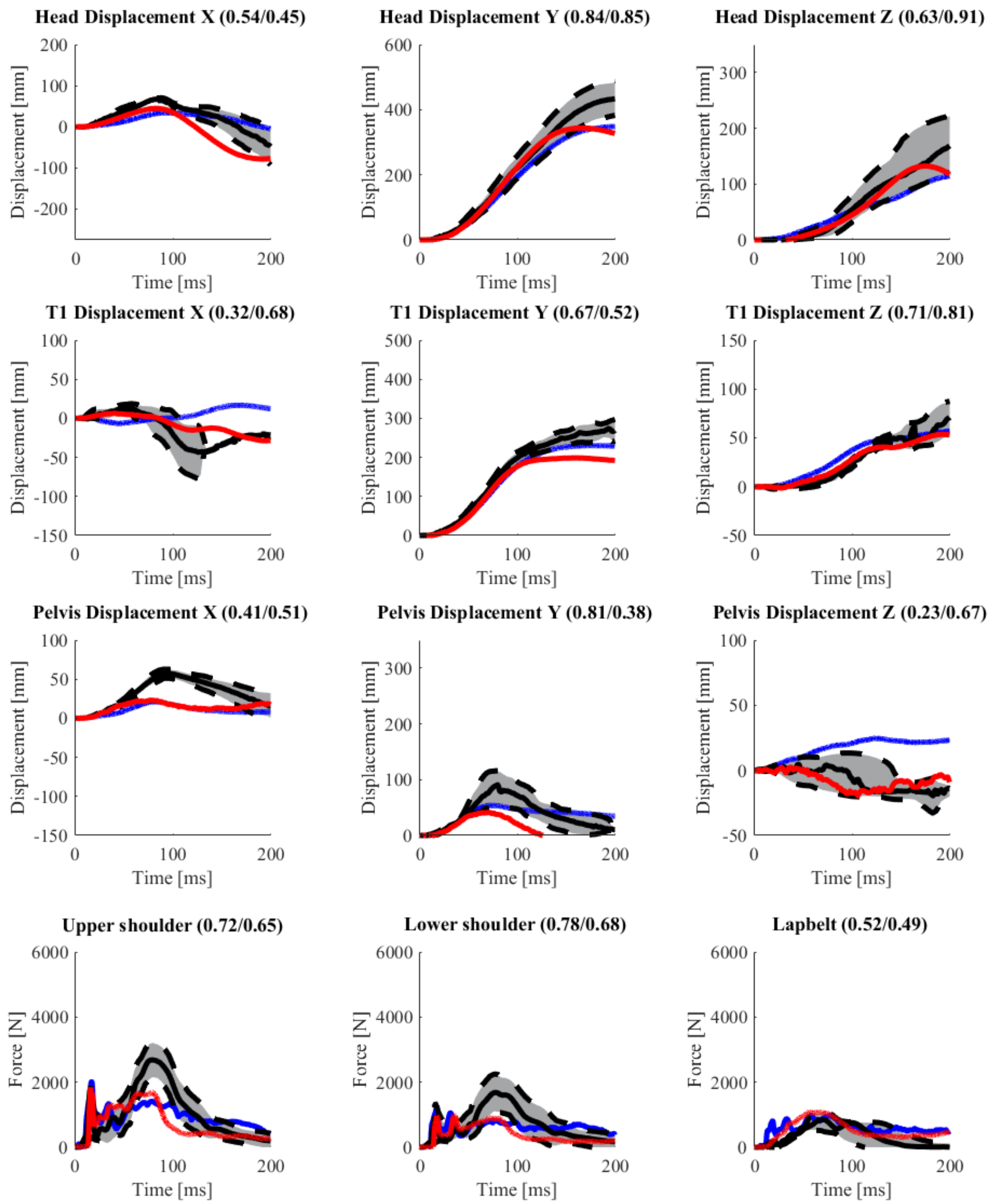

Figure G.4: GHBMC (blue), WorldSID(red) and PMHS corridors (gray) for configuration 4. CORA scores in parenthesis (GHBMC/WorldSID)

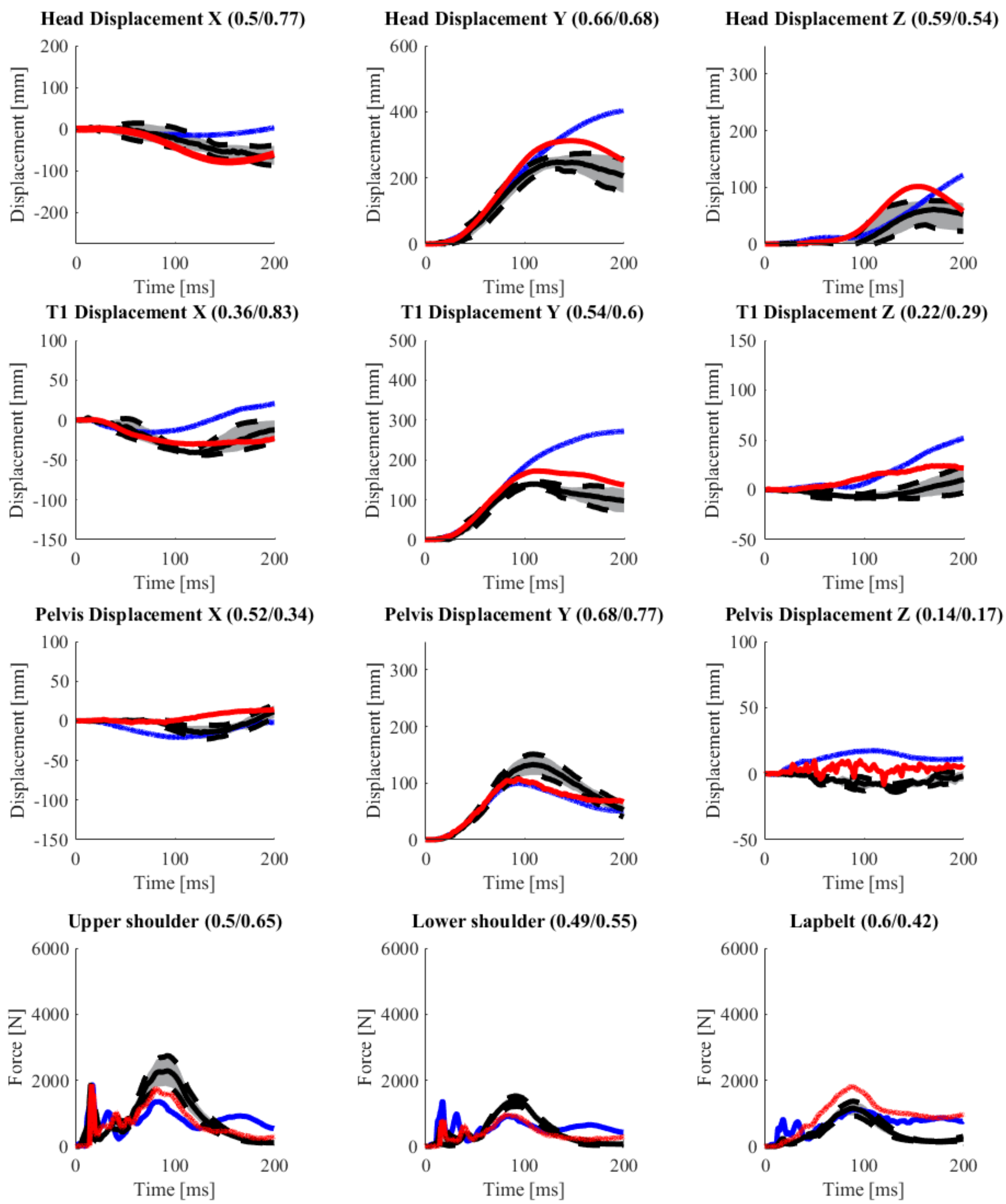

Figure G.5: GHBMC (blue), WorldSID(red) and PMHS corridors (gray) for configuration 5. CORA scores in parenthesis (GHBMC/WorldSID)

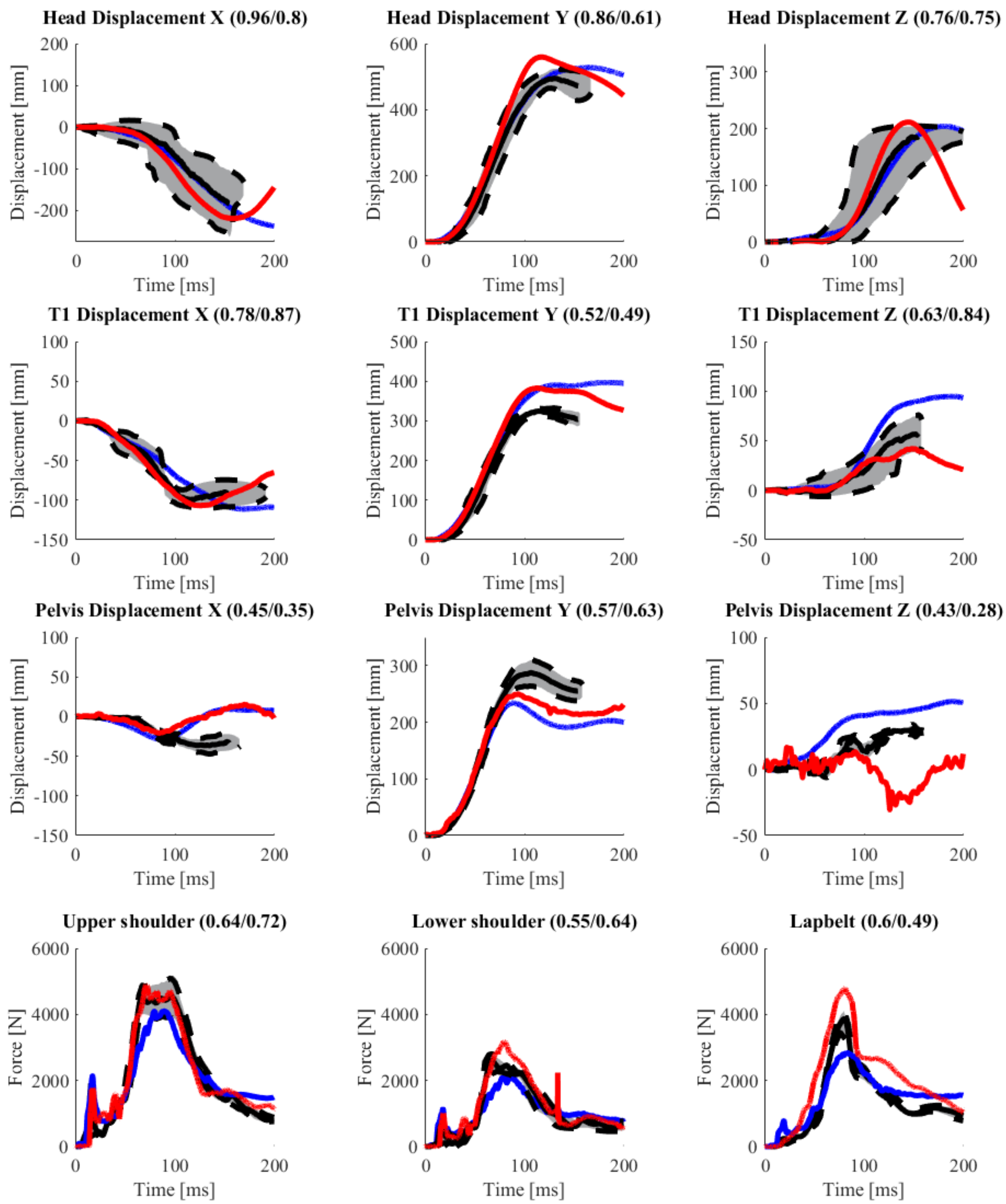

Figure G.6: GHBMC (blue), WorldSID(red) and PMHS corridors (gray) for configuration 6. CORA scores in parenthesis (GHBMC/WorldSID)

THIS PAGE INTENTIONALLY LEFT BLANK

Appendix H

WorldSID and GHBMC Video Snapshots in Simplified Sled

Figure H.1: WorldSID, GHBMC and PMHS response for configuration 1 at 50 ms (up), 100 ms (center) and 150 ms (down)

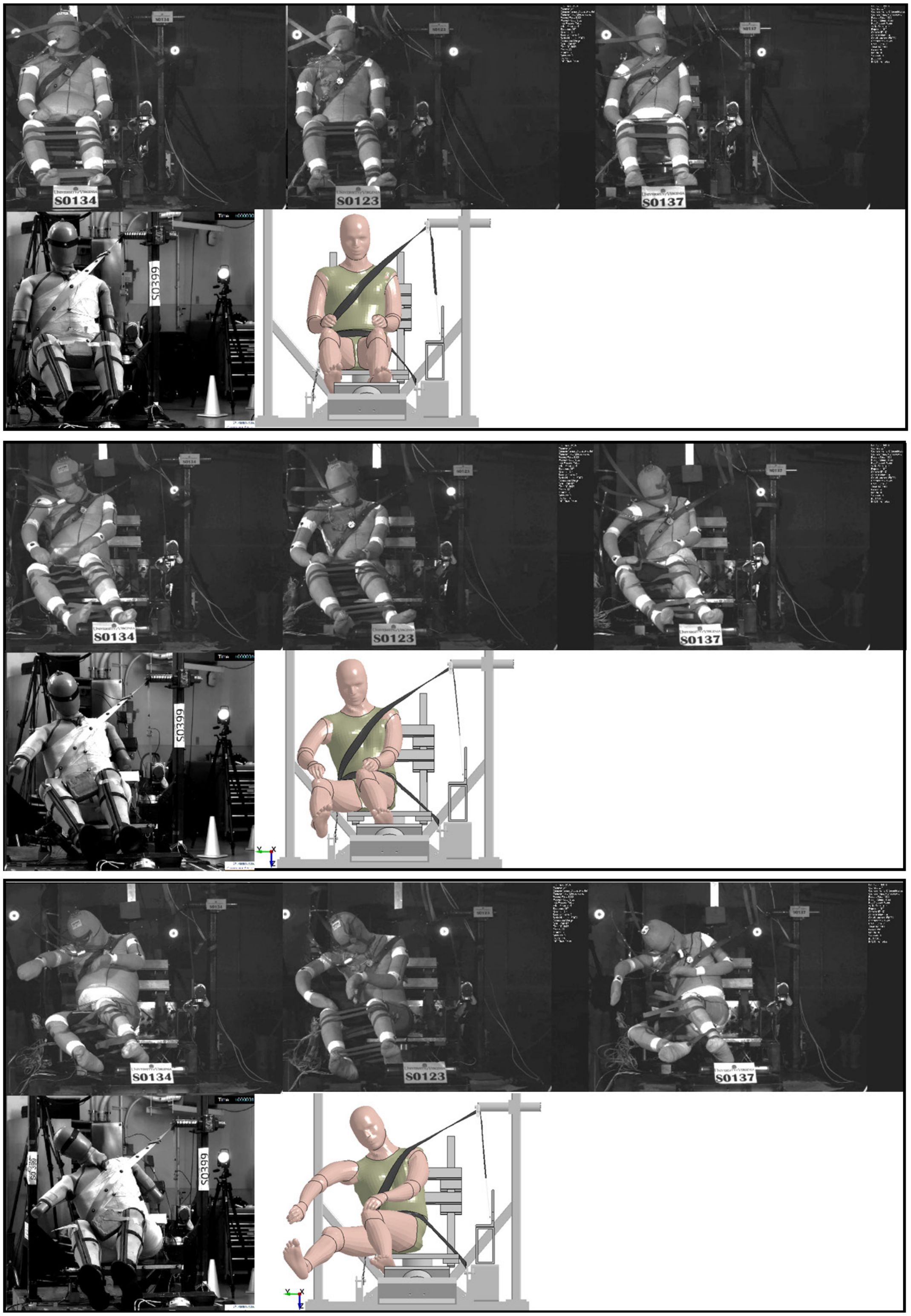

Figure H.2: WorldSID, GHBMC and PMHS response for configuration 2 at 50 ms (up), 100 ms (center) and 150 ms (down)

Figure H.3: WorldSID, GHBMC and PMHS response for configuration 3 at 50 ms (up), 100 ms (center) and 150 ms (down)

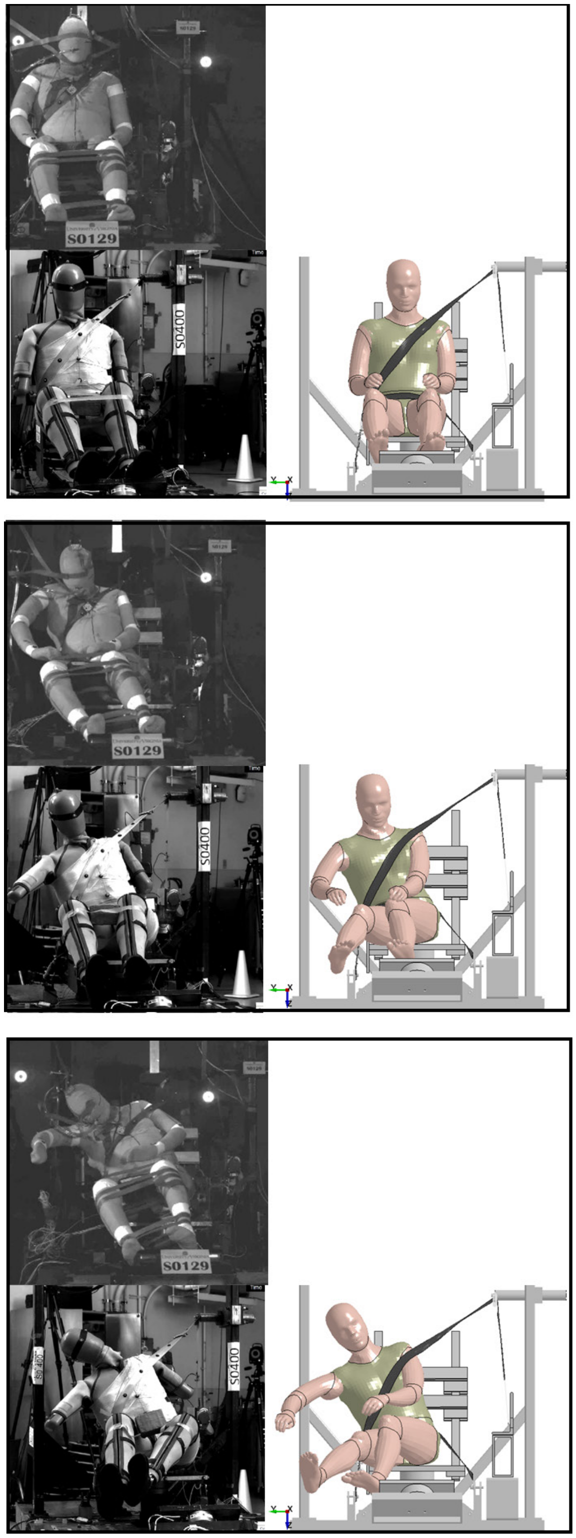

Figure H.4: WorldSID, GHBMC and PMHS response for configuration 4 at 50 ms (up), 100 ms (center) and 150 ms (down)

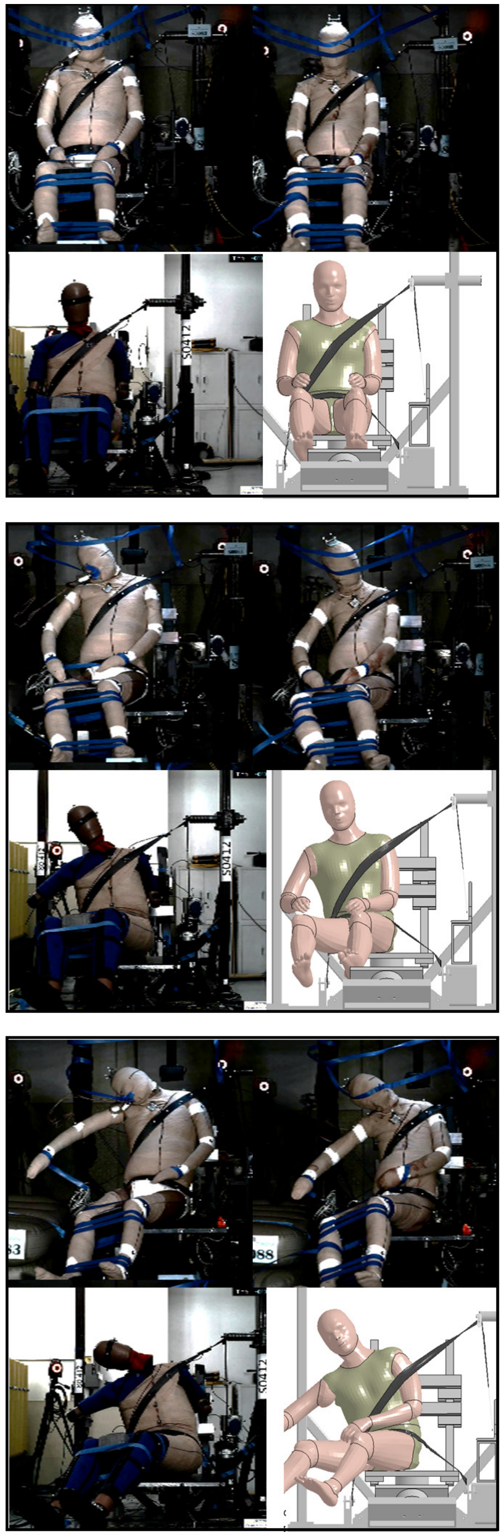

Figure H.5: WorldSID, GHBMC and PMHS response for configuration 5 at 50 ms (up), 100 ms (center) and 150 ms (down)

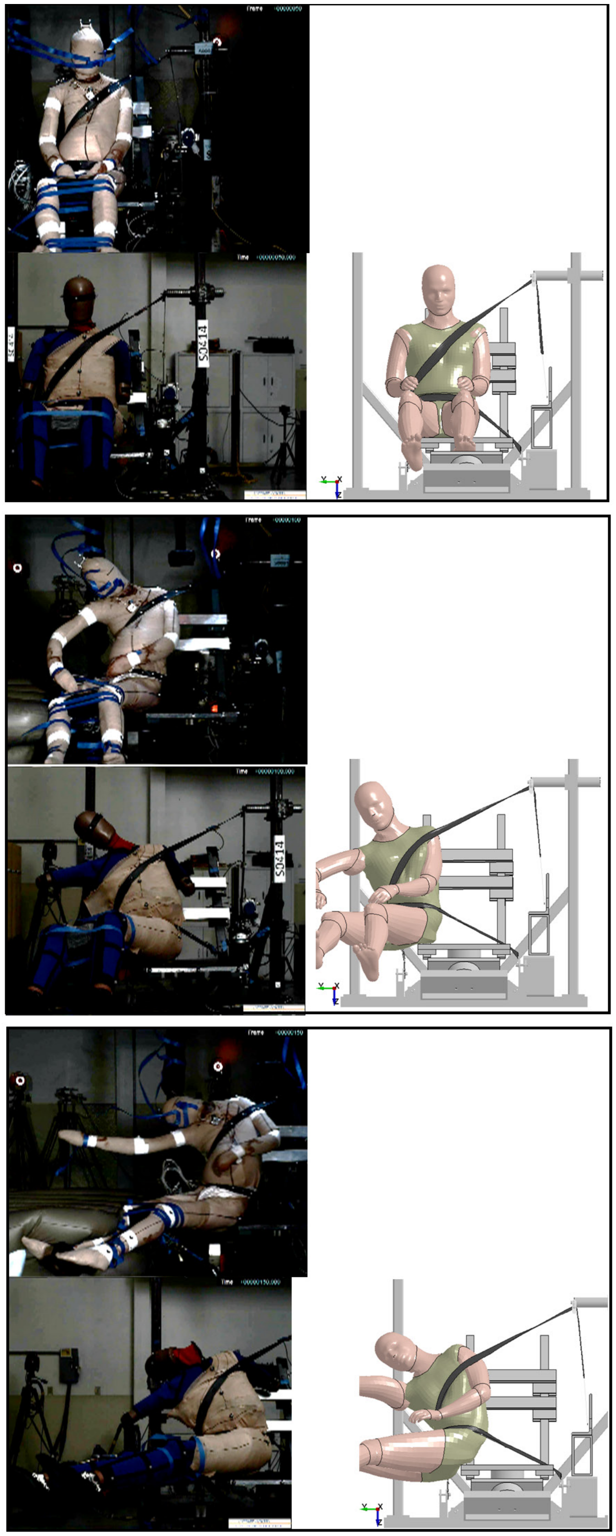

Figure H.6: WorldSID, GHBMC and PMHS response for configuration 6 at 50 ms (up), 100 ms (center) and 150 ms (down)

THIS PAGE INTENTIONALLY LEFT BLANK

Appendix I

PMHS, WorldSID and GHBMC Video Snapshots in Vehicle-Based Sled

Figure I.1: Time: 0 ms.

Top row; left to right: PMHS# 758, 847, 764, WorldSID and GHBMC kinematics with large bolster structure.

Bottom row; left to right: PMHS# 897, 765, WorldSID and GHBMC kinematics (bottom row; left to right) with small bolster structure.

The dotted line is located approximately at the inboard edge of the driver seat.

Figure I.2: Time: 50 ms.

Top row; left to right: PMHS# 758, 847, 764, WorldSID and GHBMC kinematics with large bolster structure.

Bottom row; left to right: PMHS# 897, 765, WorldSID and GHBMC kinematics (bottom row; left to right) with small bolster structure.

The dotted line is located approximately at the inboard edge of the driver seat.

Figure I.3: Time: 85 ms.

Top row; left to right: PMHS# 758, 847, 764, WorldSID and GHBMC kinematics with large bolster structure.

Bottom row; left to right: PMHS# 897, 765, WorldSID and GHBMC kinematics (bottom row; left to right) with small bolster structure.

The dashed and solid lines are located approximately at the inboard edge of the passenger seat and the center of the passenger seat, respectively.

Figure I.4: Time: 120 ms.

Top row; left to right: PMHS# 758, 847, 764, WorldSID and GHBMC kinematics with large bolster structure.

Bottom row; left to right: PMHS# 897, 765, WorldSID and GHBMC kinematics (bottom row; left to right) with small bolster structure.

The dashed and solid lines are located approximately at the inboard edge of the passenger seat and the center of the passenger seat, respectively.

Figure I.5: Time: 175 ms.

Top row; left to right: PMHS# 758, 847, 764, WorldSID and GHBMC kinematics with large bolster structure.

Bottom row; left to right: PMHS# 897, 765, WorldSID and GHBMC kinematics (bottom row; left to right) with small bolster structure.

The dotted line is located approximately at the inboard edge of the driver seat.

Appendix J

Sampling Technique

Sampling the space for this particular application requires the exploration of a non-rectangular, correlated space. For this purpose, a model-free, distance-based algorithm was coded in Matlab. The sampling algorithm operates in the eight-dimensional space formed by the parameters shown in table 7.1. The algorithm uses a Simulated Annealing (SA) optimization technique (Kirkpatrick et al., 1983). This non-linear optimization technique requires the definition of a loss function to be minimized, a second algorithm to generate a valid first guess for the introduction of new datapoints and a third algorithm the generate random, valid samples for the SA algorithm to iterate.

The base Simulated Annealing optimization script was adopted from Vandekerckhove (2008). The loss function was set to create a maximin-distance criterion. That is, the goal of the loss function is to maximize the minimum distance between any two points. The loss function was defined as $L = exp\{\frac{1}{N}[\sum_{i=1}^{N} log(d_i^*)]\}$, where d_i^* is the distance from the i^{th} point to its nearest neighbor and "N" is the total number of datapoints in the sample, including the points from the current and all previous iterations. (Pronzato and Müller, 2012).

The "first guess" algorithm to generate "n" new eight-dimensional points follows these steps:

1. Estimate the probability (P_{min}) of the elements that conform the boundaries

of 90% of the ANSUR II population using Monte-Carlo analysis on the joint probability distribution defined in chapter 3

2. Identify the absolute maximum and minimum height, weight and waist circumference within the 90% of the population

3. Randomly select N points with their anthropometry measurements defined within the anthropometry measurements within the limits defined in step 2 and the rest of the parameters defined within the limits defined in table 7.1

4. Re-sample the anthropometry points until all the points show a probability of occurrence greater than P_{min}

5. Algorithm finished

The algorithm to generate a random valid point for the SA algorithm to iterate follows these steps:

1. Randomly select one point with its anthropometry measurements defined within the limits defined in step 2 of the previous list and the rest of the parameters defined within the limits defined in table 7.1

2. Re-sample the anthropometry until all the points show a probability of occurrence greater than P_{min}

3. Algorithm finished

The SA parameters (e.g. cooling speed) were set to approximate the performace of other maximin algorithms found in the literature (Auffray et al., 2012). The comparative performance of the algorithm was considered to be a good balance between sampling optimization and computational time (table J.1)

Table J.1: Comparative performance of sampling algorithm

	Present Algorithm	Auffray et al. (2012)
# Samples	400	400
# Dimensions	8	8
d_{min}	0.61	0.66
# Iterations	450k	1M
Max # iteration	1M	1M
Time to completion	1h	N/A

Appendix K

Detailed Regression Model Information

The following plots can be found in this appendix:

- Evolution λ and the number of neurons in the regression models
- Predicted PMHS response using NN
- Predicted and actual values
- Error whiskers
- Weighted error whiskers
- Prediction error for the last two iteration models created in chapter 7 with respect to the control sampling parameters.
- Training output histogram before and after oversampling in the last iteration

The predictions shown in figures K.3 and K.4 include uncertainty in seatbelt friction, center console ultimate strain and the anthropometry parameters that could not be measured during the tests (i.e., pelvic link, thigh link and bicristal breadth).

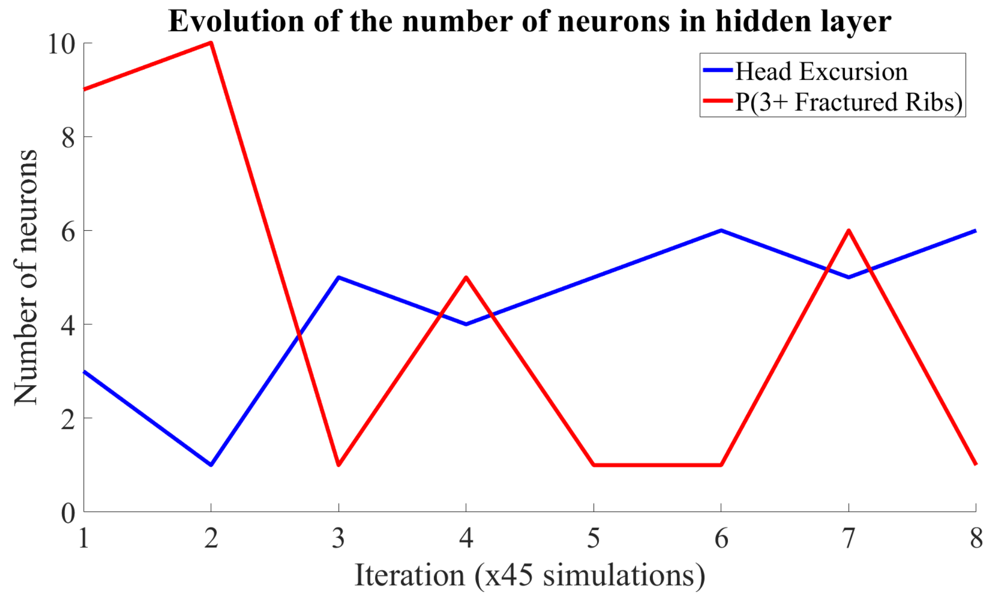

Figure K.1: Evolution of the number of neurons in the hidden layer

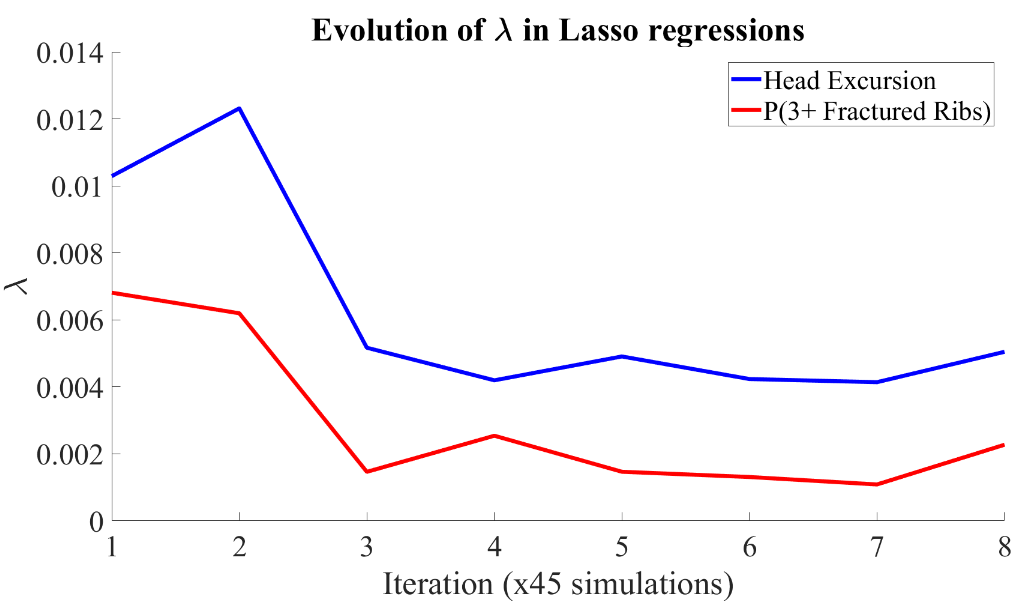

Figure K.2: Evolution of λ in the LASSO regressions

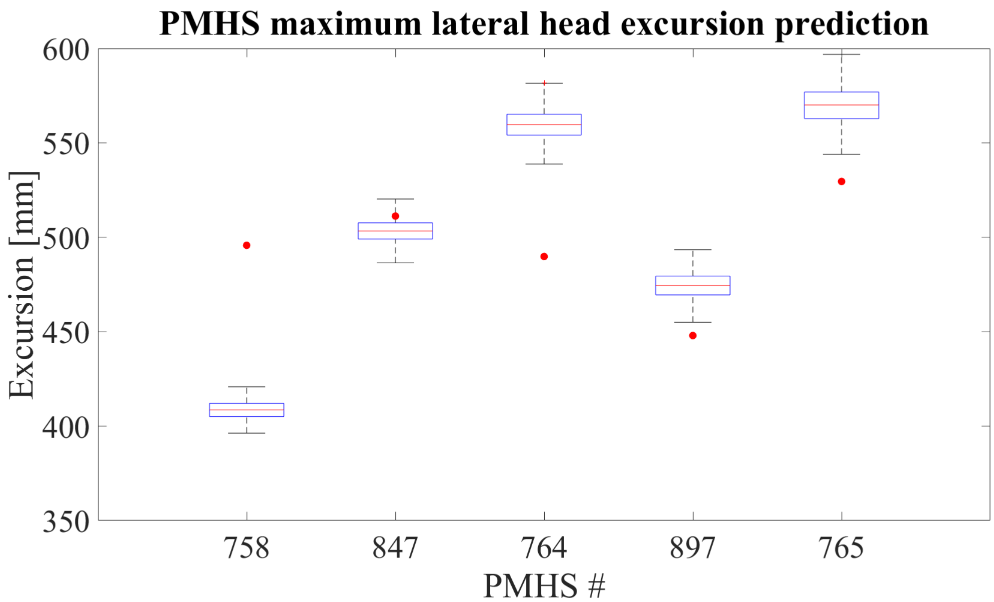

Figure K.3: PMHS maximum lateral head excursion predicted by the NN (box plots) and PMHS actual maximum lateral excursion (red points)

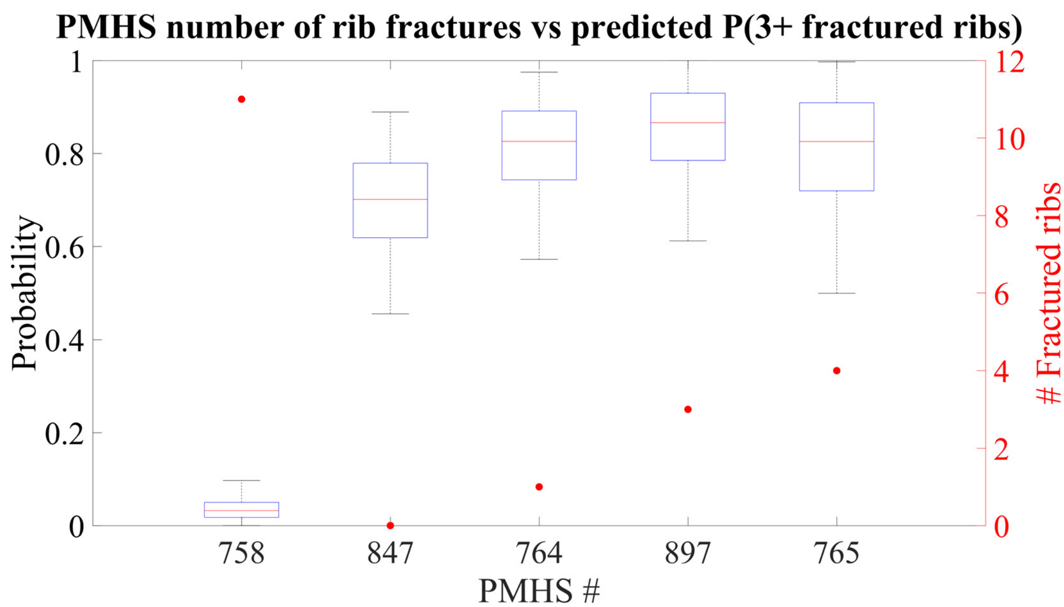

Figure K.4: PMHS probability of 3+ fractured ribs predicted by the NN (box plots) and PMHS actual number of fractured ribs (red points)

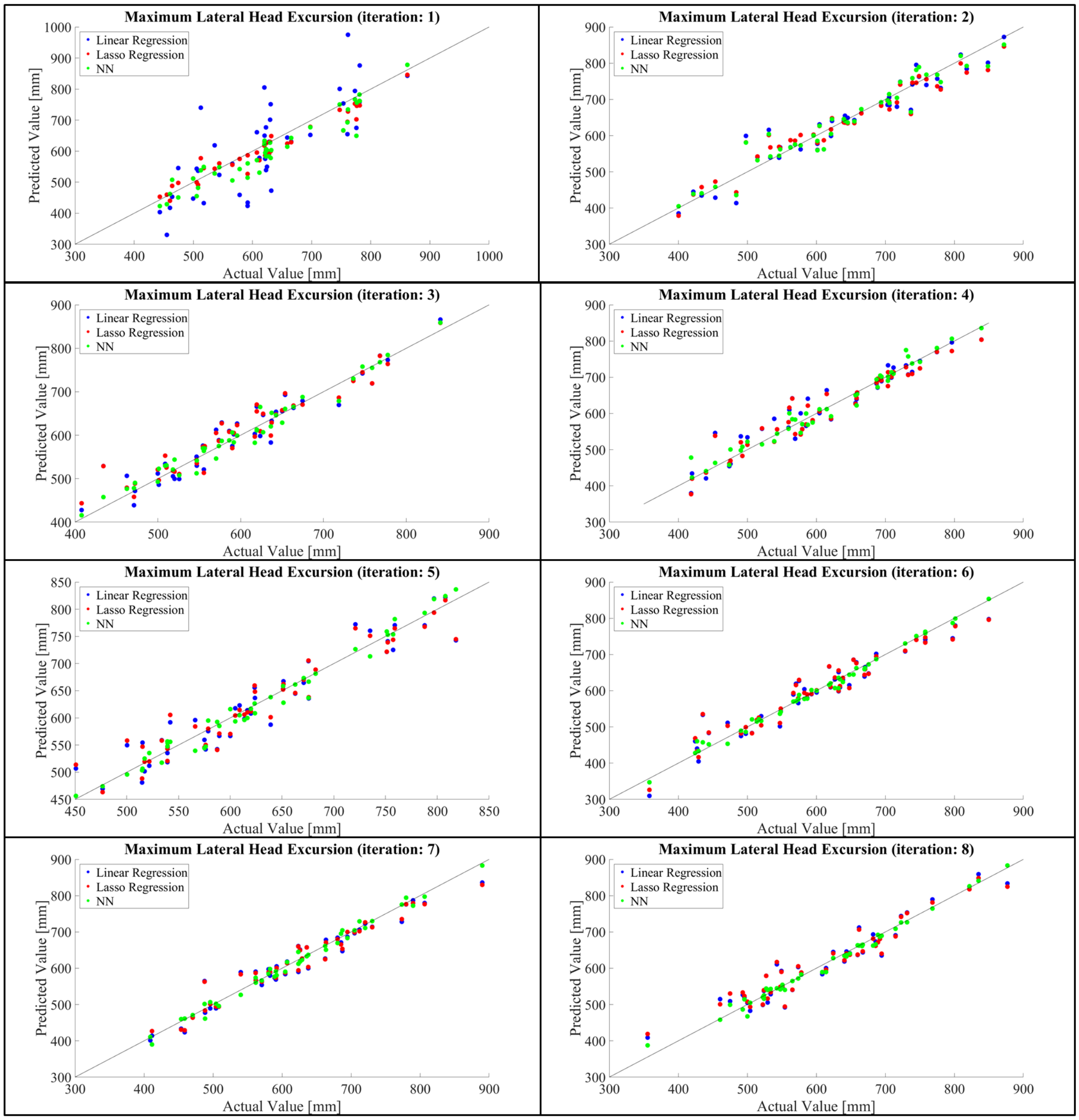

Figure K.5: Predicted and actual maximum lateral head excursion

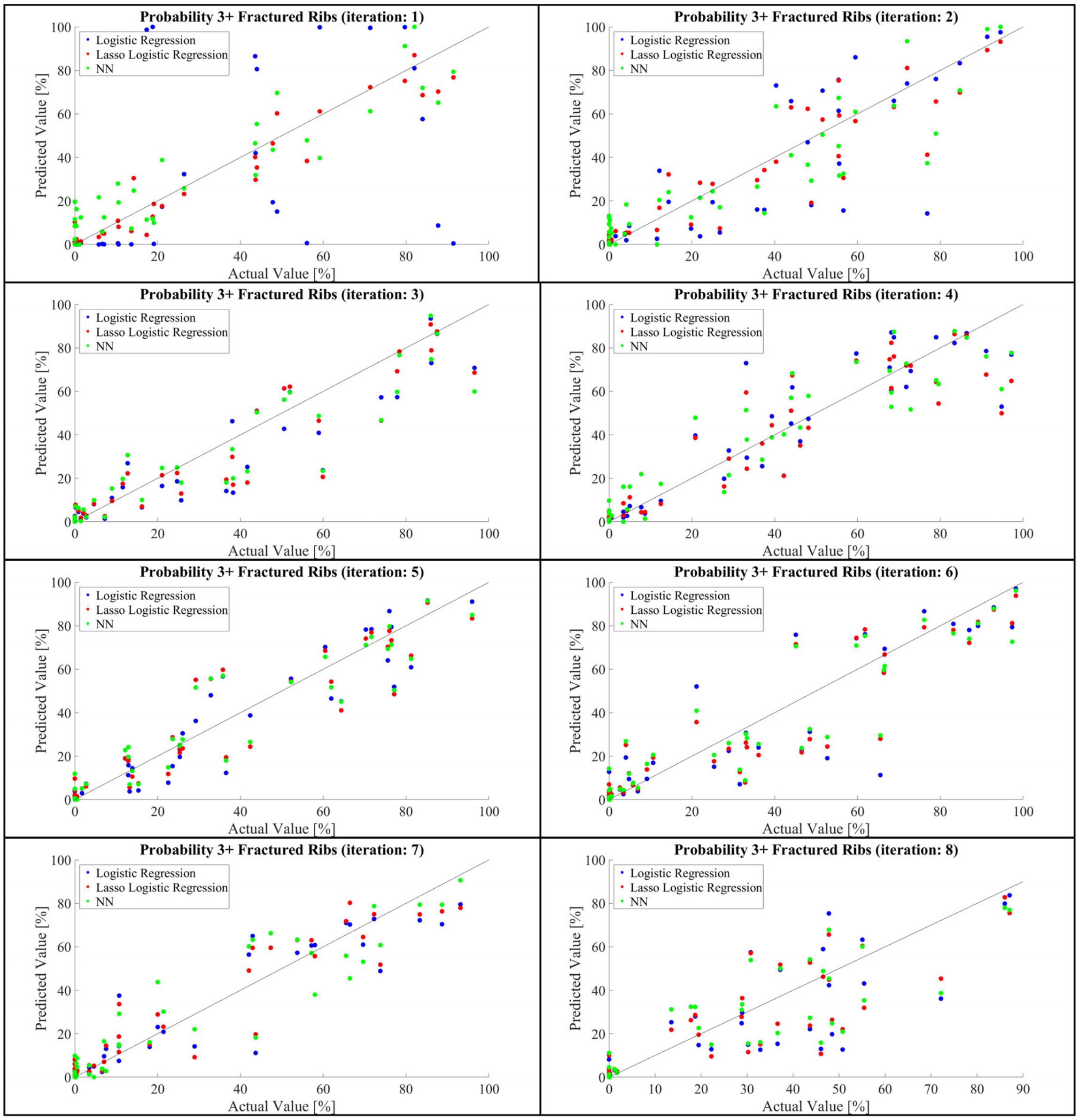

Figure K.6: Predicted and actual probability of 3+ fractured ribs

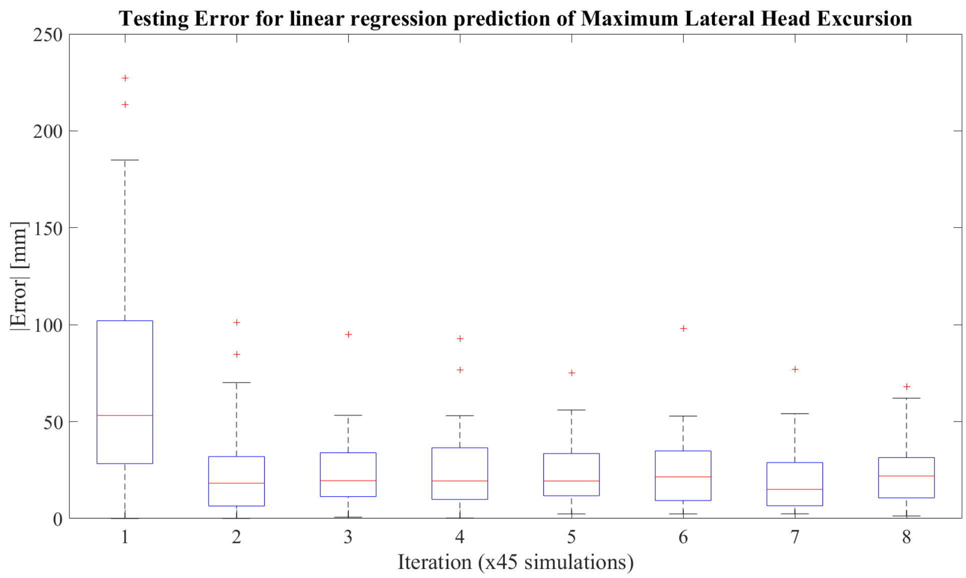

Figure K.7: Maximum lateral head excursion prediction error whisker for linear regression

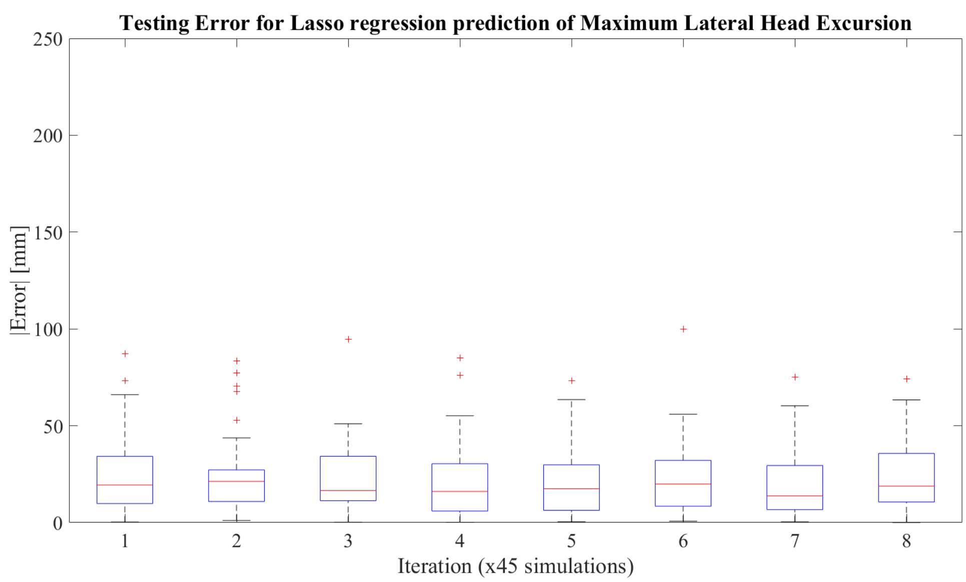

Figure K.8: Maximum lateral head excursion prediction error whisker for LASSO regression

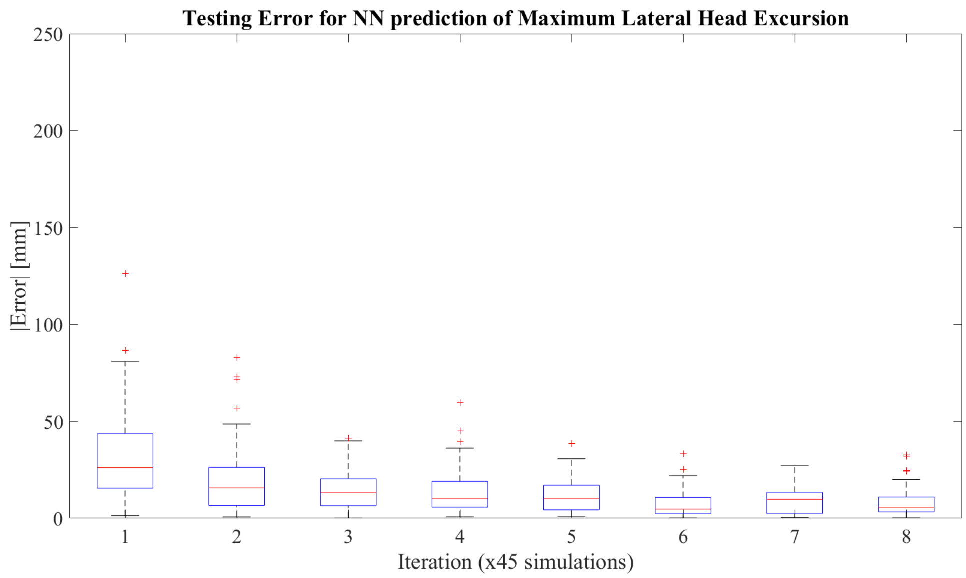

Figure K.9: Maximum lateral head excursion prediction error whisker for NN regression

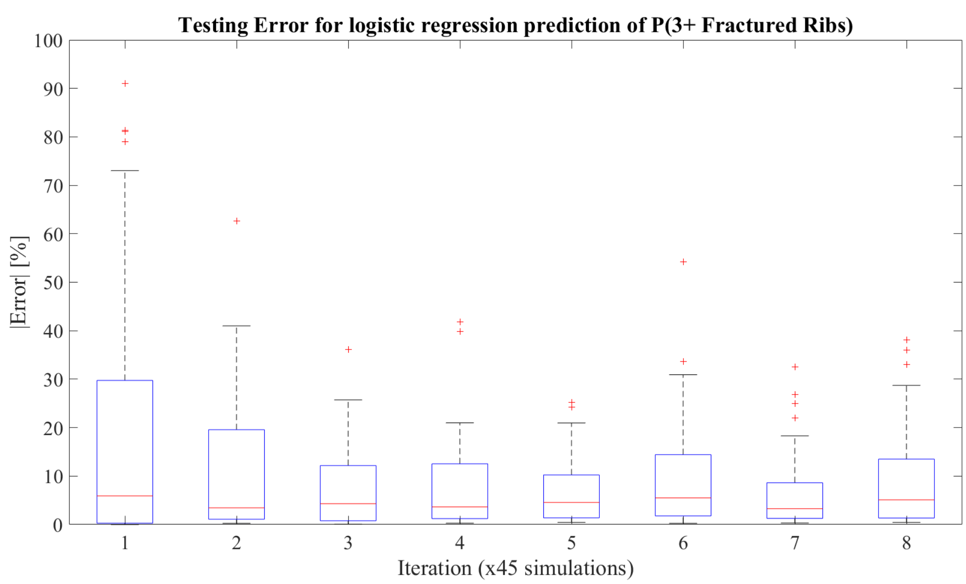

Figure K.10: Probability of 3+ fractured ribs prediction error whisker for logistic regression

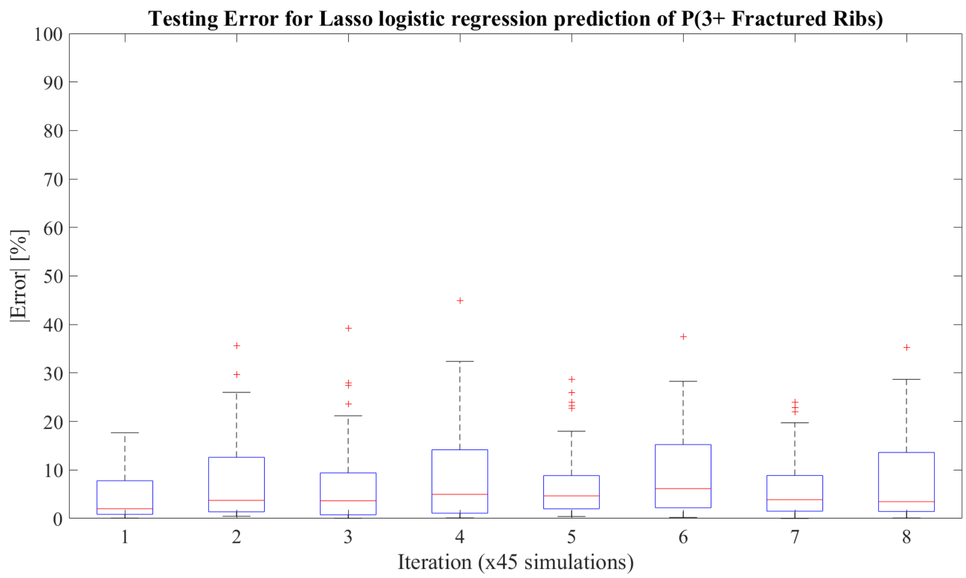

Figure K.11: Probability of 3+ fractured ribs prediction error whisker for LASSO logistic regression

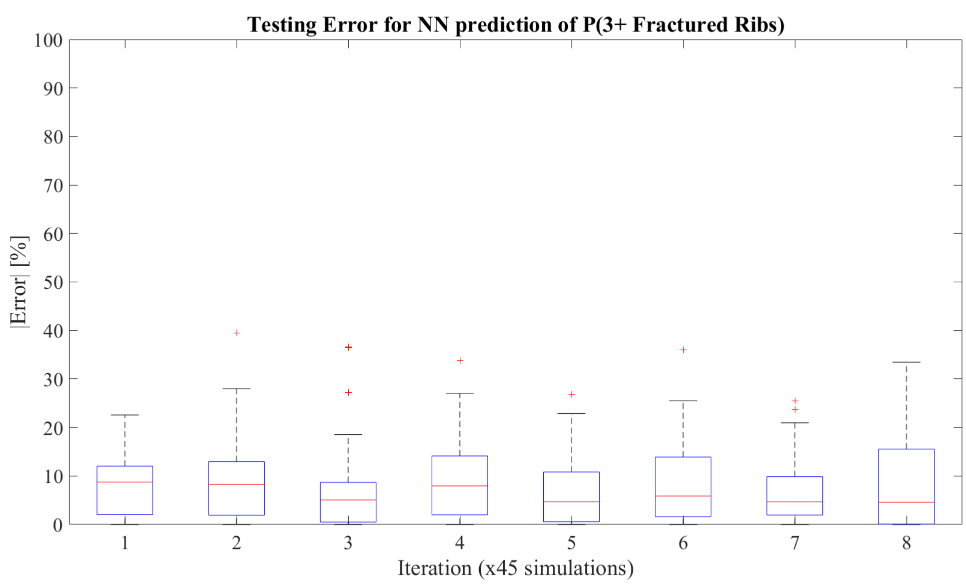

Figure K.12: Probability of 3+ fractured ribs prediction error whisker for NN regression

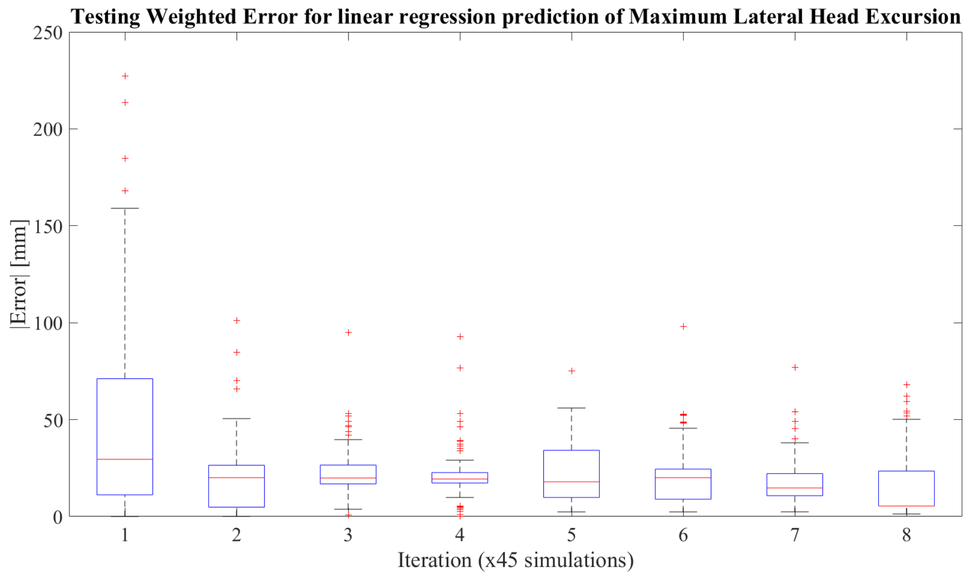

Figure K.13: Maximum lateral head excursion weighted prediction error whisker for linear regression

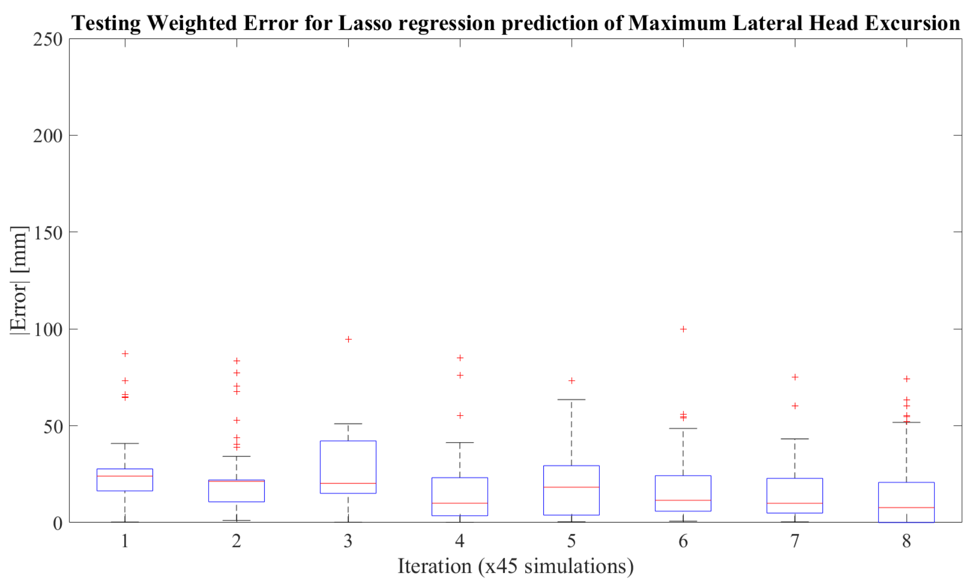

Figure K.14: Maximum lateral head excursion weighted prediction error whisker for LASSO regression

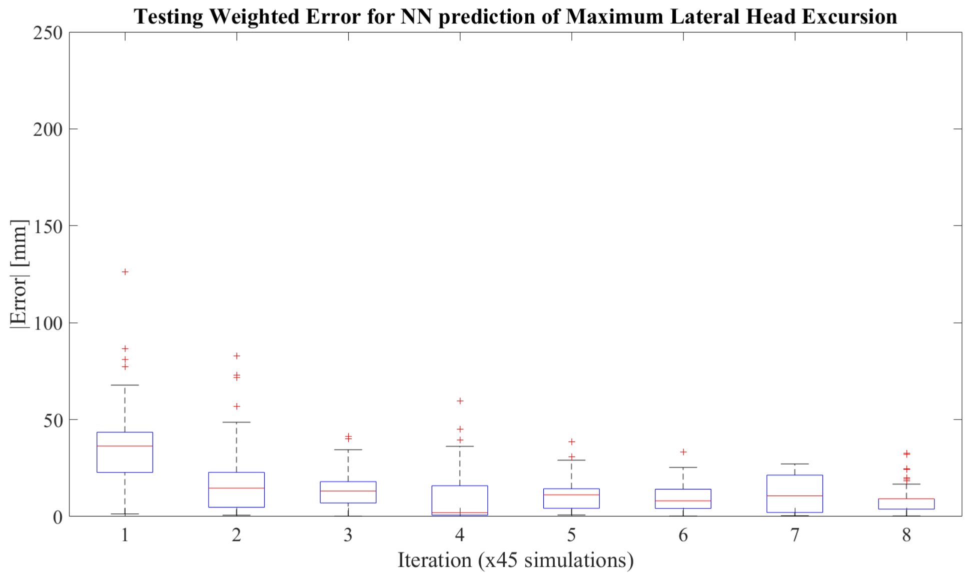

Figure K.15: Maximum lateral head excursion weighted prediction error whisker for NN regression

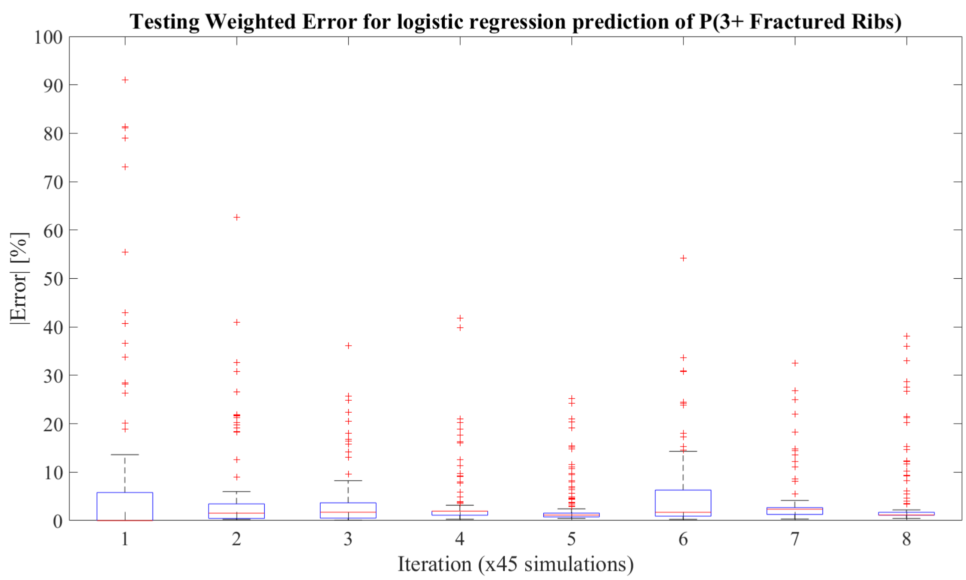

Figure K.16: Probability of 3+ fractured ribs weighted prediction error whisker for logistic regression

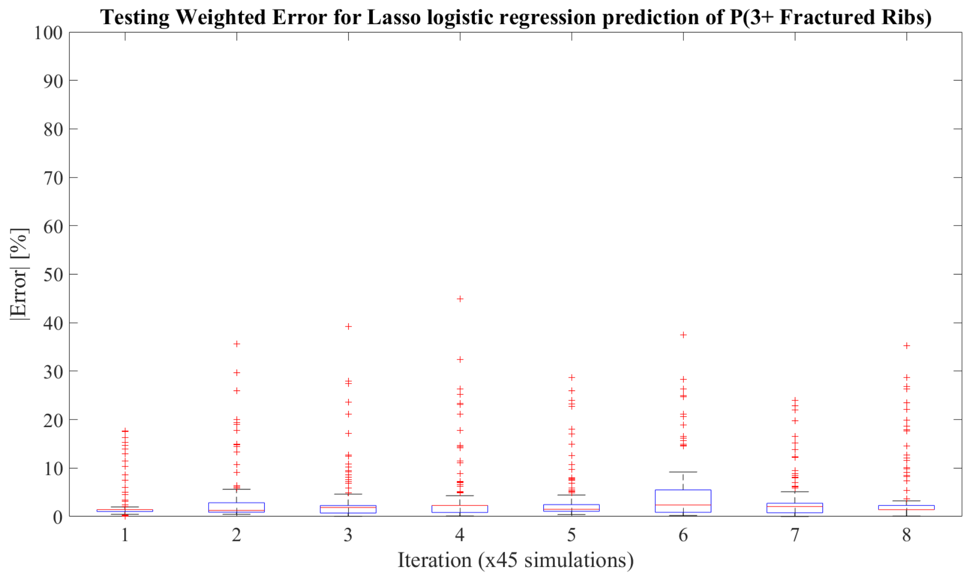

Figure K.17: Probability of 3+ fractured ribs weighted prediction error whisker for LASSO logistic regression

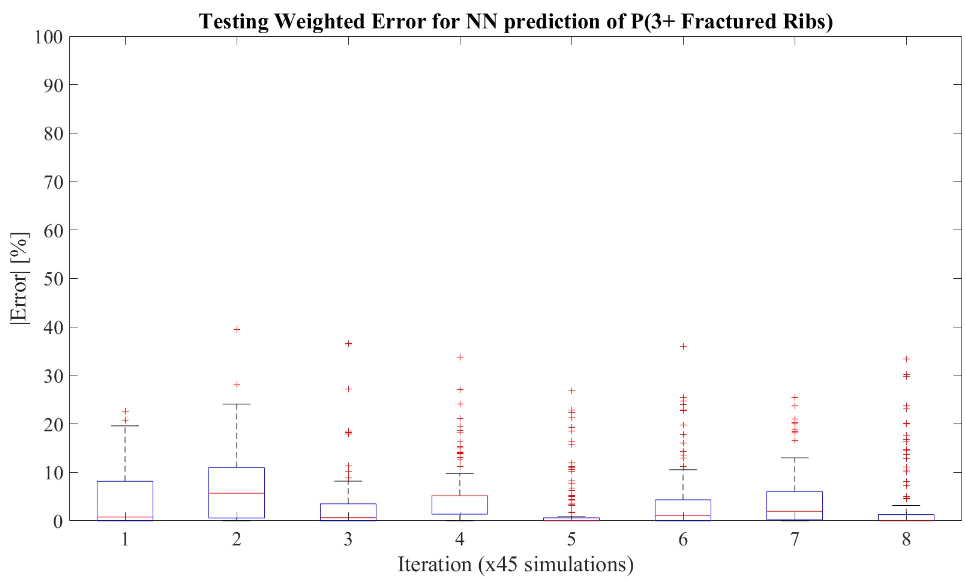

Figure K.18: Probability of 3+ fractured ribs weighted prediction error whisker for NN regression

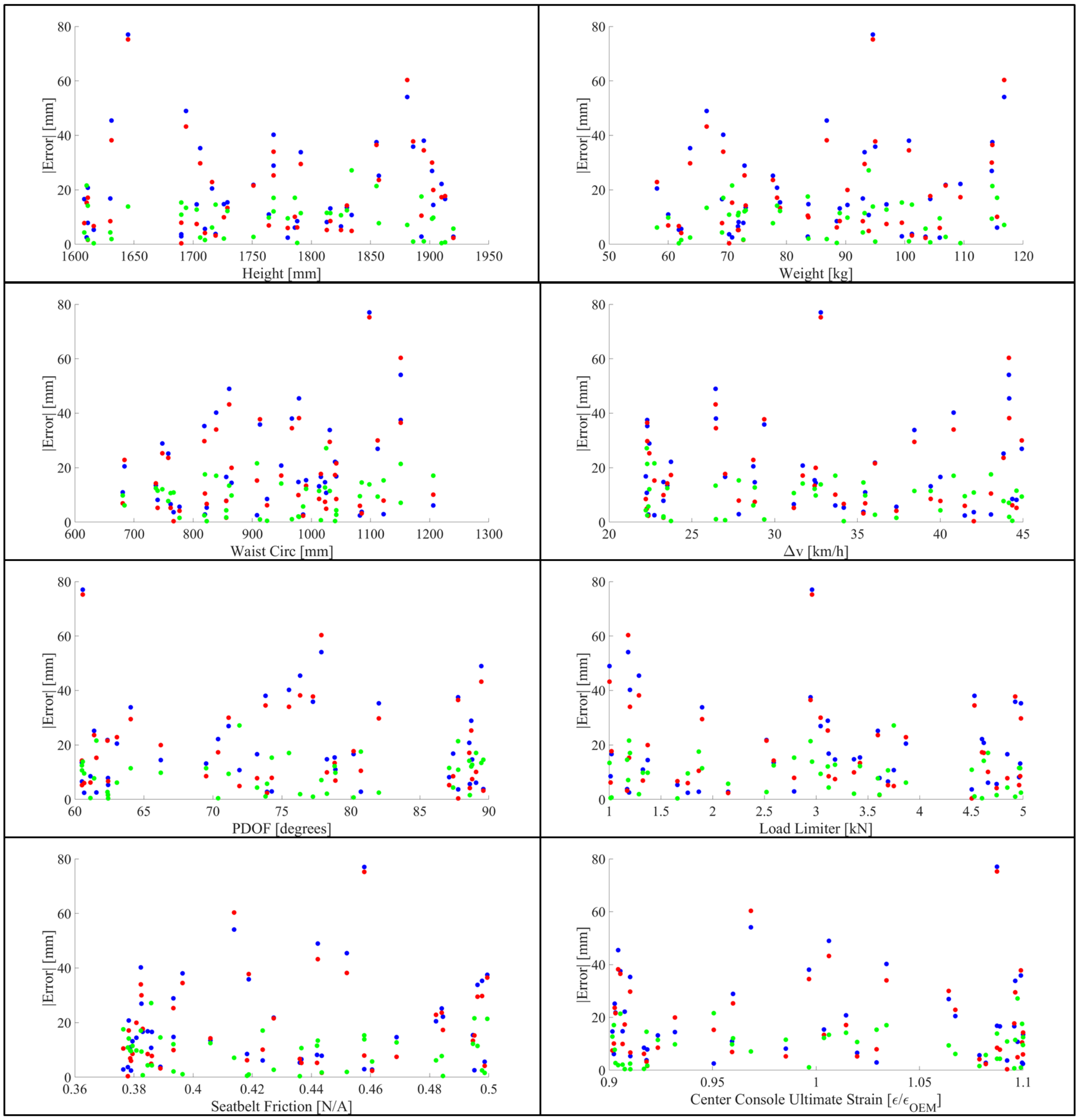

Figure K.19: Maximum lateral head excursion prediction error in iteration 7 (blue: linear regression; red: LASSO regression; green: NN)

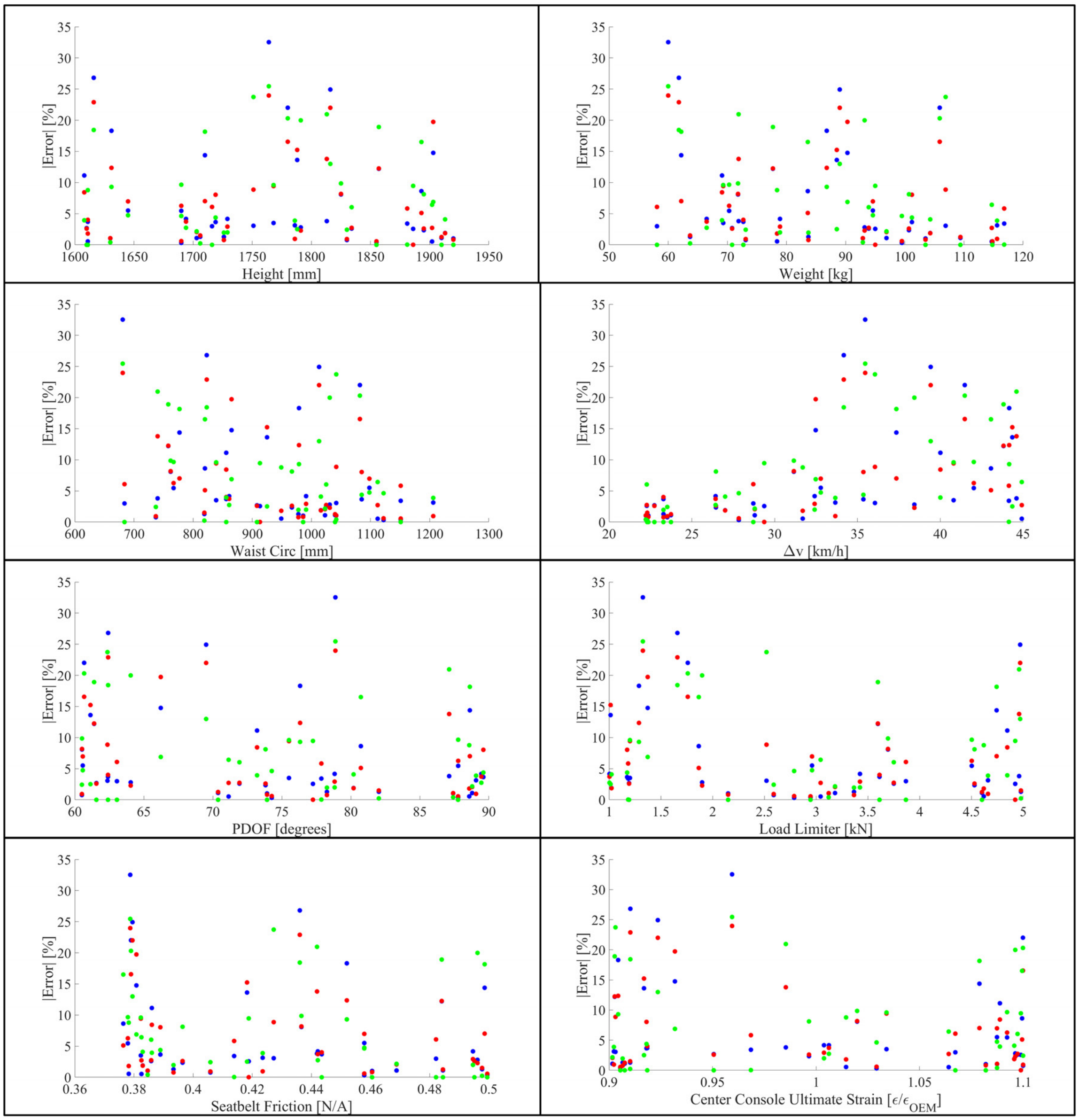

Figure K.20: 3+ fractured ribs prediction error in iteration 7 (blue: logistic regression; red: LASSO logistic regression; green: NN)

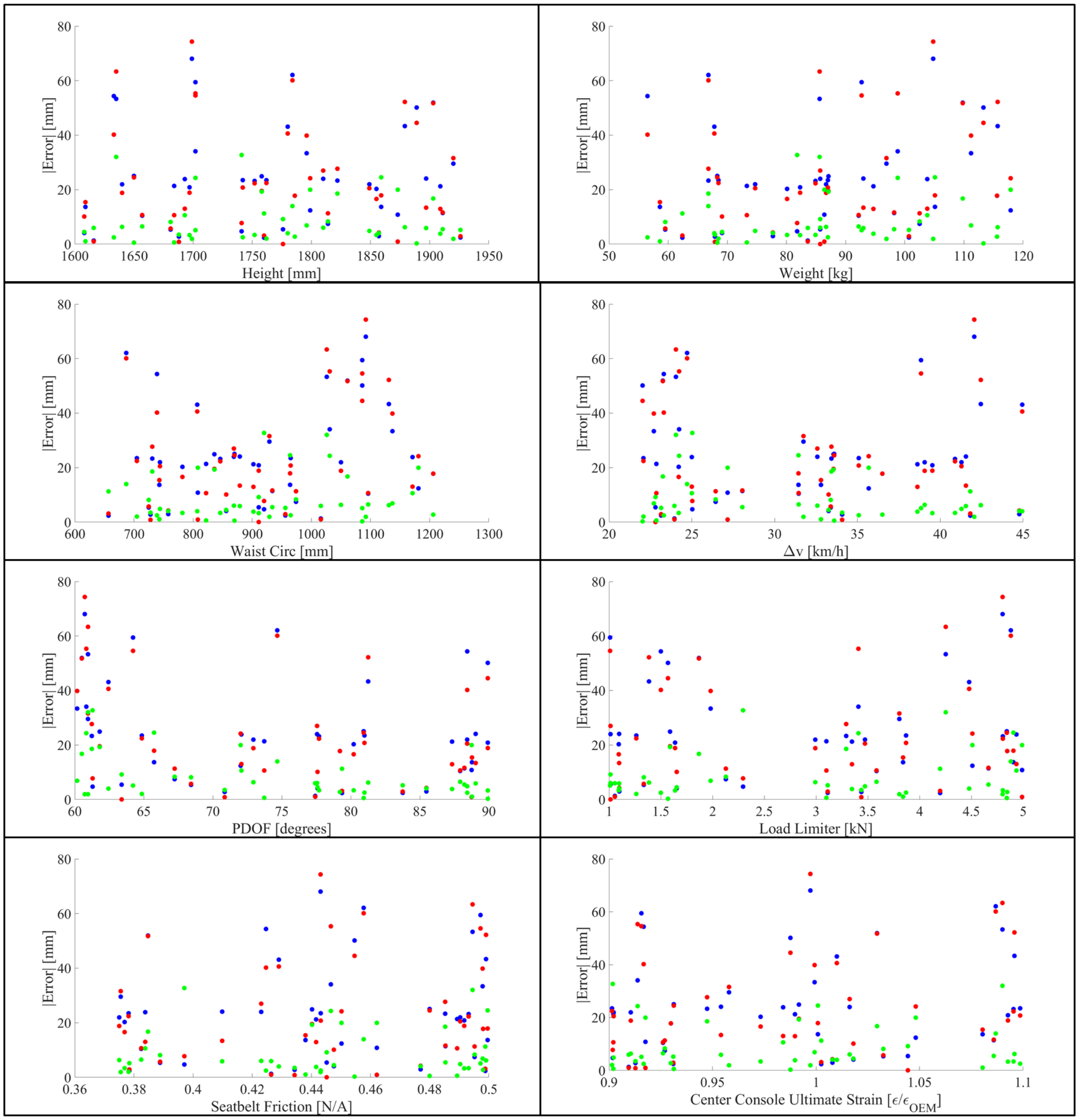

Figure K.21: Maximum lateral head excursion prediction error in iteration 8 (blue: linear regression; red: LASSO regression; green: NN)

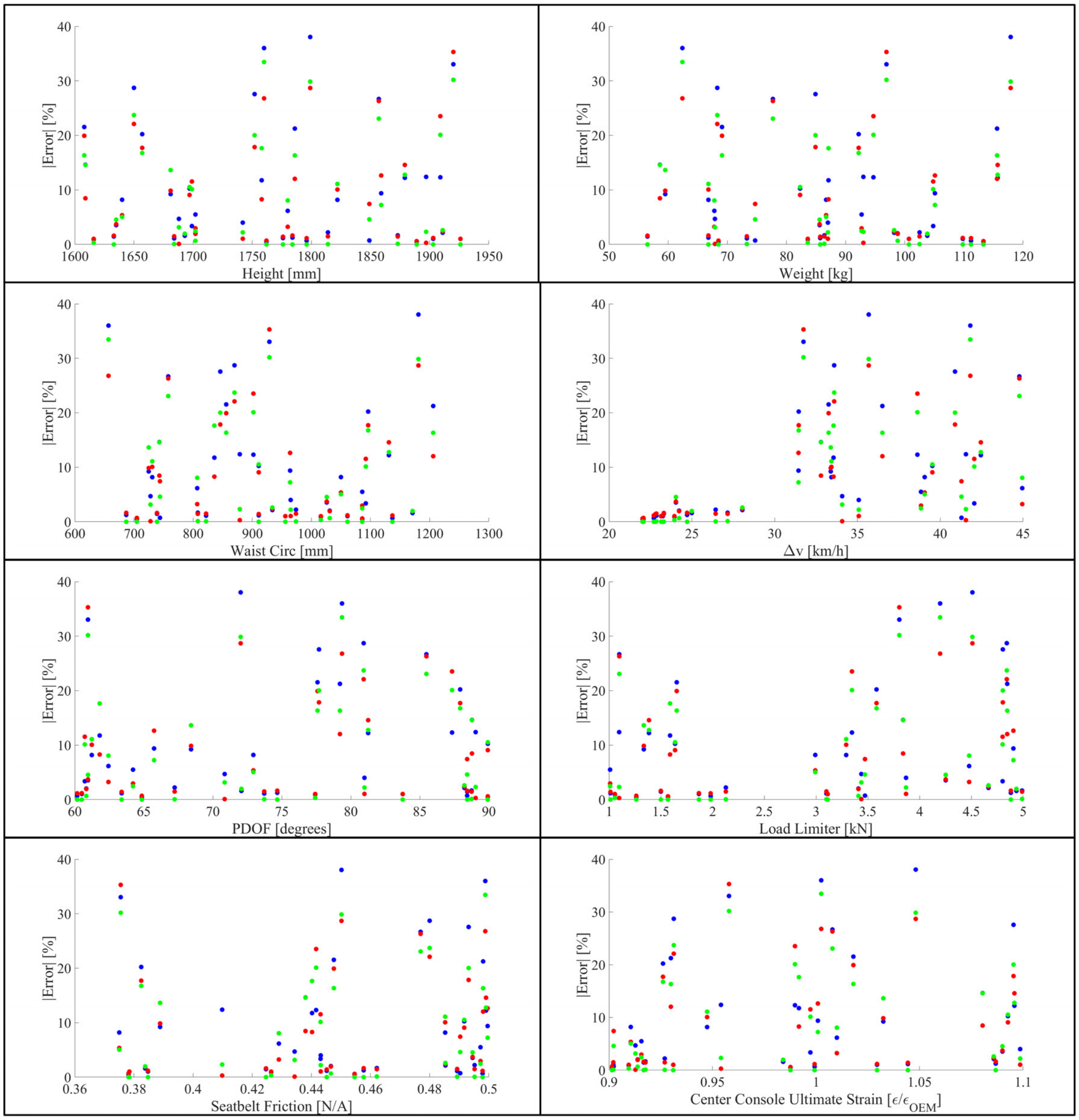

Figure K.22: 3+ fractured ribs prediction error in iteration 8 (blue: logistic regression; red: LASSO logistic regression; green: NN)

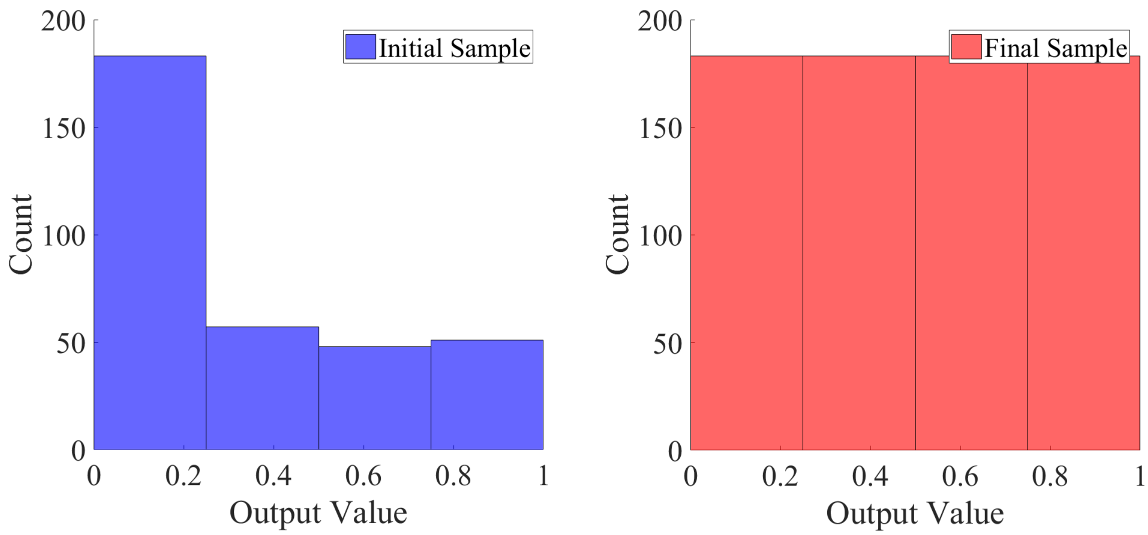

Figure K.23: Training output histogram before and after oversampling in the last iteration

Bibliography

AAAM. The Abbreviated Injury Scale, 2015.

R. Alejo, V. García, J. M. Sotoca, R. A. Mollineda, and J. S. Sánchez. Improving the performance of the RBF neural networks trained with imbalanced samples. In *International Work-Conference on Artificial Neural Networks*, pages 162–169. Springer, 2007.

Y. Auffray, P. Barbillon, and J.-M. Marin. Maximin design on non hypercube domains and kernel interpolation. *Statistics and Computing*, 22(3):703–712, May 2012. ISSN 0960-3174, 1573-1375. doi: 10.1007/s11222-011-9273-9. URL http://link.springer.com/10.1007/s11222-011-9273-9.

G. T. Bahouth, D. Murakhovskiy, K. H. Digges, H. Rist, and R. Wiik. Opportunities for reducing far-side casualties. In *24th International Technical Conference on the Enhanced Safety of Vehicles*, Gothenburg, Sweden, 2015.

D. Bose, M. Segui-Gomez, ScD, and J. R. Crandall. Vulnerability of Female Drivers Involved in Motor Vehicle Crashes: An Analysis of US Population at Risk. *American Journal of Public Health*, 101(12):2368–2373, Dec. 2011. ISSN 0090-0036, 1541-0048. doi: 10.2105/AJPH.2011.300275. URL http://ajph.aphapublications.org/doi/10.2105/AJPH.2011.300275.

M. L. Brumbelow, B. C. Mueller, and R. A. Arbelaez. Occurrence of serious injury in real-world side impacts of vehicles with good side-impact protection ratings. *Traffic Injury Prevention*, 16(sup1):S125–S132, June 2015. ISSN 1538-9588, 1538-957X.

doi: 10.1080/15389588.2015.1020112. URL http://www.tandfonline.com/doi/full/10.1080/15389588.2015.1020112.

W. L. Buntine and A. S. Weigend. Bayesian back-propagation. *Complex systems*, 5 (6):603–643, 1991.

F. Burden and D. Winkler. Bayesian Regularization of Neural Networks. In D. J. Livingstone, editor, *Artificial Neural Networks: Methods and Applications*, Methods in Molecular Biology, pages 23–42. Humana Press, Totowa, NJ, 2009. ISBN 978-1-60327-101-1. doi: 10.1007/978-1-60327-101-1_3. URL https://doi.org/10.1007/978-1-60327-101-1_3.

N. V. Chawla, K. W. Bowyer, L. O. Hall, and W. P. Kegelmeyer. SMOTE: Synthetic Minority Over-sampling Technique. *Journal of Artificial Intelligence Research*, 16: 321–357, June 2002. ISSN 1076-9757. doi: 10.1613/jair.953. URL https://www.jair.org/index.php/jair/article/view/10302.

J. R. Cochran, Q. Zhang, and J. R. Kerrigan. Comparison of human body model and PMHS occupant kinematic response in laboratory rollover tests. page 16, 2015.

J. Crandall, D. Bose, J. Forman, C. Untaroiu, C. Arregui-Dalmases, C. Shaw, and J. Kerrigan. Human surrogates for injury biomechanics research. *Clinical Anatomy*, 24(3):362–371, Apr. 2011. ISSN 08973806. doi: 10.1002/ca.21152. URL http://doi.wiley.com/10.1002/ca.21152.

K. Digges and D. Dalmotas. Injuries to restrained occupants in far-side crashes. *SAE Technical Paper*, 2001.

C. F. Dormann, J. Elith, S. Bacher, C. Buchmann, G. Carl, G. Carré, J. R. G. Marquéz, B. Gruber, B. Lafourcade, P. J. Leitão, T. Münkemüller, C. McClean, P. E. Osborne, B. Reineking, B. Schröder, A. K. Skidmore, D. Zurell, and S. Lautenbach. Collinearity: a review of methods to deal with it and a simulation study evaluating their performance. *Ecography*, 36(1):27–46, 2013. ISSN 1600-0587.

doi: 10.1111/j.1600-0587.2012.07348.x. URL https://onlinelibrary.wiley.com/doi/abs/10.1111/j.1600-0587.2012.07348.x.

J. D. Ellway, M. Van Ratingen, T. Versmissen, S. van Montfort, T. Langner, J. Dobberstein, P. Goutas, P. Gay, A. Malak, and C. Denker. *The advanced European mobile deformable barrier specification for use in Euro NCAP side impact testing*. Nhtsa, 2013.

J. L. Elman. Finding Structure in Time. *Cognitive Science*, 14(2):179–211, Mar. 1990. ISSN 03640213. doi: 10.1207/s15516709cog1402_1. URL http://doi.wiley.com/10.1207/s15516709cog1402_1.

B. Fildes, L. Sparke, O. Bostrom, F. Pintar, N. Yoganandan, and A. Morris. Suitability of current side impact test dummies in far-side impacts. In *IRCOBI Conference*, Munich, Germany, 2002.

B. Fildes, M. Fitzharris, H. C. Gabler, K. Digges, and S. Smith. Chest and abdominal injuries to occupants in far side crashes. In *20th International Technical Conference on Enhanced Safety of Vehicles*, Lyon, France, 2007.

J. Forman, G. S. Poplin, C. G. Shaw, T. L. McMurry, K. Schmidt, J. Ash, and C. Sunnevang. Automobile injury trends in the contemporary fleet: Belted occupants in frontal collisions. *Traffic Injury Prevention*, 0(0):1–6, July 2019. ISSN 1538-9588. doi: 10.1080/15389588.2019.1630825. URL https://doi.org/10.1080/15389588.2019.1630825.

J. L. Forman, R. W. Kent, K. Mroz, B. Pipkorn, O. Bostrom, and M. Segui-Gomez. Predicting rib fracture risk with whole-body finite element models: development and preliminary evaluation of a probabilistic analytical framework. In *Annals of Advances in Automotive Medicine/Annual Scientific Conference*, volume 56, page 109. Association for the Advancement of Automotive Medicine, 2012.

J. L. Forman, F. Lopez-Valdes, D. J. Lessley, P. Riley, M. Sochor, T. Seacrist, K. B. Arbogast, H. Tanji, and K. Higuchi. Occupant kinematics and shoulder belt retention in far-side lateral and oblique collisions: a parametric study. *Stapp Car Crash Journal*, 57:343–385, Nov. 2013.

R. Frampton, R. Welsh, P. Thomas, and P. Fay. The importance of non-struck side occupants in side collisions. *Journal of Crash Prevention and Injury Control*, 2 (2):151–163, Aug. 2000. ISSN 1028-6586. doi: 10.1080/10286580008902560. URL https://doi.org/10.1080/10286580008902560.

M. Frank, V. Schorge, K. Hegenscheid, A. Angermaier, A. Ekkernkamp, N. Hosten, R. Puls, and S. Langner. Sturdivan's formula revisited: MRI assessment of anterior chest wall thickness for injury risk prediction of blunt ballistic impact trauma. *Forensic Science International*, 212(1):110–114, Oct. 2011. ISSN 0379-0738. doi: 10.1016/j.forsciint.2011.05.022. URL http://www.sciencedirect.com/science/article/pii/S0379073811002532.

H. C. Gabler, M. Fitzharris, J. Scully, B. N. Fildes, K. Digges, and L. Sparke. Far side impact injury risk for belted occupants in Australia and the United States. In *19th International Technical Conference on Enhanced Safety of Vehicles*, Washington D.C., June 2005.

F. S. Gayzik, D. P. Moreno, N. A. Vavalle, A. C. Rhyne, and J. D. Stitzel. Development of the global human body models consortium mid-sized male full body model. In *International Workshop on Human Subjects for Biomechanical Research*, volume 39, 2011.

C. Gehre, H. Gades, and P. Wernicke. Objective Rating of Signals Using Test and Simulation Responses. *Proceedings: International Technical Conference on the Enhanced Safety of Vehicles*, 2009. URL https://www.safetylit.org/citations/index.php?fuseaction=citations.viewdetails&citationIds[]=citjournalarticle_245656_38.

C. C. Gordon, C. L. Blackwell, B. Bradtmiller, J. L. Parham, P. Barrientos, S. P. Paquette, B. D. Corner, J. M. Carson, J. C. Venezia, and B. M. Rockwell. 2012

Anthropometric survey of US Army personnel: Methods and summary statistics. Technical Report Natick/TR-15/007, U.S. Army Natick Soldier Research Development and Engineering Center, MA, 2014. URL https://www.hsdl.org/?view&did=762624.

W. N. Hardy, M. J. Mason, C. D. Foster, C. S. Shah, J. M. Kopacz, K. H. Yang, A. I. King, J. Bishop, M. Bey, W. Anderst, and S. Tashman. A Study of the Response of the Human Cadaver Head to Impact. *Stapp car crash journal*, 51:17–80, Oct. 2007. ISSN 1532-8546. URL https://www.ncbi.nlm.nih.gov/pmc/articles/PMC2474809/.

A. E. Hoerl and R. W. Kennard. Ridge regression: applications to nonorthogonal problems. *Technometrics*, 12(1):69–82, 1970.

W. T. Hollowell, H. C. Gabler, S. L. Stucki, S. Summers, and J. R. Hackney. Review of potential test procedures for FMVSS No. 208. *National Highway Traffic Safety Administration,(September 1998)*, page 110, 1998.

J. Hu, K. Zhang, A. Fanta, M. Jones, M. Reed, M. Neal, J.-T. Wang, C.-H. Lin, and L. Cao. Stature and Body Shape Effects on Driver Injury Risks in Frontal Crashes: A Parametric Human Modelling Study. page 12, 2017.

S. H. Huddleston and G. G. Brown. Machine Learning. In J. J. Cochran, editor, *INFORMS analytics body of knowledge*, Wiley series in operations research and management science. John Wiley and Sons, Inc, Hoboken, NJ, 2019. ISBN 978-1-119-48321-2. OCLC: on1042351047.

E. Hwang, J. Hallman, K. Klein, J. Rupp, M. Reed, and J. Hu. Rapid Development of Diverse Human Body Models for Crash Simulations through Mesh Morphing. Technical report, SAE Technical Paper, 2016.

ISO. Road vehicles. Anthropomorphic side impact dummy. Lateral impact response requirements to assess the biofidelity of the dummy. Technical Report ISO/TR-9790, 1999.

ISO. ISO 15830 Road vehicles. Design and performance specifications for the WorldSID 50th percentile male side-impact dummy. Part 1, 2013.

G. James, D. Witten, T. Hastie, and R. Tibshirani. *An Introduction to Statistical Learning*, volume 103 of *Springer Texts in Statistics*. Springer New York, New York, NY, 2013. ISBN 978-1-4614-7137-0 978-1-4614-7138-7. doi: 10.1007/978-1-4614-7138-7. URL http://link.springer.com/10.1007/978-1-4614-7138-7.

R. Jin, W. Chen, and T. Simpson. Comparative studies of metamodelling techniques under multiple modelling criteria. *Structural and Multidisciplinary Optimization*, 23 (1):1–13, Dec. 2001. ISSN 1615-147X, 1615-1488. doi: 10.1007/s00158-001-0160-4. URL http://link.springer.com/10.1007/s00158-001-0160-4.

C. J. Kahane. Lives saved by vehicle safety technologies and associated Federal Motor Vehicle Safety Standards, 1960 to 2012Passenger cars and LTVsWith reviews of 26 FMVSS and the effectiveness of their associated safety technologies in reducing fatalities, injuries, and crashes. Technical Report DOT HS 812 069, National Highway Traffic Safety Administration, 2015.

M. Katagiri, J. Zhao, J. Kerrigan, R. Kent, and J. Forman. Comparison of Whole-Body Kinematic Behaviour of the GHBMC Occupant Model to PMHS in Far-Side Sled Tests. In *IRCOBI Conference Proceedings*, page 15, Malaga, Spain, 2016.

R. W. Kent, J. L. Forman, and O. Bostrom. Is There Really a Cushion Effect?: A Biomechanical Investigation of Crash Injury Mechanisms in the Obese. *Obesity*, 18(4):749–753, 2010. ISSN 1930-739X. doi: 10.1038/oby.2009.315. URL https://onlinelibrary.wiley.com/doi/abs/10.1038/oby.2009.315.

T. Kim, G. Shaw, D. Lessley, G. Park, J. Crandall, A. Svendsen, B. Whitcomb, M. Ayyagari, P. Mishra, and C. Markusic. Biofidelity evaluation of WorldSID and ES-2re under side impact conditions with and without airbag. *Accident Analysis & Prevention*, 90:140–151, May 2016. ISSN 00014575. doi: 10.1016/j.aap.2016.02.010. URL https://linkinghub.elsevier.com/retrieve/pii/S0001457516300434.

S. Kirkpatrick, C. D. Gelatt, and M. P. Vecchi. Optimization by Simulated Annealing. *Science*, 220(4598):671–680, 1983. ISSN 0036-8075. URL https://www.jstor.org/stable/1690046.

C. Klug, F. Feist, M. Raffler, W. Sinz, P. Petit, and J. Ellway. Development of a Procedure to Compare Kinematics of Human Body Models for Pedestrian Simulations. page 23, 2017.

B. Krawczyk. Learning from imbalanced data: open challenges and future directions. *Progress in Artificial Intelligence*, 5(4):221–232, Nov. 2016. ISSN 2192-6360. doi: 10.1007/s13748-016-0094-0. URL https://doi.org/10.1007/s13748-016-0094-0.

S. Lawrence, C. L. Giles, and A. C. Tsoi. What size neural network gives optimal generalization? Convergence properties of backpropagation. Technical report, 1998.

D. Lessley, G. Shaw, P. Riley, J. Forman, and J. Crandall. Assessment and validation of a methodology for measuring anatomical kinematics of restrained occupants during motor vehicle collisions. *Journal of Biosensors and Bioelectronics*, S1, 2011.

G. M. Mackay, J. Hill, S. Parkin, and J. A. R. Munns. Restrained occupants on the nonstruck side in lateral collisions. *Accident Analysis & Prevention*, 25(2):147–152, 1993.

M. A. Manary, L. W. Schneider, C. C. Flannagan, and B. H. Eby. Evaluation of the SAE J826 3-D manikin measures of driver positioning and posture. Technical report, SAE Technical Paper, 1994.

D. Masko and P. Hensman. *The impact of imbalanced training data for convolutional neural networks.* 2015.

E. NCAP. Side impact mobile deformable barrier testing protocol. Technical report, Euro NCAP, Leuven, Belgium, Nov. 2017a.

E. NCAP. Euro NCAP 2025 Roadmap. Technical report, Euro NCAP, Leuven, Belgium, Sept. 2017b.

E. NCAP. Far side occupant test and assessment procedure. Technical report, Euro NCAP, Leuven, Belgium, Nov. 2017c.

NHTSA. Federal automated vehicles policy, Sept. 2016. URL https://www.transportation.gov/AV/federal-automated-vehicles-policy-september-2016.

NHTSA. Traffic Safety Facts 2017. Technical Report DOT HS 812 806, U.S. Department of Transportation, Washington, DC, Sept. 2019.

A. Nicholas Refenes, A. Zapranis, and G. Francis. Stock performance modeling using neural networks: A comparative study with regression models. *Neural Networks*, 7 (2):375–388, Jan. 1994. ISSN 08936080. doi: 10.1016/0893-6080(94)90030-2. URL http://linkinghub.elsevier.com/retrieve/pii/0893608094900302.

B. Nie, Y. Xia, Q. Zhou, J. Huang, B. Deng, and M. Neal. Response surface generation for kinematics and injury prediction in pedestrian impact simulations. *SAE International journal of transportation safety*, 1(2):286–296, 2013.

M. Otto. *Chemometrics: statistics and computer application in analytical chemistry*. John Wiley & Sons, 2016.

C. I. Paek, G. Shaw, J. Crandall, Y. H. Baek, and O. S. Ko. Responses of Hybrid-III 50th and Thor-NT 50th in Sled Tests With Different Seat Belt Pretensioner Configurations. In *ASME 2006 International Mechanical Engineering Congress and Exposition*, pages 27–40. American Society of Mechanical Engineers, 2006. URL http://proceedings.asmedigitalcollection.asme.org/proceeding.aspx?articleid=1604660. 00003.

G. Park, T. Kim, J. R. Crandall, and C. Arregui. Comparison of Kinematics of GHBMC to PMHS on the Side Impact Condition. page 12, 2013.

D. Perez-Rapela, C. Markusic, B. Whitcomb, B. Pipkorn, J. Forman, J.-P. Donlon, S. Montesinos-Acosta, and J. Crandall. Comparison of WorldSID to PMHS kinematics in far-side impact. In *IRCOBI Conference Proceedings*, Athens, Greece, Sept. 2018.

D. Perez-Rapela, J.-P. Donlon, J. L. Forman, J. R. Crandall, B. Pipkorn, B. K. Shurtz, and C. Markusic. PMHS and WorldSID kinematic and injury response in far-side events in a vehicle-based test environment. *Stapp Car Crash Journal*, 63, Nov. 2019a.

D. Perez-Rapela, C. Markusic, B. Whitcomb, B. Pipkorn, J. Forman, J.-P. Donlon, S. Montesinos-Acosta, and J. Crandall. Comparison of the simplified GHBMC to PMHS kinematics in far-side impact. In *IRCOBI Conference Proceedings*, Florence, Italy, Sept. 2019b.

A. Petitjean, X. Trosseille, N. Praxl, D. Hynd, and A. Irwin. Injury Risk Curves for the WorldSID 50th Male Dummy. Technical report, SAE Technical Paper, 2012.

F. A. Pintar, N. Yoganandan, B. D. Stemper, O. Bostrom, S. W. Rouhana, K. H. Digges, and B. N. Fildes. Comparison of PMHS, WorldSID, and THOR-NT responses in simulated far side impact. *Stapp Car Crash Journal*, 51:313–360, Oct. 2007.

PIPER-Project, Nov. 2019. URL http://www.piper-project.eu/.

B. Pipkorn, K. Larsson, D. P. Rapela, C. Markusic, B. Whitcomb, M. Ayyagari, and C. Sunnevång. Occupant protection in far-side impacts. In *IRCOBI Conference Proceedings*, page 30, Athens, Greece, Sept. 2018.

D. Poulard, Q. Zhang, J. R. Cochran, B. Gepner, and J. Kerrigan. Quantitative evaluation of the occupant kinematic response of the THUMS 50th-percentile male model relative to PMHS laboratory rollover tests. *Traffic Injury Prevention*, 17 (sup1):101–108, Sept. 2016. ISSN 1538-9588. doi: 10.1080/15389588.2016.1192282. URL https://doi.org/10.1080/15389588.2016.1192282.

A. Prasad and D. Weston. NHTSA's rear seat safety research. In *The 22nd International Technical Conference on the Enhanced Safety of Vehicles, Washington DC*, 2011.

L. Pronzato and W. G. Müller. Design of computer experiments: space filling and beyond. *Statistics and Computing*, 22(3):681–701, May 2012. ISSN 0960-3174, 1573-1375. doi: 10.1007/s11222-011-9242-3. URL http://link.springer.com/10.1007/s11222-011-9242-3.

J. O. Rawlings, S. G. Pantula, and D. A. Dickey. *Applied regression analysis: a research tool*. Springer texts in statistics. Springer, New York, 2nd ed edition, 1998. ISBN 978-0-387-98454-4.

D. H. Robbins. Anthropometric specifications for mid-sized male dummy, Volume 2, Report number UMTRI-83-53-2. Technical report, The University of Michigan Transportation Research Institute, Ann Arbor, MI, 1983.

J. D. Rodriguez, A. Perez, and J. A. Lozano. Sensitivity Analysis of k-Fold Cross Validation in Prediction Error Estimation. *IEEE Transactions on Pattern Analysis and Machine Intelligence*, 32(3):569–575, Mar. 2010. ISSN 0162-8828. doi: 10.1109/TPAMI.2009.187.

G. E. Ryb, P. C. Dischinger, E. R. Braver, C. A. Burch, S. M. Ho, and J. A. Kufera. Expected differences and unexpected commonalities in mortality, injury severity, and injury patterns between near versus far occupants of side impact crashes. *The Journal of Trauma: Injury, Infection, and Critical Care*, 66(2):499–503, Feb. 2009. ISSN 0022-5282. doi: 10.1097/TA.0b013e3181615626. URL https://insights.ovid.com/crossref?an=00005373-200902000-00032.

SAE. SAE J224: Collision Deformation Classification, 1980.

SAE. Vehicle Dynamics Terminology, Jan. 2008.

T. J. Santner, B. J. Williams, and W. I. Notz. Space-Filling Designs for Computer Experiments. In T. J. Santner, B. J. Williams, and W. I. Notz, editors, *The Design* *and Analysis of Computer Experiments*, Springer Series in Statistics, pages 121–161. Springer New York, New York, NY, 2003. ISBN 978-1-4757-3799-8. doi: 10.1007/978-1-4757-3799-8_5. URL https://doi.org/10.1007/978-1-4757-3799-8_5.

D. Schwartz, B. Guleyupoglu, B. Koya, J. D. Stitzel, and F. S. Gayzik. Development of a Computationally Efficient Full Human Body Finite Element Model. *Traffic Injury Prevention*, 16(sup1):S49–S56, June 2015. ISSN 1538-9588. doi: 10.1080/15389588.2015.1021418. URL https://doi.org/10.1080/15389588.2015.1021418.

C. G. Shaw, D. J. Lessley, J. H. Ash, J. R. Crandall, and D. P. Parent. Response Comparison for the Hybrid III, THOR Mod Kit with SD-3 Shoulder, and PMHS in a Simulated Frontal Crash. In *23rd ESV Conference, Paper*, 2013. URL http://www-esv.nhtsa.dot.gov/Proceedings/23/files/23ESV-000130.PDF. 00001.

G. Shaw, J. Crandall, and J. Butcher. Comparative evaluation of the THOR advanced frontal crash test dummy. *International Journal of Crashworthiness*, 7(3):239–254, 2002. URL http://www.tandfonline.com/doi/abs/10.1533/cras.2002.0217. 00010.

G. Shaw, D. Parent, S. Purtsezov, D. Lessley, J. Crandall, R. Kent, H. Guillemot, S. A. Ridella, E. Takhounts, and P. Martin. Impact response of restrained PMHS in frontal sled tests: skeletal deformation patterns under seat belt loading. *Stapp car crash journal*, 53:1–48, 2009. URL http://people.virginia.edu/~rwk3c/papers/Shaw2009-Impact%20response%20of%20restrained%20PMHS%20in%20frontal%20sled%20tests.pdf. 00057.

J. A. Stimson, E. G. Carmines, and R. A. Zeller. Interpreting polynomial regression. *Sociological Methods & Research*, 6(4):515–524, 1978.

C. Sunnevång, E. Rosén, O. Boström, and U. Lechelt. Thoracic Injury Risk as a Function of Crash Severity Car-to-car Side Impact Tests with WorldSID Compared to Real-life Crashes. page 10, 2010.

C. Sunnevång, E. Lecuyer, D. Hynd, J. Carroll, D. Kruse, and O. Boström. Evaluation of Near-Side Oblique Frontal Impacts Using THOR With SD3 Shoulder. *Traffic Injury Prevention*, 15(sup1):S96–S102, Sept. 2014. ISSN 1538-9588, 1538-957X. doi: 10.1080/15389588.2014.934367. URL http://www.tandfonline.com/doi/abs/10.1080/15389588.2014.934367.

J. Thomason. The influence of fibre length and concentration on the properties of glass fibre reinforced polypropylene: 5. Injection moulded long and short fibre PP. *Composites Part A: Applied Science and Manufacturing*, 33(12):1641–1652, Dec. 2002. ISSN 1359835X. doi: 10.1016/S1359-835X(02)00179-3. URL http://linkinghub.elsevier.com/retrieve/pii/S1359835X02001793.

R. Tibshirani. Regression Shrinkage and Selection Via the Lasso. *Journal of the Royal Statistical Society: Series B (Methodological)*, 58(1):267–288, Jan. 1996. ISSN 0035-9246. doi: 10.1111/j.2517-6161.1996.tb02080.x. URL http://doi.wiley.com/10.1111/j.2517-6161.1996.tb02080.x.

L. Torgo, P. Branco, R. P. Ribeiro, and B. Pfahringer. Resampling strategies for regression. *Expert Systems*, 32(3):465–476, 2015. ISSN 1468-0394. doi: 10.1111/exsy.12081. URL https://onlinelibrary.wiley.com/doi/abs/10.1111/exsy.12081.

F. Trochu. A contouring program based on dual kriging interpolation. *Engineering with Computers*, 9(3):160–177, Sept. 1993. ISSN 1435-5663. doi: 10.1007/BF01206346. URL https://doi.org/10.1007/BF01206346.

S. Umale, N. Yoganandan, F. A. Pintar, and M. W. J. Arun. Factors influencing the effectiveness of occupant retention under far-side impacts: A parametric study. *Journal of the Mechanical Behavior of Biomedical Materials*, 84:235–248, Aug. 2018. ISSN 1751-6161. doi: 10.1016/j.jmbbm.2018.05.021. URL http://www.sciencedirect.com/science/article/pii/S1751616118307331.

J. Vandekerckhove. General simulated annealing algorithm, June 2008.

URL https://www.mathworks.com/matlabcentral/fileexchange/10548-general-simulated-annealing-algorithm.

D. C. Viano and C. S. Parenteau. Severe injury to near- and far-seated occupants in side impacts by crash severity and belt use. *Traffic Injury Prevention*, 11(1):69–78, Jan. 2010. ISSN 1538-9588, 1538-957X. doi: 10.1080/15389580903479178. URL http://www.tandfonline.com/doi/abs/10.1080/15389580903479178.

D. C. Viano, C. S. Parenteau, and M. L. Edwards. Crash Injury Risks for Obese Occupants Using a Matched-Pair Analysis. *Traffic Injury Prevention*, 9(1):59–64, Feb. 2008. ISSN 1538-9588, 1538-957X. doi: 10.1080/15389580701737645. URL http://www.tandfonline.com/doi/abs/10.1080/15389580701737645.

WHO. Global Status Report on Road Safety : Time for Action. Technical report, World Health Organization, Geneva, Switzerland, 2017.

G. Wu, S. Siegler, P. Allard, C. Kirtley, A. Leardini, D. Rosenbaum, M. Whittle, D. D. DLima, L. Cristofolini, H. Witte, and others. ISB recommendation on definitions of joint coordinate system of various joints for the reporting of human joint motionpart I: ankle, hip, and spine. *Journal of biomechanics*, 35(4):543–548, 2002. URL http://www.sciencedirect.com/science/article/pii/S0021929001002226. 01370.

S. Xiao, J. Yang, J. Forman, M. Panzer, Z. Xiao, and J. Crandall. Effect of Contact Friction between Seatbelt and Human Body Model on Simulation of Rib Fracture in Frontal Impact. In *2016 Eighth International Conference on Measuring Technology and Mechatronics Automation (ICMTMA)*, pages 255–257, Mar. 2016. doi: 10.1109/ICMTMA.2016.69.

K. H. Yang, J. Hu, N. A. White, A. I. King, C. C. Chou, and P. Prasad. Development of numerical models for injury biomechanics research: a review of 50 years of publications in the Stapp Car Crash Conference. Technical report, SAE Technical Paper, 2006.

N. Yoganandan, M. W. J. Arun, D. E. Halloway, F. A. Pintar, D. J. Maiman, A. Szabo, and R. W. Rudd. Crash characteristics and injury patterns of restrained front seat occupants in far-side impacts. *Traffic Injury Prevention*, 15(sup1):S27–S34, Sept. 2014. ISSN 1538-9588, 1538-957X. doi: 10.1080/15389588.2014.935771. URL http://www.tandfonline.com/doi/abs/10.1080/15389588.2014.935771.

H. Yu and B. M. Wilamowski. Levenberg-marquardt training. In *Industrial electronics handbook*, volume 5, page 1. 2011.

X. Zhou, K. Sun, P. Roos, P. Li, and B. Corner. Anthropometry model generation based on ANSUR II database. *Int. J. Digit. Hum*, 1(4):321–343, 2016.